Technische Universität München

Max-Planck-Institut für Quantenoptik

Optical microcavities for quantum communication with single atoms

Manuel Uphoff

Vollständiger Abdruck der von der Fakultät für Physik der Technischen Universität München zur Erlangung des akademischen Grades eines

Doktors der Naturwissenschaften (Dr. rer. nat.)

genehmigten Dissertation.

Vorsitzender:		Prof. Dr. Michael Knap
Prüfer der Dissertation:	1.	Hon.-Prof. Dr. Gerhard Rempe
	2.	Prof. Jonathan J. Finley, Ph.D.
	3.	Prof. Dr. Jakob Reichel (nur schriftliche Beurteilung)

Die Dissertation wurde am 19.07.2016 bei der Technischen Universität München eingereicht und durch die Fakultät für Physik am 04.10.2017 angenommen.

Abstract

Long-distance quantum communication requires a highly efficient interface between light and matter. This thesis describes optical Fabry–Perot microcavities based on CO_2 laser-machined mirror substrates that are ideal to couple single photons and single atoms. The surfaces of the mirrors show ultra-low roughness, which enables cavities with a finesse of up to 1.9×10^5. Because of the small radii of curvature on the order of 100 µm achieved with this technique, deviations from the paraxial approximation become relevant, resulting in a frequency splitting of polarization eigenmodes. A theoretical model has been derived and confirmed by measured values and this understanding can be used to tailor this frequency splitting for specific applications. A prime application for these cavities is heralded entanglement generation between single atoms and telecom-wavelength photons, which is proposed and analyzed in this thesis. In a theoretical study of a quantum repeater protocol based on this scheme and cavity-assisted quantum gates, remote entanglement is generated faster than without repeater nodes if the distance between the end nodes exceeds 50 km.

Zusammenfassung

Quantenkommunikation über lange Distanzen erfordert eine hocheffiziente Schnittstelle zwischen Licht und Materie. In der vorliegenden Arbeit werden optische Fabry-Perot-Mikroresonatoren beschrieben, deren Spiegelsubstrate mit einem CO_2-Laser bearbeitet wurden und die ideal geeignet sind, um einzelne Photonen und einzelne Atomen miteinander zu koppeln. Die Spiegeloberflächen zeichnen sich durch extrem niedrige Rauhigkeiten aus, sodass Resonatoren mit einer Finesse von bis zu 1.9×10^5 erreicht werden. Aufgrund der kleinen Krümmungsradien in der Größenordnung von 100 µm, die mit dieser Methode erreicht wurden, werden Abweichungen von der paraxialen Näherung relevant, die zu einer Frequenzufspaltung der Polarisationseigenmoden führen. Es wurde ein theoretisches Modell erstellt und mit Messungen verifiziert, das benutzt werden kann, um die Frequenzaufspaltung zu kontrollieren. Eine wichtige Anwendung für diese Resonatoren ist die angekündigte Verschränkungserzeugung zwischen Einzelatomen und Photonen bei Telekomwellenlängen, die in dieser Arbeit vorgeschlagen und untersucht wird. In einer theoretischen Analyse eines Quantenrepeaterprotokolls, das auf diesem Schema und resonatorunterstützten Quantengattern basiert, wird Verschränkung zwischen zwei Orten schneller erzeugt als ohne Repeaterstationen, wenn die Entfernung zwischen diesen 50 km übersteigt.

Contents

1 Introduction

Thought experiments involving distant quantum objects that had become entangled due to local interactions were the key to deduce the seemingly paradoxical behavior predicted by quantum mechanics [1–3]. The goal of *quantum communication* is to bring these experiments into the realm of reality by transporting quantum states over long distances. Triggered by the discovery of Bell's inequalities [4], quantum communication has started as the effort to verify these quantum mechanical predictions [5] and since then they have been subject to increasingly stringent tests [6–10]. Besides these investigations of fundamental questions, there have also been numerous proposals for applications of quantum communication protocols. Of these, quantum key distribution [11, 12] has attracted the most attention, because of its immediate applicability. It promises the distribution of a physically secure key without requiring assumptions about the transmission channel and in case of device-independent protocols [13, 14] even trust in the key-generating devices themselves can be significantly relaxed. In addition to the secure transfer of classical information, the development of quantum computing might add the demand to transfer quantum information. The quantum state resulting from a complex calculation could be deterministically transferred to another location by the means of quantum teleportation [15]. This would ultimately enable distributed quantum computing [16], which would connect several smaller quantum computers to solve a complex problem and has been proposed as one of the roads toward a large-scale quantum computer [17].

Light in the visible and near infrared spectrum is the obvious choice as the physical system to implement quantum communication, because quantum states encoded in photonic states can travel at the speed of light to cover large distances with minimal decoherence, allowing for the generation of widely separated entangled states [18]. But even at optimized wavelengths, photons are eventually scattered or absorbed in any medium, limiting the distance for quantum communication protocols. There are two possibilities to circumvent this limitation. At night, satellite relays could enable quantum communication between distant locations through the vacuum in space [19]. The alternative is to divide a transmission line into parts with nodes running a quantum repeater protocol in between [20], which could enhance the communication rate. In combination with photons at telecom wavelength, this could extend the ability to perform quantum communication via optical fiber links between distant locations.

However, quantum repeater protocols require the ability to store a quantum state and then retrieve it on demand, which cannot be done in purely photonic systems. Therefore, a material quantum system is necessary that offers a long coherence time and that can be efficiently interfaced with photonic states. This has triggered very active and ongoing research into light-matter interfaces at the quantum level and very different physical systems have been developed that could meet these demands. These include many-body systems like atomic ensembles [21–24] and ion-doped solids [25], single-particle-like states in solid state systems embedded in nanophotonic structures [26–28], and neutral atoms

and ions coupled to optical resonators [29–32]. Yet, no system has been demonstrated with a combination of efficiency and coherence time that is sufficient to implement a quantum repeater protocol that accomplishes a quantum communication task faster than without a repeater.

Single neutral atoms in high-finesse Fabry–Perot cavities show great promise toward this goal: They enable strong coupling between light and matter [33], have been demonstrated to be an efficient interface between qubits encoded in photons and atoms [34–37], and possess states suitable for low-decoherence qubit storage [38, 39]. However, experiments with atoms in optical cavities have not been performed at telecom wavelength so far, due to the lack of suitable transitions from ground states of atoms that are easily laser cooled. If this is not addressed, the range of a repeater system would be severely limited and likely offer no benefit compared to a photonic system operating at telecom wavelength. Although there is active research into wavelength conversion at the single photon level [40, 41], such approaches would come at the price of increased technological overhead and reduced efficiency. The alternative is to use atomic transitions at telecom wavelength between excited states to perform quantum communication directly at the correct wavelength [42]. In this thesis, a cascaded scheme is proposed to efficiently generate heralded entanglement of a photon at telecom wavelength with a single atom. The scheme utilizes one cavity at telecom wavelength to enhance the emission of single photons entangled with the atom into a single-mode fiber with near-unity efficiency. A second cavity, orthogonal to the first, enhances and heralds the transfer of the unstable state created by the entanglement generation process to a stable, long-lived state. With cavity-mediated atom-atom gates [43], this scheme could be extended to a quantum repeater protocol with all functionality integrated into one experimental platform consisting of a quantum repeater node and linear optics.

The realization of a quantum repeater that follows this concept and outperforms direct transmission requires cavities with the following properties: First, the cavities need to have a large coupling strength to the atomic transitions involved in the scheme to ensure a high success probability for emitting photons into the cavities. Second, the cavities need to be single-sided and efficiently couple to a single spatial mode such that almost all generated photons can be collected and distributed to other nodes and detectors. Third, the physical size of the cavities needs to be small enough that it is possible to simultaneously couple an atom to the modes of two perpendicular cavities without the cavity mirrors occluding each other. Satisfying these requirements in one system is very difficult with mirrors based on superpolished substrates and a new type of resonator is required. A recent technological development in this direction has been the invention of CO_2 laser machined mirrors [44–46]. These enable high-finesse mirrors with extremely small radii of curvature [47] and thus tight confinement of the cavity mode to enhance the coupling between a single atom and a single photon to unprecedented values [48]. This high coupling strength would enable cavities that reach the strong-coupling regime even if one of the mirrors is highly transmissive for single-sided operation despite the intrinsic losses of the mirrors. If the mirror substrate is the end facet of an optical fiber [44], the cavity diameter is more than an order of magnitude smaller than for superpolished substrates, facilitating the integration into microscopic systems [48] and enabling new cavity geometries. With an optimized overlap between the mode of such a cavity with the mode of a single-mode fiber, emitted photons would be intrinsically fiber-coupled and could be transmitted over long distances without the use of free-space

optics while profiting from the rapid developments in fiber-optic communication. In order to realize such cavities that would be suitable for a quantum repeater with single atoms, the project described in this thesis was concerned with fabricating fiber mirrors adapted to single-atom experiments, developing improvements in the fabrication method, and exploring the new capabilities that the resulting system would have.

A potential issue for quantum communication experiments with fiber cavities was the frequency splitting of polarization eigenmodes. One distinct feature of high-finesse Fabry–Perot cavities is that degeneracy of their polarization eigenmodes can be achieved [49]. Then, the coupling of the cavity to external, propagating modes is independent of polarization, and the polarization-specific interaction of the atom with the cavity mode only depends on the internal structure of the atom. This allows to encode quantum information in the polarization states of single photons for transfer between nodes in a network [50]. In contrast to cavities based on superpolished substrates, fiber cavities were shown to have a much larger typical splitting of polarization eigenmodes [44, 48], resulting in detrimental effects on experiments [51]. It is therefore essential for future experiments with this type of cavity to understand and control the source of this splitting. During the work described in this thesis, a theoretical model was developed that explains the dominant source of the frequency splitting between polarization eigenmodes to be of geometrical origin and the fabricated cavities were used to validate this model. From the results, it is immediately evident how this splitting can be controlled and tailored to specific applications. Although investigated in the context of CO_2 laser-machined mirrors, the results are not limited to them but apply to all microscopic, high-finesse Fabry–Perot resonators.

The experimentally determined characteristics of the CO_2 laser machined cavities presented in this work enable an estimation of the performance of a quantum repeater that utilizes these cavities according to the presented proposal. Under a few realistic, additional assumptions, this repeater would generate entanglement between nodes separated by 100 km faster than without repeater nodes. This shows that the demonstration of a quantum repeater with single atoms in optical cavities is in reach with current technology.

This thesis is organized in the following way: A brief review of cavity quantum electrodynamics and the requirements for efficient light-matter coupling are given in Ch. 2. The fabrication and characterization of CO_2 laser machined mirrors and cavities based on these are described in Ch. 3. The theoretical and experimental investigation of the frequency splitting of polarization eigenmodes is the subject of Ch. 4. Ch. 5 is concerned with the proposal for a quantum repeater protocol based on the fabricated cavities. The results are summarized and perspectives for future research are discussed in Ch. 6.

2 Cavity QED and optical microcavities

Cavity quantum electrodynamics (QED) describes the interaction of quantum emitters, like single atoms, with a quantized field in a cavity. In the case of an emitter with a dominant dipole emission pattern that is near resonant with the cavity field, the dipole approximation and the rotating-wave approximation can be applied and the system can be described with the Jaynes-Cummings model [52]. In this model the coupling between light and matter can be described by the interaction Hamiltonian

$$H_{\mathrm{int}} = \hbar g \sigma_{\mathrm{eu}} a_{\mathrm{m}} + \hbar g^{\dagger} a_{\mathrm{m}}^{\dagger} \sigma_{\mathrm{ue}}, \tag{2.1}$$

where σ_{eu} is an operator that transfers the emitter from state $|u\rangle$ to excited state $|e\rangle$ and a_{m} is the photon annihilation operator for cavity mode m. The coupling g between the emitter and the cavity field is half the single-photon Rabi frequency and can be calculated as

$$g = \frac{1}{2\hbar} \vec{d}_{\mathrm{eu}} \cdot \vec{E}_{\mathrm{p}}, \tag{2.2}$$

where $\vec{d}_{\mathrm{eu}}$ is the transition dipole matrix element between $|u\rangle$ and $|e\rangle$ and $\vec{E}_{\mathrm{p}}$ is the electric field of a single photon confined to the cavity mode. Using the mode function $\Psi(\vec{r})$ of the cavity normalized to its maximum value and the population decay rate Γ_{eu} from $|e\rangle$ to $|u\rangle$, this expression can be rewritten as

$$g = \sqrt{\frac{3\pi c \Gamma_{\mathrm{eu}}}{2k^2 V_{\mathrm{m}}}} \Psi(\vec{r}), \tag{2.3}$$

where V_{m} is the cavity mode volume, k the wavenumber of the resonant mode, and c the speed of light. The magnitude of this coherent coupling has to be compared to the coupling of the emitter and the cavity mode to the environment. As these processes involve infinitely many modes, they are usually treated as incoherent decay with total field decay rate κ for the cavity mode and total population decay rate of the excited state Γ. A convenient figure of merit for the comparison of these rates to the coupling strength in cavity QED is the single-emitter cooperativity C, defined as

$$C = \frac{g^2}{\kappa \Gamma}. \tag{2.4}$$

In this definition[1], it is equal to half of the Purcell factor [53], which is the relative strength of the emitter decaying via emission of a photon into the cavity compared to free-space decay. To ensure efficient coupling of an atom to the cavity field, the atom–cavity system should feature $C \gg 1$.

[1] Note that multiple definitions of the cooperativity can be found in the literature, which differ by factors of two.

2.1 Single-sided cavities

In order to enable quantum communication with single atoms in optical cavities, efficient coupling of the atom to the cavity field is not the only requirement, but this cavity field also needs to be efficiently coupled to a single spatial mode that can be guided over long distances to reach the next node in a quantum network. The coupling to one defined external mode contributes to the total loss rate of the cavity field κ and can be described with the extrinsic loss rate κ_{ex}. Its value has to be compared to the intrinsic loss rate κ_{in}, which quantifies the decay of the cavity field into undesired channels. These channels are typically scattering and absorption in the cavity and can also include the coupling to additional external modes that are well-defined, but are not part of a particular quantum communication protocol and thus have the same effect as losses inside the cavity. A cavity is called *single-sided* if the extrinsic losses dominate the intrinsic losses of the cavity as well as the scattering rate of the atom, i.e., $\kappa_{\mathrm{ex}} \gg \kappa_{\mathrm{in}}, \Gamma$. The fabrication technology for any type of cavity limits the intrinsic losses that can be achieved. These losses can be compensated by increasing the extrinsic losses to maximize the probability that a photon inside the cavity leaves it in the desired channel. However, this also increases the total losses $\kappa = \kappa_{\mathrm{ex}} + \kappa_{\mathrm{in}}$ and thus reduces the cooperativity, such that a tradeoff between single-sidedness and cooperativity has to be made.

A basic element of quantum communication and the first step in a quantum repeater protocol is the generation of entanglement between a single atom and a single photon [34]. The theoretical description of its implementation by means of fast excitation [54] illustrates the requirements mentioned above for efficient quantum communication. The atom is excited by an external laser with a short π-pulse and can then decay to two degenerate ground states by the emission of a single photon in one of two degenerate polarization modes of a single-sided cavity. The single photon leaves the cavity in one particular spatial mode with high probability, resulting in entanglement between the polarization of the photon leaving the cavity and the atomic state. The system can be modeled as depicted in Fig. 2.1 and is characterized by the decay rates $\Gamma_{1,2}$ from the excited states to the ground states that form the atomic qubit, the corresponding cavity coupling strengths $g_{1,2}$, the extrinsic cavity decay rate κ_{ex}, and the loss rates caused either by unwanted cavity decay κ_{in} or atomic decay to the initial state Γ_0 and to other atomic states Γ_{n}. The probability of such a system to emit a photon into the cavity P_{cav} can be expressed as a function that solely depends on the cooperativity [55]

$$P_{\mathrm{cav}} = \frac{2C_{\mathrm{eff}}}{2C_{\mathrm{eff}} + 1}. \tag{2.5}$$

As the process involves two degenerate cavity-enhanced transitions, the effective cooperativity is the sum of the cooperativities of the individual transitions $C_{\mathrm{eff}} = C_1 + C_2$. After the emission of a photon into the cavity, the photon can be reabsorbed by the atom and spontaneously decay [56]. Therefore, the rate of the photon leaving the cavity in the desired mode $2\kappa_{\mathrm{ex}}$ does not only compete with cavity decay caused by other loss channels $2\kappa_{\mathrm{in}}$ but also with free-space decay rate of the atom Γ. Hence, the probability P_{out} to get an entangled photon out of the cavity in the desired mode is

$$P_{\mathrm{out}} = \frac{\kappa_{\mathrm{ex}}}{\kappa_{\mathrm{ex}} + \kappa_{\mathrm{in}} + \Gamma/2} \left(\frac{2C_{\mathrm{eff}}}{2C_{\mathrm{eff}} + 1} \right). \tag{2.6}$$

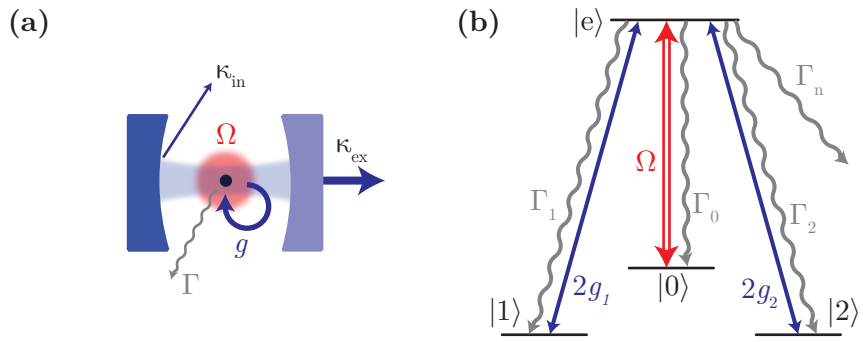

Figure 2.1: (a) Single photon production in a single-sided cavity (depicted here as a Fabry–Perot cavity). The cavity field is primarily lost by the coupling to one defined mode with the extrinsic loss rate κ_{ex}, but a small fraction of the cavity field is lost to the environment, constituting the intrinsic loss rate κ_{in}. There is a coherent coupling between the cavity field and a single atom (g). Atomic excitation can be lost via emission into free space at a rate Γ. An external laser beam with Rabi frequency Ω is used to excite the atom. (b) Level scheme for the production of atom-photon entanglement. The atom is prepared in state $|0\rangle$ and coupled to state $|e\rangle$ by the external laser. The cavity has degenerate polarization eigenmodes and the system is oriented in such a way that the two polarization modes couple this state to $|1\rangle$ and $|2\rangle$ with vacuum Rabi frequency $2g_{1,2}$. The atom can decay by free-space emission into states $|0\rangle$, $|1\rangle$, and $|2\rangle$ with rates Γ_0, Γ_1, and Γ_2, respectively. Decay to all other states is modeled by an additional decay rate Γ_{n}.

To optimize the efficiency of this entanglement generation scheme, one has to maximize the effective cooperativity C_{eff} and the directivity $\chi = \kappa_{\mathrm{ex}}/(\kappa + \Gamma/2)$. The former could be achieved by decreasing the cavity decay rate, but the latter sets a limit to that. If the intrinsic losses κ_{in} are set by the fabrication process, the only way to increase χ is to increase the extrinsic losses and accept a decrease in cooperativity. For this reason, it is important to minimize the intrinsic losses of the cavity, such that a χ close to unity can be achieved at high cooperativity. The intrinsic loss rate of a cavity is therefore one of the most important figures of merit in the fabrication process of cavities suitable for quantum information processing.

2.2 Optical microcavities

The bright prospects of atomic systems coupled to optical cavities for quantum communication have spawned numerous efforts to develop microscopic cavities with small mode volumes and low intrinsic losses to achieve high cooperativity. These approaches fall into two categories: open resonators with direct access to the mode, which allow placing the emitter at the position of maximal field strength, and monolithic resonators with atoms coupled to their evanescent field.

The second category encompasses resonators inside transparent media that rely on refractive index differences to contain the light inside the resonator. By using resonators

with microscopic extent, the cavity fields can have strong transverse confinement and extremely small mode volumes. Since placing the atom inside the medium would disturb the atom, it cannot be placed in the resonator itself, but needs to be in the evanescent field close to the resonator surface.

The first examples of this category featuring strong coupling to atoms were whispering-gallery modes in fused silica microtoroids [57]. Since then, whispering gallery modes have also been used in bottle microresonators [58] and microspheres [59]. These resonators have the advantage of low intrinsic losses and tunable coupling to an external mode by placing a nanofiber close to the resonator at varying distances. Although these resonators cannot be single-sided due to the running-wave mode, nonparaxial effects lead to spin-orbit coupling of the light and enable chiral interfaces that link the polarization of the light to the propagation direction, which can be used for directional emission [60]. However, trapping atoms near these resonators at the required distance is difficult and has not been achieved so far. This limits the interaction time of single atoms with the resonators and prevents long-time storage of qubits in these systems.

An alternative are photonic crystal cavities, which can be designed to feature extremely low mode volumes with a reasonable quality factor [61]. The resulting high coupling strength has been used to reach the intermediate coupling regime with quantum dots placed inside the mode [62]. Unperturbed neutral atoms cannot be placed inside a photonic crystal cavity, but can be trapped in the evanescent field, resulting in very large light-atom coupling [31]. However, resonators fabricated so far suffer from high intrinsic losses, such that single-sided operations are not possible without increasing the loss rate above the value necessary for high cooperativity.

Instead of a small mode volume, there is also the possibility to ensure strong transverse confinement along the whole resonator length using optical nanofibers [63]. Fiber Bragg gratings in the untapered part of the fiber create a cavity inside the fiber[2], which can be coupled strongly to single atoms trapped along the fiber [32]. The length of this cavity has the advantage that many atoms can be trapped along its axis [64] with similar coupling strength. However, for quantum communication, this type of cavity has the disadvantage of small cavity decay rates compared to the atomic decay.

In contrast to monolithic resonators, open resonators offer direct access to the mode, such that objects can be placed directly at the position of highest intensity. This enables coupling to larger objects like atomic ensembles [65–68], ion crystals [69], or micromechanical objects [70, 71]. For single emitters, an open geometry enables relatively easy trapping of neutral atoms [72, 73] and single ions [74] inside the resonator, far from any perturbing surface. The open geometry also enables optical access from multiple directions for cooling, optical pumping, and imaging of atoms in the cavity [75].

The most simple open-cavity design is the Fabry–Perot cavity with two parallel mirrors facing each other. Compared to more complex designs like ring cavities [65], Fabry–Perot cavities are compact and enable the smallest mode volumes. Additionally, the polarization eigenmodes of Fabry–Perot cavities can be degenerate even for the very narrow lines of cavities with ultra-low losses [49], which provides full control over

[2] A cavity inside an optical fiber is often referred to as *fiber cavity*. This is ambiguous with cavities consisting of two mirrors on the end facets of optical fibers, which are sometimes also called *fiber cavities*. The more accurate term for the latter type of cavity would therefore be *fiber Fabry–Perot cavities*. Nevertheless, for conciseness, the term *fiber cavity* will always refer to the second type, when it is used throughout this thesis.

the polarization of the cavity modes. These cavities optimized for high cooperativity with a single atom and single-sided operation are therefore ideally suited for quantum communication experiments.

2.3 High-finesse Fabry–Perot cavities

To design the optimal Fabry–Perot cavity for a particular experiment, its mode volume and losses need to be considered. In the paraxial approximation, a fundamental mode of a Fabry–Perot cavity with length L and mode waist[3] w_0 has a mode volume of $V_\mathrm{m} = \pi w_0^2 L/4$. An emitter placed at the field maximum of such a mode therefore has a coupling strength of (see Eq. (2.3))

$$|g_0| = \sqrt{\frac{6c\Gamma_\mathrm{eu}}{k^2 w_0^2 L}}. \tag{2.7}$$

The most efficient way to gain information about the field inside the cavity is to detect light leaking out of the cavity via the mirror with the higher transmission T_oc, which is called the *output coupler*. In such a configuration, the decay rate $\kappa_\mathrm{oc} = \kappa_\mathrm{ex}$ corresponding to the transmission of this mirror leads to the desired signal. It should therefore be distinguished from all other decay rates, which describe loss of information to the environment. This loss can either be caused by transmission T_hr of the other mirror, called the *high reflector*, or by parasitic losses $\mathcal{L}$ due to scattering from the mirror surface, absorption in the coating, or clipping caused by finite mirror size. These losses can be treated with a composite decay rate κ_in and the total loss rate κ is then described by

$$\kappa = \kappa_\mathrm{oc} + \kappa_\mathrm{in} = \frac{c}{4L}\left(T_\mathrm{oc} + (T_\mathrm{hr} + \mathcal{L})\right) \approx \frac{\pi c}{2L\mathcal{F}}. \tag{2.8}$$

In the last step, the finesse was introduced, which is a measure for the reflectivity of the mirrors and is defined by the ratio of the free spectral range $\nu_\mathrm{FSR} = c/(2L)$ and the cavity linewidth $\Delta\nu$:

$$\mathcal{F} = \frac{\nu_\mathrm{FSR}}{\Delta\nu} \approx \frac{2\pi}{T_\mathrm{oc} + T_\mathrm{hr} + \mathcal{L}}. \tag{2.9}$$

The relative error of the approximation made here is on the order of $1/\mathcal{F}$ and can be neglected for high finesse cavities.

Inserting Eqs. (2.7) and (2.8) into Eq. (2.4) yields the cooperativity for an emitter placed at the intensity maximum of a mode in a Fabry–Perot cavity

$$C = \frac{12\mathcal{F}}{\pi k^2 w_0^2}\frac{\Gamma_\mathrm{eu}}{\Gamma}. \tag{2.10}$$

For a closed transition, $\Gamma = \Gamma_\mathrm{eu}$ and the cooperativity only depends on the mode waist compared to the wavenumber of the mode, kw_0, and the finesse. If the transition is not closed, but decay from the excited state to other states can occur, the cooperativity is reduced by the relative decay strength $\Gamma_\mathrm{eu}/\Gamma < 1$.

By varying the thickness and number of layers of a dielectric coating, the transmissions T_oc and T_hr of the two mirrors can be freely chosen. The scattering, absorption, and

[3] The 1/e field radius or $1/e^2$ intensity radius at the waist of the mode.

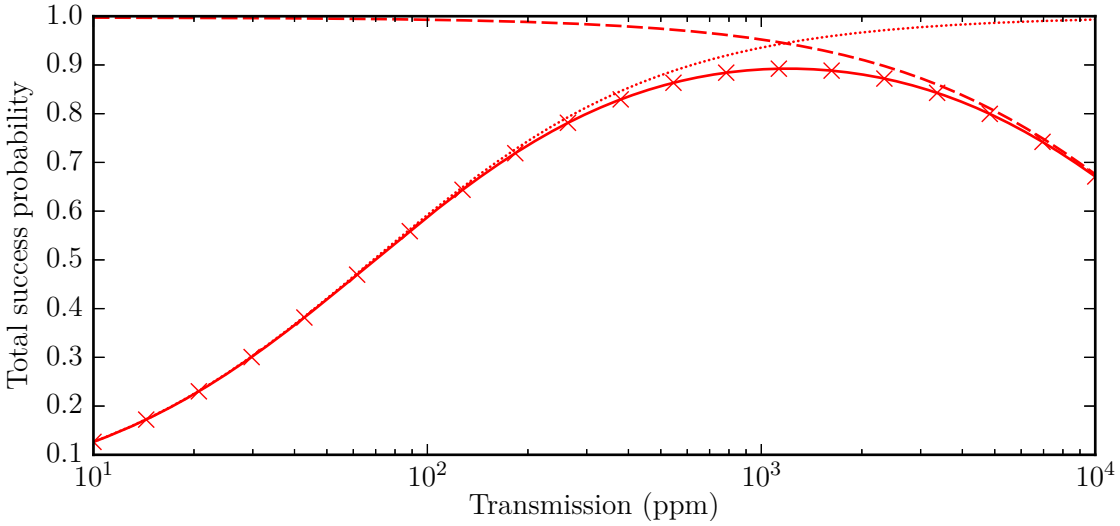

Figure 2.2: Influence of the transmission of the output coupler on the photon output probability. The solid line is the analytic result of Eq. (2.6). The dashed line indicates the probability for the atom to emit a photon into the cavity, which limits the efficiency in case of high transmission of the output coupler and therefore lower finesse of the cavity. The dotted line denotes the probability of a photon in the cavity to leave it through the output coupler, which limits the total success probability in the case of it having low transmission. The crosses are results of numeric simulations that confirm the analytic results. The calculations were made using $g = 2\pi \times 100\,\mathrm{MHz}$, $\Gamma = 2\pi \times 6.0\,\mathrm{MHz}$, $\Gamma_1 = \Gamma_2 = 5/12 \times \Gamma$, $T_{\mathrm{hr}} + \mathcal{L} = 50\,\mathrm{ppm}$ and $L = 100\,\mu\mathrm{m}$.

clipping losses of the mirrors set a lower limit for κ_{in} and a non-zero transmission of the high reflector is required to be able to perform transmission measurements of the cavity. If κ_{in} is then fixed, T_{oc} needs to be set to a value high enough to enable single-sided operation, but low enough to retain high finesse and high cooperativity.

The influence of T_{oc} on single photon production by fast excitation described by Eq. (2.6) is depicted in Fig. 2.2, which shows the probability to generate a single entangled photon per trial as a function of the transmission of the output coupler for one set of parameters. If the transmission of the output coupler is too low, the cooperativity is high and the photon is emitted into the cavity with high probability, but the photon is lost most of the time instead of leaving the cavity through the output coupler. If the transmission of the output coupler is too high, any photon inside the cavity is efficiently coupled to a single external mode, but the low cooperativity prevents efficient coupling of the atom to the cavity. Therefore, the only parameter that can increase the cooperativity without compromising the single-sidedness of the cavity is the transverse size of the mode. Minimizing kw_0 while maintaining low intrinsic losses is thus the path to follow to maximize efficiency.

The cooperativity has no explicit length dependence[4]. As a consequence, efficient

[4]There is an implicit length dependence, because the mode waist depends on the length (see Sec 2.4). However, the length dependence of the waist can in principle always be eliminated by adjusting the curvature of the mirrors.

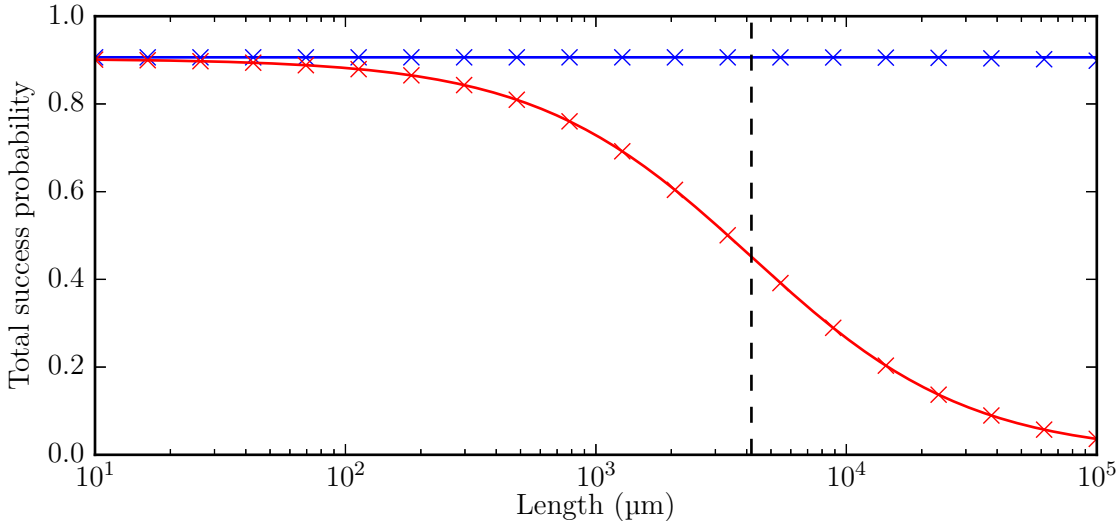

Figure 2.3: Success probability of a photon leaving the cavity through the output coupler with varying cavity length. The radii of curvature of the mirrors are adjusted to keep the mode waist constant at $w_0 = 4.0\,\mu\text{m}$ (requires a near concentric geometry for long cavities). The solid lines are the analytic results for fast excitation (red, Eq. (2.6)) and an adiabatic control pulse (blue, Eq. (2.11)). The crosses denote simulation results. For adiabatic driving, the result is independent of the length. In the limit of very short cavities, the probability reaches the same value for fast excitation as in the adiabatic case. κ decreases with cavity length, but Γ is constant, such that the probability of free-space decay increases with cavity length for fast excitation. The dashed vertical line indicates the cavity length, where $2\kappa = \Gamma$ and the fast-excitation efficiency is exactly half the efficiency for adiabatic driving. The calculations were made with $\lambda = 780\,\text{nm}$, $\Gamma = 2\pi \times 6.0\,\text{MHz}$, $\Gamma_1 = \Gamma_2 = 5/12 \times \Gamma$, $T_\text{hr} + \mathcal{L} = 50\,\text{ppm}$ and $T_\text{oc} = 1000\,\text{ppm}$.

coupling of an atom to the cavity is possible at any cavity length. However, the ratio $2\kappa_\text{oc}/\Gamma$ does depend on the cavity length. If the system is in a state where an excitation can oscillate between the excited state of the atom and a photon in the cavity, this ratio determines the probability of free-space decay compared to transmission through the output coupler. Therefore, any scheme that puts the system in such a state will benefit from a short cavity (see Fig. 2.3), because the probability for a photon to leave the cavity via the output coupler is increased. Instead of using fast excitation, atom-photon entanglement can also be generated with an adiabatic control pulse [55, 76], in analogy to stimulated Raman adiabatic passage [77]. This scheme avoids reexcitation of the atom and therefore Γ can be eliminated in Eq. (2.6) such that

$$P_\text{out} = \frac{\kappa_\text{ex}}{\kappa_\text{ex} + \kappa_\text{in}} \left(\frac{2C_\text{eff}}{2C_\text{eff} + 1} \right). \tag{2.11}$$

However, this requires the duration of the control pulse t_c to be much longer than the timescale set by the coupling strength $t_\text{c} \gg 1/g$ [77] and thus reduces the available bandwidth range for the generated photons. A short cavity is therefore not necessary

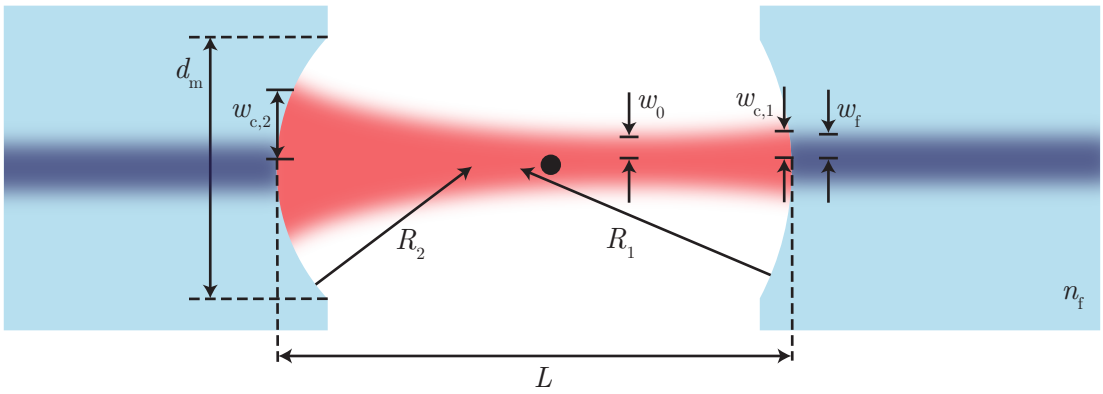

Figure 2.4: Parameters relevant for the geometry of a (fiber) Fabry–Perot cavity. The radii of curvature R_1 and R_2 of the two mirrors and the cavity length L determine the waist w_0 of the mode. If these radii are different, the position of the waist is not in the center of the cavity and the coupling rate of an emitter placed at the center is reduced by the increased mode radius there. The mode radii on the two mirrors $w_{c,1}$ and $w_{c,2}$ have to be compared to the finite mirror diameter d_m. For a fiber cavity, the mode radius of the fiber mode w_f and the refractive index of the fiber material n_f are additional parameters that influence the coupling of the cavity mode to the fiber mode on each side.

to construct an efficient light-matter interface, but it enhances the variety of possible schemes and the bandwidth range of the system.

2.4 Cavity geometry

The parameters that describe the mode of a Fabry–Perot cavity are depicted in Fig. 2.4. As described in the previous section, a small mode waist is the key to a high-cooperativity atom–cavity system with the reduced finesse that is required for a single-sided cavity. In the paraxial approximation[5], the mode waist w_0 of a Fabry–Perot cavity is a function of the cavity length L, the radii of curvature of both mirrors R_1 and R_2 and the wavelength λ [79]

$$w_0 = \sqrt{\frac{L\lambda}{\pi}\sqrt{\frac{g_1 g_2(1-g_1 g_2)}{(g_1+g_2-2g_1 g_2)^2}}}. \tag{2.12}$$

Here, the dimensionless parameters $g_{1,2} = 1 - L/R_{1,2}$ describe the geometry of the cavity and $\sqrt{L\lambda/\pi}$ sets the scale. Eq. (2.12) only results in real values for the mode waist and thus a stable cavity, if $0 \leq g_1 g_2 \leq 1$. Within this stability region, the mode waist generally decreases with the radii of curvature (see Fig. 2.5a), except at the edges of this region, where the mode waist either diverges for a planar geometry, i.e., $R_1 = R_2 = \infty$,

[5] The paraxial approximation requires $kw_0 \gg 1$ [78]. As this parameter is to be minimized, it is questionable whether the paraxial approximation is valid for the cavities discussed here. This issue is neglected here, but will be discussed in Sec. 4.2.

or vanishes like it does in the concentric case, i.e., $R_1 = R_2 = L/2$, or if one of the radii of curvatures approaches the cavity length. It would be tempting to operate a cavity near the edge of the stability region, where a small mode waist can be achieved for any cavity length. However, the mode size on the mirrors has to be considered, which is [79]

$$w_{\mathrm{c},1} = \sqrt{\frac{L\lambda}{\pi}\sqrt{\frac{g_2}{g_1(1-g_1g_2)}}} \tag{2.13}$$

on the mirror with radius of curvature R_1 and the same equation with g_1 and g_2 exchanged for the other mirror. The larger of the two as a function of the cavity geometry is shown in Fig. 2.5b. One can see that near the edge of the stability region where the mode waist vanishes, the mode size on at least one of the mirrors diverges and very large mirrors would be needed. This is especially true for long cavities, because the cavity length enters the scale factor. Producing such large mirrors with sufficiently low deviation from the perfect shape is difficult and although there are promising efforts in that direction [80], high finesse has not been reached for such cavities, yet.

As past single-atom cavity QED experiments were built with cavities in the near-planar regime [35, 49, 54, 73, 76, 81–85], reducing the curvature of the mirrors would decrease the mode waist as well as the size of the mode on the mirrors. Such cavities would therefore not only provide higher cooperativity, but would also allow the use of smaller mirrors and enable the combination of multiple cavities in new geometries. The minimum mode size for a given cavity length L on the mirror where the mode is larger is $\sqrt{L\lambda/\pi}$, which is reached in a confocal geometry, i.e., $R_1 = R_2 = L$. A further reduction in mode waist and mode size on the mirrors could then be achieved by also reducing the length, while keeping the confocal geometry.

However, there is a considerable drawback of reducing the cavity length to very small values. Long Fabry–Perot cavities offer good optical access to an atom coupled to the cavity mode, which allows to trap, cool, image, optically pump, or drive the atom with laser beams on axes perpendicular to the cavity axis. A considerable reduction of the optical access would hinder these operations and reduce the capabilities of the system. Most critical in terms of scattering and mirror heating is trapping single atoms inside the cavity with a far-offresonant optical dipole trap perpendicular to the cavity axis [73], because it requires a high-power laser beam passing between the mirrors. It can therefore be used to estimate the minimum required distance that will not excessively constrict optical access. To get full control over the motion of the atom, a 3D-trap involving an intra-cavity optical dipole trap is desirable [86]. Light from the intra-cavity trap will be scattered and absorbed by the mirrors on a ppm-level and cannot be detuned by more than a few THz to obtain a large region where the trapping sites coincide with the antinodes of the cavity mode, where the coupling strength is maximal. A far off-resonant trap, for example at a wavelength of 1064 nm for rubidium, has a detuning on the order of 100 THz and will thus require two orders of magnitude more power to reach a trap depth similar to the intra-cavity trap. If less than 10^{-8} of its light intersected the mirrors, scattering and absorption would be less than the intra-cavity trap and could therefore not lead to excessive problems. Taking a Gaussian fundamental transverse mode, the minimum required distance between the edges of the substrates can be calculated for a given mirror diameter. For example, if the mirror substrates had the diameter of standard optical fibers (125 µm), a minimum distance between the substrates of 40 µm

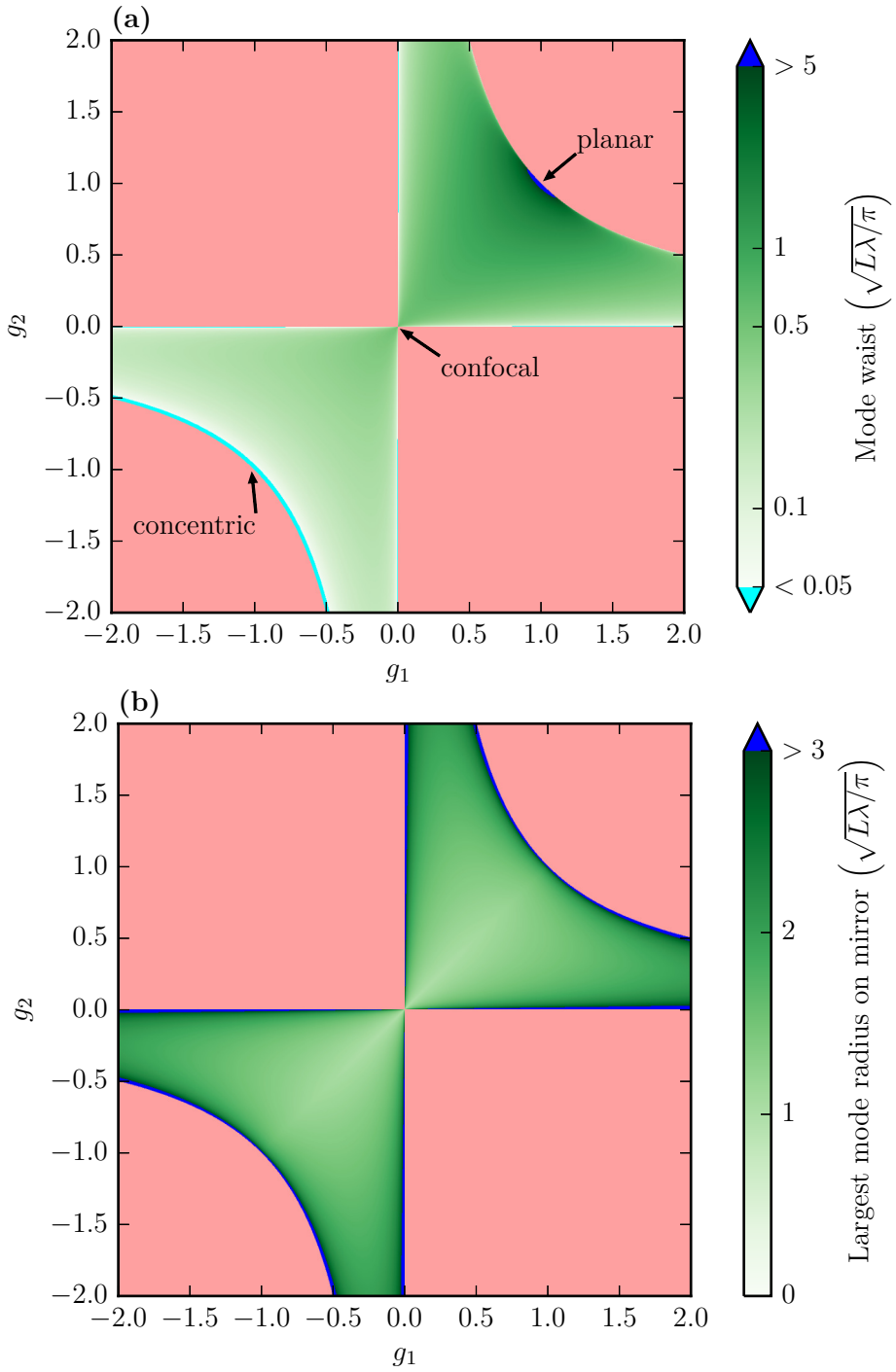

Figure 2.5: (a) The mode waist as a function of the g-parameters in units of the scale factor $\sqrt{L\lambda/\pi}$. The cavity is unstable in the red-shaded regions. The mode waist diverges (indicated by blue) for a planar cavity and vanishes for a concentric cavity (indicated by cyan) and when one and only one of the g-parameters is zero. (b) Corresponding mode size on the mirror on which the mode is larger. At the edge of the stability region, where the mode waist vanishes, the mode size on at least one of the mirrors diverges (indicated by blue). The mode size is minimal on the mirrors for a given length if the cavity is confocal.

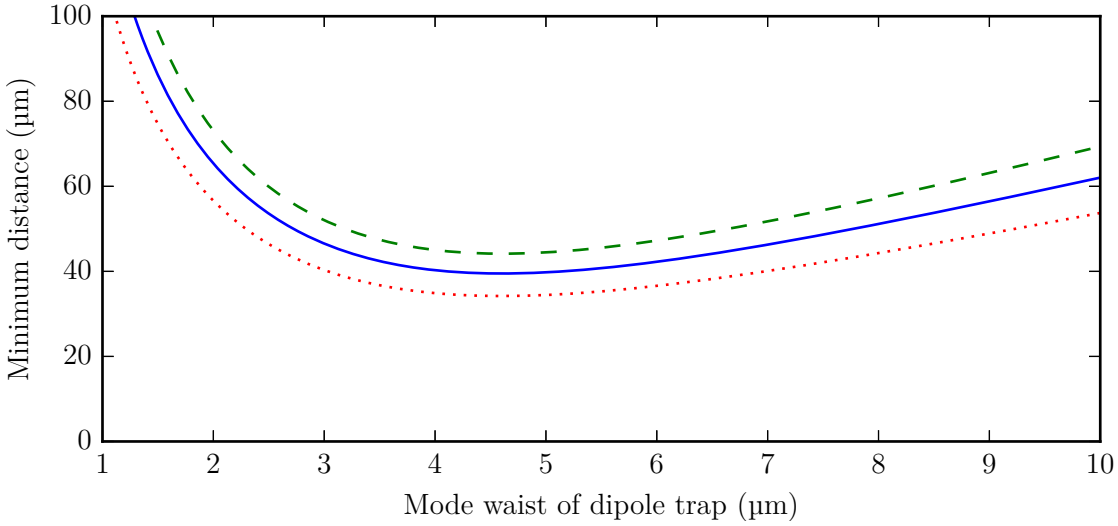

Figure 2.6: Minimum distance between mirror substrates with a diameter of 125 µm as a function of the mode waist of an optical dipole trap at 1064 nm wavelength, which is perpendicular to the cavity and has its focus in the center of the cavity. The solid blue line corresponds to possible scattering and absorption of 10^{-8} of the mode intensity, the green dashed line to 10^{-10} and the red dotted line to 10^{-6}. For these parameters, the optimum mode waist of the trap is at 4.6 µm, which requires a distance of 40 µm between the mirror edges.

would be required to fulfill the criterion explained above (see Fig. 2.6). As this calculation assumed perfect alignment and the cavity length is slightly longer than the substrate distance, due to the concave shape of the mirrors, a safety margin of at least 15 µm should be added on each side, such that the minimum cavity length for unproblematic dipole trapping is around 70 µm.

Extending the system to include two crossed cavities with an atom coupled to both simultaneously, requires at least one of the cavities to have a length exceeding the mirror substrate diameter of the other cavity in order to avoid collisions between the mirrors. A mirror substrate diameter of 125 µm for one cavity would thus require a cavity perpendicular to it to have a length $L > 140$ µm (see Fig. 2.7).

2.4.1 Mode matching

To achieve long distance quantum communication in optical fibers, the mode of the cavity output must be matched to a single-mode optical fiber. For entangled photon production [34] or storage of a photonic qubit [35], imperfect mode matching reduces the efficiency of the protocol. Additionally, imperfect mode matching also reduces the fidelity for schemes based on reflection of a single photon [36, 37, 87], exacerbated by the spatial filtering of the fiber mode, which can lead to undesired interference effects [88, 89]. Therefore, it is essential to maximize the overlap of the cavity mode with a fiber mode. This can be achieved by placing and adjusting optical elements between the cavity and the fiber, which can be very sensitive to temperature changes. As an alternative,

Figure 2.7: The space required for two crossed cavities based on substrates with a diameter of 125 µm. The short cavity (vertical) has a length of 70 µm to allow a far off-resonant trap to be focused between the mirrors without excessive scattering. The long cavity (horizontal) has to have a length $L > 140\,\mu\text{m}$, such that the short cavity fits between its mirrors.

using an optical fiber as mirror substrate can integrate the fiber coupling into the cavity and provide intrinsic direct coupling between the cavity mode and the fiber mode. This eliminates free parameters that need to be aligned, but requires incorporating fiber coupling into the design process, as the mirrors need to be fabricated with the right radii of curvature, such that good mode matching is possible.

The mode launched from the end facet of a single-mode fiber, operated near the multi-mode cutoff wavelength has an overlap $> 99.5\,\%$ with a fundamental transverse Gaussian mode that has its waist on the end facet [90]. Therefore the fiber mode can be approximated by the corresponding Gaussian mode and the mode matching efficiency ϵ can be calculated as the overlap between this mode and the cavity mode [44, 91]:

$$\epsilon = \frac{4}{\left(\frac{w_\mathrm{f}}{w_\mathrm{c,oc}} + \frac{w_\mathrm{c,oc}}{w_\mathrm{f}}\right)^2 + \left(\frac{k\, n_\mathrm{f}\, w_\mathrm{f}\, w_\mathrm{c,oc}}{2R}\right)^2}, \tag{2.14}$$

where w_f is the waist of the fiber mode, $w_\mathrm{c,oc}$ is the mode radius of the cavity mode on the output coupler, n_f is the refractive index of the fiber and R is the radius of curvature of the output coupler (see Fig. 2.4). The first term in the denominator characterizes the mode size mismatch and is minimal with a value of 4 at $w_\mathrm{f} = w_\mathrm{c}$. The second term characterizes the wavefront curvature mismatch, taking into account lensing by the concave mirror surface. It vanishes for $R \to \infty$ and becomes worse for smaller radii of curvature. It follows, that for symmetric cavities, which have equal radius of curvature for both mirrors, best mode matching is achieved for very short cavities, because a large radius of curvature can be chosen to match the cavity mode size to the fiber mode due to the length-depending scale factor in Eq. (2.13). Longer cavities need to be asymmetric to achieve good mode matching. By increasing the radius of curvature of the output

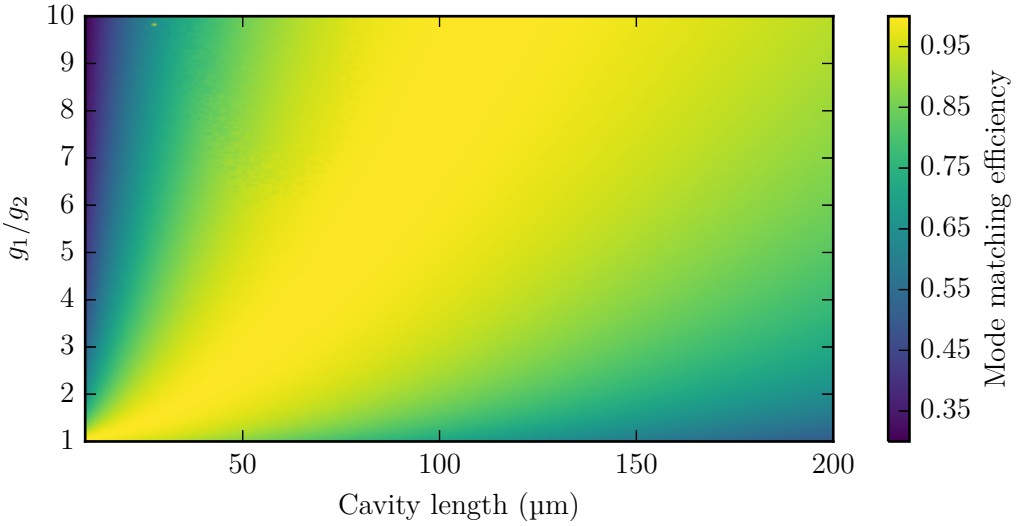

Figure 2.8: Best mode matching efficiency between cavity mode and fiber mode with the radii of curvature optimized for a given length and cavity asymmetry expressed in the ratio of g_1 and g_2. A symmetric cavity, i.e., $g_1 = g_2$ is only optimal for very short cavities. Long cavities need a high degree of asymmetry to achieve good mode matching. The plot has been generated using a fiber mode waist of $w_\mathrm{f} = 3\,\mu\mathrm{m}$ and a wavelength of $\lambda = 780\,\mathrm{nm}$.

coupler, the waist of the cavity mode can be moved towards it, resulting in a less curved wavefront on the mirror and thus higher mode matching efficiency (see Fig. 2.8). There are, however, three disadvantages to this method. First, it decreases the mode matching efficiency at the other mirror. This is not a severe issue for single-sided cavities, because efficient detection is not possible at the high reflector, anyway, but it does reduce the signal of transmission measurements. Second, the center of the cavity is the best place to trap an atom inside the cavity in terms of optical access. Displacing the waist of the cavity due to asymmetric radii of curvature results in a reduced coupling strength to the cavity of an atom trapped at the center. Third, the mode size on the high reflector becomes larger, such that a larger mirror is required on that side to prevent additional losses.

A simple clipping model can be used to estimate the required mirror size by assuming that the part of the mode that is inside of an effective mirror diameter is fully reflected and everything else is lost. The clipping loss $\mathcal{L}_\mathrm{cl}$ for a mirror with diameter d_m and mode size on the mirror w_c is then [44]

$$\mathcal{L}_\mathrm{cl} = \mathrm{e}^{-d_\mathrm{m}^2/(2w_\mathrm{c}^2)}. \tag{2.15}$$

Solving for d_m yields

$$d_\mathrm{m} = w_\mathrm{c}\sqrt{-2\ln(\mathcal{L}_\mathrm{cl})}, \tag{2.16}$$

which is the minimum mirror diameter to keep clipping losses below a given $\mathcal{L}_\mathrm{cl}$. For example, a cavity with a length $L = 140\,\mu\mathrm{m}$ and symmetric radii of curvature could reach a mode matching efficiency of at most 61 % and would require a mirror with $d_\mathrm{m} > 32\,\mu\mathrm{m}$ to reach that value with $\mathcal{L}_\mathrm{cl} < 1\,\mathrm{ppm}$. With an asymmetry of $g_1/g_2 > 4.2$, a mode

matching efficiency exceeding 90 % could be reached, but the required mirror diameter would increase to $d_\mathrm{m} > 45\,\mu\mathrm{m}$. The combination of cavity length and required mode matching efficiency thus sets a minimum size for the mirror.

2.4.2 Optimized cavity geometries

Examples for optimized cavity geometries are listed in Tab. 2.1. To minimize the mode size on the mirrors, these all feature a radius of curvature that is close to the cavity length for the high reflector. This results in a near-confocal geometry for symmetric radii of curvature and near-hemispherical in the highly asymmetric case. It is, however, undesirable to operate exactly at the confocal or hemispherical point, because of two reasons. First, these border the unstable region, such that fabrication tolerances and deviations from the ideal paraxial case might result in an unstable cavity. Second, higher order transverse modes of even order are degenerate with the fundamental transverse mode at these points, resulting in a multi-mode output when an atom is resonant with these modes. Hence, there should be a safety margin between the radius of curvature of the high reflector and the cavity length, determined by the tolerance of mirror fabrication and characterization.

In general, a tradeoff has to be made between cooperativity, mode matching efficiency, and required mirror size. Depending on the application, the optimum geometry might be different. The highest cooperativity is achieved for both radii of curvature smaller than the cavity length, but this also results in the worst mode matching. A near-confocal geometry, with both radii of curvature slightly larger than the length, results in the smallest mode size on the mirrors for a given length. Increasing the radius of curvature of the output coupler increases the mode matching, but reduces the cooperativity and increases the mode size on the high reflector. The asymmetry of the mirror curvatures can therefore be increased to improve the coupling to a single mode fiber until either the coupling strength at the center of the cavity becomes too small, or the mode size on the high reflector becomes larger than the usable area of the mirror. A fabrication process should therefore be able to produce various radii of curvature and maximize the area where deviations from a chosen curvature are minimal in order to prevent limitations by the mirror size.

Cavity length	Radius of curvature		Cooperativity	Mode matching		Mirror size
L	R_{hr}	R_{oc}	C	ϵ_{oc}	ϵ_{hr}	d_{m}
µm	µm	µm		%	%	µm
70	50	50	61.9	57.9	57.9	22.9
	100	100	29.8	78.8	78.8	22.4
	100	200	24.0	94.2	62.9	28.1
	100	400	21.6	97.3	57.3	30.3
140	110	110	26.8	55.7	55.7	31.6
	170	170	17.0	61.0	61.0	31.2
	170	340	12.7	84.5	38.8	43.0
	170	800	11.2	89.7	33.3	47.4

Table 2.1: Examples for possible cavity geometries at $\lambda = 780\,\mathrm{nm}$. The cooperativity assumes a closed transition of an atom trapped at the center of the cavity and a single-sided cavity with $T_{\mathrm{oc}} = 1000\,\mathrm{ppm}$ and $T_{\mathrm{hr}} + \mathcal{L} = 50\,\mathrm{ppm}$. The mode matching to a fiber is calculated with $w_{\mathrm{f}} = 3\,\mu\mathrm{m}$. Small, symmetric radii of curvature maximize the cooperativity and, but result in lower mode matching efficiency at the output coupler. The latter can be optimized with asymmetric radii of curvature if the mirror diameter is large enough.

3 Fabrication and characterization of CO_2 laser-machined cavities

Past experiments in cavity QED with Fabery–Perot cavities have used ion-beam sputtered superpolished substrates as mirrors, which feature extremely low losses and therefore enable ultra-high finesse [92], but are limited in transverse confinement of the mode by the minimum possible radius of curvature.[1]

To combine the advantages of Fabry–Perot cavities with a small mode volume and consequently large coupling strength, new fabrication methods for microscopic Fabry–Perot cavities have been developed over the last decade. The goal of these fabrication methods is to produce substrates with a spherical, concave low-surface-roughness structure with curvatures exceeding the capabilities of polishing methods. These can then be coated with a highly reflective coating and subsequently be used as mirrors. The challenge is to fabricate the structure with the desired diameter and radius of curvature, while maintaining a shape that is as close to spherical as possible and a surface that is as smooth as possible. Of the multiple approaches that have been tried, the arguably most promising techniques are listed in the following.

The first possibility are silicon etching methods [93]. These have the advantage of easy integration into microfabrication processes to create tunable cavity arrays [94]. They can be fabricated with low surface roughness and a finesse of 6×10^4 has been reached [95]. Silicon is not transparent at visible and near-infrared wavelengths, such that only the high reflector can be produced with this method and the other mirror has to use a different substrate, but can be near-planar. It is however difficult to independently control mirror diameter and radius of curvature while maintaining low surface roughness, because these are partly determined by the properties of silicon and the mask size and etch time cannot be varied fully independently [95].

Controlling the shape, size, and radius of curvature, even for extremely small mode volumes, can be achieved with focused ion beam milling [96]. This comes at the price of increased surface roughness and reduced finesse [97], but is an interesting method for experiments with solid state emitters, where extremely small mode volumes are necessary to get coupling rates between the emitter and the cavity that are as large as the emitter linewidth [98].

The most successful new fabrication method has been CO_2 laser machining [44, 45]. With this method, the highest surface qualities have been achieved over a wide range of parameters. CO_2 laser machined mirrors have therefore been used in experiments with atomic ensembles [48], singe ions [99], solid state emitters [47, 100, 101], molecules [102], nanomechanical systems [71], and as a scanning cavity microscope [103].

[1] The smallest radius of curvature that has been used in a single-atom cavity experiment was 10 mm [84]. The smallest that is currently commercially available with sufficient surface quality is 25 mm from the company *Advanced Thin Films*.

3.1 CO_2 laser machining of glass

CO_2 laser fabrication of mirror substrates is based on rapid laser-induced heating of fused silica. Once the material gets hot enough, it starts to melt and then to evaporate. As the laser beam has a Gaussian intensity profile, the spot illuminated by the center of the beam is heated faster than the surrounding area and evaporates faster, leaving a concave depression in the substrate. This depression is extremely smooth, because surface tension during reflow of melted fused silica prevents rough structures when the material resolidifies. This polishing effect of CO_2 laser treatment on fused silica has been observed to mitigate laser-induced damage [104], enables the fabrication of ultra-high-Q microtoroid cavities [105], and creates surfaces that can be used to build high-finesse cavities after application of highly reflective coatings [44, 45]. The process only requires a flat fused silica substrate with a diameter larger than the size of the mirror that is to be fabricated. A particularly interesting substrate is the end facet of an optical fiber, because mirrors on the end facets of optical fibers enable cavities that combine a microscopic mode volume with microscopic physical dimensions and intrinsic fiber coupling of the cavity mode [44].

In a simple model of the fabrication process [46], CO_2 laser light is only absorbed on the surface of the fused silica substrate, because of the short absorption length in this material at this particular wavelength. In the limit of a semi-infinite slab of fused silica, the corresponding heat-flow equation can be solved semi-analytically [106], yielding a surface temperature distribution. Under the assumption that the evaporation can be modeled as an evaporation velocity depending only on the surface temperature, this model predicts depressions with near-Gaussian depth profiles, which are compatible with those observed on glass plates illuminated by CO_2 laser beams with a waist of $w_0 = 26\,\mu\text{m}$ [46].

According to this model, the width d of the Gaussian function

$$z(r) = A \exp\left(-\frac{r^2}{d^2}\right) \tag{3.1}$$

which fits best to the depth z of the structure as a function of the distance r to the center, depends on the waist w_0 of the beam with $d < w_0$. In the paraxial approximation, the phase of a Hermite–Gaussian mode is $\phi(x, y, z) = -k(z + x^2/(2R_\text{x}) + y^2/(2R_\text{y})) + \phi(z)$, i.e., for a slowly varying Guoy phase $\phi(z)$, the surfaces of constant phase are elliptic paraboloids $z = -(x^2/(2R_\text{x}) + y^2/(2R_\text{y}))$ with radii of curvature R_x and R_y at their origins. To minimize diffraction losses, the surface of a mirror should thus be as close to an elliptic paraboloid as possible over the cross section that covers significant intensity of the mode. The Taylor expansion of Eq. (3.1) around $r = 0$ is

$$z = A\left(1 - \frac{r^2}{d^2} + \frac{r^4}{2d^4} + \mathcal{O}\left(\frac{r^6}{d^6}\right)\right), \tag{3.2}$$

which can be approximated by a paraboloid with $R_\text{x} = R_\text{y} = d^2/(2A)$ up to the order $\mathcal{O}(r^4/d^4)$. For this approximation to be valid up to the desired mirror radius r_m, the condition $r_\text{m}/d \ll 1$ needs to be fulfilled, i.e., d needs to be much larger than r_m. To get mirrors with $2d > 45\,\mu\text{m}$ suitable for cavities with lengths over $140\,\mu\text{m}$ and mode matching efficiency $\eta > 90\,\%$ (see Sec. 2.4.1), d and thus w_0 should therefore be on the order of several hundred micrometers.

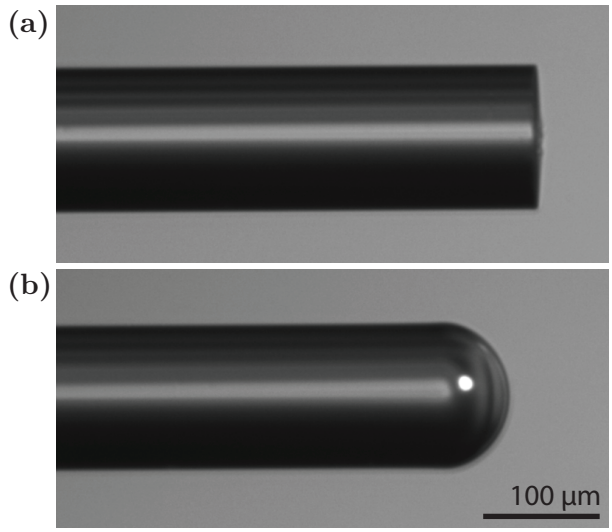

Figure 3.1: Microscope image of an optical fiber before (a) and after (b) illumination by a CO_2 laser pulse with a power of $P = 30\,\mathrm{W}$, a waist of $w_0 = 220\,\mu\mathrm{m}$, and a duration of 25 ms. Due to large scale melting and surface tension, the tip of the fiber was reshaped to a convex hemisphere. From the difference in length, the amount of material can be inferred which has been ablated by this laser pulse.

If end facets of typical optical fibers with a cladding diameter of 125 µm are used, the diameter of such a beam exceeds the diameter of the end facet. Nevertheless, it should result in a structure with the desired profile in the center of the fiber end facet. However, effects at the edge of the facet will result in different structures there and might possibly influence the structure in the center. Additionally, surface tension will force a minimization of the surface area in the melted state. Although desirable on small scales for a smooth surface, melting on the scale of the substrate will result in a convex shape, eventually collapsing the concave shape resulting from the evaporation (see. Fig. 3.1).

To prevent large scale melting, heating should be constricted to regions close to the surface that are to be evaporated and heating of deeper regions should be avoided. Two issues need to be addressed to achieve this goal. The first is the finite penetration depth of the laser light. The most common wavelength at which CO_2 lasers operate is 10.6 µm. At this wavelength, there is significant disagreement in the literature about the value of the absorption index $\mathrm{Im}(n_\lambda)$ of fused silica with values ranging over 0.02–0.2 [107]. These values correspond to an absorption length of $\alpha^{-1} = \lambda/(4\pi\,\mathrm{Im}(n_\lambda)) = 40\,\mu\mathrm{m} - 4\,\mu\mathrm{m}$, which is not insignificant compared to the expected depth of the structures. The absorption depth can be reduced by an order of magnitude by using a laser with a wavelength closer to the absorption resonance at 9.2 µm in fused silica caused by a stretching vibration of SiO_2 [107]. The second strongest CO_2 laser transition at 9.3 µm [108] is close to this resonance, has an absorption index (absorption length) of $\mathrm{Im}(n_\lambda) = 2$ ($\alpha^{-1} = 0.4\,\mu\mathrm{m}$) [107], and can therefore be used to limit absorption to the surface of the substrate. The second issue is thermal conduction during application of the laser pulse. Even if all absorption happens at the surface, heat will be transferred to deeper regions if the pulse

has low intensity and long duration. To minimize this effect, the laser pulse should be short, which requires high intensities to achieve sufficient heating for evaporation.

To estimate the size of these effects, the heat conduction model needs to be extended to include a source that penetrates the material. For a semi-infinite solid with constant illumination, an analytic closed form of the heat flow equation exists for the increase in temperature ΔT caused by the laser [106]:

$$\begin{aligned}\Delta T(t,z) = \frac{I(1-R)}{K}\Bigg(&\delta\,\mathrm{ierfc}\left(\frac{z}{\delta}\right) - \frac{1}{\alpha}\exp(-\alpha z) + \frac{1}{2\alpha}\exp\left(\frac{\alpha^2\delta^2}{4}\right)\\ &\times\left[\exp(-\alpha z)\,\mathrm{erfc}\left(\frac{\alpha\delta}{2}-\frac{z}{\delta}\right) + \exp(\alpha z)\,\mathrm{erfc}\left(\frac{\alpha\delta}{2}+\frac{z}{\delta}\right)\right]\Bigg).\end{aligned} \tag{3.3}$$

Here, $\mathrm{erfc}(x)$ is the complementary error function, $\mathrm{ierfc}(x) = \exp(-x^2)/\sqrt{\pi} - x\,\mathrm{erfc}(x)$ is its integral, I is the laser intensity, R is the reflectivity of the substrate, K is the heat conductivity, and $\delta = 2\sqrt{Dt}$ is the diffusion length, calculated from the heat diffusivity D and the duration of the laser pulse t. This solution only considers heat transfer in the solid and neglects potential heat conduction by air, because the typical heat conductivity of air is two orders of magnitude smaller than the heat conductivity of fused silica. For $\alpha^{-1} \ll \delta$, numerical evaluation of Eq. (3.3) is problematic because of over- and underflow of function evaluations, so it is advantageous to evaluate the last part logarithmically:

$$\begin{aligned}\Delta T(t,z) = \frac{I(1-R)}{K}\Bigg(&\delta\,\mathrm{ierfc}\left(\frac{z}{\delta}\right) - \frac{1}{\alpha}\exp(-\alpha z)\\ &+\frac{1}{2\alpha}\left[\exp\left(\ln\left(\mathrm{erfcx}\left(\frac{\alpha\delta}{2}-\frac{z}{\delta}\right)\right) - \frac{z^2}{\delta^2}\right)\right.\\ &\left.+\ \exp\left(\ln\left(\mathrm{erfcx}\left(\frac{\alpha\delta}{2}+\frac{z}{\delta}\right)\right) - \frac{z^2}{\delta^2}\right)\right]\Bigg)\end{aligned} \tag{3.4}$$

The function $\mathrm{erfcx}(x) = \exp(x^2)\,\mathrm{erfc}(x)$ is the scaled complementary error function and can be used to calculate the logarithm $\ln(\mathrm{erfc}(x)) = \ln(\mathrm{erfcx}(x)) - x^2$.

Although K and D in fused silica depend on temperature, heating by a CO_2 laser can be approximated with the effective values $K = 2\,\mathrm{W\,m^{-1}\,K^{-1}}$ and $D = 7\times10^{-7}\,\mathrm{m^2\,s^{-1}}$ [109]. The refractive index of fused silica at a wavelength of 9.3 µm is $n = 2 + 2\mathrm{i}$ [107], leading to a reflectivity of

$$R = \left|\frac{n-1}{n+1}\right|^2 = 0.4. \tag{3.5}$$

Using these values, the temperature profile of a semi-infinite solid has been calculated for a laser intensity of $I_0 = 0.66\,\mathrm{GW\,m^{-2}}$, which corresponds to the peak intensity of a laser beam with a power of 50 W and a waist of $w_0 = 220\,\mu\mathrm{m}$. For comparison, the calculation was repeated for laser beams with different absorption lengths and for laser pulses 10 times longer (Fig. 3.2). To interpret these temperature profiles, two temperature values are of significance. The first is the softening point of fused silica of approximately 1900 K at which the glass starts to flow under its own weight. The second is the temperature of 3000 K, at which the vapor pressure of fused silica reaches 1 bar and significant evaporation occurs [110]. For the parameters given above, the latter temperature is reached after 0.22 ms. The intensity of the laser beam in all of the comparison cases was adjusted in such a way that the surface reaches that temperature

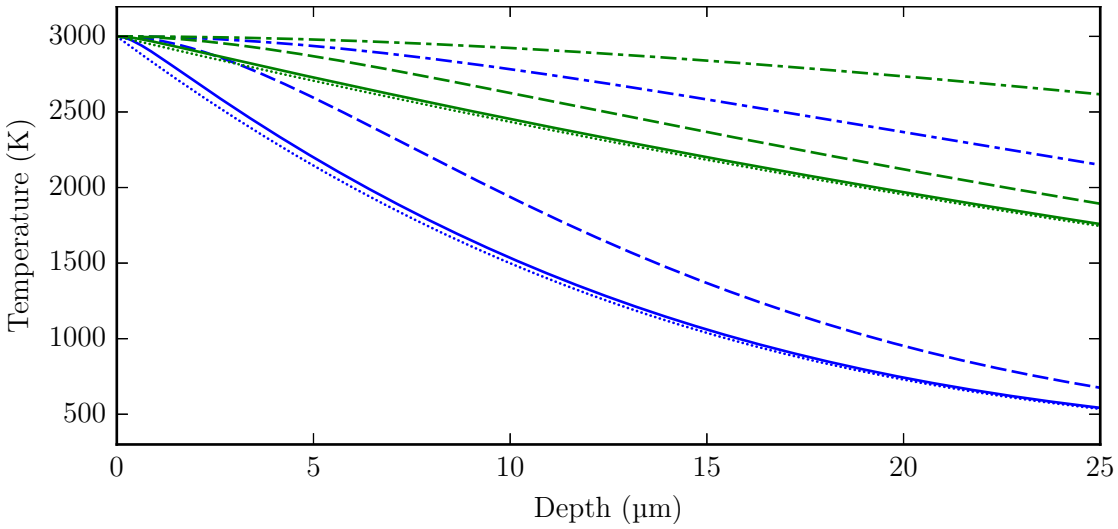

Figure 3.2: Temperature profile calculated using Eq. (3.4) of a semi-infinite solid illuminated by a laser of uniform intensity. Blue lines show the temperature profile after 0.22 ms of heating and green lines represent pulses with a duration of 2.2 ms. The intensity of the beam has been adjusted to heat the surface to 3000 K. Dotted lines denote a hypothetical perfect absorber, i.e., $\alpha^{-1} = 0$, solid lines, dashed lines, and dash-dotted lines represent $\alpha^{-1} = 0.4\,\mu\text{m}$, $4\,\mu\text{m}$ and $40\,\mu\text{m}$, respectively.

at the end of the pulse to enable evaporation there. With the considered parameters, there is almost no difference in the temperature profile between light at $\lambda = 9.3\,\mu\text{m}$ with an absorption length of $\alpha^{-1} = 0.4\,\mu\text{m}$ and light at a hypothetical wavelength with an absorption length of 0 that is completely absorbed at the surface. Unless significantly shorter pulses are used, the penetration depth of a laser at $\lambda = 9.3\,\mu\text{m}$ can hence be neglected.

In contrast, a laser at $\lambda = 10.6\,\mu\text{m}$ increases the region where the material is above the softening point by more than 50 % for $\alpha^{-1} = 4\,\mu\text{m}$ and roughly 500 % if the largest reported value $\alpha^{-1} = 40\,\mu\text{m}$ is used. Longer pulses have a similar effect as a penetrating source: During the pulse, the heat can propagate through the medium and melt lower regions. Fabrication using a wavelength with a short absorption length can thus prevent excessive melting, if short, intense pulses are used. The short absorption length is not a disadvantage if increased melting would be desired to smooth out large-scale roughness, because a longer absorption length can always be mimicked by increasing the duration of the laser pulse.

An additional advantage of using short, nonpenetrating pulses is fast resolidification of the material, because less heat has to be transported away to cool the sample. For uniform illumination by a laser pulse of finite duration that is absorbed directly at the surface of a semi-infinite solid, i.e., $\alpha^{-1} = 0$, the heat flow equation can be solved exactly [111]:

$$\Delta T(t, z) = \frac{I_0(1 - R)}{K} \left(\delta \,\text{ierfc}(z/\delta) - \delta_0 \,\text{ierfc}(z/\delta_0)\right), \tag{3.6}$$

where t is the time since the start of the laser pulse and $\delta_0 = 2\sqrt{D(t - t_0)}$ contains

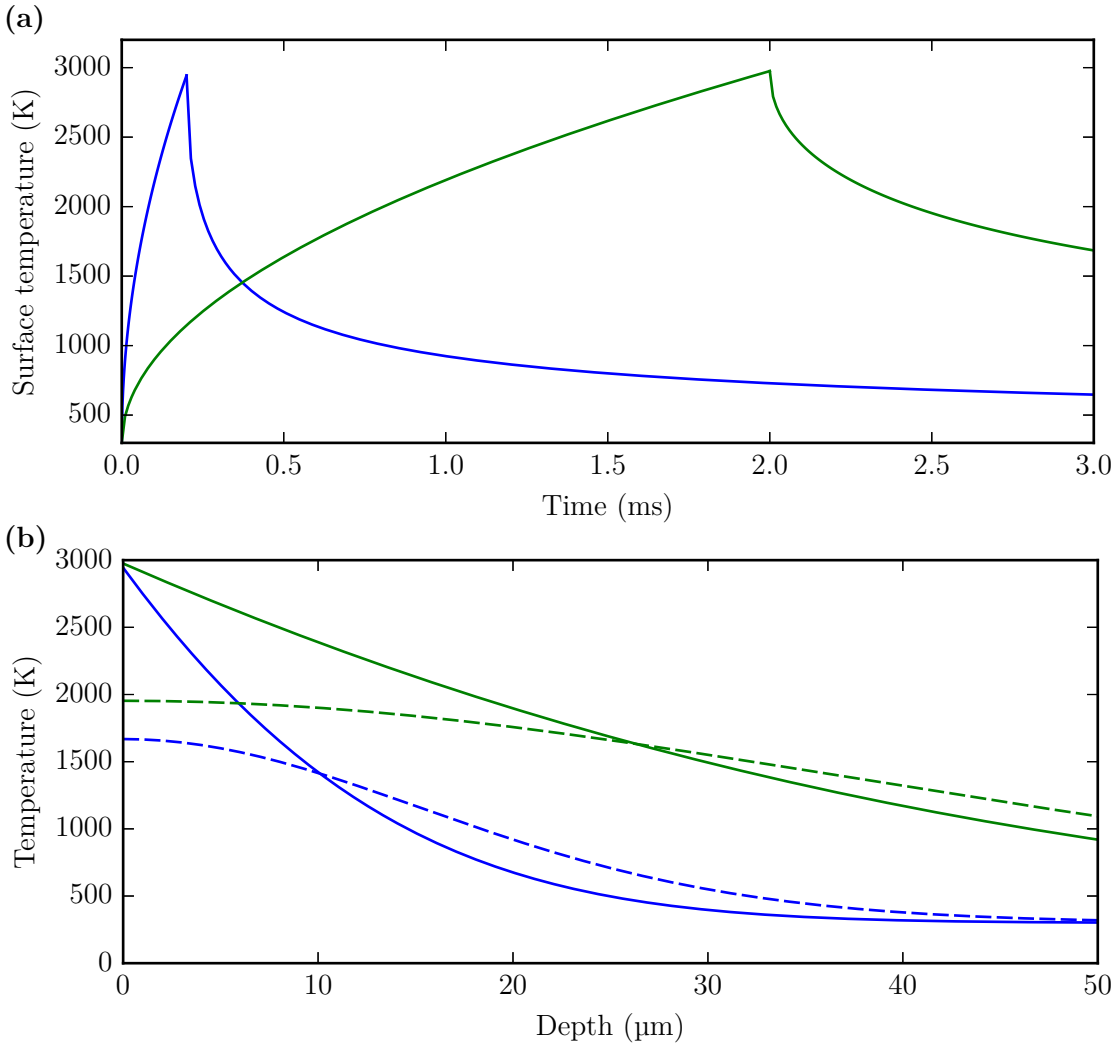

Figure 3.3: (a) Temperature on the surface of a uniformly illuminated semi-infinite solid calculated with Eq. (3.6). The blue line denotes a pulse with $I_0 = 0.66\,\mathrm{GW\,m^{-2}}$ starting at $t = 0$ and stopping at $t = t_0 = 0.2\,\mathrm{ms}$. The green line denotes a longer pulse with $t_0' = 10t_0$ with an intensity of $0.32I_0$. Although the same surface temperature is reached, the material cools much more quickly after the short pulse, because the laser has added less total heat to the substrate. (b) Corresponding temperature profile immediately after the laser beam has been turned off (solid lines) and after 0.1 ms of cooling in case of the short pulse (blue dashed line) and 0.5 ms of cooling in case of the longer pulse (green dashed line). In the former case, the material has already cooled well below the softening point, while in the latter case, the first 10 µm below the surface are still hot enough to flow.

the duration of the laser pulse t_0. Using the same parameters as above, the surface temperatures and the temperature profiles for a pulse with 0.2 ms and 2 ms were calculated and are shown in Fig. 3.3. The intensity of the longer pulse has been adjusted to $0.32I_0$ to get the same temperature at the time the laser is turned off. After turn off, the material heated by the short laser pulse cools much more quickly and the surface temperature is below 1900 K after 60 µs and no significant mass flow of the glass should occur after this time. For a pulse 10 times longer, the surface also takes 10 times longer to cool to that temperature and the material is hot enough to flow under its own weight for a much longer time. The model can be tested by measurements of the white-light emission of a fused silica substrate during CO_2 laser fabrication of mirrors with short pulses. It has been shown [112] that the material cools quickly to half its temperature within 100 µs after the laser beam has been shut off, compatible with the calculations of cooling by heat transfer made above.

Since all calculations in this section have assumed a semi-infinite solid, it is questionable how well the results hold for optical fibers. The boundary condition at the edge of the end facet is clearly different from that of a semi-infinite solid. Therefore, only the center of the fiber could possibly be described as a semi-infinite solid as long as the dimensions of the fiber are much larger than the diffusion length, which is $\delta = 2\sqrt{Dt} = 50\,\mu\text{m}$ for $t = 1\,\text{ms}$. This is clearly a good approximation along the length of the fiber, but is not fulfilled in the plane of the end facets for typical fibers with a diameter of 125 µm. This simple theory will therefore only be a good description for very short pulses, but as it does not include material loss, material flow, or surface tension, it is unlikely to give accurate results for long pulses, anyway. If a laser beam with a waist of 220 µm is used, the intensity varies by less than 15 % over the end facet of a fiber with a diameter of 125 µm, so uniform illumination should be a good approximation in the center of the fiber.

3.2 Fabrication setup

3.2.1 CO_2 laser

The setup used to fabricate mirror substrates on fiber end facets as well as on fused silica plates is illustrated in Fig. 3.4. The CO_2 laser was operated at 9.3 µm wavelength and had a maximum CW output power of 35 W. Its microwave pump could be controlled by a TTL input to quickly toggle the laser output and perform pulse width modulation to adjust the output power. This input was driven by a microcontroller to create pulses with durations on the order of 1 ms with a repetition rate of 2 Hz. A small fraction of the beam was directed onto a HgCdTe photodetector with a bandwidth of 1 MHz to monitor the output power and determine the pulse shape. When creating pulses, a comparison to a calibration performed at CW operation revealed that the laser output was considerably higher in the first millisecond after turn on than the specified and measured average output power over longer time scales (see Fig. 3.5). For unknown reasons, the pulse shapes of subsequent pulsed were not identical, but differed significantly from pulse to pulse. The signal of the photodetector could be integrated and used as feedback to the microcontroller to stabilize the total pulse energy by stopping the pulse after a predetermined pulse energy had been reached, at the cost of a varying pulse length. A shutter with an opening and closing time of 15 ms each was used to pick single pulses for

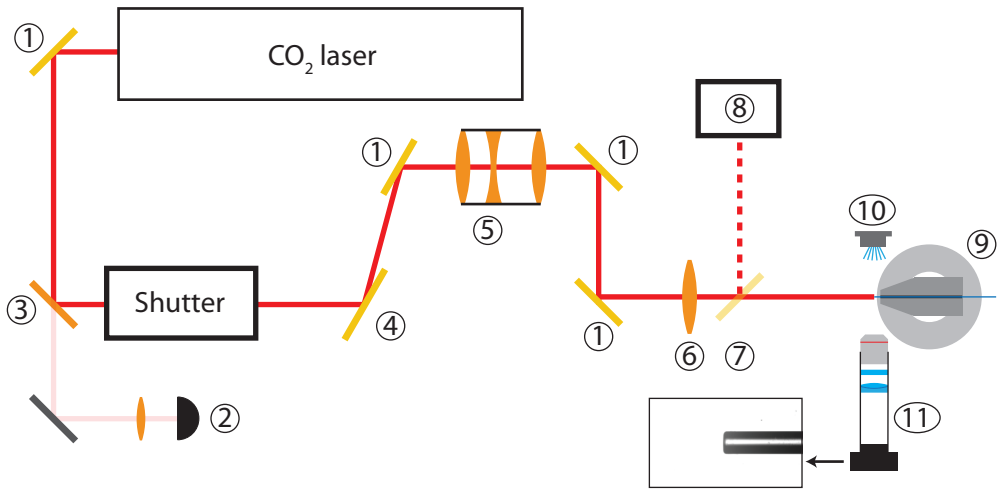

Figure 3.4: Setup for the shaping of fiber end facets with a CO_2 laser. The orientation of the main CO_2 laser beam is adjusted with gold-coated copper mirrors (1). A small part of the beam is coupled out with a ZnSe 99:1 beam splitter (3) and directed onto a HgCdTe photodetector (2) to continuously monitor the laser output power. The polarization can be switched from linear to circular by a phase shifting mirror (4), which requires an out-of-plane geometry. The size of the beam can be adjusted with a variable beam expander (5) with a magnification of 0.5x-2.5x. The beam is focused on the end face of an optical fiber by a ZnSe/ZnS achromatic lens (6) with a focal length of 200 mm. To image the generated spot, the light can be redirected with a removable mirror (7) to a scanning slit beam profiler (8), placed at the same optical path length from the lens as the fiber end. The fiber is placed in a metallic V-groove holder and mounted on a six-axes positioning stage (9). To determine the position of the optical fiber, it is illuminated by a blue LED (10) and imaged with a microscope (11), consisting of a 4x microscope objective, a blue color filter, an achromatic lens with 200 mm focal length, and a CMOS camera. An example image shows a fiber with a diameter of 125 µm as imaged by the microscope. Not shown is a similar microscope perpendicular to the figure plane used to image the fiber in the figure plane. The schematic is not to scale.

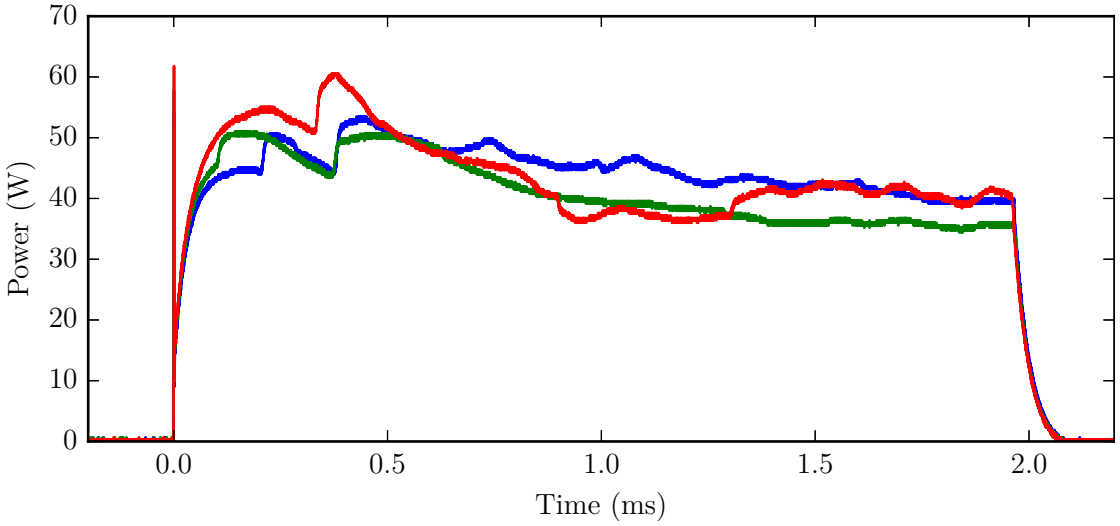

Figure 3.5: Three pulses of the CO_2 laser with 2 ms duration recorded shortly after each other. The pulse shape varies significantly from pulse to pulse and the output power is considerably higher than the maximum power of 35 W observed during continuous-wave (CW) operation. The average power during the first millisecond of the pulse is 47 W for the pulse marked in blue, 45 W for the pulse in green, and 48 W for the red pulse. Most of the time a spike in laser power is measured for 1 µs directly after turning on the microwave pump. The real duration of this spike could be even shorter, because the measured signal is limited by the bandwidth of the detector. Due to the short duration, the spike contains a pulse energy that is negligible compared to the rest of the pulse. The calibration of the photodetector was performed by comparison to a thermal power meter during CW operation. As this could not be done with powers exceeding 35 W, the calibration for higher powers had to be extrapolated, assuming linear response of the detector.

fabrication by opening on command to let a single pulse pass.

At an output power of 1 W, the polarization of the laser was measured to be vertical with an extinction ratio of 60:1. Due to the damage threshold of the polarizer used for this measurement, this could not be verified for higher output powers. Two different configuration were used for machining fiber ends with different polarization of the CO_2 laser beam on the fiber end facets. In the first configuration, the beam was reflected off a phase shifting mirror with the outgoing beam being 45° out of plane. A second mirror reflected the beam into a plane parallel to the original plane, creating a beam with circular polarization. In the second configuration, the phase-shifting mirror was replaced with a gold-coated mirror that reflected the beam 90° out of plane. This resulted in horizontal polarization of the beam after reflection off the second mirror.

The laser beam was focused on the substrate to be machined with an achromatic ZnS/ZnSe lens with a focal length of 200 mm. Best results were achieved with the substrate at the position of the laser beam waist. Significant deviations from this position along the laser beam resulted in a reduced quality of the beam profile and asymmetric structures on the substrates after machining. In front of the focusing lens,

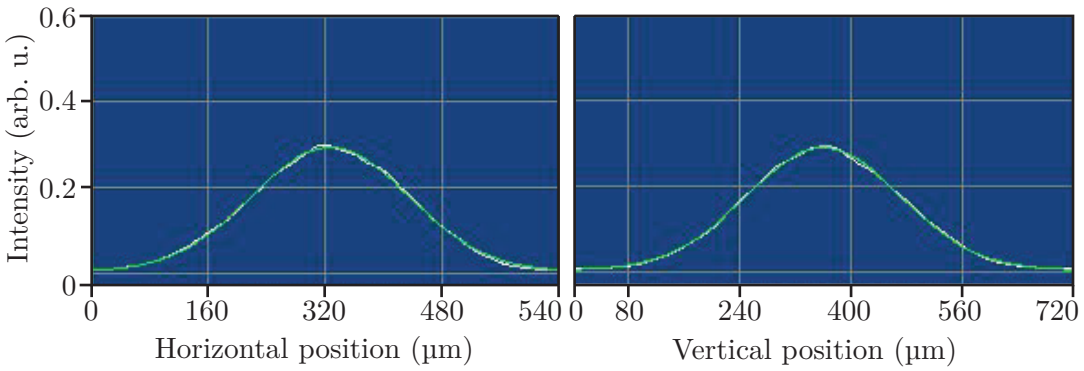

Figure 3.6: Example of a beam profile used for fabrication. The white lines represent the measured intensity and the green lines are Gaussian fits thereof. From the fits the waist can be determined to be $(219 \pm 2)\,\mu m$ in the vertical direction and $(214 \pm 2)\,\mu m$ in the horizontal direction, with the error being the standard deviation resulting from fits to a hundred measurements.

the size and divergence of the beam was adjusted using a variable beam expander with a magnification between 0.5x and 2.5x. To image the resulting spot, a removable mirror was placed between the lens and the substrate that directed the beam on a scanning-slit beam profiler. The distance between the lens and the beam profiler was set to be the same as the distance between the lens and the substrate, such that the spot on the beam profiler should resemble the spot on the substrate when the mirror is removed. As the beam profile could not be measured at the position of the substrate, this could not be verified, but due to the large spot sizes used for fabrication, a mismatch of 5 mm between the position of the beam profiler and the position of the substrate would result in an error of only 5 % for the beam waist as measured by the beam profiler. The beams used for almost all fabricated mirrors had a waist in the range of 210 µm to 220 µm and close to rotational symmetry around their axes with the difference between major and minor axis of the waist being 2 % or less (see Fig. 3.6).

3.2.2 Substrate alignment

All substrates were mounted on a six-axis positioning stage that allowed translations up to ±10 mm and rotations up to ±10° around its central position. When glass plates with a diameter much larger than the beam waist were used as substrates, alignment in the plane perpendicular to the CO_2 laser beam axis was uncritical and the stage could be used to create series of structures with a defined distance between them. Because of the large Rayleigh length of the beam, alignment along the beam axis was uncritical as well.

In contrast, when end facets of optical fibers were used as substrates, alignment in the plane perpendicular to the beam axis was crucial to fabricate useful structures, because the center of the structure needs to be in the center of the fiber end facet to enable good coupling between the cavity mode and the fiber mode guided by the fiber core. To determine the position of the fibers, two microscopes with magnification close to 4x imaged the fiber from the horizontal and the vertical direction in that plane onto CMOS cameras. The resulting images were analyzed by an image recognition algorithm that

could detect the position of the fiber and its orientation with respect to the camera with a precision of 0.5 µm and 0.1°. The values produced by that algorithm could be used to automatically position a fiber at the same position as a previous fiber, allowing iterative optimization from one attempt to the next.

3.2.3 Characterization of structures

To optimize the fabrication process and to characterize the fabricated structures in order to select the best ones before applying a coating, all structures were imaged with a commercial white-light interferometer. Due to a combination of vertical-scanning interferometry and phase-shifting interferometry, the device had a specified vertical resolution of below 0.1 nm. The lateral resolution was diffraction limited and depended on the objective: the 50x (5x) objective had a resolution of 0.5 µm (2.2 µm) with a field of view of 166 µm x 125 µm (1.7 mm x 1.3 mm). The light collection efficiency from angled surfaces limited the maximum slope with respect to the objective that could be successfully imaged to 27° (5.5°) for the 50x (5x) objective. Therefore, the structures fabricated on glass plates could not be fully imaged, because the size of the CO_2 laser beam was larger than the field of view of the 50x objective and except for the center of the structures, the slopes were to steep for the 5x objective. Nevertheless, the field of view for the 50x objective was large enough to cover all areas of a structure that would influence a cavity mode in the center of the structure and the 5x objective could be used to measure the depth of the structure relative to the surface of the glass plate.

The end facets of optical fibers with a diameter of 125 µm could be found with the 5x objective and then fit completely in the field of view of the 50x objective, with which all data was then taken. As the CO_2 laser beam was larger than the end facets, they were fully transformed during the fabrication and no reference to the original end facet remained. Therefore, it was necessary to calibrate the angle of the reference plane in the objective to get accurate measurements of the angle of any structure with respect to the fiber axis. The calibration was performed by imaging a cleaved fiber end in the V-groove holder used for fabrication and multiple rotations of the fiber by 180° around its axis. From these measurements, the angle of the reference plane could be determined and the stage the holder was placed on could be adjusted to compensate for this angle. Multiple insertions of the same fiber under the same rotation into the holder showed that the orientation of the fiber axis could be reproduced with an error of ±0.1°, such that the angle of any structure with respect to the fiber axis could be measured by the white-light interferometer up to this error.

3.3 Fabrication results

3.3.1 Materials and substrates

The fabrication process was tested with polished substrates of three different base materials, fused silica, N-BK7, and sapphire, to get an indication about the influence the material composition has on the process (Fig. 3.7). As reported previously [112], the process works very well with planar fused silica substrates. After a 1 ms CO_2 laser pulse with the beam profile depicted in Fig. 3.6 at full output power of about 50 W on average during the first millisecond (cf. Fig. 3.5), the resulting surface was very smooth

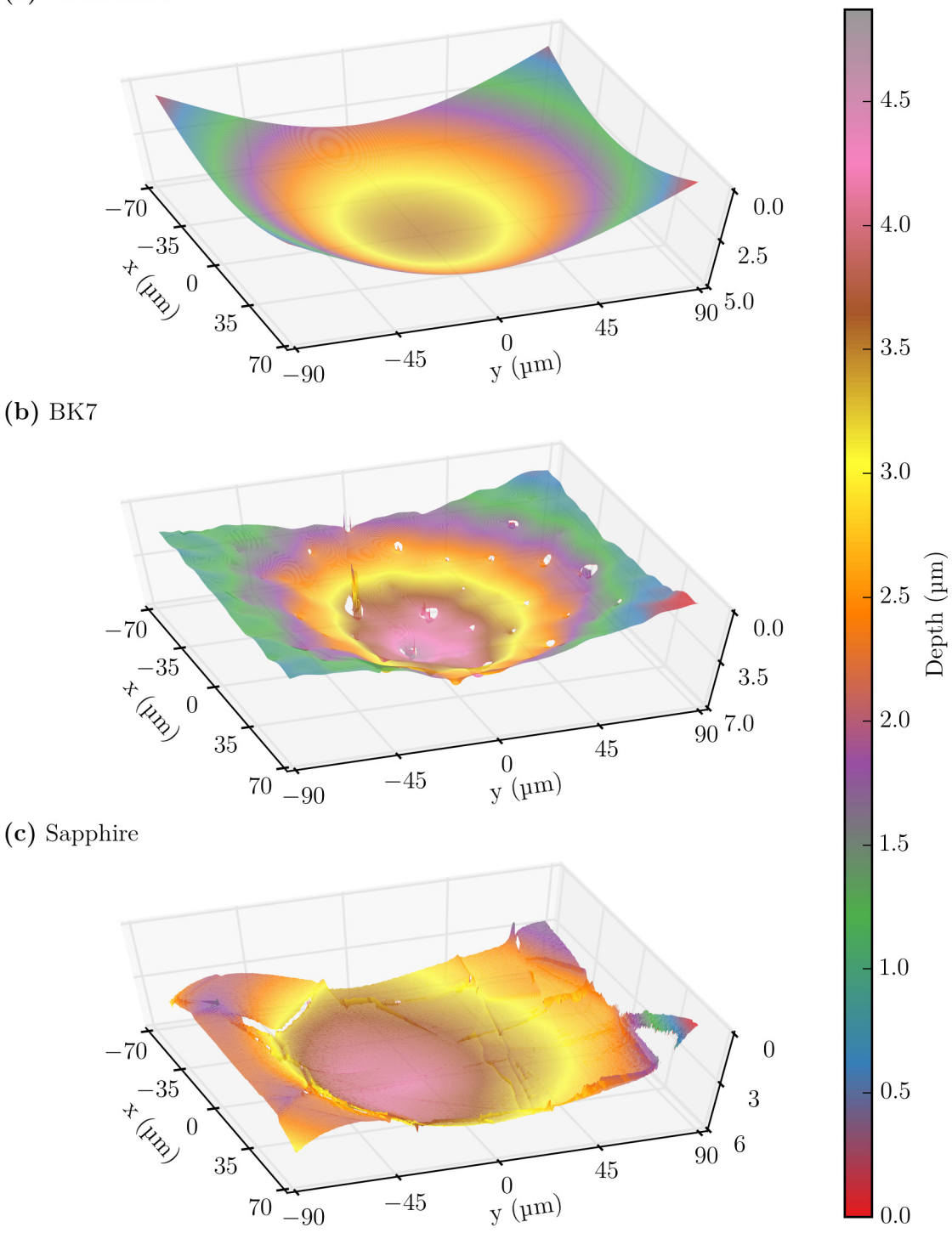

Figure 3.7: Surface profiles after CO_2 laser illumination of large substrates, consisting of different materials. The profiles were taken at the respective center of the resulting structures. The laser pulses were all made at full laser output power. (a) UV-grade fused silica after a laser pulse with 1.0 ms duration. (b) N-BK7 after a 0.95 ms pulse. (c) Sapphire, after a 4 ms pulse. See text for further description.

and was dominated by the desired curvature with no obvious local variation (Fig. 3.7a). In comparison, the borosilicate glass N-BK7 treated with a similar laser pulse yielded a structure with similar depth and radius of curvature (Fig. 3.7b), consistent with similar absorption and evaporation properties due to silica being the main component in both glasses. In addition to the desired concave structure, however, the fabricated structure on N-BK7 showed smaller-scale dimples, the centers of which were often too steep to be measured by the white-light interferometer, leading to holes in the measured data. A possible explanation for these dimples could be bubbles formed during the fabrication process, which deform the structure locally. These dimples render the resulting structure unsuitable as a mirror substrate and show that the process is highly dependent on the material properties of the glass.

For comparison with crystalline materials, the fabrication process was also tried on sapphire substrates. Due to the higher heat conductance and lower absorption index of sapphire, more energy and therefore longer pulses were required for ablation to occur. Although a concave structure was created (Fig. 3.7c), it was rougher, irregular, had multiple cracks and could not be used as a mirror substrate.

Optical fibers

Although CO_2 laser fabrication of mirror substrates on glass plates can result in microscopic structures, the glass plates themselves are still macroscopic structures, which limit optical access to the inside of the cavity and applicability in a crossed cavity geometry. If these qualities are important, it is therefore necessary to use substrates of smaller lateral dimensions. End facets of optical fibers are a particularly interesting option as initial substrates, because standard optical fibers have a diameter just above the desired mirror diameter and are cheaply available. If the mirror is centered on the end facet, the guided mode of single mode fibers can provide intrinsic coupling to the cavity mode, greatly simplifying that process. The material of optical fibers is almost pure fused silica and therefore suitable for CO_2 laser fabrication, except for the dopant required to create the refractive index profile which is necessary to guide modes. Although the dopant concentration is $< 1\,\%$ germanium for typical single-mode fibers for near-infrared wavelengths, the fabrication process is highly dependent on the material composition, as described above. To estimate whether there is an influence of the dopant, end-facets of single-mode and graded-index multi-mode fibers were both used as initial substrates with the only specified difference being the dopant concentration profile. Any systematic difference in the results of the fabrication process can thus be attributed to the dopant concentration.

Typical optical fibers are coated with an acrylate polymer that protects the fiber from mechanical damage. Fibers with these protective coatings cannot be used as fiber mirrors, because these polymers are not vacuum-compatible and the fibers need to be exposed to high vacuum during the application of a highly reflective coating on the end facet and ultra-high vacuum if used in a cold-atom experiment. As the fibers are too fragile to consistently survive the coating process without a protective layer, fibers with a $20\,\mu m$ thick outer copper coating were used. To prepare the fibers for fabrication, the copper coating was chemically removed over the length of a few centimeters at the end of the fibers using nitric acid and the fibers were cleaned in an ultrasonic bath. Flat end facets were produced with a standard telecommunication precision cleaver, which uses a

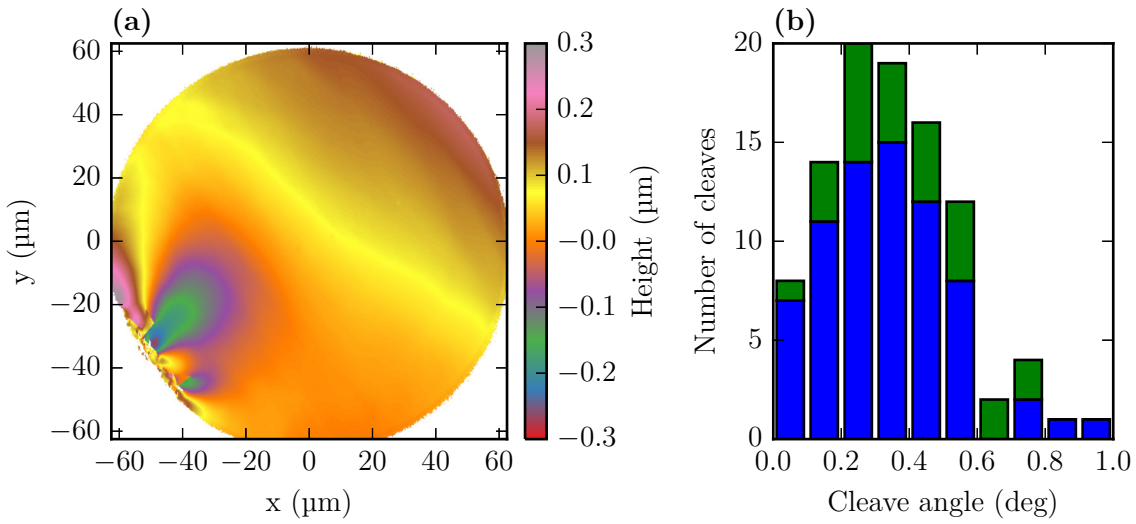

Figure 3.8: (a) Surface profile of a fiber end after cleaving. On the left side typical artifacts of the cleave process can be seen. (b) Histogram of the angle of the fiber end facet to the plane normal to the fiber axis for a total of 100 cleaves. Of these, 72 were cleaves of single mode fibers (blue) and 28 of multi-mode fibers (green, stacked). The mean angle was 0.37° with a standard deviation of 0.24°

diamond blade to incise the fiber and then applies pressure to induce a clean break at this position. This method has the advantage of the preparation of fairly good plane end facets with little effort. However, it almost always resulted in a small defect at one point at the edge of the end facets and the resulting end facets were also not exactly perpendicular to the fiber axis, but had an angle that varied around a mean value of 0.37° with a standard deviation of 0.24°, as measured with the calibrated white-light interferometer and 100 cleaves (cf. Fig. 3.8). It was noticed, that particularly bad cleaves characterized by large defects led to bad results during fabrication. Therefore, the randomness introduced by the cleave might have had an influence on the reproducibility of the fabrication results.

The removal of the copper coating was considerably more time-consuming than mechanical removal of acrylate polymer coating on standard fibers. Therefore, single-mode and multi-mode fibers with a similar refractive index profile, but an acrylate polymer coating were used for iterative alignment of the fabrication setup and copper-coated fibers were used only after the setup had been adjusted to produce the desired results.

3.3.2 Diameter, depth and radius of curvature

Glass plates

Glass plates as initial substrates have the advantage of a uniform surface that can be described by a simple model. The glass plates used were circular with a diameter of 7.75 mm and a thickness of 4 mm. These dimensions are much bigger than the diameter of the CO_2 laser beam, the penetration depth, or the diffusion length during pulses with

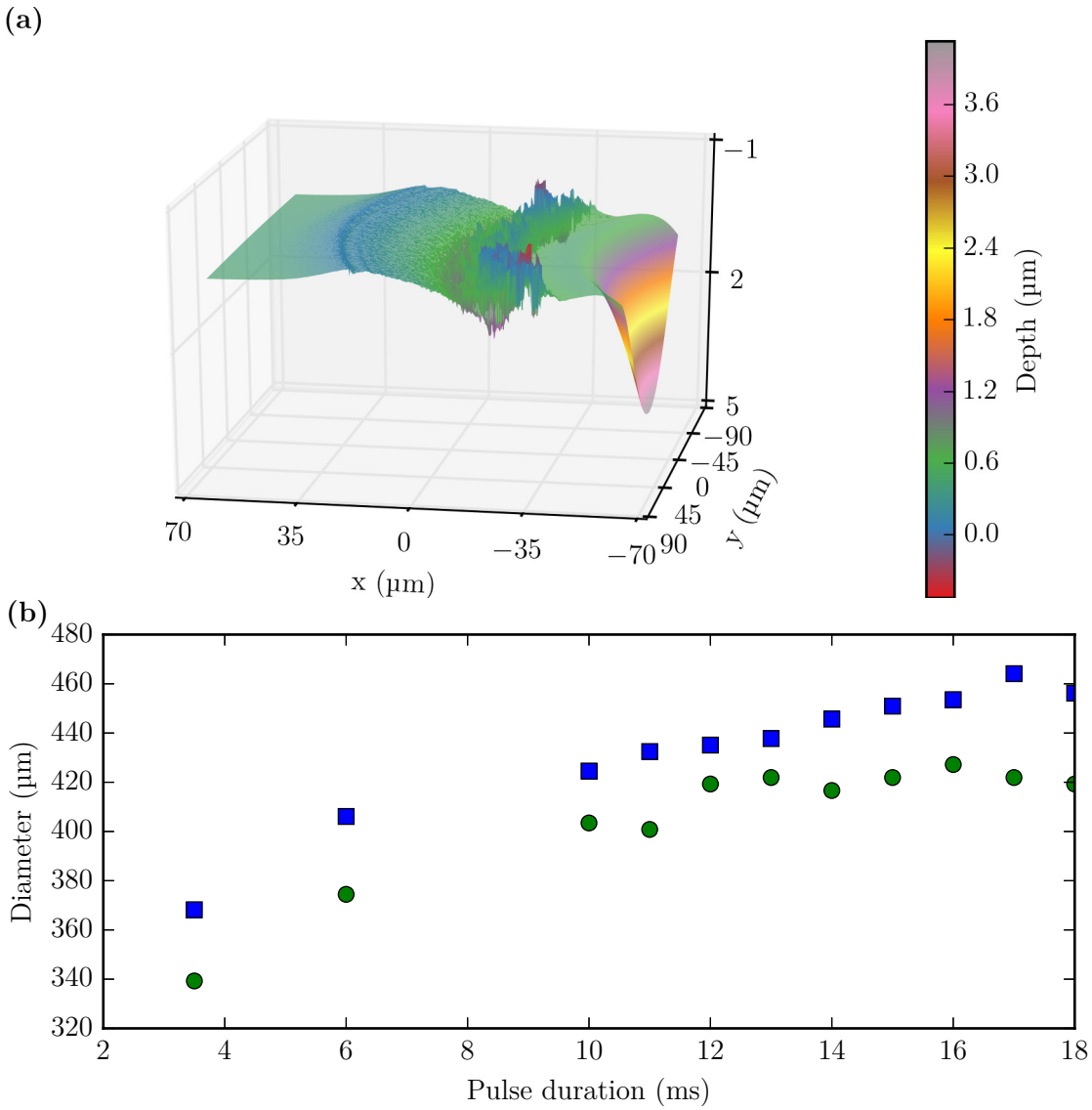

Figure 3.9: (a) Edge of a structure on a glass plate fabricated with a CO_2 laser pulse of 18 ms duration. On the left the unmodified glass plate starts and the concave part of the structure extends to the right. In between there is a ridge that is rougher than the original glass surface and the center of the fabricated structure. (b) Inner diameter of that ridge as a proxy for the structure diameter in the direction that was vertical during fabrication (blue squares) and in the horizontal direction (green circles) as a function of the pulse length. The structures are not rotationally symmetric, but are on average 5 % larger in the vertical direction.

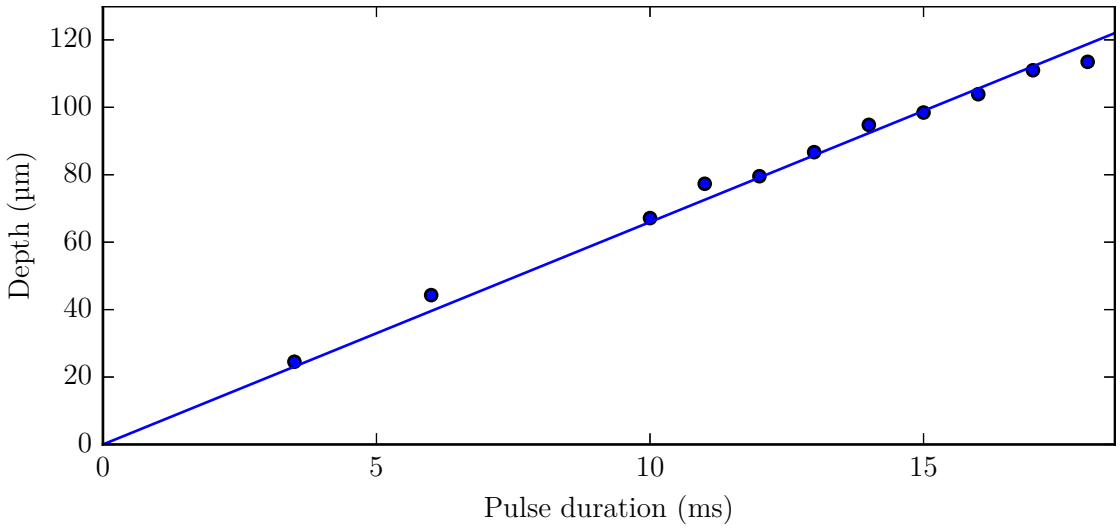

Figure 3.10: Depth of structures fabricated in glass plates with CO_2 laser pulses of varying duration. The data points are measurement results and the solid line is a linear fit through the origin, which results in an ablation speed of $v = (6.6 \pm 0.1)\,\mathrm{mm\,s^{-1}}$

durations on the order of milliseconds. Therefore, the glass plate can be described as a semi-infinite solid if the position of the laser beam is sufficiently far away from any of its edges and under this condition, the resulting structure should be independent of its position on the substrate.

At the edge of the structure, there was not a smooth transition from the unmodified glass plate to the concave part in the center of the structure. Instead, the fabrication process resulted in a ridge that was higher and rougher than both the unmodified substrate and the center of the structure (Fig. 3.9a). The most likely explanation is the resolidification of glass that had been evaporated from the center of the structure. Between this ridge and the center of the structure, the slope was too step for interferometric measurements such that only the extent of the ridge and the center of the structure could be measured. Therefore, the inner diameter of the ridge was taken as a proxy for the structure size, in the absence of other suitable criteria. The resulting diameter as a function of the pulse duration at full output power of the CO_2 laser is depicted in Fig. 3.9b. The diameter was mainly determined by the diameter of the laser beam, with only a slight dependency on the pulse duration. The structures were slightly elliptic, with the diameter in the vertical direction being 5 % larger than the diameter in the horizontal direction with a standard deviation of 3 %. The orientation is compatible with the orientation of the CO_2 laser beam, which was also slightly larger in the vertical direction by 2 % (Fig. 3.6).

The depth of the structure as a function of the pulse duration, defined as the height difference between the unmodified glass plate and the height minimum of the structure, is plotted in Fig. 3.10. The data shows a linear dependence of the depth on the pulse duration with a constant evaporation speed of $(6.6 \pm 0.1)\,\mathrm{mm\,s^{-1}}$. This is in direct contradiction of the model presented in Ref. [46], which would predict the depth to exponentially increase with the pulse duration. The difference is in the parameter regime.

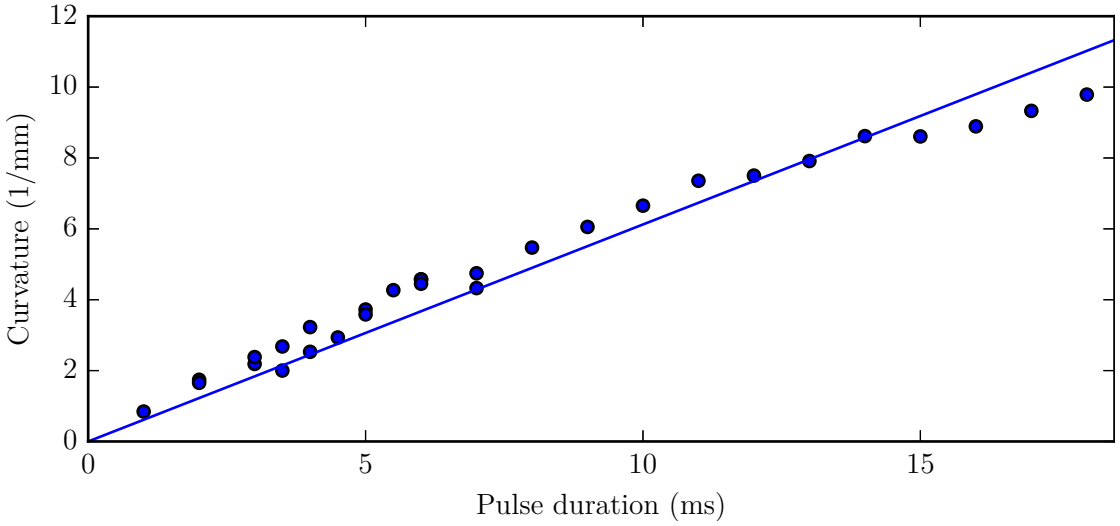

Figure 3.11: Curvature along the major axis, i.e., the axis with the largest radius of curvature, of the structures fabricated on glass plates plotted against the CO_2 laser pulse duration. The relation is close to linear with a fitted slope of $(0.61 \pm 0.01)\,\mathrm{mm}^{-1}\,\mathrm{ms}^{-1}$

The experiments reported on in Ref. [46], which fit the model, were done with a smaller CO_2 laser beam waist of 51 µm and pulses with durations of up to 50 ms. Therefore the ratio of the diffusion length $\delta = 2\sqrt{Dt}$ to the beam waist was larger than one and the model predicts only a small increase in temperature with longer pulse durations in this regime, thus effectively resulting in a constant evaporation speed. In contrast, the experiments presented here were performed with a larger beam waist and shorter pulse duration, reducing that ratio. In this case, the model predicts a steep increase in temperature at the center of the CO_2 laser beam with longer pulses, up to a theoretical temperature of 15 kK for a pulse duration of 18 ms. This temperature is much larger than the boiling point of fused silica, such that heat loss due to evaporation has a strong influence on the temperature distribution and cannot be ignored as it has been in the model. As an alternative, one can assume that in the center of the beam the material quickly heats up until it reaches a steady-state temperature, at which heat loss from thermal conduction and evaporation equals heating by the laser beam. In that case, the steady-state temperature in the center of the beam can be determined from the velocity of the evaporation front with

$$T = \frac{-U}{k_\mathrm{B} \ln(v/v_0)} = 3150\,\mathrm{K}, \tag{3.7}$$

where $v_0 = 3800\,\mathrm{m\,s^{-1}}$ and $U = 3.6\,\mathrm{eV}$ [46]. This is consistent with the observation of the temperature of fused silica as measured by black body radiation asymptotically approaching 3100 K, when continuously heated by a CO_2 laser beam [109].

This simple model fails to make a prediction of the curvature at the center of the fabricated structures, because it is not accurate enough to estimate the relative ablation velocity, which determines the radius of curvature. A plot of the curvature in the center of the structure against the pulse duration (Fig. 3.11) also reveals a close to linear

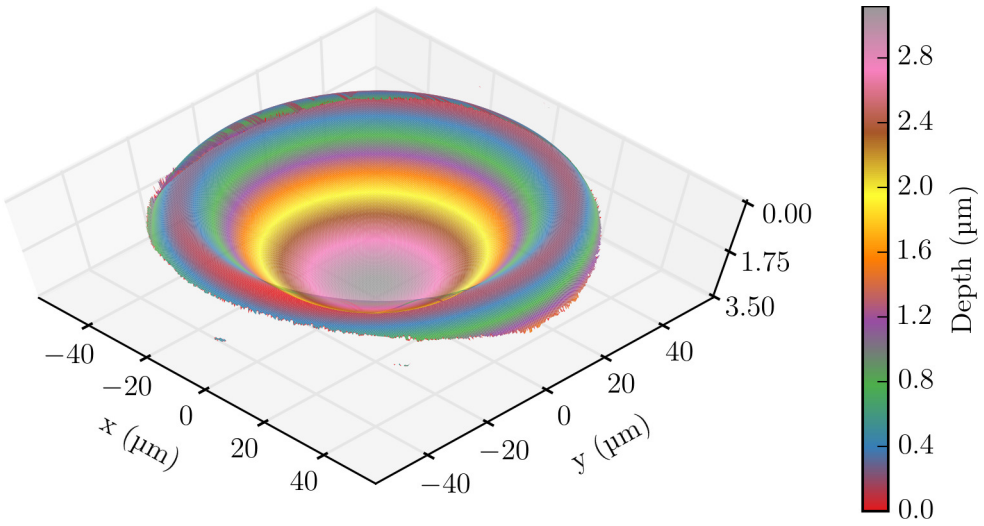

Figure 3.12: Profile of the surface of a fiber end facet after illumination with the CO_2 laser. In the center a concave structure has been formed by evaporation. Due to the high surface tension at the edge of the end facet, the edge shows a convex shape. Note that the diameter of the measured surface is less than the diameter of an untreated end facet (Fig. 3.8), because the edge becomes too steep to be measured with the white-light interferometer.

relationship with a slope of $(0.61 \pm 0.01)\,\mathrm{mm}^{-1}\,\mathrm{ms}^{-1}$. This suggests that the curvature depends linearly on the depth, but the proportionality factor of $(92 \pm 2)\,\mathrm{mm}^{-2}$ remains to be explained by a quantitative model.

Fiber end facets

The structures fabricated on fiber end facets differed from those fabricated on glass plates, because of the finite size of the end facet, which at a diameter of 125 µm was considerably smaller than the $1/e^2$ beam diameter of 440 µm, and the surface tension at the edge of the end facet. A typical structure fabricated on a fiber end facet is shown in Fig. 3.12. At the edge, the effect of the surface tension can clearly be seen, as the surface has a convex curvature that increases towards the edge of the fiber, to the point where the surface becomes too steep to be measured with the white-light interferometer. In contrast, the curvature of the structure is concave at its center due to ablation of the material, similar to the structures fabricated on glass plates.

At full output power of the CO_2 laser, the minimum pulse length that was observed to have an effect on the fiber end facet was 0.24 ms, in good agreement with the value of 0.22 ms at which the surface reaches 3000 K that was calculated in Sec. 3.1. Longer pulses in the range of 0.65 ms–1.15 ms resulted in the desired structures. In contrast to the structures fabricated on glass substrates, where the depth of the structure could be referenced to the untreated surface and a linear relation between pulse length and structure depth was observed, structures on fiber end facets required a different definition of structure depth because the whole fiber end facet was modified by the laser pulse. Nevertheless, one might expect the height differences between the lowest and the highest

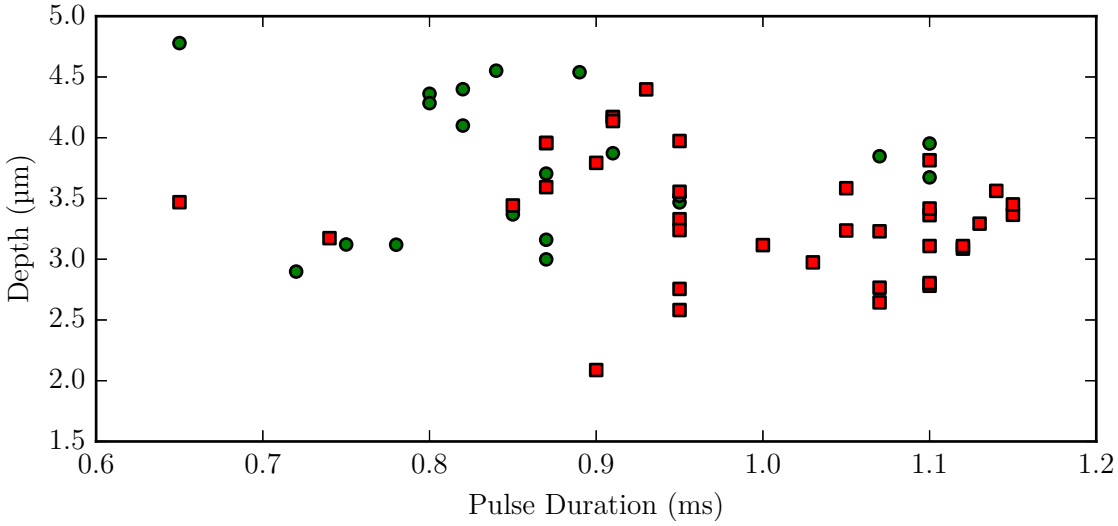

Figure 3.13: Depth of the fabricated structure, defined as the height difference between lowest and highest point of the structure as a function of the pulse length for multi-mode fibers (green circles) and single-mode fibers (red squares). No clear relation between pulse duration and structure depth can be made out. Multi-mode fibers seem to require shorter pulse durations that single-mode fibers.

point of the structure to depend on the duration of the CO_2 laser pulse. However, there was no clear relation between pulse length and structure depth for those fabricated on fiber end facets (Fig. 3.13). The only thing that could be observed was that multi-mode fibers required shorter pulses to achieve a certain structure depth than single-mode fibers. This hints at subtle differences in the behavior during ablation caused by different dopant concentration profiles. There are two possible reasons for the observed depth distribution. The first one is the fluctuation of the laser output power from pulse to pulse, which could not be controlled (cf. Fig. 3.5), such that two pulses with the same length do not have the same pulse profile and thus might lead to different structures. The second reason might be the preparation of the initial fiber end facet by cleaving, which results in different surfaces from fiber to fiber (cf. Fig. 3.8) and might also lead to different results under the same conditions. These two issues would be the prime targets for improvements to the reproducibility of the fabricated structures, but at the moment the data is not sufficient to quantify their influence.

To determine the curvature of the structure, an elliptic paraboloid can be fitted to the measured structure. However, the surface is not exactly an elliptic paraboloid, which is especially evident at the convex edge of the structure. Therefore, the best fitting paraboloid depends on the region of interest chosen for the fit (Fig. 3.14). An estimate of the effective radius of curvature, which is the radius of curvature of spherical mirrors which would produce the mode with the most overlap with the real cavity mode, can be made by using a region of interest around the center of the structure that has roughly the same size as a typical cavity mode. To this end, a square region of $10\,\mu m \times 10\,\mu m$ around the center was chosen and the curvature was extracted from a paraboloid fitted to the measured structure over that region. For every fiber, this method resulted in two

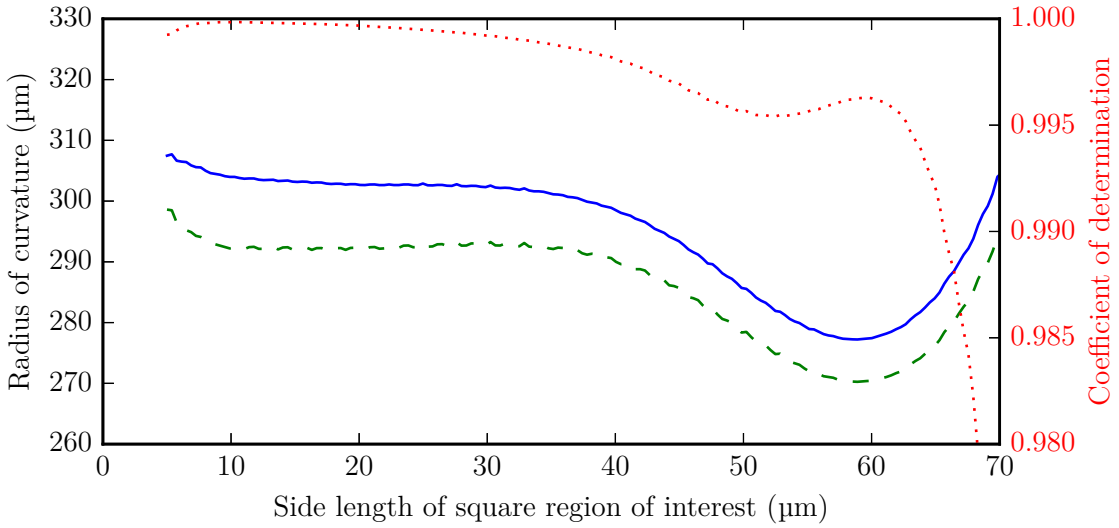

Figure 3.14: Radius of curvature in the center of a structure along the major axis (solid blue line) and minor axis (dashed green line) as extracted from fits of elliptic paraboloids with a square region of interest with different side length. The dotted red line denotes the coefficient of determination of these fits. The radii of curvature are fairly constant for small ROIs with a high coefficient of determination, indicating that the structure is very similar to a paraboloid. For larger ROIs, the fitted radius of curvature starts to change with a simultaneous drop in the coefficient of determination, which shows that the surface starts to deviate from a paraboloid.

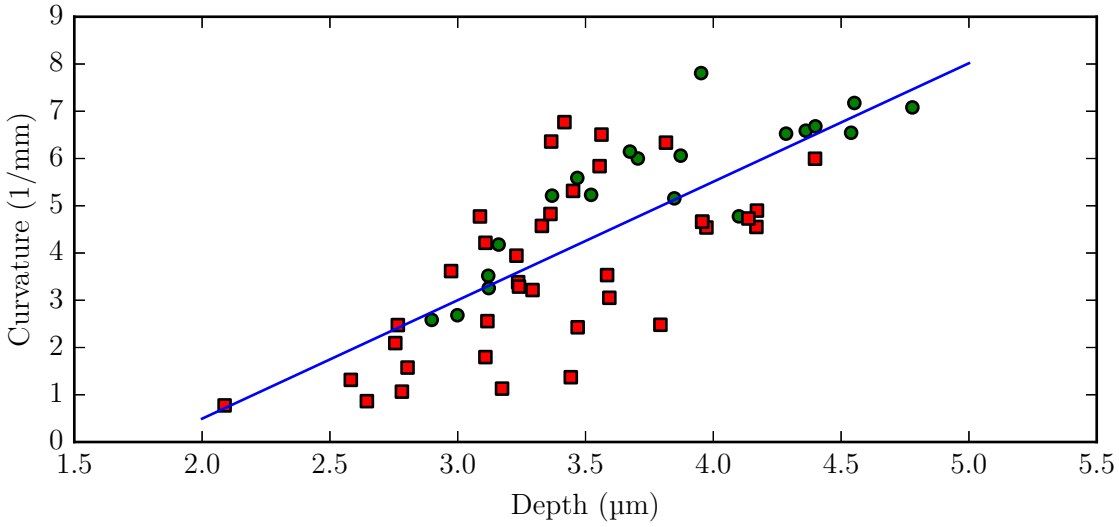

Figure 3.15: Curvature along the major axis in the center of the structure for single-mode fibers (red squares) and multi-mode fibers (green circles) plotted against the depth of the structure. A larger depth is correlated with a larger curvature. The solid blue line is a linear fit to all points with slope $(2500 \pm 300)\,\mathrm{mm}^{-2}$ and intercept of $(-4.5 \pm 1.1)\,\mathrm{mm}^{-1}$.

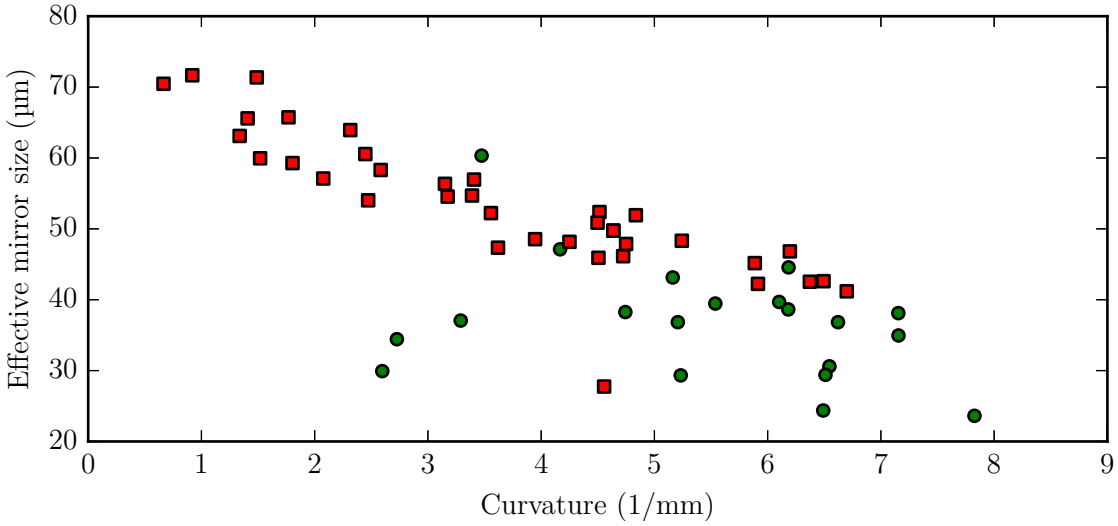

Figure 3.16: Effective mirror size, defined as the width of a square region of interest where an elliptic paraboloid provides a good fit to the surface (see main text for details), plotted against the curvature in the center of the structure for single-mode fibers (red squares) and multi-mode fibers (green circles). For single-mode fibers, the width decreases with the curvature, for multi-mode fibers, the relation is not as evident.

radii of curvature from 120 µm to 1.3 mm and corresponding curvatures from 8.3 mm^{-1} to 0.77 mm^{-1}. As in the case with glass plates, the curvature can be related to the structure depth using a linear model (Fig. 3.15), but the slope of $(2500 \pm 300)\,\mathrm{mm}^{-2}$ is much larger and the intercept is not at the origin, but zero curvature is reached at a depth of (1.8 ± 0.5) µm. The larger slope is not surprising, since the size of the structure has to be smaller to fit on the end facet of the fiber and this smaller structure needs to be more curved to reach the same depth, but a quantitative description of this relation is yet to be found for the parameter regime described here. The nonzero intercept might be explained by the convex ridge at the edge of the fiber being formed by the surface tension acting on molten glass before any ablation occurs, such that the fabricated structure can have a nonzero depth without any curvature in the center. As there is no reference to the position of the untreated end facet left after the CO_2 laser pulse, measurements of the surface profile cannot determine its relative position to the convex ridge, so this explanation cannot be verified with this method.

Although the measured diameters of the structures were up to 90 µm, it is obvious that the convex edge does not fit a concave paraboloid and is therefore not suitable as a cavity mirror. The size of the part of the surface that is useful as a mirror substrate is thus smaller than the structure itself and can be estimated by finding the largest region, where a paraboloid fits the measured surface. As the transition from a good fit to a bad fit is continuous, one needs to find a criterion at which point to reject the fit due to excessive deviation. One possible criterion is to calculate the coefficient of determination

R^2, which is defined as

$$R^2 = 1 - \frac{\sum_i (z_i - \zeta_i)^2}{\sum_i (z_i - \bar{z})^2}, \tag{3.8}$$

where z_i are the measured values of the surface profile, $\bar{z}$ is their mean value and ζ_i are the values explained by the best fitting paraboloid. One can now define the effective mirror size as the maximum size of a square region of interest where the deviation of the coefficient of determination from 1 is smaller than 10 times its minimum deviation. The resulting effective mirror size is plotted against the curvature in the center of the structure in Fig. 3.16. From this analysis it can be deduced, that for single-mode fibers the effective size of the mirror decreases with increasing curvature, indicating that deeper and thus more curved structures reduce the usable size of the entire structure. The mean value of the effective mirror sizes calculated with this method is 47 µm with a standard deviation of 12 µm, which is on the order of the required mirror size for a cavity with a length of 140 µm and mode matching efficiency of 90 % calculated in Sec. 2.4.1. Doubling the allowed deviation of the coefficient of determination results in sizes less than 7 % bigger, but the criterion chosen is nevertheless somewhat arbitrary. Due to the continuous transition from a parabolic shape to a nonparabolic shape, any model that assumes a finite diameter and discards all light outside of this fixed shape, is too simple to describe losses due to mirror size in a cavity. A more thorough, but computationally much more expensive treatment of this issue can be made using an analysis of mode mixing in a cavity, which will be described in Sec. 3.5.5.

3.3.3 Eccentricity

The fabricated structures were in general not rotationally symmetric, but slightly elliptic with the curvature varying with direction. This ellipticity allows two axes in the plane perpendicular to the fiber axis to be distinguished: one with the largest radius of curvature R_1, the major axis, and one with the smallest radius of curvature R_2, the minor axis. The amount of ellipticity can be quantified using the eccentricity ϵ, which is defined as

$$\epsilon = \sqrt{1 - \frac{R_2}{R_1}}. \tag{3.9}$$

The eccentricity of the structure can be understood geometrically as the eccentricity of the spheroid that provides the best description of the surface or as the eccentricity of the ellipses formed by the contours of the surface.

To calculate the eccentricity, the curvatures of the minor and major axis in the center of the best fitting elliptic paraboloid were extracted as described in the previous section. The result is shown in Fig. 3.17. Structures fabricated on glass plates with a circularly polarized CO_2 laser beam showed a consistent orientation of the major axis of the radius of curvature along the major axes of the beam (compare to Fig. 3.6), but the mean eccentricity of 0.31 (standard deviation 0.03) of the radius of curvature was larger than the measured eccentricity of the CO_2 laser beam of 0.21 ± 0.06. This could either be due to an enhanced sensitivity of the fabrication process to the eccentricity of the beam, resulting in amplification, or due to the beam profiler not measuring at exactly the same distance from the lens as the glass plate and thus measuring a different value for the eccentricity than was actually used.

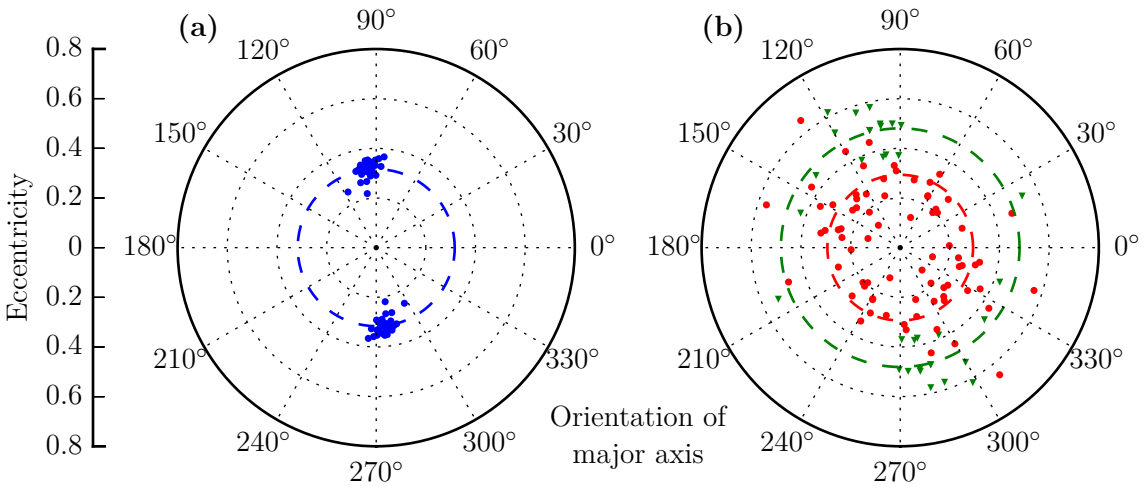

Figure 3.17: Eccentricity (radial axis) and orientation with respect to the CO_2 laser beam of the major axis (polar angle). To reflect the π-periodicity, all points have been duplicated and rotated by π. The angles are relative to the horizontal direction during fabrication. (a) Eccentricity of structures fabricated on glass plates using circular polarization of the CO_2 laser. All major axes lie close to the vertical direction with a mean eccentricity of 0.31 (dashed blue line, standard deviation 0.03). (b) Eccentricity of structures fabricated on fiber end facets with light polarized linearly in the vertical direction (green triangles) and circularly (red circles). With linear polarization most major axes are rotated by about 90° with respect to the polarization axis with a mean eccentricity of 0.48 (green dashed line, standard deviation 0.07). Structures fabricated with circular CO_2 laser polarization had no preferred orientation and a mean eccentricity of 0.29 (red dashed line, standard deviation 0.11). Adapted from Ref. [113].

Using the same beam on fiber end facets yielded a similar mean value of 0.29 (standard deviation 0.11) for the eccentricity, but with no preferred orientation (Fig. 3.17b). This suggests that either minor differences in alignment of the fiber or the initial cleaved surface have an influence on the orientation of the eccentricity that is at least as large as the influence of the eccentricity of the CO_2 laser beam. With linear polarization of the CO_2 laser beam in the horizontal direction, the fabricated structures on fiber end facets showed an increased eccentricity of 0.48 (standard deviation 0.07) and the major axes of most of the structures were aligned with the major axis of the CO_2 laser beam and rotated by 90° with respect to the polarization axis. The increased eccentricity of the structures with linear polarization suggest that the polarization of the CO_2 laser beam influences the fabrication process. However, as circular polarization was achieved with a phase shifting mirror that required an out of plane beam path, the beam had to be realigned when the polarization was switched from linear to circular. Therefore it cannot be completely excluded that because of the beam realignment, the eccentricity of the beam was considerably different in these two situations and that this is the only reason for the observed difference. There are two arguments against the latter scenario: First, for both configurations, the eccentricity of the beam as measured by the beam profiler

matched within the error bars. Second, with linear polarization the fabricated structures had consistently higher eccentricities than those achieved with circular polarization, despite trying several beam configurations. Nevertheless, additional measurements would be necessary to unambiguously confirm the dependency on CO_2 laser polarization.

3.3.4 Surface roughness

For applications in quantum information processing, it is of utmost importance to keep the intrinsic losses of a mirror as low as possible (cf. Sec. 2.1). The quality of the substrate before the coating process sets a limit to the quality of the coated mirror surface that determines the intrinsic losses of the final mirror. Therefore the fabrication process of the surface has to ensure that the surface is as smooth as possible to minimize scattering losses.

To be suitable for a high finesse cavity, the deviations of a mirror surface from its perfect form need to be much smaller than the wavelength of the desired resonance. In that case, diffuse scattering can be neglected and only diffractive losses have to be considered [114]. For a plane wave with normal incidence on a plane, slightly rough, reflecting surface, these losses $\mathcal{L}_\mathrm{s}$ can be treated statistically and expressed as a function of just one parameter, the root mean square (RMS) roughness σ_RMS [114, 115]:

$$\mathcal{L}_\mathrm{s} = \left(\frac{4\pi\sigma_\mathrm{RMS}}{\lambda}\right)^2 \tag{3.10}$$

Although cavity mirrors are usually not plane, the RMS roughness value has been employed to estimate the quality of substrates for ultra-low-loss mirrors and values of $\sigma_\mathrm{RMS} < 0.1\,\mathrm{nm}$ have been reported for highest-quality superpolished substrates [92]. These values are given under the assumption that the mirror surface can be characterized with global curvature, which determines the geometry of the mode, and a microroughness parameter that can be treated statistically and determines the losses.

At $< 0.1\,\mathrm{nm}$, the vertical precision of the white-light interferometer used to measure the surface profile of the CO_2 laser machined structures was sufficient to estimate whether these could reach the required surface quality. To eliminate the global shape, a function describing that curvature needs to be fitted to and subtracted from the data. The choice of this function is somewhat arbitrary and hints at the underlying drawback of this method, namely that there is no clear distinction between global shape and microroughness. For the data presented here, a fourth-order polynomial was chosen in order to maintain comparability with Refs. [44, 46].

However, even with the same function for the global shape, the value for the RMS roughness is not well defined, because it depends on the size of the region of interest (ROI) from which the data for the calculation is taken (Fig. 3.18). Hence, Eq. (3.10) predicts very different scatter losses, depending on how large the ROI is chosen. Taking one single-mode fiber (magenta dashed line in Fig. 3.18) as an example, the predicted losses would be 8 ppm for a $8\,\mu\mathrm{m} \times 8\,\mu\mathrm{m}$ ROI, which is on the order of a typical $1/e^2$ diameter of a fiber cavity mode, but 2 % for a $40\,\mu\mathrm{m} \times 40\,\mu\mathrm{m}$ ROI, which is on the order of the mirror size required by a simple clipping model for 1 ppm losses (see Sec. 2.4.1). It is therefore evident that the description by an RMS roughness parameter is too simple for this kind of structures.

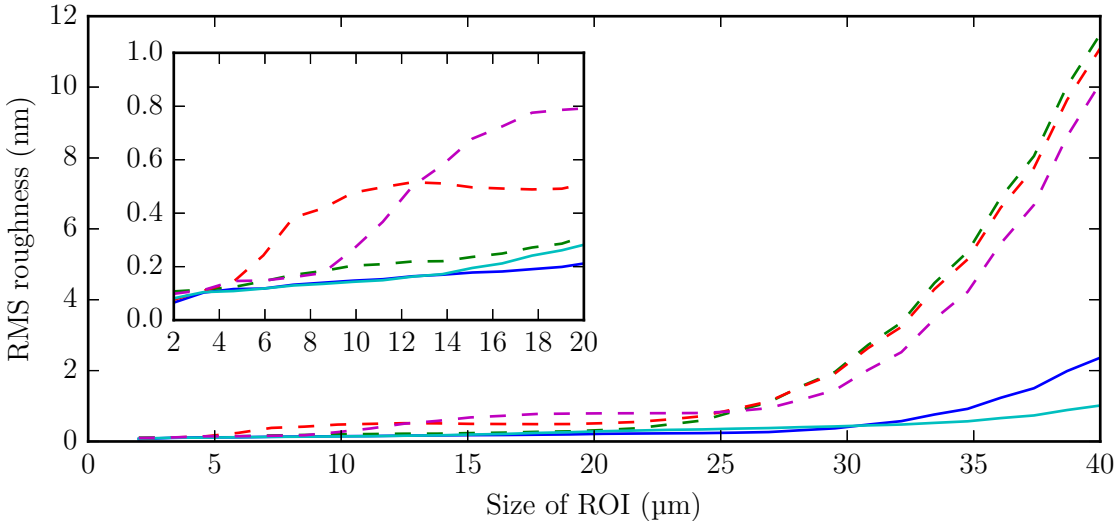

Figure 3.18: RMS roughness as a function of the side length of a square region of interest (ROI) in the center of two structures fabricated on multi-mode fibers (solid lines) and of three fabricated on single-mode fibers (dashed line). In general, the variation of the surface and thus the calculated roughness are low on small length scales and grow with the size of the ROI. On large length scales, the behavior of single-mode and multi-mode fibers is consistent within the fiber type, but multi-mode fibers show much smaller deviations than single mode fibers. The inset shows a zoom into the lower left part of the graph. On small scales, some single-mode fibers show a steep increase of the roughness that might be linked to the properties of the core (cf. Fig. 3.19).

Nevertheless, the measurements reveal that the CO_2 laser fabrication process results in locally very smooth structures with the measured RMS roughness for small ROIs approaching 0.1 nm. Deviations from the perfect shape occur mostly on scales comparable with the mode size, which can not be adequately described as microroughness. The measurements also show a distinct difference in the behavior of single-mode and multi-mode fibers during the fabrication process, with structures fabricated on multi-mode fibers showing far less deviations from the global shape than single-mode fibers. The difference can be seen in Fig. 3.19: The residual height after a fourth-order polynomial has been subtracted shows a bump in the center of the structure that has roughly the size of the differently doped core for the single-mode fiber. The height of this bump is only a few nanometers, less than 1 % of the wavelength the cavity is supposed to be operated at, but might lead to a worse performance of cavities built from single-mode fibers compared to cavities with multi-mode fibers, especially for longer cavities with a larger mode diameter on the mirrors.

The white-light interferometry (WLI) measurements of the CO_2 machined structures showed ring-like features after the subtraction of a fourth-order polynomial, which might be either due to the fabrication process or artifacts of the measurement method. The WLI method scans the position of the objective relative to the measured object and extracts the height of the surface from the interference fringes. Vibrations during this scan can lead to a global modulation of a linear slope, because contours with the same height

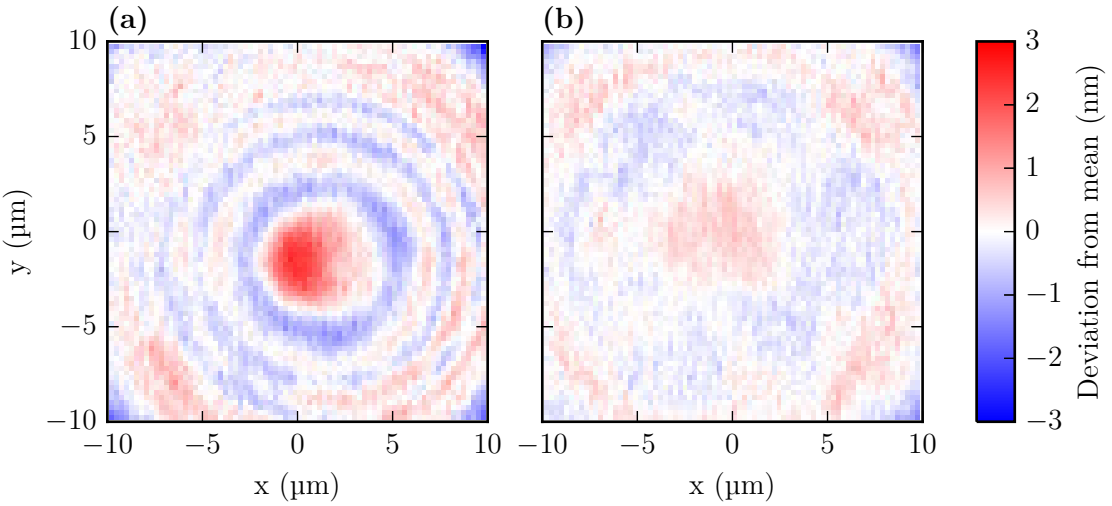

Figure 3.19: Residual deviation from a fitted fourth-order polynomial for two CO_2 laser-machined structures fabricated on (a) a single-mode fiber (the same as the red dashed line in Fig. 3.18) and (b) a multi-mode fiber (cyan solid line in Fig. 3.18). The single-mode fiber shows a bump in the middle, likely caused by the properties of the differently doped core, which the multi-mode fiber does not show. Both measurements show ring-like deviations which might be either due to the fabrication process or a measurement artifact of the white-light interferometer (cf. Fig. 3.20).

are measured at the same time and this effect was observed on tilted plane substrates. Applied to the convex shape of the fabricated structures, this effect could lead to ring-like features. To avoid this, all measurements were averaged over 20 scans, but a residual effect might persist. Therefore, atomic force microscopy (AFM) measurements were performed on a few samples to validate the WLI measurements (Fig. 3.20). Measurements on single-mode fibers also showed ring-like features, demonstrating that they are at least partly an effect of the fabrication process, but they were less pronounced. This could be either due to residual artifacts of the WLI measurements or due to masking by the increased noise floor of the AFM measurement and additional measurements would be required to fully determine the origin of these features. The lateral resolution of the AFM measurement was a factor of 4 better than the diffraction-limited WLI resolution and could have revealed deviations with a spatial frequency beyond the detection limit of the WLI. No such irregularities were detectable above the noise floor of the AFM, which sets a limit of $\sigma_{\mathrm{RMS}} < 0.29\,\mathrm{nm}$ or 22 ppm losses due to microroughness undetectable by the WLI measurements.

3.3.5 Photonic crystal fibers

As described in Sec. 2.4.1, coupling of a fiber cavity mode to the guided mode of a single-mode optical fiber is inefficient for long, symmetric cavities (cf. Fig. 2.8), because matching the mode size on the mirrors to the fiber mode would require highly curved mirrors, which would then result in a mismatch of wavefront curvature. This can be alleviated by using single-mode fibers whose guided mode has a larger diameter that can

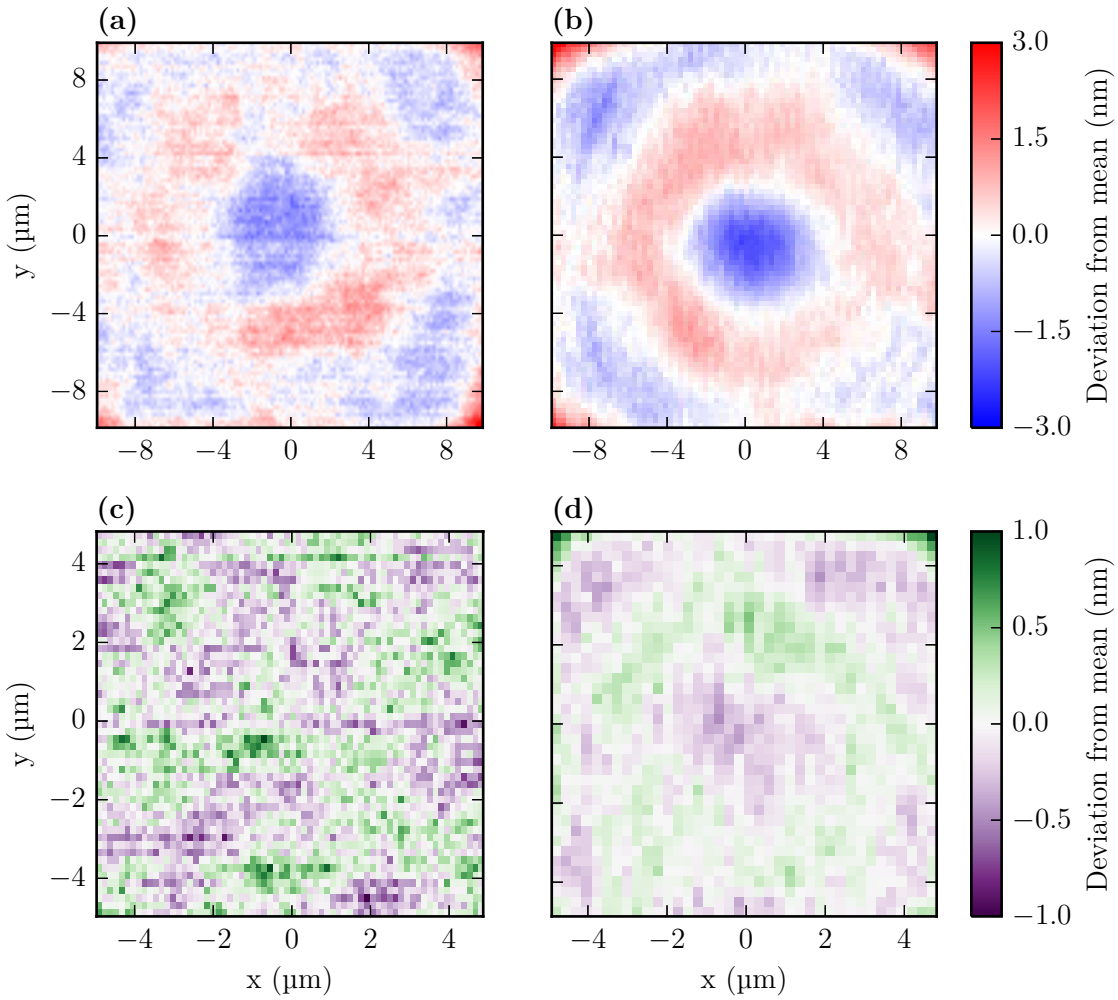

Figure 3.20: Comparison of atomic force microscopy (AFM) measurements (a,c) and white-light interferometry (WLI) measurements (b,d) of a single-mode fiber with a fourth-order polynomial subtracted. The top row (a-b) shows a 20 µm × 20 µm ROI. Although ring-like features can be seen with both methods, they are more pronounced with white-light interferometry, which also yields the larger roughness value ($\sigma_{\mathrm{RMS,WLI}} = 0.58\,\mathrm{nm} > \sigma_{\mathrm{RMS,AFM}} = 0.51\,\mathrm{nm}$. The opposite is true for a smaller ROI of 10 µm × 10 µm in the bottom row (c-d). The calculated roughness value for the AFM measurement is $\sigma_{\mathrm{RMS,AFM}} = 0.29\,\mathrm{nm}$ and the deviations are correlated with the horizontal scanning direction of the AFM tip. The noise floor of the WLI measurement is clearly lower ($\sigma_{\mathrm{RMS,WLI}} = 0.17\,\mathrm{nm}$) and the ring structure persists.

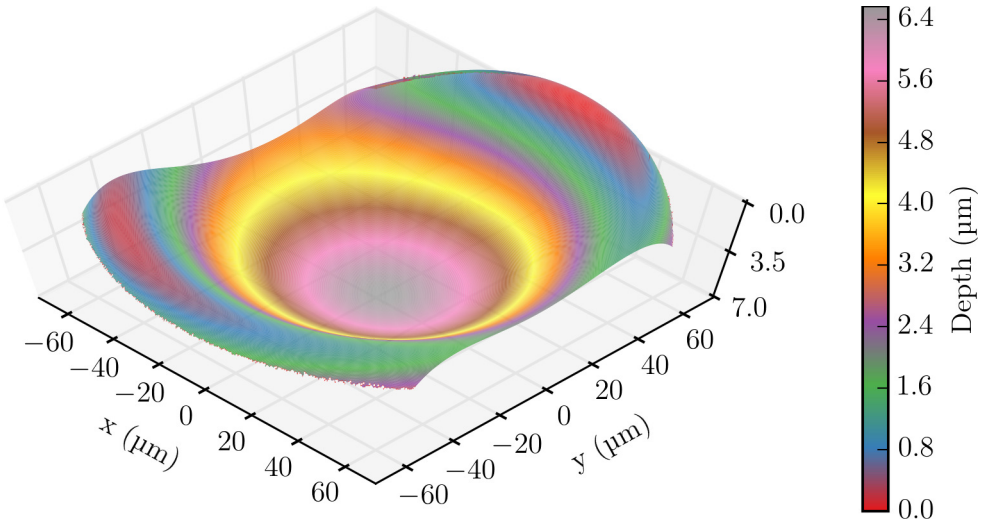

Figure 3.21: Depth profile of a endlessly single-mode photonic crystal fiber after a 3 ms pulse of the CO_2 laser. The holes that form the photonic crystal structure have completely collapsed on the surface, such that the structure could be coated and used as a mirror in a high-finesse cavity. The structure has a larger diameter than those on standard single-mode fibers because the diameter of the used photonic crystal fiber was 200 µm instead of the usual 125 µm.

be matched to the size of the cavity mode with less curved mirrors, thus achieving a better mode matching efficiency. One way to increase the diameter of the guided mode is to use endlessly single-mode photonic-crystal fibers [116], which can be made to support single modes with very large diameters [117]. These have the additional advantage that they have no cut-off wavelength for single mode operation and can therefore guide light with very different wavelengths, which could be interesting for far off-resonant intra-cavity traps at twice the resonant wavelength to provide homogeneous coupling over all trapping sites [118]. Therefore, it was tested, whether the fabrication process also works with photonic crystal fibers, where the holes of the photonic crystal structure pose a potential complication.

An endlessly single-mode photonic crystal fiber with a core diameter of 8 µm and an outer diameter of 200 µm was machined with a CO_2 laser pulse of 3.0 ms duration and a beam waist of 230 µm. The laser was operated at full output power, but the beam was enlarged by partially closing an iris, which reduced the power reaching the fiber. The resulting structure is shown in Fig. 3.21. In the center, no trace of the holes that form the photonic crystal structure can be found, as the laser heats the fiber enough to collapse the holes. The fabrication process thus results in a surface that is suitable as a mirror substrate, without any additional steps in the process. Whether the holes in the unmachined surface require different laser parameters to achieve the same desired structures could not be determined, because the different fiber diameter already demanded a longer pulse and no regular single-mode fibers with this diameter were available.

To measure the depth of the region where the holes were collapsed by the CO_2 laser,

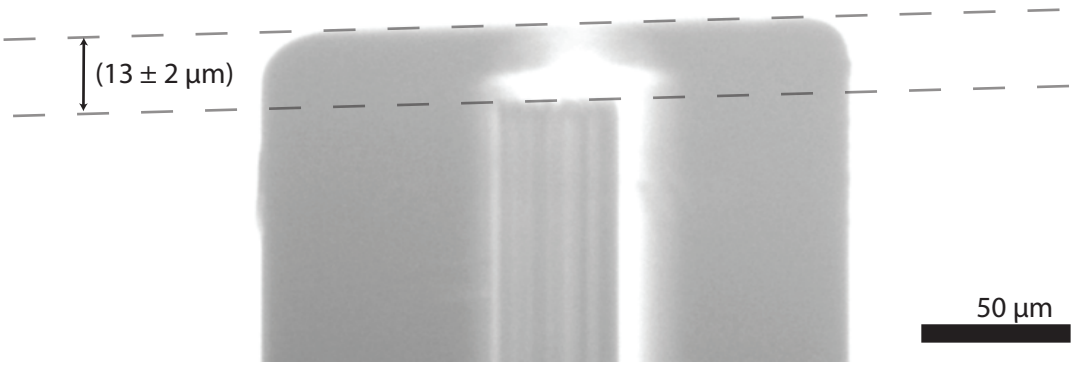

Figure 3.22: Microscope image of a photonic crystal fiber after machining with a CO_2 laser pulse coming from the right. The edge of the end facet is convex and rounded due to surface tension (cf. Fig. 3.12). The concave shape in the center of the end facets cannot be seen from this angle. The image is similar to an image of a regular single-mode fiber, except for the vertical lines in the center of the fiber which are an artifact of the photonic crystal structure. Because the CO_2 laser pulse collapsed the holes, these lines do not reach the end facet. From the position at which the lines end, one can estimate the region from the end facet where the holes are collapsed to be (13 ± 2) µm deep.

the fiber was glued into a slitted cylinder and the structure on the end facets was carefully polished away until the holes reappeared. The amount of material that had been polished away could then be calculated from the reduced distance of the polished fiber end facet to the cylinder surface to be (13 ± 1) µm, in good agreement with an estimate from a microscope image of the fiber (Fig. 3.22).

The collapse of the holes has a detrimental effect on the coupling efficiency. In the region near the cavity mirror, the fiber mode is not guided by the photonic crystal structure any more, but diverges during propagation through the glass, leading to additional mode mismatch between the fiber mode and the cavity mode compared to a fiber mode that starts directly at the cavity mirror. The mismatch can be calculated with the ABCD-matrix formalism for Gaussian beams [79] that accounts for refraction at the coating layers whose curvature follows the curvature of the machined fiber end facet. The coupling efficiency as a function of the distance between fiber mode and cavity mirror is shown for two example cavities in Fig. 3.23. These calculations are for Gaussian beams and do not take the exact mode geometry of the photonic crystal fiber into account, which means that they present an upper limit of how much can be gained with a photonic crystal fiber, where the holes are partially collapsed. For a short, asymmetric cavity with highly curved mirrors, there is little to gain, because the mode-matching to an off-the-shelf fiber with a mode radius of 3 µm is already quite good and gains from designing a photonic crystal fiber with the best mode radius would be offset by the unguided propagation in the melted region of the fibers. The situation is different for a longer, symmetric cavity with less curved mirrors. In the example depicted by Fig. 3.23b, the off-the-shelf fiber has a mode-matching efficiency of only 45 %, which

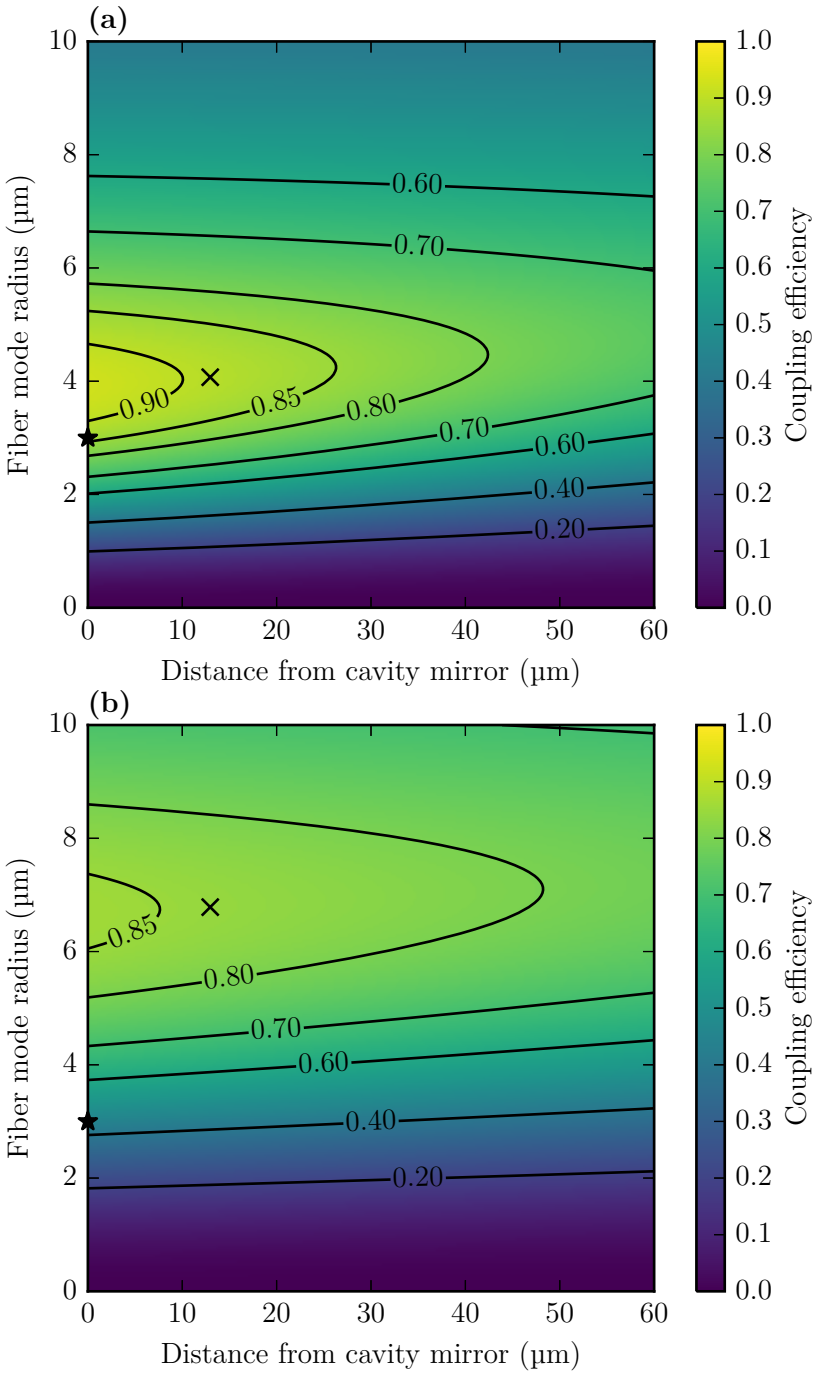

Figure 3.23: Coupling efficiency as a function of the fiber mode radius and the length of the region, where the mode is not guided, i.e., the distance between the cavity mirror and the start of the photonic-crystal fiber mode. The cross marks the best coupling efficiency for a 13 µm thick region without holes. The star marks a single-mode fiber with a waist of 3 µm. (a) Cavity length 80 µm, radii of curvature 120 µm (high reflector) and 200 µm (output coupler). (b) Cavity length 200 µm, radii of curvature 400 µm for both mirrors. Using a photonic crystal fiber would lead to little improvement for short, asymmetric cavities, but to a large gain in coupling efficiency for longer, symmetric cavities

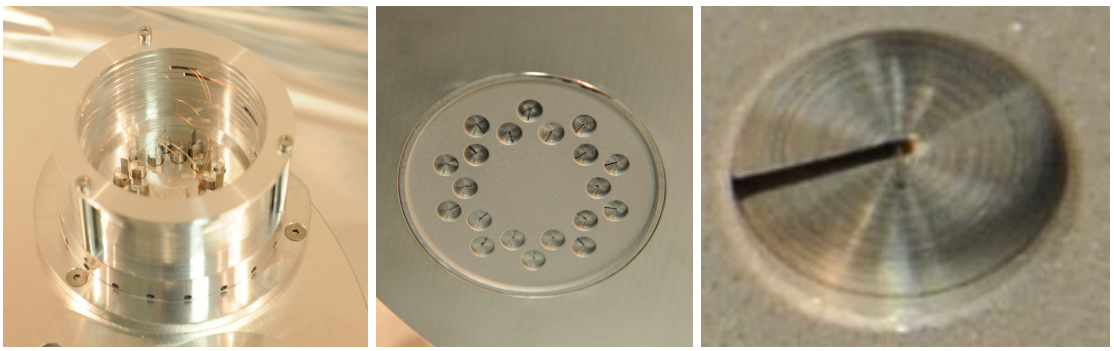

Figure 3.24: Pictures of the assembly that holds the fibers during the coating process. The fibers are kept in slitted aluminum cylinders with a steel sheet that fits in the slit. (left) View of the back side of the holder, i.e., the side that is not coated. Most of the fiber length is coiled up inside rings to prevent damage by loose fiber ends during the coating process. 20 fibers fit into one module like the one depicted here and the total assembly had 3 of these modules. (middle) Front side of the holder, which the coating was applied to. The facet of the module depicted here is designed to be exactly in the coating plane and the cylinders inserted from the other side are stopped 1 mm behind that plane because the diameter of the hole changes at that point. (right) Close up of one of the cylinders inserted in the holder. The fiber sticks out 1 mm beyond the end facet of the cylinder, such that the end facet of the fiber is in the coating plane.

could be increased to 84 % for a fiber with a custom mode radius and no holes over a length of 13 µm.

3.4 Coating

A batch of 59 fibers, each with a CO_2 laser-machined structure on one end facet, and 38 CO_2 laser machined structures on 6 glass plates were sent to the company *LASEROPTIK* (Garbsen, Germany) for the application of a highly reflective coating using ion beam sputtering [119]. For reference, 10 superpolished substrates manufactured by *Advanced Thin Films* were also included in the same coating run. The glass plates were mounted inside the coating machine using the same techniques that are used for superpolished substrates, but the fibers required the design and fabrication of a custom holder (see Fig. 3.24). The end of the fiber to be coated was put in a slitted aluminum cylinder with a steel sheet matched to the slit holding it in place. These cylinders were placed into modules that had rings to hold the rest of the fiber. The thickness of each coating layer slightly depends on the distance from the sputter target for ion beam sputtering, leading to a shift of the wavelength at which the coating has maximum reflectivity. Therefore, the end facets of all fibers should ideally be at the same height in the same plane as the reference substrate that is used to monitor the coating thickness. The cylinders holding the fibers were designed in such a way that this is the case when the fibers stick out by 1 mm from the end facet of the cylinder. Visual alignment of the fiber in the

cylinder was found to be reproducible with an error of less than 100 µm. The wavelength shift as a function of the height mismatch was specified to be less than 10 nm mm^{-1}, such that the error in alignment should lead to a shift of less than 1 nm. Considering the specified change in transmission of less than 0.5 ppm in a 20 nm region around the central wavelength, this shift can be neglected.

The goal of the first coating run was to asses the performance of CO_2 laser-machined mirrors suitable for cavity QED experiments with neutral rubidium atoms on the D_1-line at 795 nm and the D_2-line at 780 nm, with the intrinsic losses $\mathcal{L}$ as the most important criterion. The uncertainty of the transmission of the coating limits the accuracy with which one can determine the intrinsic losses, because it is difficult to separate these two in a single measurement. Therefore, the mirror coating for the first coating run was chosen to have a very low transmission of 3.5 ppm at the wavelengths of 780 nm and 795 nm to get a small absolute error on transmission measurements at the cost of low total transmission of a cavity built from these mirrors. The transmission of plane, superpolished substrates included as reference in the same coating run could be determined directly by measuring the transmitted part of laser light with a power of 10 mW to 30 mW at wavelengths of 761 nm to 800 nm (Fig. 3.25). Because the light was generated by an external cavity diode laser, spectral filtering of the light to suppress the light produced by spontaneous emission of the laser diode was necessary for consistent results. The measured transmission matched the targeted center wavelength very well, but the measured transmission was slightly below target with (2.9 ± 0.1) ppm at 780 nm and 795 nm.

The transmission of coated fiber end facets could not be determined in exactly the same way, because the edge of the fiber end facet was not correctly coated and transmission of residual light in the fiber cladding distorted the results. Therefore, a spatially resolved power measurement was performed, using an imaging system in combination with a CMOS camera to only measure transmission of light in the fundamental transverse mode of a single-mode fiber. This measurement yielded results compatible with the transmission of the plane mirror in the wavelength range from 775 nm to 800 nm (see Fig. 3.25), but spurious reflections in the imaging system resulted in interference, which limited the accuracy of the measurement.

3.4.1 Annealing

Annealing the deposited coating by heating it in an atmosphere containing oxygen can improve the homogeneity and stoichiometry of the coating layers [120] and reduce losses in the coating [121]. Annealing is therefore a requirement to reach the lowest possible coating losses. The reference substrates, the structures fabricated on glass plates and a portion of the fiber mirrors were annealed by *LASEROPTIK* for 5 hours at 300 °C after coating. With the same temperature and hold time, fibers were also annealed in an oven in the MPQ workshop at ambient atmosphere. The remaining fibers were left untreated for comparison. As detailed in the following section, cavities with mirrors that had been annealed showed a significant improvement in finesse on the order of a factor of two, showing that the annealing process can reduce the losses of fiber mirrors and is critical to achieve the lowest possible losses.

A potential complication in the annealing process is the protective copper coating of the fibers. At the temperatures required for annealing, the copper starts to oxidize. At

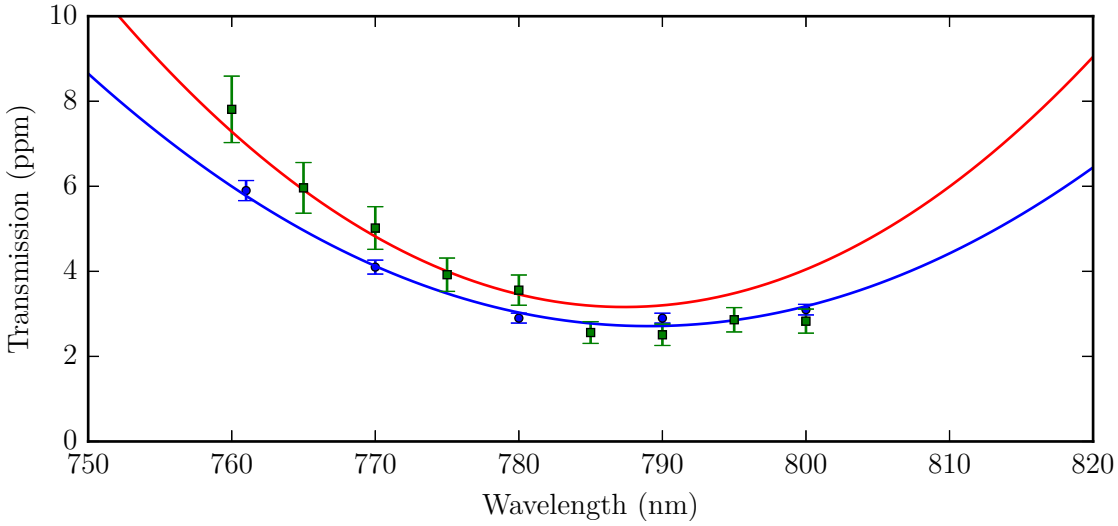

Figure 3.25: Transmission of a plane mirror on a superpolished substrate. Blue dots indicate the measured value with the error bars dominated by the measurement uncertainty of the employed power meter. The solid blue line is a fit of a parabola to the data. The solid red line indicates the targeted transmission curve specified before the coating process. The measured center wavelength is in agreement with the target, but the coating was slightly less transmissive than intended. The green squares denote the transmission of a coated end facet of a fiber, which is compatible with the plane mirror measurement in the wavelength range of 775 nm to 800 nm

excessive temperatures and exposure times, the oxidized fiber coating became brittle, rendering it almost impossible to handle without breaking it. After 5 hours at 300 °C, the fibers were visibly tarnished but showed no reduced resistance to damage, such that annealing with these parameters could be implemented for fibers without any special consideration. Longer exposure time or higher temperatures might lead to a slight further reduction of losses, but an exploration of these effects would require a protective coating that is not only vacuum compatible but also more resistant to oxidation at high temperatures, for example a protective gold coating.

3.5 Finesse

The most important characteristics of a cavity are its mode profile, which can be inferred from the mirror geometry, and the intrinsic losses of a cavity, as discussed in Sec. 2.1. In the limit of high-finesse cavities, the finesse is inversely proportional to the sum of all losses, either intrinsic or extrinsic by transmission of the mirrors. If the transmission of the mirrors is known, the finesse can be used as a measure for the intrinsic losses and if the transmission of the mirrors is small compared against these, the finesse is a good indicator for the performance of a cavity.

3.5.1 Characterization methods

To calculate the finesse, the linewidth of the cavity and its free spectral range need to be determined. The easiest way to measure the free spectral range was to tune two lasers to cavity resonances one free spectral range apart and measure the frequency difference of the two lasers. To ensure that the frequency difference did not amount to a multiple of the free spectral range, the lasers were first tuned to the same fundamental transverse mode and then one of the lasers was detuned until it was resonant with the next fundamental transverse mode. The frequency difference between the lasers was measured with a wavemeter that had a specified accuracy of 600 MHz. As the free spectral range of the characterized cavities was usually in the range of several THz, the resulting error was below 1×10^{-3} and could be neglected when compared to the error introduced by the linewidth measurement.

Two methods were employed to measure the cavity linewidth, both with advantages for specific cavity parameters. The first method is a direct spectroscopic measurement of the linewidth by scanning over a resonance and measuring its width. This can be either achieved with a fixed laser frequency while scanning the cavity length or a fixed resonance frequency while scanning the laser frequency. For short scan amplitudes, a scan of the laser frequency by modulating the diode current and turning the grating of an external cavity diode laser as well as a scan of the cavity length by applying a voltage to a piezoelectric ceramic can be assumed to show a linear behavior when a linear ramp is applied as control signal. However, in both cases, the conversion factor from control signal to frequency can be nonlinear at large scan amplitudes, such that a global calibration would be error prone. Therefore, the scans were calibrated locally, by modulating the light with an electro-optic phase modulator to generate sidebands as frequency markers. The time difference between the resonance of the carrier and each of the sidebands with the cavity resonance was used to calibrate the current scan speed in frequency space and convert the time axis on an oscilloscope trace to a frequency axis. As the calibration only required one sideband, the second sideband could be used to verify whether the scan speed stayed constant during the scan by performing two calibrations for each trace and requiring the results to agree. An example of this method is shown in Fig. 3.26.

The method only produces consistent results if two requirements are met: The scan speed must be slow compared to the decay rate of the cavity, to ensure that the cavity output depends only on the current state of the cavity and not its history. If this condition is not met, the transmission signal has an asymmetric lineshape and the results cannot be trusted. The second condition is that the scan is fast compared to fluctuations of the cavity length that could result in a nonconstant scan speed, which also distorts the results. If the cavity resonance to be measured is broad, because it has low finesse or a large free spectral range, as it tends to be the case for fiber cavities, both conditions can easily be met, but for narrow lines, it can be difficult to satisfy both conditions, such that the method is more suitable for the broad resonances. Additionally, the linewidth of the laser might not be negligible compared to the cavity linewidth for very narrow resonances, leading to another potential source of error.

The second method to determine the linewidth is cavity ring-down [122]. When light in resonance with the cavity is instantly switched off, the light intensity inside the cavity decays exponentially with decay constant $2\kappa = 2\pi\Delta\nu$, where $\Delta\nu$ is the linewidth.

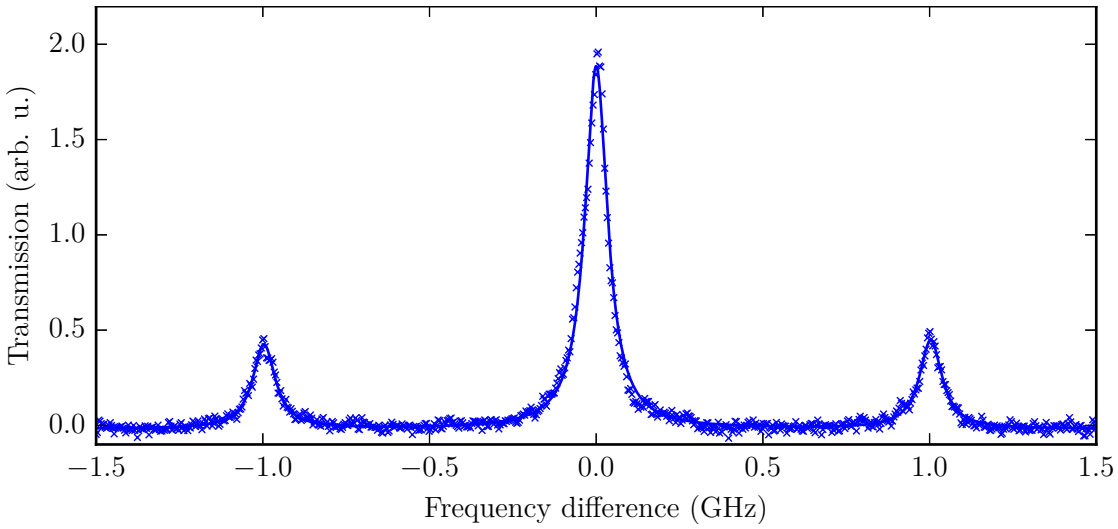

Figure 3.26: Example of a spectroscopic linewidth measurement for a fiber cavity. Sidebands at a frequency of ±1 GHz were modulated onto the probe light with an electro-optic phase modulator. The cavity length and with it the resonance frequency was scanned by applying a voltage to the piezo-electric ceramic one of the fibers was mounted on. The crosses denote the measured transmission during the scan. The solid line is a fit of three Lorentzians with equal width and independent location and amplitude. The sidebands have been used to calibrate the frequency axis and the width of the peak is 82 MHz in this instance. Averaging 100 scans over the same resonance yielded a mean linewidth of 89 MHz with a standard deviation of 9 MHz.

Measuring the decay constant thus provides a value for the linewidth that is independent from the influence of small-amplitude cavity length fluctuations caused by vibrations that can distort spectroscopic measurements. Three conditions are required for an accurate measurement: The first requires the probe light to be switched off completely to avoid ringing of the cavity when light that is Doppler-shifted by a moving cavity interferes with the probing light [123]. The second condition is that the switching time needs to be short compared to the decay constant to avoid distortions of the measured decay constant by finite switching time. Finally, the bandwidth of the detection setup needs to be high enough to determine the decay constant. These conditions are easy to fulfill for cavities with narrow linewidths, but are difficult for the fiber cavities investigated here, which had decay constants on the order of a few nanoseconds. This parameter regime can be approached by using a waveguide-based electro-optic amplitude modulator, which has sub-nanosecond switching times, and a fast, high-gain avalanche photodiode with a decay time of 2 ns for detection. As the waveguide-based electro-optic modulator suffered from offset drifts due to charge accumulation, the input light to the cavity was monitored by a DC-coupled photodetector to ensure that the remaining input light is negligible after switching off. Before the probe light is switched off for a ring-down measurement, it needs to be resonant with the cavity. This can be either achieved by locking the cavity to a fixed frequency or by scanning the cavity slowly over the resonance, periodically switching the light, and postselecting on events when the light was switched off when the

cavity was resonant. The latter method is simpler to implement and has the advantage that the probe light can be more intense and thus more signal can be collected in a single trace without damage to the cavity, because it is off-resonant most of the time.

3.5.2 Reference mirrors

Cavities built from two reference mirrors based on superpolished substrates with radii of curvature between 25 mm and infinity that were included in the coating run were characterized to get an indication of the performance of the coating itself, independent of possible imperfections introduced by the CO_2 laser machining process. The best cavity had a finesse of $(3.21 \pm 0.01) \times 10^5$ as measured by cavity ring-down. With the spectroscopic method, the linewidth was measured to be (1.1 ± 0.3) MHz. Assuming that the laser with a linewidth of 0.15 MHz and the cavity resonances are described by Lorentzians in frequency space and the convoluted linewidth is therefore the sum of both, the resulting finesse is $(3.0 \pm 0.7) \times 10^5$. The results of both methods agree with each other, but the ring-down measurement is much more accurate, because of the narrow linewidth ((0.90 ± 0.01) MHz, measured by ring-down) due to the high finesse and the length of the cavity (0.52 mm). The finesse of cavities build from reference mirrors was found to be very sensitive to contamination with dirt during their assembly and the finesse mentioned above was only reached after the mirrors had been cleaned multiple times. The total losses corresponding to the measured highest finesse are 20 ppm (cf. Eq. (2.9)). As it cannot be excluded that some of the intrinsic losses of that cavity were due to residual contamination, this gives an upper limit on the performance of the coating. With a measured transmission of 3 ppm for each mirror (Sec. 3.4), the intrinsic losses by scattering and absorption on reference mirrors are therefore 7 ppm per mirror or less.

3.5.3 Fiber cavities

To measure the finesse of fiber cavities, two fiber mirrors were clamped on top of two shear piezo ceramics that could each be used to fine-tune the cavity length by 0.5 µm. One of these assemblies was attached to a fixed mount and the other to a 3-axis translation stage combined with a two-axis tip-tilt stage. Probe light was coupled into one of the fibers by fusion splicing the uncoated fiber end to one arm of a fiber beamsplitter, whose other port could be used to monitor the input power. The resonances of higher-order transverse modes split into multiplets of the same order, as expected for not perfectly spherical mirrors. Resonances corresponding to fundamental transverse modes could be identified by the absence of such a multiplet. The position of the fiber mirror on the stages was adjusted to obtain maximum transmission for these modes. Most of the characterized fiber cavities showed a frequency splitting of the polarization eigenmodes (see Ch. 4). If the frequency splitting is on the order of a linewidth, partial excitation of a second polarization eigenmode might be mistaken for a broader line and thus lower finesse with the spectroscopic method. The polarization of the probe light was therefore adjusted to only excite one of the polarization eigenmodes.

The linewidths of the characterized fiber cavities were up to 90 MHz (e.g., Fig. 3.26), corresponding to a decay time of less than 2 ns, which could not be resolved by any detector with sufficient sensitivity to measure the transmitted light. Therefore, cavity

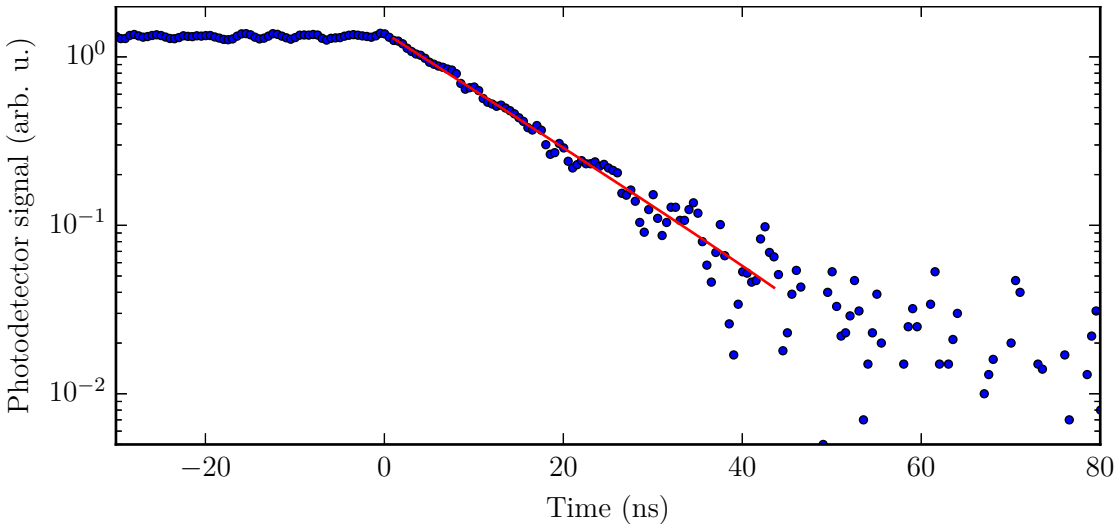

Figure 3.27: Ring-down measurement of a fiber cavity. The blue points denote the measured signal on a logarithmic scale and the red line is an exponential fit corresponding to a linewidth of (12.5 ± 0.4) MHz. The spectroscopic method resulted in a linewidth of (14.2 ± 0.9) MHz. The ring-down method results in a slightly smaller value, pointing at a potential systematic error in the spectroscopic method.

ring-down was not an option to determine the linewidth for short fiber cavities, which had a broad resonance. To compare the two methods for measuring the linewidth, both methods were applied to select longer fiber cavities with narrow resonances (Fig. 3.27). In general, the ring-down method resulted in slightly smaller values for the linewidth, which suggests, there is a small systematic error in the spectroscopic method that broadens the line. Therefore, spectroscopic measurements of the linewidth might result in a slight underestimate of the finesse.

Using the spectroscopic method, a finesse of up to $(7.8 \pm 1.0) \times 10^4$ was measured at a wavelength of 780 nm for fiber cavities with mirrors that had not been annealed. With a transmission of 3 ppm, this corresponds to 37 ppm intrinsic losses per mirror. The same measurement with cavities that had annealed mirrors yielded a finesse of up to $(1.92 \pm 0.11) \times 10^5$ (see Fig. 3.28), corresponding to losses of 13 ppm per mirror. These losses are only 6 ppm larger than those measured for reference mirrors (see Sec. 3.5.2) and indicate that the surface created by the CO_2 laser machining process only scatters a very small fraction of the light due to microroughness. This is compatible with the white-light interferometer measurement of the roughness (see Sec. 3.3.4) and Eq. (3.10) only if the evaluation of the roughness is restricted to a region with a side length smaller than the $1/e^2$ intensity diameter of the cavity mode. Extending this region to one that contains 99 % of the intensity would increase the estimated additional losses due to roughness to 21 ppm per mirror, which is clearly incompatible with the measured finesse. This indicates that describing the roughness with one statistical parameter is inadequate and only part of the measured roughness is microroughness in the sense that it leads to scattering losses. The remaining deviations from a parabolic mirror shape might lead to slight deviations from a Hermite–Gaussian field distribution, but not to additional

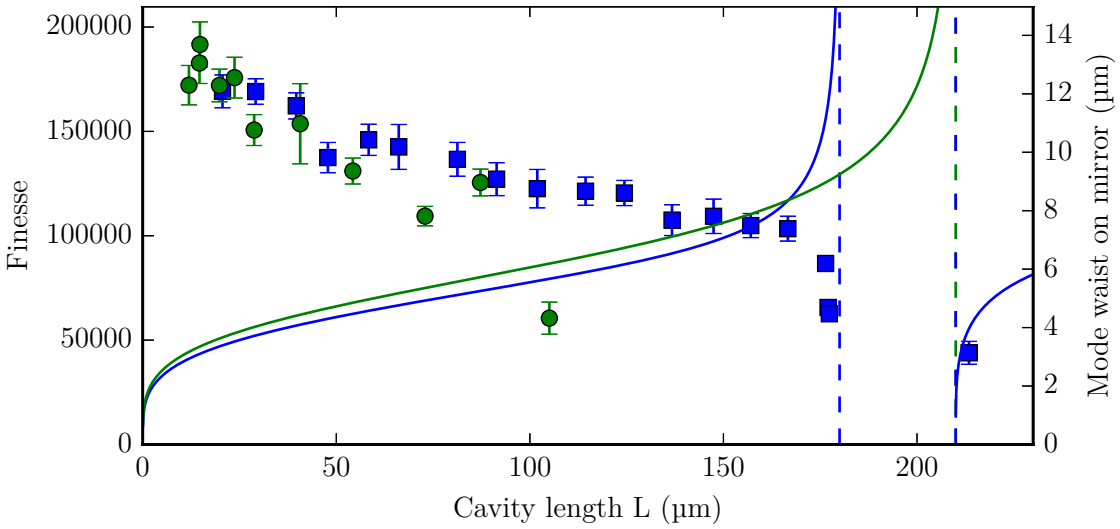

Figure 3.28: The finesse of a fiber cavity consisting of one fiber mirror with 180 µm radius of curvature (ROC, indicated by dashed lines) on a multi-mode fiber and one mirror with 210 µm ROC on a single-mode fiber plotted against the cavity length (blue squares, left y-axis). The finesse was high for very short cavities and dropped with length L until the start of the unstable region at $L = 180\,\mu\text{m}$, where the calculated mode size on the mirror with the smaller ROC (blue line, right y-axis) diverges. After the end of the unstable region, a mode could be observed again. A second cavity was built by removing the multi-mode fiber and inserting a single-mode fiber with a mirror on top that had an ROC of 350 µm (green dots). That cavity reached a finesse of $(1.92 \pm 0.11) \times 10^5$ at $L = 14.8\,\mu\text{m}$ and showed a similar decline of finesse with length. However, the finesse dropped at $L \approx 100\,\mu\text{m}$ and no mode could be observed beyond that length, despite the calculated mode size on the mirror with the smaller ROC (green line) not being considerably different than for the first cavity.

losses, because the distorted mode is an eigenmode of the cavity with nonparabolic mirrors. These effects cannot be described with the simple stochastic scattering model and therefore a new model is required for CO_2 laser-machined mirrors.

The requirement for a better scattering model is further emphasized by the dependency of the finesse on the cavity length. If scattering is described by microroughness, which does not change with increasing cavity mode size, the finesse of a cavity should not depend on its length, unless the instability region is approached, where the size of the mode diverges. For cavities built from reference mirrors, this was validated by the observation that there was no significant dependence of the finesse on the cavity length.

In contrast, the finesse of fiber cavities steadily decreased with increasing cavity length L. For example, the finesse in the measurement shown in Fig. 3.28 for a cavity with one mirror based on a single mode fiber and one on a multi-mode fiber dropped from $(1.69 \pm 0.08) \times 10^5$ at $L = 20.6\,\mu\text{m}$ to $(1.03 \pm 0.06) \times 10^5$ at $L = 166.6\,\mu\text{m}$. Near the instability region between $L = 180\,\mu\text{m}$ and $L = 210\,\mu\text{m}$, the finesse dropped sharply and no mode could be observed within that region, as expected from the paraxial theory.

By increasing the length beyond the instability region, a mode could be observed again, but with comparably low finesse. For a second cavity, built with two mirrors based on single-mode fibers, the finesse showed a similar decline with length, but the finesse dropped at $L \approx 100\,\mu\text{m}$ and no mode could be observed beyond that length. The stability region for that cavity should have extended to a length of 210 µm, so it cannot explain the sudden drop in finesse.

Previous work with fiber cavities has ascribed the sudden loss of finesse to the finite size of the fiber mirrors and applied a simple model that defined an effective mirror size and considered any part of the mode beyond that size to be lost [44, 121]. As the part that is lost increases exponentially with mode diameter and thus with cavity length (see Eq. (2.15)), a comparison with the losses independent of length, e.g., absorption in the coating, yields a rapid decrease of finesse beyond the length where losses due to finite mirror size start to dominate. However, this model cannot explain the drop in finesse before that point, as already noticed in Ref. [121] and it fails to account for considerably different mode sizes at which the finesse breaks down for the two example cavities displayed in Fig. 3.28. Therefore, this effect also requires a different description, which will be covered in Sec. 3.5.5.

Despite the drop in finesse, the considered cavities still have high finesse at $L \approx 80\,\mu\text{m}$, which is sufficiently large to allow for high-power laser beams perpendicular to the cavity, e.g. for a far-detuned optical dipole trap. At this length, the cavities have approximately 20 ppm intrinsic losses per mirror. The first cavity also had a finesse exceeding 1×10^5 up to $L = 167\,\mu\text{m}$, leaving more than enough space to fit fibers with a diameter of 125 µm inside to get a crossed cavity geometry with two fiber cavities.

3.5.4 CO_2 laser machined substrates

To characterize the losses of the structures fabricated with the CO_2 laser on glass plates, a cavity was built, which consisted of one of these structures with 360 µm radius of curvature and a plane reference mirror. The finesse of this cavity was measured as a function of cavity length. The result is shown in Fig. 3.29. The maximum of $(2.1 \pm 0.6) \times 10^5$ corresponds to intrinsic losses of 17 ppm per mirror under the assumption that the reference mirror has the same transmission and losses as the reference mirrors characterized in the measurement described in Sec. 3.5.2. These losses are higher than the 13 ppm measured for fiber mirrors, but were measured at a substantially larger cavity length of 105 µm instead of 14.8 µm. The depth of the structure machined on glass plates sets a minimum distance at which the plane mirror can be placed, such that very short cavities cannot be built in this configuration and a direct comparison with very short fiber cavities is therefore not possible.

Similar to fiber cavities, the finesse decreases with the cavity length with a sharp drop at the edge of the stability region. However, the slope of the decrease is much smaller such longer cavities retain a much higher finesse. As the mode of a half-symmetric resonator, which has one concave and one plane mirror, is equivalent to half the mode of a symmetric resonator with twice the length, the measurement suggests that it is possible to construct a high-finesse cavity with a length of up to 720 µm using two of such structures, only limited by the radius of curvature.

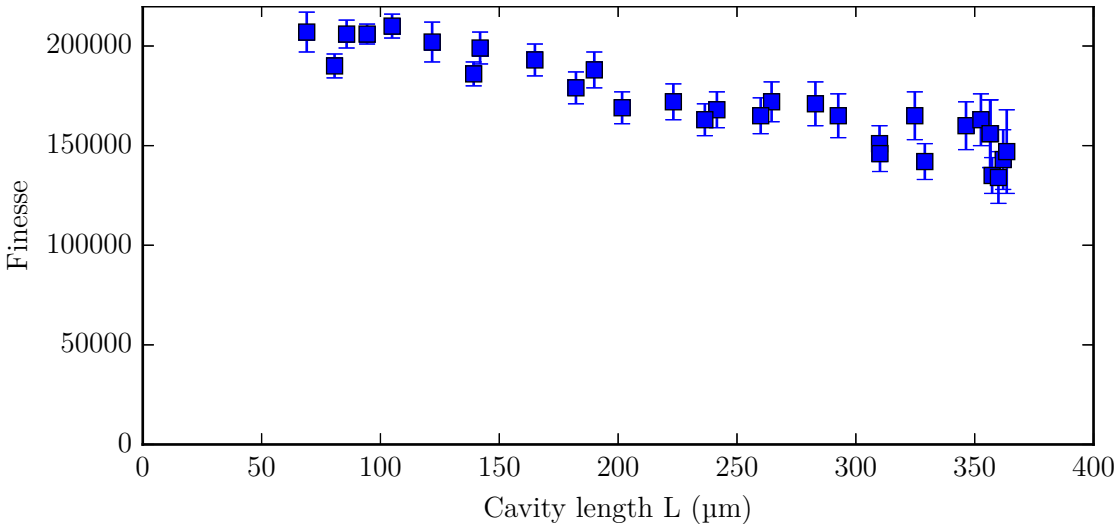

Figure 3.29: Finesse of a cavity consisting of one plane reference mirror and one coated CO_2 laser machined structure on a glass plate with 360 µm radius of curvature. Similar to the fiber cavities (cf. Fig. 3.28), the finesse decreases with length until the length of the cavity is larger than the radius of curvature and the cavity becomes unstable.

3.5.5 Mode mixing as model for cavity finesse

In order to understand the observed finesse of fiber cavities, a model is required that takes irregularities with a spatial frequency comparable with the mode size into account and can describe a mode adapted to the mirror shape. The most direct approach would be to take the measured surface of the mirror substrates as boundary conditions and solve Maxwell's equations. However, the measurements described in Sec. 3.3.4 showed that deviations from the global curvature are on the order of $10^{-4}\lambda$ and a grid with this resolution would not be computable with current technology over the volume of $10^5\lambda^3$ required for the cavities presented here.

An alternative is to consider a basis of Hermite–Gaussian modes, for which propagation between the mirrors is described by the paraxial wave equation and does not need to be calculated. Imperfect mirrors introduce a coupling between these modes, which results in new eigenmodes of the cavity [124]. This approach has recently been employed to describe the finesse of hybrid cavities, which have one plane mirror assumed to be perfect and one CO_2 laser-machined fiber mirror [125]. These calculations can be adapted to a fiber cavity with two fiber mirrors by extending the procedure to choose the basis modes. Although the mode could in principle be described in any basis, a badly chosen basis would require the consideration of an infinite number of basis modes. Therefore, the basis modes must be chosen carefully to tolerate truncation of the number of modes without introducing excessive errors. For a cavity with one plane mirror, the waist of the mode has to be located on the plane mirror and the propagation direction of the mode needs to be perpendicular to the plane mirror. The basis can thus be chosen by numerically optimizing the waist of the fundamental transverse mode to have the best overlap with itself after being reflected by the fiber mirror. For two fiber mirrors,

the waist position and the propagation direction are a priori unknown and need to be optimized. However, optimizing the overlap of the fundamental transverse mode with itself would require many calculations of the complete round-trip coupling matrix, which is very computationally expensive and therefore unsuitable for optimization. Instead, a two step approach can be taken, by fixing the waist position to a fixed distance from the first mirror. The basis modes can then be optimized for the first mirror in the same way as for a hybrid cavity. As the second step, the position and orientation of the second mirror can then be optimized such that the chosen fundamental transverse mode has the best overlap with itself. The individual optimization for each mirror requires the calculation of only one overlap integral per optimization step and increases the computational complexity only by a constant factor compared to the hybrid cavity situation. A slight drawback of this method is that the total length of the cavity is a result of the calculation, such that a calculation using multiple waist positions is required to get a value for a specific cavity length.

Once the basis modes have been chosen, the mixing matrices for each mirror $\mathbb{M}_1$ and $\mathbb{M}_2$ can be calculated from the overlap integrals of all modes with each other after reflection [124, 125]. These overlap integrals can only be evaluated on the area for which the surface profile has been measured. Any amplitude of the modes outside of this area does not contribute to the calculated overlap integral and therefore reduces its magnitude, which can be interpreted as clipping by a finite-sized mirror. The total mixing matrix $\mathbb{M}$ is the matrix product of the two single-mirror mixing matrices

$$\mathbb{M} = \mathrm{e}^{2\mathrm{i}kL}\mathbb{M}_1\mathbb{M}_2 \tag{3.11}$$

The eigenvectors of $\mathbb{M}$ describe the eigenmodes of the cavity in the chosen basis and the losses of these modes can be calculated by $\mathcal{L}_\mathrm{i} = 1 - |\gamma_\mathrm{i}|^2$ from the corresponding eigenvalues γ_i. Among these new eigenmodes, the mode that has the eigenvector with the highest TEM_{00} component is the one most relevant for the experiment, as this mode will be the one identified as the fundamental transverse mode. In most of the cases, the TEM_{00} component is larger than 99 %, such that for most purposes it can be treated like a TEM_{00} mode. However, at certain lengths, this mode is considerably mixed with another mode, such that any calculation assuming a TEM_{00} mode is likely to give incorrect results. Modes for which this is the case tend to have higher losses and can therefore be avoided by optimizing the alignment for high finesse.

For an infinitely sized, perfect mirror, all eigenvalues would be unity and for perfect, finite-size mirrors, the losses could be calculated with a clipping model (Eq. (2.15)). In addition to these, mode mixing describes diffraction into higher order transverse modes which have a larger size on the mirrors and therefore higher losses. Finally, a mode can be coupled to modes of very high order, which have to be truncated by the calculation. These modes are not likely to be reflected into the cavity by the mirrors and light coupled to them can be understood as scatter losses. Not described by this model is the transmission of the mirrors, absorption in the mirror coating, and scatter losses due to roughness not resolved by the surface measurement. These losses have to be added to the calculated losses to get a value for the finesse.

The described calculations have been performed for the cavities whose finesse is depicted in Fig. 3.28. The surface profiles measured by the white-light interferometer were used as input and all $\mathrm{TEM}_{\mathrm{nm}}$ Hermite–Gaussian modes with $n + m \leq 50$ (i.e., 1326

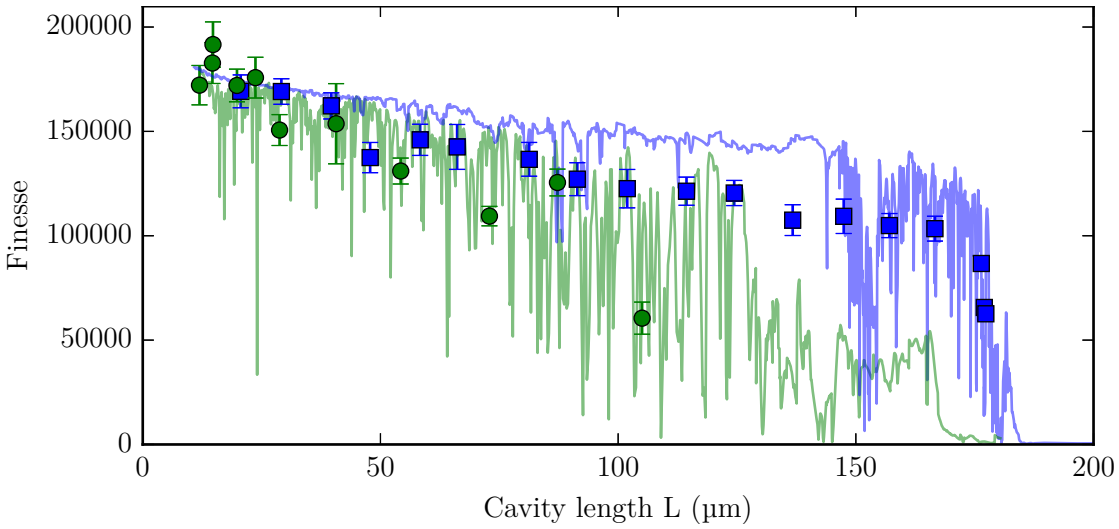

Figure 3.30: Finesse of the fundamental transverse mode as a function of cavity length as calculated from mode mixing with additional losses of 15 ppm per mirror (solid lines). The measured values have been copied from Fig. 3.28 for comparison and same colors indicate the same cavity. The calculations show a trend of finesse decreasing with length, which is interrupted by very sharp drops in finesse at certain lengths. The frequency of occurrence of these drops increases with length and beyond a certain length, the cavity cannot reach very high finesse.

modes) were considered. The resulting finesse as a function of the length with 15 ppm per mirror additional losses due to transmission, absorption, or scattering are shown in Fig. 3.30 with the measured values as comparison. Qualitatively, the model explains the decrease in finesse with length and confirms that the cavity with two single-mode fibers as substrates performs worse than the one with a single-mode fiber and a multi-mode fiber due to larger deviations from the global curvature (see Sec. 3.3.4). It is also a good indicator of the maximum cavity length that can be achieved with a set of mirrors and can therefore be used to judge the quality of fabricated mirror substrates and their suitability for a planned cavity after CO_2 laser machining. Quantitatively, the calculated values are in the range of the measured values, but an exact comparison is difficult to make, because the calculated values depend on the alignment of the mirrors with respect to reach other, which is unlikely to be perfect in the experiment.

A distinct feature of the calculated finesse, which is not evident from the measured data are very sharp drops in finesse at certain cavity lengths. These occur, when the resonance frequency of the TEM_{00} mode is degenerate with another transverse mode and the overlap integral between these modes is large. The higher order transverse mode has greater losses, such that the hybridized mode also suffers from increased loss. These mixing resonances are very sharp and depend on the alignment. Therefore, adjusting the alignment of the cavity for maximum transmission usually does not result in a hybrid mode as the local optimum, because additional losses result in less signal and the hybrid mode has less overlap with the fiber mode and thus reduced mode matching efficiency. This effect can be observed, when one fiber mirror is translated with respect to the other

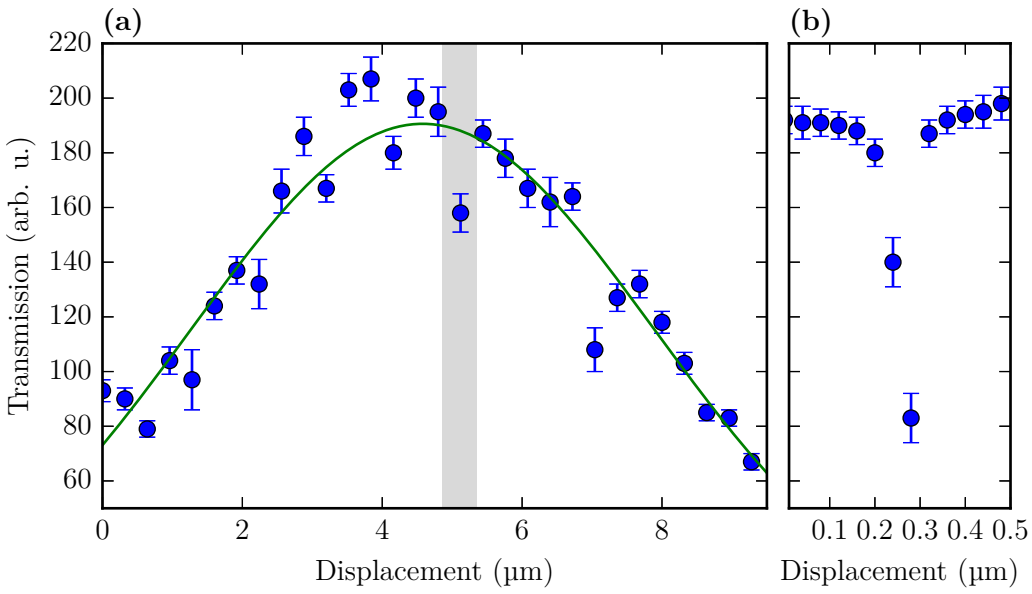

Figure 3.31: Transmission on resonance of a fiber cavity when one of the fiber mirror is displaced laterally with respect to the other. The cavity was scanned over the resonance and the maximum measured transmission was recorded. The error bars denote the standard deviation over many scans. (a) In general, the transmission is a Gaussian function of the lateral offset (green line), as expected for the coupling of two Gaussian modes. However, there are significant deviations at certain positions. (b) The shaded region in (a) with a smaller step size. Because of hysteresis in the translation stage on direction change, the values on the x-axis are relative to the start of the scan. The drop in transmission is very sharp and even more pronounced than in the scan with larger step size.

in a lateral direction (see Fig. 3.31). The transmission as a function of the translation distance is a Gaussian function, as expected for the mode matching efficiency due to the overlap integral of the fiber mode and the cavity mode [91], but there is a very sharp drop in transmission with a lateral width of less than 100 nm caused by mode mixing. These resonances can be avoided by slight translation of one of the mirrors, but need to be considered when working with cavities with imperfect mirror shapes.

3.6 Comparison of results to other approaches

The fabrication process presented here differs from previous approaches [44–46] in two major aspect. First, the wavelength of the CO_2 laser was 9.3 µm instead of 10.6 µm, which was used in all other reported CO_2 laser fabrication attempts. Second, the waist of the CO_2 laser beam was chosen to be large compared to the diameter of the fiber. The achieved fiber-cavity finesse was higher than any other finesse for a Fabry–Perot cavity with two microscopic mirrors that has been reported so far, but fiber mirrors with similar losses and higher transmission have recently been fabricated with a CO_2 laser at 10.6 µm [126]. Hence, there is no indication that the wavelength of the CO_2 laser

directly influences the resulting surface quality and the evidence points to the coating limiting the finesse for very short cavities.

At a cavity length of 150 µm, which would provide more than enough optical access for single-atom cavity QED experiments and also allows a crossed cavity geometry, the finesse exceeds 10^5. This has not been achieved with any fiber cavity fabricated differently and is owed to the large beam-diameter of the CO_2 laser, which enabled the fabrication of structures that approach the diameter of the fiber. As discussed in Sec. 3.1, a wavelength with less absorption can be simulated by decreasing the power and increasing the pulse length and the best structures have been achieved with full power of the CO_2 laser and short pulses. Therefore, a CO_2 laser at 10.6 µm wavelength with the same parameters would probably have resulted in worse structures, but no attempts at a direct comparison have been made.

The alternative to a single pulse with a large diameter is to use multiple short pulses and move the fiber between pulses [127, 128]. With this method, high-finesse fiber cavities longer than the ones presented here have been realized, with a cavity length of more than 1 mm [128]. However, a direct comparison is difficult, because in those instances fibers with larger diameters were used as substrates, which allows larger structures independent of the fabrication method. Therefore, further investigation and direct comparisons would be required to determine which method is preferable for a given substrate and desired cavity geometry.

4 Frequency splitting of polarization eigenmodes

The content of this chapter has been partially published in:
M. Uphoff, M. Brekenfeld, G. Rempe, and S. Ritter. Frequency splitting of polarization eigenmodes in microscopic Fabry–Perot cavities. *New J. Phys.* **17**, 013053 (2015).

As noted during the discussion of the finesse measurements (see Sec. 3.5.3), most of the investigated microcavities do not have degenerate polarization eigenmodes, but show a frequency splitting between two polarization eigenmodes, ranging from sub-linewidth to several linewidths. For a large number of applications, the polarization of these eigenmodes as well as the size of the splitting are important parameters that need to be controlled. Examples can be found in various fields, like metrology with cavity-enhanced polarimetry [129–131] or cavity-ringdown spectroscopy [132, 133], but also in the intended applications in quantum information processing. An instance of the latter is efficient and coherent coupling of atomic states to the polarization of single photons [34, 35], which requires the polarization eigenmodes to be degenerate. This has been achieved for Fabry–Perot cavities built from superpolished mirror substrates [49], but microscopic, high-finesse Fabry–Perot cavities have been observed to show an increased frequency splitting, in this work as well as in previous experiments with the same type of cavity [44, 48, 121]. In these works, the splitting was on the order of one linewidth, which can have detrimental effects on all kinds of experiments [51, 134, 135] and therefore needs to be controlled. This control can take two forms, either a reduction of the splitting until it becomes negligible or an increase until the eigenmodes are well separated [135]. To achieve this control and identify the parameters that influence the splitting, it is necessary to understand its source.

4.1 Potential sources

The frequency shift $\delta\nu$ of one polarization mode with respect to the mode with orthogonal polarization can be described by the phaseshift $\Delta\varphi_{\mathrm{rt}}$ this mode acquires during one round trip with respect to the other polarization mode:

$$\Delta\varphi_{\mathrm{rt}} = \frac{2\pi\delta\nu}{\nu_{\mathrm{FSR}}}. \tag{4.1}$$

The splitting in units of the linewidth $\Delta\nu$ can be expressed by this phaseshift and the finesse $\mathcal{F}$, independent of the cavity length:

$$\frac{\delta\nu}{\Delta\nu} = \frac{\Delta\varphi_{\mathrm{rt}}\,\nu_{\mathrm{FSR}}}{2\pi\Delta\nu} = \frac{\Delta\varphi_{\mathrm{rt}}\,\mathcal{F}}{2\pi}. \tag{4.2}$$

Thus, high-finesse cavities are very susceptible to small phaseshifts, because the effect becomes more noticeable with higher finesse. At a finesse of 10^5, a phaseshift of $2\times10^{-5}\pi$

is sufficient to get a splitting equal to the linewidth, which means that effects on that order of magnitude need to be considered.

Although quantum electrodynamics predicts birefringence of the vacuum [136], the effect is so small that it has not yet been detected even in the presence of strong magnetic fields [129]. Hence, any effect needs to be caused either by the mirrors or by the boundary conditions imposed by them on the modes. Therefore, a single-mirror phaseshift[1] φ_1 and φ_2 and a set of eigenaxes can be attributed to each mirror and the round-trip phaseshift is a function of only these two parameters and the relative orientation of the mirrors. In case of $\Delta\varphi_1, \Delta\varphi_2 \ll 1$ this function is [137–139]

$$\Delta\varphi_{\mathrm{rt}} = \sqrt{\Delta\varphi_1^2 + \Delta\varphi_2^2 + 2\Delta\varphi_1\Delta\varphi_2 \cos(2\vartheta)}, \tag{4.3}$$

where ϑ is the relative angle between the eigenaxes of the two mirrors. To determine the origin of the phaseshift it is sufficient to first look at the effect of one mirror and assume the other mirror to be perfect, such that $\Delta\varphi_{\mathrm{rt}} = \Delta\varphi_1 \equiv \Delta\varphi$, and return to the two-mirror case later.

The obvious source of a phaseshift between two polarization modes at a highly reflecting mirror is birefringence of the mirror coating. Dielectric Bragg reflection coatings, which are used for these mirrors, do not reflect all light at the surface, but have an effective penetration depth on the order of one wavelength [140]. Hence, a difference in the refractive index for different polarizations with a magnitude on the order of the measured phase shift might explain the frequency splitting. The materials used in ion beam sputtering to apply highly reflective coatings are amorphous and should have no intrinsic birefringence. That leaves extrinsic fields—electric, magnetic, or mechanical stress—which could induce birefringence in the coating. In fused silica, the Kerr constant [141] for the DC Kerr effect and the Verdet constant [142] for the Faraday effect are too small for significant contributions of electric and magnetic fields without intentionally applying high external fields [139]. Contrarily, ion beam sputtered coating have high intrinsic stress [143] and mounting of mirrors can result in additional extrinsic stress, such that the contribution of stress-induced birefringence is not negligible. Therefore, residual frequency splittings of polarization eigenmodes of mirrors based on superpolished substrates have been attributed to mechanical stress [134] and it has been speculated that increased intrinsic stress is responsible for increased birefringence and thus an increase of this splitting [121].

However, there is a second potential source of a frequency splitting of polarization eigenmodes, not related to birefringence. A perfectly conducting mirror sets the boundary condition that the electric field tangential to the mirror surface must vanish on the surface ($\vec{E}_{\mathrm{tan}} = 0$). If a mirror is not cylindrically symmetric, this might impose different boundary conditions on the electric fields of different polarization. This could lead to the polarization modes having slightly different spatial modes and thus different resonance frequencies. As CO_2 laser-machined mirrors do not show perfect cylindrical symmetry, but are elliptic with a significant eccentricity (see Sec. 3.3.3 and Fig. 3.17), these boundary conditions could be a source of the frequency splitting. However, the effect is not evident in a paraxial descriptions of the cavity modes [144], because in that description a propagating field has only transverse components and no longitudinal field

[1] Although it is possible to work with negative phaseshifts, all phaseshifts will be assumed to be positive throughout this chapter. It is always possible to define the axes in such a way that this is the case.

exists. The result of this approximation is the simplification of the vectorial boundary condition $\vec{E}_{\mathrm{tan}} = 0$ to the scalar boundary condition $E = 0$ on the mirror surface. This boundary condition is the same for all polarizations, enabling the description of the polarization modes by the same scalar mode function, which have the same resonance frequency. Hence, the effect of boundary conditions on the polarization modes can only be explored when taking nonparaxial corrections into account.

4.2 Nonparaxial corrections

The approximations made in deriving the paraxial wave equation enable the description of a light beam propagating in the z-direction by only transverse field components, e.g. $\vec{E} = (E_{\mathrm{x}}, 0, 0)$. As a consequence of these approximations, these solutions of the paraxial wave equation are not exact solutions of Maxwell's equations. This is most evident with Gauss's law, which states that in absence of electrical charges $\vec{\nabla} \cdot \vec{E} = 0$. A purely transverse field could only satisfy this condition, if it was a plane wave and had no varying envelope. Therefore, any beam with a varying envelope, such as a cavity mode, needs to have a small nonparaxial longitudinal component to fulfill Maxwell's equations. Solutions to these equations that contain the paraxial solution are required to quantify this nonparaxial correction. Lax *et al.* [78] have shown that the vector field of a beam propagating along the unit vector $\vec{e}_{\mathrm{z}}$ can be expressed as a power series in $\xi = 1/(kw_0)$

$$\vec{E} = \mathrm{e}^{\mathrm{i}kz}\left(\vec{F}_{\mathrm{T}} + \vec{e}_{\mathrm{z}} F_{\mathrm{z}}\right) \tag{4.4}$$

with

$$\begin{aligned} \vec{F}_{\mathrm{T}} &= \vec{F}_{\mathrm{T}}^{(0)} + \xi^2 \vec{F}_{\mathrm{T}}^{(2)} + \mathcal{O}(\xi^4) \\ F_{\mathrm{z}} &= \xi F_{\mathrm{z}}^{(1)} + \xi^3 F_{\mathrm{z}}^{(3)} + \mathcal{O}(\xi^5). \end{aligned} \tag{4.5}$$

The lowest order term $\vec{F}_{\mathrm{T}}^{(0)}$ is a solution to the equation

$$\vec{\nabla}_{\mathrm{T}}^2 \vec{F}_{\mathrm{T}}^{(0)} + 2\mathrm{i}k \frac{\partial \vec{F}_{\mathrm{T}}^{(0)}}{\partial z} = 0, \tag{4.6}$$

which is the paraxial wave equation. Corrections to the lowest order approximation scale with ξ. It is interesting to note that, for a given finesse, the only way to increase cooperativity is to increase ξ, so considering nonparaxial corrections becomes unavoidable if extremely high cooperativities are desired. The parameters for the cavities presented in this thesis lead to $\xi \lessapprox 1/30$ and thus are still in the regime of $\xi \ll 1$. Therefore, all terms scaling with $\mathcal{O}(\xi^2)$ or higher orders of ξ will be neglected and only the first correction $\xi F_{\mathrm{z}}^{(1)}$ will be considered. This correction is a longitudinal component that can be derived from the transverse field by [78]

$$\xi F_{\mathrm{z}}^{(1)} = \frac{\mathrm{i}}{k} \vec{\nabla}_{\mathrm{T}} \cdot \vec{F}_{\mathrm{T}}^{(0)}. \tag{4.7}$$

It points along the direction of propagation and is 90° out of phase with the transverse field component. Such a field is depicted in Fig. 4.1, with the transverse field component chosen to point along x.

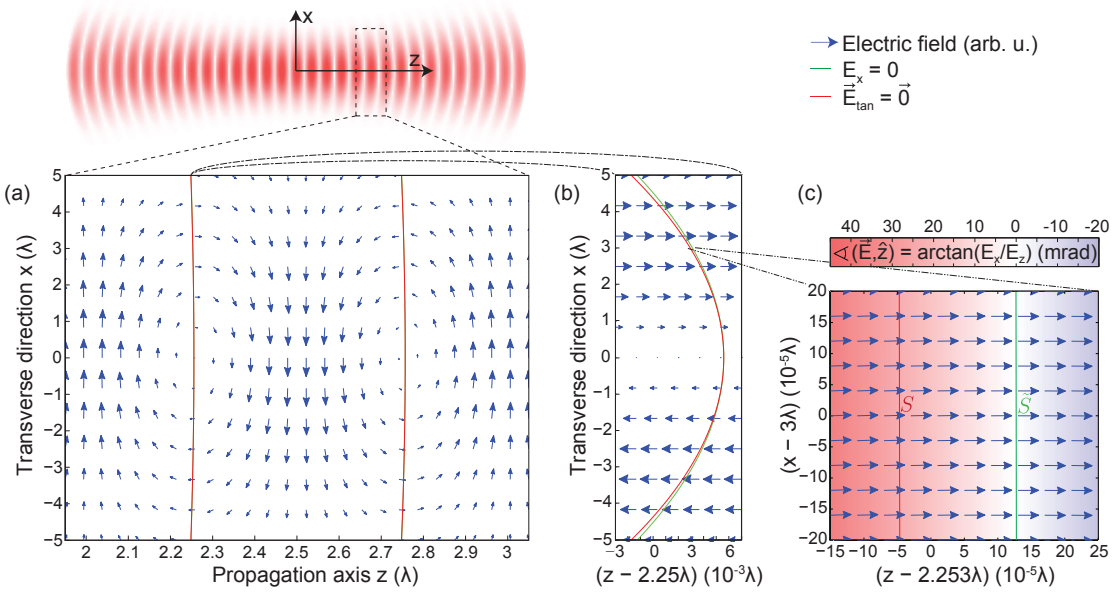

Figure 4.1: Electric field distribution of a Gaussian TEM_{00}-mode (wavelength 780 nm, mode waist 3.5 µm) polarized along the x-direction combined with the longitudinal field of the first-order nonparaxial correction calculated with Eq. (4.7). The scaling of the spatial axes determines the relative scaling of E_x and E_z, which does not preserve angles (most pronounced in (b)). All three subplots contain lines that indicate the positions where $E_\mathrm{x}|_{\tilde{\mathrm{S}}} = 0$ (green) and $\vec{E}_\mathrm{tan}|_\mathrm{S} = \vec{0}$ (red), but they can only be resolved in the enlarged plots (b) and (c). These lines coincide at $x = 0$ but separate away from the cavity axis because of slightly different radii of curvature. From Ref. [113].

On the cavity axis, the longitudinal component is zero and the boundary conditions $\vec{E}_\mathrm{tan} = \vec{0}$ and $E_\mathrm{x} = 0$ are equivalent. When going off-axis along the polarization direction (x in this case), the longitudinal field starts to appear and the boundary conditions differ. The correct boundary condition for a perfectly conducting mirror, $\vec{E}_\mathrm{tan} = \vec{0}$, is indicated by the red lines labeled S. A mirror matching one of these lines would support the depicted mode. The green lines, labeled $\tilde{S}$, are illustrating the boundary condition $E_\mathrm{x} = 0$, which would be used for the scalar, paraxial theory. One can see that the green lines have a larger radius of curvature (Fig. 4.1b). To describe the cavity field by a paraxial mode function, one would have to choose an effective radius of curvature $R_\mathrm{x}^\mathrm{eff}$ larger than the actual radius of curvature R_x of the mirror. A mode with a larger radius of curvature has a lower Gouy phase shift and thus a lower resonance frequency than the resonance frequency one would calculate by applying the paraxial theory. Hence, the nonparaxial correction and the modified boundary condition lead to a negative frequency shift.

A calculation by Cullen [145], who was the first to point out the existence of this frequency shift, will be followed to calculate its value. This calculation is extended to explicitly include elliptic mirrors and to be valid for arbitrary Hermite–Gaussian modes. To this end, a mode polarized in x-direction and propagating in the z-direction is considered in the paraxial and the nonparaxial description. In the paraxial case,

the mode is described by a mode function E_x, which fulfills the Helmholtz equation $\triangle E_\mathrm{x} + k^2 E_\mathrm{x} = 0$ and vanishes on the mirror surface S, i.e., $E_\mathrm{x}|_\mathrm{S} = 0$. This leads to the resonance frequency ν_x, which is related to the wavenumber k by $\nu_\mathrm{x} = kc/(2\pi)$. This description is compared to the nonparaxial case, in which the transverse field component of the vector field is described by an almost identical mode function $\tilde{E}_\mathrm{x} \approxeq E_\mathrm{x}$. This mode function matches the boundary condition $\vec{E}_\mathrm{tan} = \vec{0}$ and thus takes nonvanishing values on the mirror surface $\tilde{E}_\mathrm{x}^\mathrm{S} \equiv \tilde{E}_\mathrm{x}|_\mathrm{S}$. The resonance frequency $\tilde{\nu}_\mathrm{x}$ is slightly different and it fulfills the Helmholtz equation $\triangle \tilde{E}_\mathrm{x} + \tilde{k}^2 \tilde{E}_\mathrm{x} = 0$. The frequency difference between these modes $\delta\nu_\mathrm{x} = \tilde{\nu}_\mathrm{x} - \nu_\mathrm{x}$ can be calculated using Green's second identity

$$\int_\mathrm{V} \left(E_\mathrm{x} \triangle \tilde{E}_\mathrm{x} - \tilde{E}_\mathrm{x} \triangle E_\mathrm{x} \right) \mathrm{d}V = \int_\mathrm{S} \left(E_\mathrm{x} \vec{\nabla} \tilde{E}_\mathrm{x} - \tilde{E}_\mathrm{x} \vec{\nabla} E_\mathrm{x} \right) \cdot \mathrm{d}\vec{S}, \tag{4.8}$$

where V is a volume with surface S, and $\mathrm{d}\vec{S}$ is an outward pointing infinitesimal area element [146]. Under the assumption $|\delta\nu_\mathrm{x}| \ll \nu$, Eq. (4.8) leads to an expression for the frequency difference [145]

$$\delta\nu_\mathrm{x} \approx \frac{c}{4\pi k} \frac{\int_\mathrm{S} \tilde{E}_\mathrm{x}^\mathrm{S} \vec{\nabla} E_\mathrm{x} \cdot \mathrm{d}\vec{S}}{\int_\mathrm{V} E_\mathrm{x}^2 \, \mathrm{d}V}, \tag{4.9}$$

where terms of order $\mathcal{O}(\delta\nu_\mathrm{x}/\nu)$ have been neglected. The volume integral has to be taken over the whole resonator volume and the surface integral over the surface of both resonator mirrors. To calculate the contribution of one mirror, the other mirror is set to be a perfect planar mirror, such that $\tilde{E}_\mathrm{x}^\mathrm{S} = 0$ on the surface of that mirror and the corresponding surface integral is zero. Therefore, the surface integral in Eq. (4.9) only needs to be taken over the elliptic mirror to be investigated.

To calculate the surface integral in Eq. (4.9), a transverse mode function E_x is assumed that is separable in the x- and y-directions and, in complex notation, can be written as

$$E_\mathrm{x}^\mathbb{C}(x, y, z) = \mathrm{e}^{\mathrm{i}kz} u_\mathrm{x}(x, z) u_\mathrm{y}(y, z). \tag{4.10}$$

As polarization in x-direction is assumed, the E_y field component is zero. The first-order nonparaxial correction is the longitudinal field that can be calculated by applying Eq. (4.7)

$$E_\mathrm{z}^\mathbb{C} = \frac{\mathrm{i}}{k} \frac{\partial E_\mathrm{x}^\mathbb{C}}{\partial x}, \tag{4.11}$$

where contributions of the order $\mathcal{O}(\xi^3)$ have been neglected. To get standing-wave solutions corresponding to modes which have a node at the planar cavity mirror placed at $z = 0$, the imaginary part of the complex mode functions is taken,

$$E_\mathrm{x} = \mathrm{Im}(E_\mathrm{x}^\mathbb{C}), \qquad E_\mathrm{z} = \mathrm{Im}(E_\mathrm{z}^\mathbb{C}). \tag{4.12}$$

The complex mode function $E_\mathrm{x}^\mathbb{C}$ is assumed to be normalized, such that

$$\int_\mathrm{V} E_\mathrm{x}^2 \, \mathrm{d}V = \frac{L}{2}, \tag{4.13}$$

where L is the length of the cavity.

The mirror placed at $z = L$ is assumed to be elliptic, i.e., instead of being cylindrically symmetric, it has two principal axes with two different radii of curvature R_x and R_y. To

satisfy the separability postulated in Eq. (4.10), one of the principal axes needs to be aligned with the polarization of the mode. This axis is taken to be the one associated with R_x, because the mode was assumed to be polarized along the x-direction. The mirror surface S is then described by:

$$S: \quad z = L - \frac{x^2}{2R_\mathrm{x}} - \frac{y^2}{2R_\mathrm{y}} \tag{4.14}$$

For the surface integral in Eq. (4.9), the electric field in the nonparaxial description on this surface is necessary. This field can be calculated by taking E_z and the boundary condition $\vec{E}_\mathrm{tan} = \vec{0}$, which requires $\vec{E}^\mathrm{S} = \tilde{E}^\mathrm{S}_\mathrm{x} + E^\mathrm{S}_\mathrm{z}$ to be parallel to the normal $\vec{N} = (x/R_\mathrm{x}; y/R_\mathrm{y}; 1)^\mathrm{T}$ of S. This condition and Eqs. (4.11) and (4.12) yield

$$\tilde{E}^\mathrm{S}_\mathrm{x} = \frac{x}{R_\mathrm{x}} E^\mathrm{S}_\mathrm{z} = \frac{x}{kR_\mathrm{x}} \mathrm{Re}\left(\left. \frac{\partial E^\mathbb{C}_\mathrm{x}}{\partial x} \right|_\mathrm{S} \right). \tag{4.15}$$

The remaining constituent of the surface integral in Eq. (4.9) is the expression $\vec{\nabla} E_\mathrm{x} \cdot \mathrm{d}\vec{S}$ on the mirror surface S. $\mathrm{d}\vec{S} = (x/R_\mathrm{x}; y/R_\mathrm{y}; 1)^\mathrm{T}\, \mathrm{d}x\, \mathrm{d}y$ can be deduced from the gradient of the mirror surface, Eq. (4.14). To approximate $\vec{\nabla} E_\mathrm{x}$, further assumptions about the mode function E_x are necessary: The gradient is dominated by fast varying z-dependence of the carrier and contributions of the slowly varying envelope are suppressed by factor on the order of $\mathcal{O}(\xi^2)$ for the z-direction and $\mathcal{O}(\xi)$ for the transverse directions. In the inner product with $\mathrm{d}\vec{S}$ the transverse directions are multiplied with factors x/R_x and y/R_y, such that these contributions are suppressed by a total factor of $\mathcal{O}(\xi^2)$. Therefore, the complete expression can be approximated by

$$\vec{\nabla} E_\mathrm{x} \cdot \mathrm{d}\vec{S} \approx \frac{\partial E_\mathrm{x}}{\partial z}\, \mathrm{d}x\, \mathrm{d}y \approx \mathrm{Im}\left(\mathrm{i}k E^\mathbb{C}_\mathrm{x} \right) \mathrm{d}x\, \mathrm{d}y = k \mathrm{Re}\left(E^\mathbb{C}_\mathrm{x} \right) \mathrm{d}x\, \mathrm{d}y. \tag{4.16}$$

Using Eqs. (4.15) and (4.16) and the boundary condition for the paraxial description $E_\mathrm{x}|_\mathrm{S} = 0$, the surface integral in Eq. (4.9) can be solved by employing integration by parts:

$$\int_\mathrm{S} \tilde{E}^\mathrm{S}_\mathrm{x} \vec{\nabla} E_\mathrm{x} \cdot \mathrm{d}\vec{S} = \frac{1}{R_\mathrm{x}} \iint x\, \mathrm{Re}\left(E^\mathbb{C}_\mathrm{x} \right) \frac{\partial\, \mathrm{Re}\left(E^\mathbb{C}_\mathrm{x} \right)}{\partial x}\, \mathrm{d}x\, \mathrm{d}y = -\frac{1}{2R_\mathrm{x}} \tag{4.17}$$

Inserting Eqs. (4.17) and (4.13) into Eq. (4.9) yields an expression for the frequency shift of the considered nonparaxial mode with respect to the prediction of the paraxial theory due to the refined boundary condition $E_\mathrm{x}|_\mathrm{S} = 0 \to \vec{E}_\mathrm{tan} = \vec{0}$, up to terms of the order $\mathcal{O}(\xi^2)$

$$\delta\nu_\mathrm{x} \approx -\frac{c}{4\pi k L} \frac{1}{R_\mathrm{x}}. \tag{4.18}$$

Repeating the calculation with a mode polarized along the y-direction results in an analogous expression for the frequency shift of that mode $\delta\nu_\mathrm{y}$. The difference between $\delta\nu_\mathrm{x}$ and $\delta\nu_\mathrm{y}$ is the frequency splitting of the polarization eigenmodes due to this effect:

$$\delta\nu = \delta\nu_\mathrm{x} - \delta\nu_\mathrm{y} = -\frac{c}{4\pi k L} \frac{R_\mathrm{y} - R_\mathrm{x}}{R_\mathrm{y} R_\mathrm{x}}. \tag{4.19}$$

As the phaseshift of the other, plane mirror was set to zero, this value can be converted into an equivalent phase shift per reflection off the elliptical mirror using Eq. (4.1), which

only depends on the wavenumber and the geometry of the mirror

$$\Delta\varphi = \frac{1}{k}\frac{R_\mathrm{x} - R_\mathrm{y}}{R_\mathrm{x} R_\mathrm{y}}. \tag{4.20}$$

This phaseshift can also be expressed as a function of the eccentricity ϵ:

$$\Delta\varphi = \frac{\epsilon^2}{k R_\mathrm{y}}, \tag{4.21}$$

for $R_\mathrm{x} > R_\mathrm{y}$.

Taking the difference between the two approximated values $\delta\nu_\mathrm{x}$ and $\delta\nu_\mathrm{y}$ in Eq. (4.19) is only valid when the resulting difference $\delta\nu$ is large compared to the terms which have been neglected by those approximations. Therefore, Eqs. (4.19), (4.20), and (4.21) require $\delta\nu \gg \xi^4 \nu_\mathrm{FSR}/(2\pi)$ or equivalently, $\Delta\varphi \gg \xi^4$. For $\xi \lessapprox 1/30$ this corresponds to $\Delta\varphi \gg 1\,\mu\mathrm{rad}$.

The calculation applies to all mode functions that meet the postulated assumptions: They need to fulfill the Helmholtz equation, they need to be separable in the transverse direction, and the envelope must vary slowly compared to the carrier wave to meet the assumptions made in the approximation of Eq. (4.16). The first requirement can be further relaxed: The mode function can fulfill the paraxial wave equation instead of the Helmholtz equation, as long as the mode functions are polarization independent. Then, the approximation made in going from the Helmholtz equation to the paraxial wave equation is polarization independent and any resulting error does not matter in the first order perturbation calculation performed here.

In particular, all Hermite–Gaussian mode functions meet these requirements. Therefore, the fundamental as well as higher order transverse modes should show the effective phase shift between polarization eigenmodes of Eq. (4.21) in the presence of an elliptic mirror. The theory results in three predictions that can be experimentally tested for a cavity with one elliptic mirror. First, the polarization eigenmodes should be of linear polarization with the eigenaxes of the polarization aligned with the geometric principal axes of the elliptic mirror. Second, the frequency shift is negative and increases with smaller radius of curvature, according to Eq. (4.18). Hence, the polarization eigenmode associated with the smaller radius of curvature should have a lower resonance frequency than the polarization eigenmode associated with the larger radius of curvature. Third, the magnitude of the frequency splitting should match the value predicted by Eq. (4.19).

4.3 Experimental setup

The simplest way to test the theory outlined above is a test cavity consisting of one elliptic mirror to be tested and a known reference mirror that induces a negligible phase shift.

4.3.1 Characterization of reference mirror

The reference mirror was based on a superpolished substrate, had a transmission of 25 ppm and a radius of curvature of 100 mm. Due to the large radius of curvature, any eccentricity of the mirror had a negligible effect on the phase. Even if the mirror had

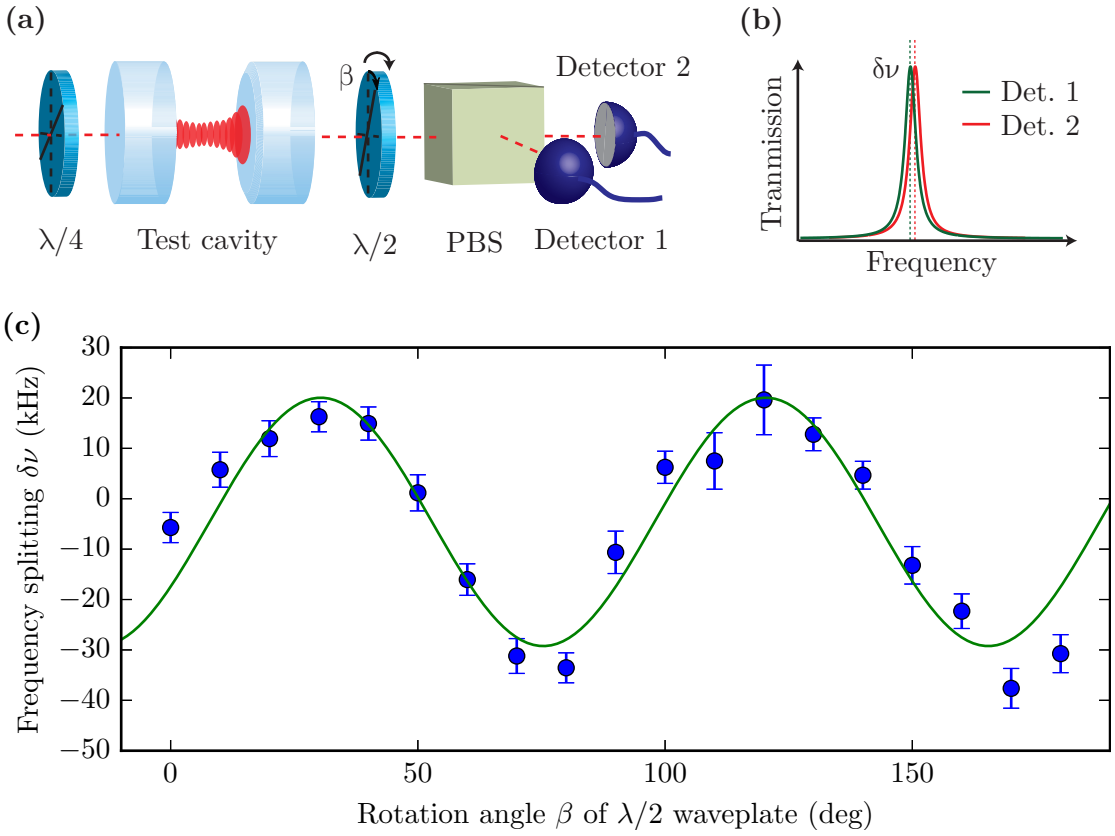

Figure 4.2: (a) Experimental setup for the characterization of the reference mirror. The test cavity is probed with circularly polarized light, which is detected using a polarization sensitive setup. The $\lambda/2$-waveplate is rotated to change the detection basis. (b) Sketch of the measured signal. The measured transmission was fitted by a Lorentzian for each detector and the time difference between the centers of the peaks is converted to a frequency difference using sidebands as markers. (c) Measured frequency differences (blue points) for the rotation angle defined as 0° of the mirror opposite to the reference mirror. The data has been fitted (green line) using Eq. (4.22).

been near cylindrical, i.e., an eccentricity close to 1, the phase shift would only have been 1 µrad. The effect was much smaller than that, because as typical for a superpolished substrate the eccentricity was close to zero. Therefore, only birefringence of the coating is relevant, which can be on the order of 1 µrad per reflection for this type of mirror [49].

To verify that the particular mirror used as reference is suitable as such and induces a sufficiently small phase shift between polarization modes, it was necessary to measure this phaseshift individually for this mirror. To this end, a test cavity with this mirror and another mirror also based on a superpolished substrate was built, which had a linewidth of (2.27 ± 0.06) MHz and a finesse of $(1.10 \pm 0.02) \times 10^5$. The cavity was probed with circularly polarized light to excite both polarization eigenmodes equally and the transmitted light was detected by a polarization sensitive detection setup (Fig. 4.2a). The frequency splitting between modes in a given basis was measured by slowly scanning

the length of the cavity, fitting the cavity resonance at each detector with a Lorentzian, and recording the difference in time of the central position of the fitted curves. This time difference was converted into a frequency difference with the help of sidebands on the light as frequency markers, similar to the linewidth measurements described in Sec. 3.5. The detection setup could not be aligned with the polarization eigenmodes of the cavity, because the splitting was much smaller than the linewidth of the cavity. Instead, the basis of the detection setup was rotated with a $\lambda/2$-waveplate and the frequency difference was measured for various angles.

If the frequency splitting is much smaller than the linewidth, the frequency difference is expected to oscillate sinusoidally with the maxima and minima occurring, when the detection basis matches the orientation of the polarization eigenmodes. The measured values are therefore fitted with the function

$$\delta\nu(\beta) = A\sin(4\beta + \zeta) + b, \tag{4.22}$$

where $2A$ is the frequency splitting between the polarization eigenmodes, ζ is a phase that accounts for the unknown orientation of the eigenmodes at the start of the measurement, b an offset that accounts for potential systematic differences between the detectors, e.g., different response behavior leading to different signal delays, and β is the rotation angle of the $\lambda/2$-waveplate. The period of the oscillation is 4 times the period of β, because the waveplate rotates the polarization basis by 2β and the same situation is recreated after the polarization bases have made half a turn in laboratory space. Due to the sensitivity of the fit, this method can be used to measure frequency splittings of 1/40 of the linewidth (Fig. 4.2c).

In order to access the individual phaseshifts of the mirrors, the mirror opposite to the reference mirror was rotated and the measurement of the frequency splitting was repeated for three different orientations: 0°, −45°, and 45°. The resulting frequency splittings were (50 ± 5) kHz, (122 ± 7) kHz, and (125 ± 18) kHz, respectively. With these three values, the three unknown parameters in Eq. (4.3) can be determined. A Monte Carlo calculation that solved for these parameters using normal distributions of the measured frequency splittings with their standard error results in two phaseshifts $\Delta\varphi_1 = (1.6 \pm 0.4)$ µrad and $\Delta\varphi_2 = (2.8 \pm 0.3)$ µrad, with the errors determined from the 90 % confidence interval.

The phases ζ from the fits can be used to calculate the relative change in orientation of the polarization eigenmodes of the cavity, resulting in $(30 \pm 12)°$ for a rotation of the mirror opposite to the reference mirror by −45° and $(-39 \pm 20)°$ for a rotation by 45°. These values can be compared with the expectation that the angle α between the slow eigenaxis of the cavity to the slow eigenaxis of the first mirror is [137, 139]

$$\alpha = \frac{1}{2}\arctan\left(\frac{\Delta\varphi_2\sin(2\theta)}{\Delta\varphi_1 + \Delta\varphi_2\cos(2\theta)}\right), \tag{4.23}$$

where θ is the angle between the slow axis of the first mirror and the fast axis of the second mirror. Inserting the calculated phase shifts and for each mirror and assuming that the reference mirror has the lower phaseshift leads to an expected rotation of the polarization eigenmodes of the cavity by $(32 \pm 4)°$ and $(-29 \pm 6)°$ for a rotation of the opposite mirror by −45° and 45°, respectively. Assuming the other case, i.e., that the reference mirror has the higher phaseshift, results in an expected rotation of $(14 \pm 2)°$ and $(-14 \pm 1)°$. Only the former assumption leads to consistency within the errors,

and therefore one can deduce that the reference mirror has the lower phaseshift of $(1.6 \pm 0.4)\,\mu\text{rad}$.

4.3.2 Determination of mirror geometry

A quantitative comparison of any measured frequency splitting of polarization eigenmodes with the theory explained above, requires knowledge of the orientation of the principal axes for the tested mirrors where the radius of curvature is maximal and minimal, respectively, and a precise measurement of the effective radius of curvature along these axes.

Local fits of the mirror surface

As the surface of every fiber mirror was characterized white light interferometry, the most obvious method to determine the radii of curvature of a fiber mirror is a fit to that surface. However, the local radius of curvature varies on the fiber mirror surface (see Sec. 3.3.2), which is unavoidable for any elliptic mirror, because only a perfectly spherical mirror has a constant radius of curvature at every point on the surface. Weighting the surface with the expected profile of the mode can be used to estimate an effective radius of curvature at any position.

The radii of curvature extracted from fits over the whole surface were used to estimate the size of a TEM_{00}-mode on the fiber mirror in a hybrid cavity with the reference mirror. The weights $W(x, y)$ were then chosen to be proportional to the electric field of that mode

$$W(x, y) \propto \exp\left(-\frac{(x - x_0)^2 + (y - y_0)^2}{w^2}\right), \tag{4.24}$$

where w is the $1/\text{e}^2$ intensity radius of the mode on the mirror. The obvious choice for the central point (x_0, y_0) is the estimated center of the mirror. However, if there is an inherent tilt of the fabricated structure with respect to the fiber axis or an additional tilt due to the alignment, the mode might not be exactly in the center of the mirror. Therefore, points $\pm 3\,\mu\text{m}$ away from the center in each direction are also considered and the radius of curvature is taken to be the average over these points with the standard deviation of the radius of curvature over all points as the error.

For single-mode fibers, the position of the mode guided by the core can serve as a position reference. The alignment that achieves maximum coupling to the fiber is close to the alignment where the cavity mode is positioned close to the center of the cavity. The alignment of the cavity that maximizes coupling to the fiber mode thus ensures that the assumption of the position of the mode made above is justified.

For multi-mode fibers, there is no such reference, because the core extends over the whole usable mirror surface. Careful alignment of the fiber axis with respect to the reference mirror is therefore required for the mode to be near the center of the fiber mirror.

Transverse mode distance

In a hybrid cavity setup with one fiber mirror and one reference mirror, a more accurate method exists. The resonance frequency of a Hermite-Gauss TEM_{qmn}-mode in a cavity

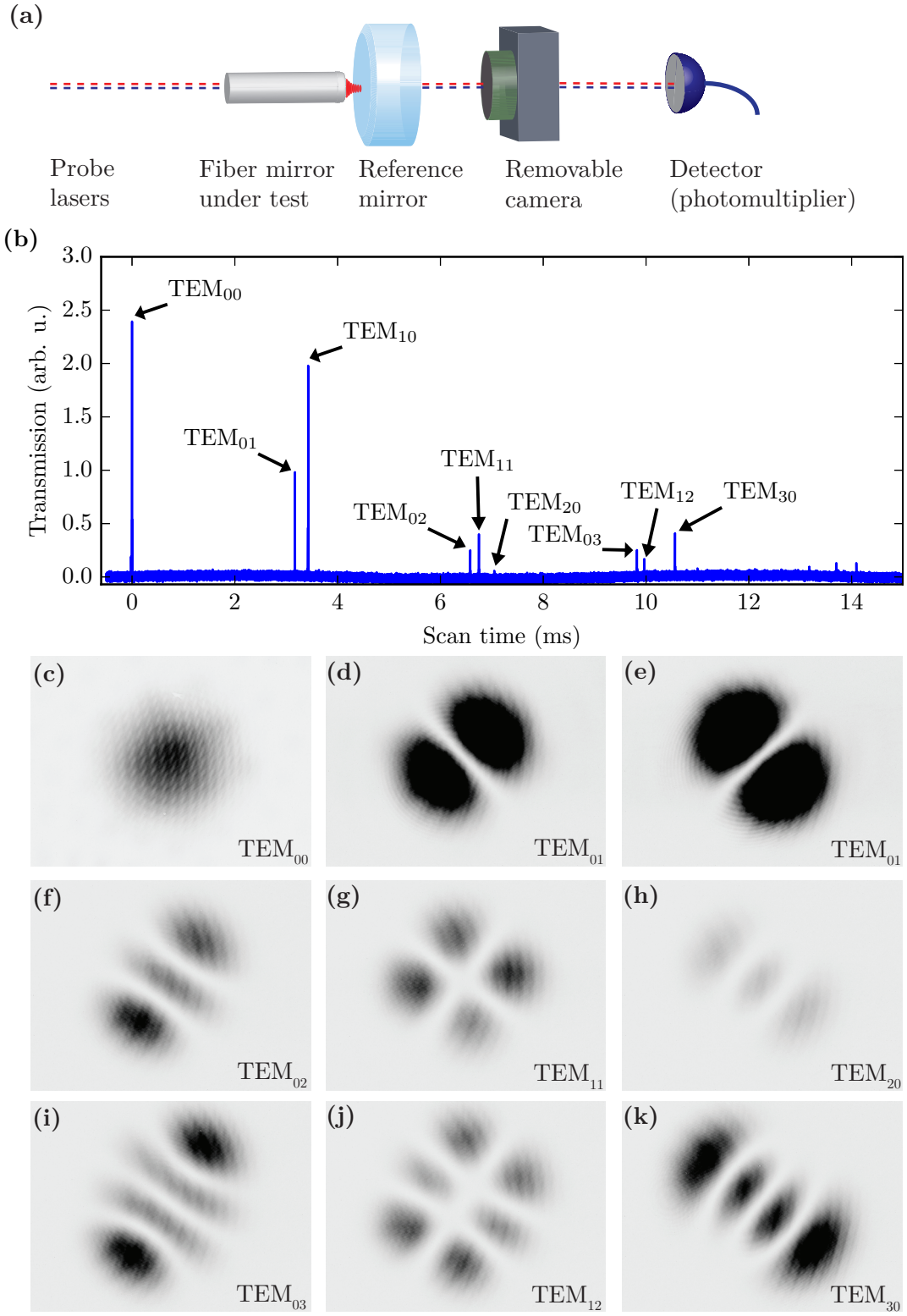

Figure 4.3: (a) Setup for determining the geometry of the fiber mirror under test. (b) Transmission of the cavity during a scan of the cavity length. (c)-(k) Mode pattern as recorded by the camera. See text for further description and Fig. 4.9 for the asymmetry between (i) and (k).

with one elliptic mirror characterized by R_x and R_y and one spherical mirror with radius of curvature R_2 is given by [144]

$$\begin{aligned}\nu_\mathrm{qmn} = \frac{\nu_\mathrm{FSR}}{\pi}\Bigg[q\pi + \left(m+\frac{1}{2}\right)\arccos\sqrt{\left(1-\frac{L}{R_\mathrm{x}}\right)\left(1-\frac{L}{R_2}\right)} \\ + \left(n+\frac{1}{2}\right)\arccos\sqrt{\left(1-\frac{L}{R_\mathrm{y}}\right)\left(1-\frac{L}{R_2}\right)}\Bigg].\end{aligned} \tag{4.25}$$

The last two terms of the sum in the brackets are due to the Gouy phase shift, which increases for higher order transverse modes. This leads to the distance in frequency space between the fundamental transverse mode $\mathrm{TEM_{q00}}$ and higher order transverse mode $\mathrm{TEM_{qm0}}$ with the same q

$$\nu_\mathrm{qm0} - \nu_\mathrm{q00} = \frac{m\,\nu_\mathrm{FSR}}{\pi}\arccos\sqrt{\left(1-\frac{L}{R_\mathrm{x}}\right)\left(1-\frac{L}{R_2}\right)}. \tag{4.26}$$

Solving for R_x and inserting $L = c/(2\nu_\mathrm{FSR})$ yields

$$R_\mathrm{x} = c\left[2\nu_\mathrm{FSR}\left(1-\cos^2\left(\frac{(\nu_\mathrm{qm0}-\nu_\mathrm{q00})\pi}{m\,\nu_\mathrm{FSR}}\right)\frac{1}{1-\frac{c}{2\nu_\mathrm{FSR}R_2}}\right)\right]^{-1}. \tag{4.27}$$

The effective radius of curvature along the principal axis x, R_x, can thus be determined from measurements of the free spectral range ν_FSR and the frequency difference $\nu_\mathrm{qm0}-\nu_\mathrm{q00}$. Similarly, the radius of curvature along the other principal axis, R_y, can be determined from an additional measurement of $\nu_\mathrm{q0n} - \nu_\mathrm{q00}$.

The advantage of this method is the determination of the effective radius of curvature exactly at the position of the mode on the mirror. Therefore, any uncertainty about the alignment of the cavity and the resulting location of the mode does not affect the result. Hence, this method was chosen for all measurements that were made with hybrid cavities.

However, there are several limitations of this method that have to be kept in mind. First, the method requires knowledge about the radii of curvature of the second mirror. If those are unknown, there are free parameters in the theory that cannot be extracted. The method works best if the second mirror is near-planar, because then the influence of the properties of the second mirror on the result is small and uncertainties about the second mirror do not lead to large errors. Second, the result is not the radius of curvature of the mirror, but the radius of curvature of the Hermite–Gaussian mode in the paraxial theory. As explained in Sec. 4.2, this radius of curvature differs from that of the mirror. However, with the parameters for the cavities investigated here, the resulting correction to the Gouy phaseshift is on the order of 1 mrad (cf. Eq. (4.18)), while the total Gouy phase shift is on the order of 1 rad. Therefore, this difference can be neglected. Third, the size of the higher order transverse mode increases with the square of the mode order. Higher order modes thus sample a larger part of the mirror and might see a different effective radius of curvature than lower-order modes if the curvature is nonuniform. This effect can be minimized by restricting the measurement to the lowest-order transverse modes. Finally, if there is significant hybridization between transverse modes (see Sec. 3.5.5),

the Gouy phaseshift and thus the frequency difference between transverse modes will differ from the results of the simple analysis outlined above. It is therefore important to avoid such hybridization by imaging the mode patterns and subsequent realignment if these patterns do not conform to basic Gaussian modes.

The images of the mode patterns required by the last point also offer the opportunity to measure the orientation of the principal axes of the elliptic mirror. Hermite–Gaussian modes are separable in the x- and y-direction if those are aligned with the principal axes of the mirror. Therefore, the symmetry axes of the mode patterns conform to these principal axes and can be used for comparison with the eigenaxes of the polarization modes.

Fig. 4.3a shows the experimental setup to determine the geometry of the elliptic mirror with this method. Two lasers were coupled into a hybrid cavity consisting of one elliptic fiber mirror and the reference mirror. Behind the reference mirror, the light was detected either with a photomultiplier to measure the transmission or a removable camera to image the mode patterns. The fiber mirror was mounted on two parallel shear piezos in order to tune the length of the cavity. A slow, high-amplitude linear ramp was applied to the piezos to record the spectrum of the cavity (Fig. 4.3b). The cavity was optimized for efficient coupling to the fundamental transverse mode to determine the radii of curvature for the same alignment that was later used to measure the frequency splitting of that mode. Therefore, the coupling to higher-order transverse modes decreased with the mode number and some of the higher-order modes were not discernible from the spectrum (e.g the TEM_{21}-mode in Fig. 4.3b).

As the response of the piezos was nonlinear, the scan time could not be directly converted into frequency. Instead, the second laser was tuned until its TEM_{00} resonance with the cavity occurred at the same length as the resonance of the first laser with the modes to be measured. The frequency of these two laser was individually measured with a wavemeter at a specified accuracy of 600 MHz. Typical lengths of the measured cavities were around 50 µm, leading to transverse mode spittings on the order of several hundred GHz, so the error introduced by the limited accuracy of the wavemeter was $< 1\,\%$.

The mode patterns were directly imaged by placing a CMOS camera directly behind the reference mirror without any optics in between and assigned a classification corresponding to the most closely matching Hermite–Gaussian mode. Examples of these mode patterns are shown in Fig. 4.3c–k. These were checked for signs of hybridization for every cavity alignment that was measured and the cavity was realigned if such signs were visible. To find the symmetry axes of a mode pattern, it was first converted from grayscale to black and white using a threshold. The center of the pattern was found by averaging over the centroids of all large connected regions. The angles of an axis through this center were found that maximized the overlap between the image and a mirror image reflected over this axis. These angles are then the orientation of the symmetry axes and thus the orientation of the principal axes of the mirror.

For single-mode fibers, there is good agreement between the radii of curvature measured using the transverse mode distance and those extracted from local fits to the surface profile. The value gathered from the transverse mode distance is more precise and hence the better value for a test of the theory. Nevertheless, it might not be available for every mirror, because it requires the construction of a hybrid cavity with a mirror whose properties are known. Especially before the coating process, local fits to the surface

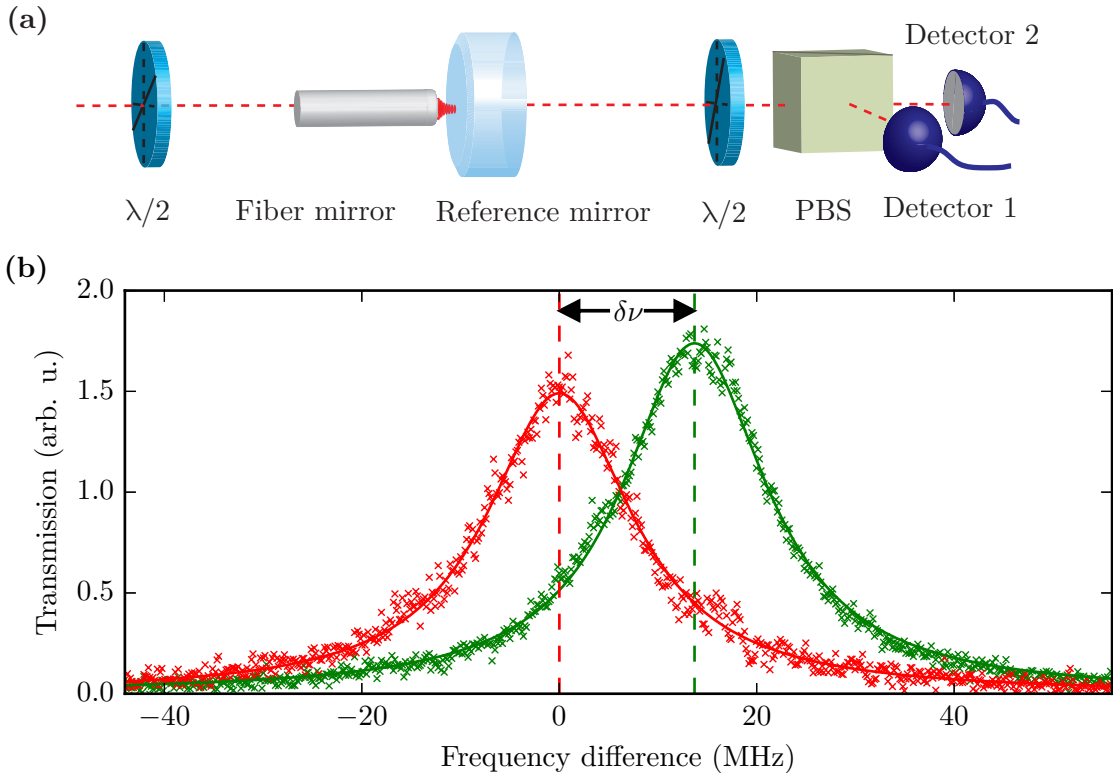

Figure 4.4: (a) Setup for direct measurement of the frequency splitting of polarization eigenmodes. The polarization of the probe laser is set to a linear polarization with an angle of 45° to the eigenaxes in order to equally excite both polarization modes. The detection setup is adjusted to measure in the eigenaxes of the polarization modes with a $\lambda/2$-waveplate, such that each detector (photomultipliers) records the response of one polarization eigenmode. (b) Example trace of one measurement of the frequency splitting. The green and red crosses denote the measured transmission by detector 1 and 2, respectively, during a simultaneous scan over both resonances. The center of each resonance is determined by fitting Lorentzians (green and red lines) to the measured data. The x-axis has been calibrated with sideband markers to convert scan time to frequency. Adapted from Ref. [113].

profile provide an estimate of the radii of curvature and can be used to select the fiber mirrors with the desired properties.

4.3.3 Frequency splitting

The frequency splitting introduced by a single elliptic mirror can be directly measured in a hybrid cavity setup by combining it with the reference mirror. As the phaseshift between polarization eigenmodes due to the latter has been characterized to be negligible compared to the expected phaseshift of the elliptic fiber mirror, the measured frequency splitting and the resulting effective phaseshift can be attributed to the fiber mirror. The setup for this method and example data are shown in Fig. 4.4.

To measure the frequency splitting of the two TEM_{00} polarization eigenmodes, the length of the cavity was adjusted such that only the desired mode is resonant with a small-amplitude scan of the cavity length. For accurate results in a direct measurement, the detection setup needs to measure in a polarization basis that is aligned with the orientation of the polarization eigenmodes of the cavity. This can be achieved by first adjusting the input polarization until only one resonance is visible on the detectors if the frequency splitting is on the order of or larger than the linewidth of the cavity, such that it can be easily resolved. In that case, a single resonance without any visible splitting indicates that the input polarization is aligned with one of the polarization eigenmodes. The polarization basis of the detection setup was then adjusted until the signal on one detector was maximal and there was no signal on the other detector. The orientation of the $\lambda/2$-waveplate in this configuration indicated the orientation of the polarization eigenmode aligned to one detector. The polarization eigenmode aligned with the other detector was orthogonal to that and the orientation of both polarization eigenmodes was compared to the orientation of the principal axes of the fiber mirror.

Subsequently, the polarization of the probe laser was rotated by 45° to equally excite both polarization modes. The length of the cavity was slowly scanned over both resonances and sidebands were used to convert the scan time to frequency (see Sec. 3.5.1). The resulting transmission as a function of frequency was fitted with Lorentzians and the frequency difference was extracted from the difference of the peak positions as estimated by the fits. After 100 repetitions the scan direction was reversed for another 100 repetitions to eliminate any systematic effects originating in different delays of the detector responses. The frequency splitting was taken as the mean of all scans with their standard deviation as the error. The sign of the frequency splitting, taking the scan direction into account, determined which polarization eigenmode had the lower frequency. The magnitude of the splitting was converted into an equivalent phase shift between the polarization modes (Eq. (4.1)) to get a value for the fiber mirror that is independent of the cavity length.

4.4 Results

4.4.1 Phase shift

The frequency splitting of polarization eigenmodes for ten different fiber mirrors was measured and compared to the theory derived in Sec. 4.2. Seven of these, labeled A–G, were measured in a hybrid cavity with the reference mirror. For all of these, the polarization eigenmodes were linear, their orientation matched the orientation of the principal axes of the elliptic mirror, and the polarization eigenmode corresponding to the smaller radius of curvature had the lower resonance frequency. All these observations match the predictions of the theory. The remaining three fiber mirrors, labeled α–γ, were measured by rotation of one fiber in a cavity of two fiber mirrors (see the following section). For these, only the magnitude of the splitting could be measured.

The phase shift per reflection between polarization eigenmodes as a function of the mirror geometry is plotted for all fiber mirrors in Fig. 4.5. The measurements are in good agreement with the values predicted by the theory without any additional free parameters.

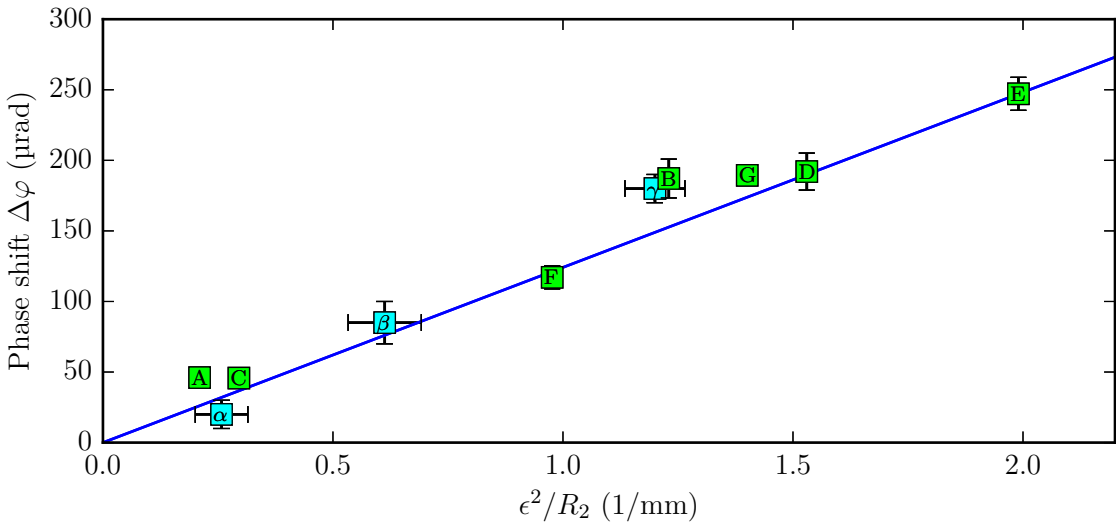

Figure 4.5: Differential phase shift between polarization modes for elliptical fiber mirrors as a function of mirror geometry. The x-axis is the eccentricity ϵ of the fiber mirror divided by its smaller radius of curvature R_2. Green squares: phaseshift measured directly in a hybrid cavity with a reference mirror. The radii of curvature were determined from the transverse mode distance. Cyan squares: phaseshift extracted from fiber rotation. The radii of curvature were determined from local fits of the surface profile. The letters indicate different fiber mirrors. The blue line with slope $1/k$ is the theoretic dependence predicted by Eq. (4.21) and does not depend on any free parameter. Adapted from Ref. [113].

4.4.2 Fiber rotation

In the hybrid cavity setup used for the characterization of single fiber mirrors, the round-trip phaseshift between polarization eigenmodes is independent of the mirror orientation and only depends on the geometry of the fiber mirror. This leaves little opportunity for tuning the frequency splitting of polarization eigenmodes after the mirror has been fabricated. The situation is different in cavities built from two elliptic fiber mirrors. According to Eq. (4.3), the angle between the polarization eigenaxes of the mirrors tunes the round-trip phaseshift between the minimum of $\Delta\varphi_{\mathrm{rt}} = |\Delta\varphi_1 - \Delta\varphi_2|$ and the maximum $\Delta\varphi_{\mathrm{rt}} = \Delta\varphi_1 + \Delta\varphi_2$.

The round-trip phaseshift can be extracted from the frequency splitting measured by the same method as was used for the hybrid cavity. To measure the phaseshift as a function of the angle between the axes, one fiber mirror was rotated around its axis. Consistent results were obtained by coupling in the probe beam through a single mode fiber, using a multi-mode fiber for the second mirror and reoptimizing the transmission of the fiber cavity after each rotation. Maximum transmission in such a configuration indicated maximum coupling of the fiber mode to the cavity mode and was necessary to ensure that the mode was at the same position on the mirror. The results for the two fibers labeled D and E in Fig. 4.5 are shown in Fig. 4.6.

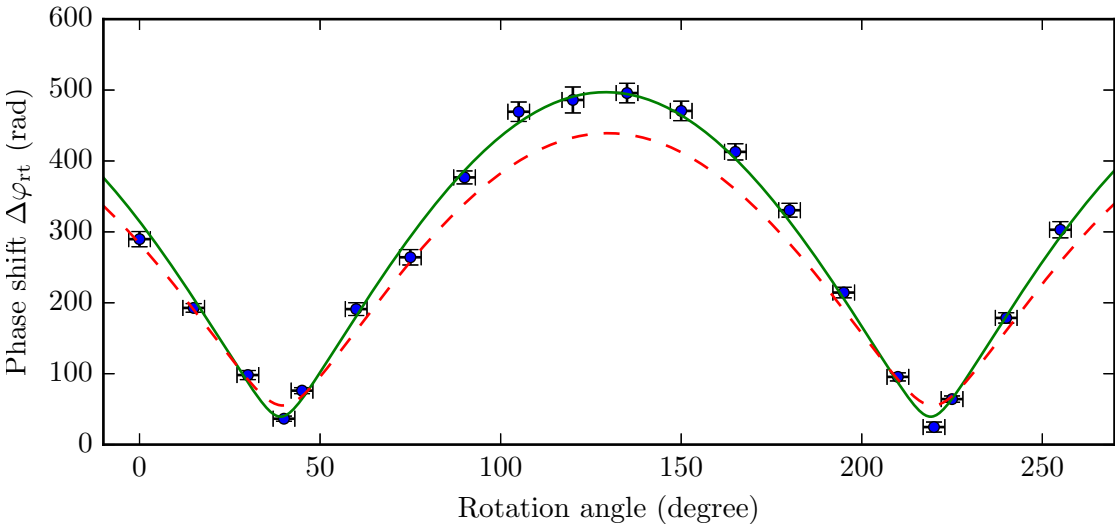

Figure 4.6: Differential phaseshift between polarization eigenmodes depending on the rotation angle for a fiber cavity consisting of the fiber mirrors labeled D and E in Fig. 4.5. The error bars denote the statistical standard error of the phaseshift and the systematic error of the rotation angle stemming from the precision of the rotation stage. The solid green line is a fit of Eq. (4.28) to the data. The dashed red line is a fit of the same equation, but with $\Delta\varphi_1$ and $\Delta\varphi_2$ fixed to the values determined from individual measurements with a hybrid cavity (see Fig. 4.5). Adapted from Ref. [113].

The measured data was fitted with the function

$$\Delta\varphi_{\mathrm{rt}} = \sqrt{\Delta\varphi_1^2 + \Delta\varphi_2^2 + 2\Delta\varphi_1\Delta\varphi_2\cos(2(\vartheta - \vartheta_0))}, \tag{4.28}$$

where an additional angle ϑ_0 compared to Eq. (4.3) accounts for the unknown initial orientation of the fiber mirrors. This fit (solid green line in Fig. 4.6) yielded two phaseshifts, one for each mirror. If the properties of one of the mirrors have been characterized with a different setup, each phaseshift can be unambiguously assigned to one mirror.

In case of the cavity built from mirrors D and E, which were both also characterized in a hybrid cavity, the resulting phaseshifts were $\Delta\varphi_1 = (230 \pm 11)\,\mu\mathrm{rad}$ and $\Delta\varphi_1 = (268 \pm 9)\,\mu\mathrm{rad}$. These values were not consistent with the independent measurements in the hybrid cavity of $\Delta\varphi_1 = (192 \pm 13)\,\mu\mathrm{rad}$ and $\Delta\varphi_1 = (247 \pm 12)\,\mu\mathrm{rad}$. The discrepancy can be attributed to a difference in mode positions on the mirror between the fiber cavity and the hybrid cavities used to characterize the fiber mirrors individually. Different positions lead to a different local effective radius of curvature and thus to a different phaseshift (see Fig. 4.7).

4.4.3 Higher-order transverse modes

Higher-order transverse modes are of much less practical interest in cavity QED than the fundamental transverse mode, because they exhibit a larger mode volume and increased spatial variation of the coupling between an emitter and the cavity mode. In fiber

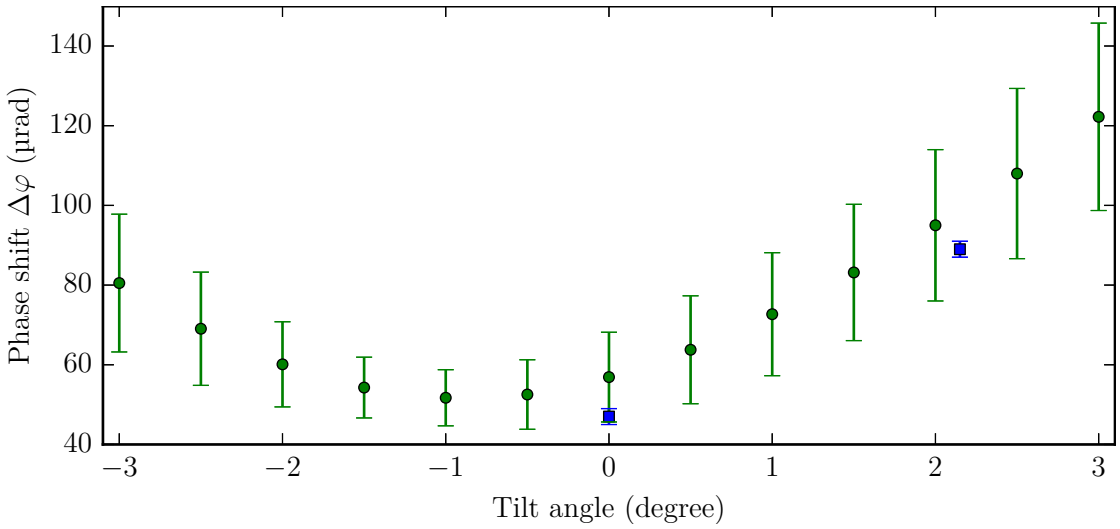

Figure 4.7: Phase shift per reflection between polarization eigenmodes calculated from the measured surface profile of a fiber mirror for different tilt angles between the axes of the fiber and the reference mirror (green dots). Depending on the alignment the local radius of curvature that determines the mode is different, leading to a variation in the expected phase shift. The blue squares denote two measurements with the same fiber at different tilt angles that show this expected alignment-dependent phase shift.

cavities there is the additional disadvantage of less efficient coupling to a single mode fiber. Therefore, the investigation of the frequency splitting of polarization eigenmodes was mainly concerned with the fundamental transverse mode. Nevertheless, it is of fundamental interest whether the predictions of the theory also hold for higher order modes. As the calculation in Sec. 4.2 does not depend on the transverse mode order, Eq. (4.21) should also apply to higher order modes.

An example for the frequency splitting of polarization eigenmodes for the TEM_{10} and TEM_{01} mode compared to the TEM_{00} mode is shown in Fig. 4.8. The data clearly shows that there is a large influence of the transverse mode order: The splitting for the TEM_{01} mode has a different sign than the splitting for the TEM_{10} mode. However, the deviation from degeneracy of polarization eigenmodes is not symmetric between these two modes, but is shifted in the same direction as the splitting of the TEM_{00} mode. This suggests, that there is an effect independent of the transverse mode order, which might be described by Eq. (4.21), but it is modified by an additional effect that does depend on the transverse mode order and has the same order of magnitude for first-order transverse modes.

Calculations assuming perfectly spherical mirrors and using Laguerre–Gaussian modes have shown that due to nonparaxial corrections, circularly polarized polarization eigenmodes arise. At each mirror a phaseshift of

$$\Delta\varphi = \frac{2l}{kR} \tag{4.29}$$

between these eigenmodes occurs, leading to a frequency splitting between them [147–149].

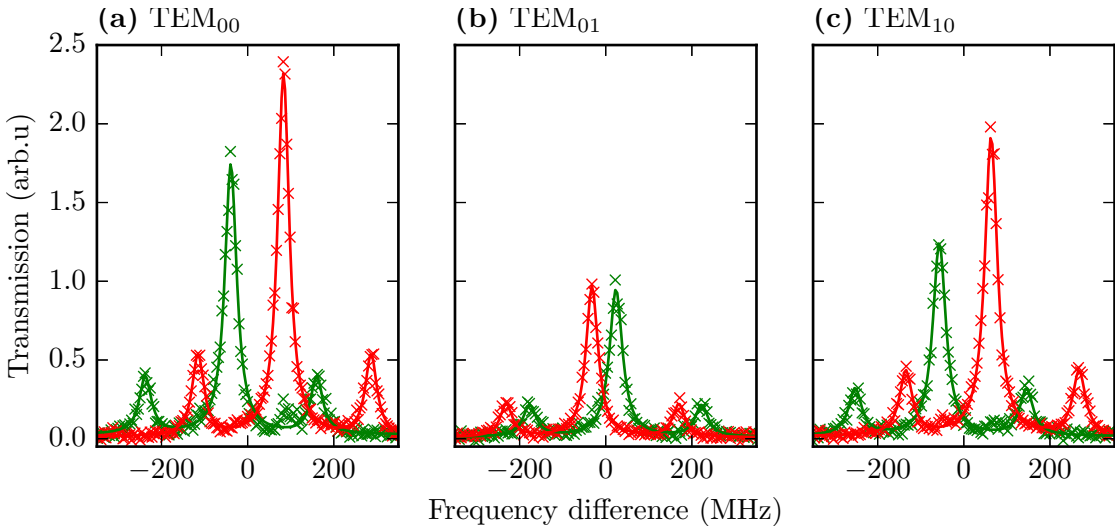

Figure 4.8: Frequency splitting of polarization eigenmodes for the fundamental (a) and first order ((b) and (c)) transverse modes. The red crosses denote the transmission data of Fig. 4.3b magnified in the vicinity of the modes of interest. The green crosses denote the transmission in the orthogonal polarization basis recorded during the same scan. The sidebands used to calibrate the frequency axis are visible right and left of the resonances. The green and red lines are fits of a triple Lorentzian to the resonance and the sidebands. The equivalent phaseshifts per reflection between the polarization eigenmodes are 0.20 mrad in (a), −0.09 mrad in (b), and 0.19 mrad in (c). These values are clearly in disagreement with the theory calculated using Hermite–Gaussian modes, which would predict the same phaseshift for all three modes.

Here, R is the radius of curvature of the spherical mirror and l is the azimuthal mode order of a $\mathrm{TEM}_{\mathrm{pl}}^{\mathrm{LG}}$ Laguerre–Gaussian mode. The fiber mirror of the cavity depicted in Figs. 4.3 and 4.8 has a mean radius of curvature of 785 µm. A spherical mirror with this radius of curvature would induce a phaseshift of 0.32 mrad for the $\mathrm{TEM}_{01}^{\mathrm{LG}}$ mode and −0.32 mrad for the $\mathrm{TEM}_{0-1}^{\mathrm{LG}}$ mode, resulting in a phaseshift difference of 0.64 mrad between these two transverse modes. The measured difference of 0.28 mrad (cf. Fig. 4.8) is smaller by more than a factor of two and not compatible with these calculations.

Neither the calculation with Hermite–Gaussian modes, nor those with Laguerre–Gaussian modes correctly predict the frequency splitting of polarization eigenmodes for higher-order modes and measured values lie in between these predictions. This suggests that neither description is adequate for higher-order modes of the presented cavities at the precision set by the cavity linewidth. The prime candidates for a better description would be Ince–Gaussian modes [150], which form a continuous transition between Laguerre–Gaussian and Hermite–Gaussian modes. Indeed, a comparison of the measured intensity patterns of higher order modes with Ince–Gaussian mode patterns (Fig. 4.9) shows that the observed eigenmodes of hybrid cavities fit Ince–Gaussian modes with an ellipticity parameter $\epsilon_{\mathrm{IG}} \approx 4$ better than Hermite–Gaussian modes. Further theoretical studies of Ince–Gaussian modes using the methods explained in Sec. 4.2 are therefore likely to result in a better description of the frequency splitting of higher

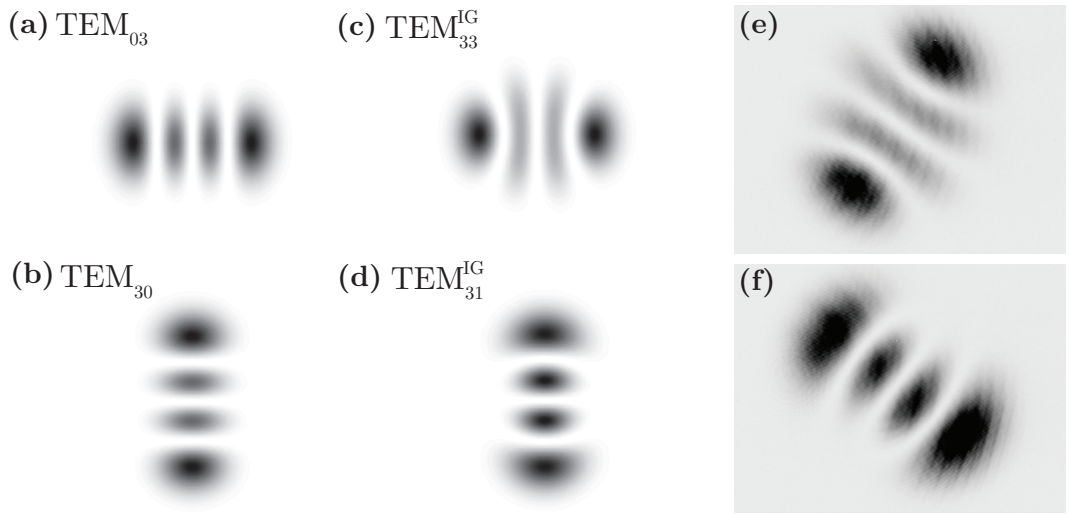

Figure 4.9: Comparison of intensity patterns for calculated Hermite–Gaussian modes ((a) and (b)), calculated Ince–Gaussian modes with ellipticity parameter $\epsilon_{IG} = 4$ ((c) and (d)), and modes measured in a hybrid cavity with one fiber mirror and the reference mirror ((e) and (f), cf. Fig. 4.3i and Fig. 4.3k). The measured intensity patterns are clearly better explained by Ince–Gaussian modes than by Hermite–Gaussian modes.

order modes, which would have to be confirmed by more systematic measurements. Since descriptions by Ince–Gaussian and Hermite–Gaussian modes result in the same fundamental transverse mode, any calculation with Ince–Gaussian modes should not change the result reported in the previous sections for this mode of most practical interest.

4.5 Discussion

The good agreement of the measurements and the theory predicting a frequency splitting of the fundamental transverse mode for cavities with elliptic mirrors due to nonparaxial corrections shows that this effect is the dominant source of the frequency splitting in the investigated cavities. The effect is inversely proportional to the smallest radius of curvature of one mirror and thus becomes increasingly important when minimizing the mode volume by reducing the radii of curvature. It is therefore unlikely to be noticeable for mirrors based on superpolished substrates. For example, a mirror with a radius of curvature of 100 mm and the maximum eccentricity of unity, i.e., with a cylindric geometry, would show a phaseshift of 1.2 µrad due to this effect at a wavelength of 780 nm. However, the effect is important for any type of microscopic, high-finesse cavity that has mirrors with significant eccentricity. A mirror with a radius of curvature of 100 µm and an eccentricity of just 0.1 would already show a phase shift per reflection of 120 µrad. Since the publication of Ref. [113], the effect has also been observed for fiber mirrors fabricated by other groups [103, 126] and silicon mirrors fabricated with focused ion beam milling [151]. The fabrication of fiber mirrors with low eccentricity has enabled

the construction of fiber cavities with almost degenerate polarization eigenmodes [127]. In all cases, the published data was compatible with Eq. (4.19).

The identification of the dominant effect in combination with a quantitative theory that depends only on the mirror geometry allows to determine the effective phase shift per reflection of a mirror during fabrication. Optimizing the fabrication process and/or selecting on mirrors with the desired phase shift can thus be used to tailor the phaseshift for different applications.

The obvious path to get degenerate polarization eigenmodes is to minimize the eccentricity of the fabricated fiber mirrors. The fabrication setup detailed in Ch. 3 can regularly achieve eccentricities of less than 0.2 (see Fig. 3.17). At a radius of curvature of 100 µm, this results in a phaseshift of 50 µrad at a wavelength of 780 nm. A fiber cavity with two mirrors exhibiting this phaseshift oriented at a random angle between the principal axes has an expected round-trip phaseshift of 64 µrad, which would result in a frequency splitting of one tenth of the linewidth at a finesse of 10 000. This value could be further reduced by optimizing the fabrication process to yield structures with increased rotational symmetry or rotating one fiber mirror with respect to the other until the minimum splitting is achieved (see Sec. 4.4.2), with no theoretical lower limit if the phaseshift of the two mirrors is equal.

The other strategy to avoid detrimental effects of the nondegenerate polarization eigenmodes on experimental results is to maximize the splitting until one of the modes is so far detuned that its influence can be neglected. This strategy requires the eccentricity to be as large as possible. Eq. (4.21) sets an upper limit of $1/(kR)$ to the phaseshift induced by the ellipticity of the mirror, which is achieved in the limit of a cylindrical mirror with no curvature in one direction and $\epsilon = 1$. With $R = 100\,\mu\text{m}$, this limit is 1.2 mrad at a wavelength of 780 nm, such that the round-trip phaseshift of a cavity with two aligned cylindrical mirrors is 2.4 mrad. At a finesse of 10 000, the corresponding frequency splitting is only 3.8 linewidths, which is not negligible for most applications. Therefore, this strategy can only fully succeed in case of an additional phaseshift due to birefringence in the coating—possibly induced by external stress—or for cavities of higher finesse. At a finesse of 190 000, this limit of ellipticity-induced frequency splitting is increased to 73 linewidths.

5 A quantum-repeater scheme at telecom wavelength

The content of this chapter has been partially published in:
M. Uphoff, M. Brekenfeld, G. Rempe, and S. Ritter. An integrated quantum repeater at telecom wavelength with single atoms in optical cavities. *Appl. Phys. B* **122**, 46.

In the previous chapters, microcavities were presented that are suitable for quantum communication experiments and can be arranged in a crossed cavity geometry. In this chapter, the possibility of using such geometries to build a quantum repeater with single atoms in optical cavities will be explored. The goal is a quantum repeater that has all functionality integrated in one type of node and can operate directly at telecom wavelength without a need for wavelength conversion.

5.1 Quantum repeaters

Quantum communication aims at the distribution of quantum states over large distances. Heralded entanglement of remote qubits is the most valuable resource to accomplish this, because it serves as a foundation for the most demanding applications. These include fundamental tests of quantum physics like loophole-free Bell tests [8, 152], deterministic teleportation [153–155] of valuable quantum states over large distances, and device-independent quantum key distribution [13, 14].

Heralded entanglement between remote nodes has been achieved by entangling a stationary qubit with a photon, coupling that photon to an optical fiber, and distributing the entanglement via optical fibers and a photonic Bell state measurement [156–158]. However, losses in optical fibers lead to an exponential decrease of transmission with length and thus an exponential decrease of the success probability. The expectation value for the number of trials $\langle Z_0 \rangle$ until two nodes have been entangled is

$$\langle Z_0 \rangle = \frac{1}{p_0} \mathrm{e}^{L_\mathrm{f}/L_\mathrm{att}}, \tag{5.1}$$

where p_0 is the probability for one attempt to succeed without fiber losses, L_f is the length of the fiber between the end nodes, and L_att is the attenuation length of the fiber, i.e., the length over which the transmission drops to 1/e. The quantum state of the stationary qubit entangled with the photon needs to be stored at least until the information about the success of the trial reaches the node. This limits the repetition rate f_0 per stationary qubit at one node to

$$f_0 = \frac{c_\mathrm{f}}{L_\mathrm{f}}, \tag{5.2}$$

where c_f is the speed of light in the optical fiber. This limitation for the maximum repetition rate posed by the time to communicate between nodes to exchange information about the success of a herald is intrinsic to all heralded schemes, although the exact relation varies between different schemes. The combination of maximum repetition rate and expected required number of attempts limits the maximum achievable distance L_f, when compared to a nonzero rate of spurious heralding events. This limit can be pushed by increasing the attenuation length, which requires operation at the *telecom wavelengths* from 1300 nm to 1600 nm for optical fibers consisting of fused silica. At these wavelengths $L_\mathrm{att} \gtrsim 22\,\mathrm{km}$ can be achieved, close to the theoretical maximum set by Rayleigh scattering and infrared absorption [159].

However, increasing the attenuation length does not affect the exponential scaling of Eq. (5.1) with distance. This scaling can only be overcome with quantum repeaters [20]. The idea is to provide feedback at intermediate nodes to increase the overall probability to produce a high-fidelity entangled state. This feedback can take the form of either error detection [160, 161], which defines signals to identify errors that require a repeat of a protocol step, or error correction [162–164], which protects the transmitted quantum information with fault-tolerant codes. The simplest protocol is to divide the total distance L_f into N partial links with length $L_0 = L_\mathrm{f}/N$ and to simultaneously attempt establishment of heralded entanglement between adjacent nodes. Once entanglement has been distributed over one link, it needs to be stored in quantum memories until entanglement between all nodes exists. Entanglement swapping can then be used to generate the desired entanglement between the end nodes.

The expectation value for the number of trials $\langle Z_\mathrm{N}\rangle$ until entanglement has been generated over N links is [165]

$$\langle Z_\mathrm{N}\rangle = \sum_{\mathrm{j}=1}^{N} \binom{N}{j} \frac{(-1)^{j+1}}{1-(1-p_0\exp\left(-L_0/L_\mathrm{att}\right))^j}. \tag{5.3}$$

For $p_0 \ll 1$ or $L_0 \gg L_\mathrm{att}$ this can be approximated by

$$\langle Z_\mathrm{N}\rangle \approx \frac{H_\mathrm{N}}{p_0} \mathrm{e}^{L_\mathrm{f}/(NL_\mathrm{att})}, \tag{5.4}$$

where H_N is the N-th harmonic number. The insertion of additional nodes increases the denominator in the exponential and a polynomial scaling of the time to entangle with length can be achieved with a logarithmic scaling of the number of required qubits [20].

Realistic implementations of quantum memories and entanglement generation, distribution, and swapping will not be perfect but introduce errors. During the multiple operations required for a quantum repeater, these errors will accumulate and the fidelity of the final state will be reduced. This can be counteracted by producing multiple copies of an entangled state and performing entanglement purification [20] to produce one state that has higher fidelity with the target state. However, entanglement purification is resource intensive and might not be optimal in every setting.

5.1.1 Performance criteria

The purpose of a quantum repeater is to enhance the success rate of a quantum communication protocol. However, a repeater protocol adds additional overhead, such that

an inefficient implementation might actually reduce this rate. To demonstrate that a quantum repeater can achieve its purpose, its performance needs to be measured and it is therefore not sufficient to just implement the protocol. The improved scaling of quantum communication involving repeater nodes is only evident if the number of nodes is a free parameter. A given system with a fixed number of nodes will still scale exponentially with length, only with a smaller factor in the exponent. The scaling is therefore not a good indicator for the performance of an experimental system. The absolute rate of generated entangled pairs over a given distance is therefore the relevant parameter. This rate needs to be compared to a reference to judge whether the quantum repeater is beneficial for quantum communication. Several benchmarks exist and from these several different criteria can be deduced that one might demand from a convincing demonstration of a quantum repeater. These are listed in ascending order of difficulty, i.e., a system that fulfills one criterion also fulfills all criteria with a lower number.

1. Demonstration of the entire repeater protocol without comparison to other systems. The rate of entangled pairs could then be used as a benchmark for future systems.

2. The entangled pair rate of the system containing at least one repeater node is greater than the rate using the same end nodes without any repeater node in between. The channel losses can be chosen freely to maximize the effect. This would serve as a proof-of-concept for the repeater protocol, but in a contrived setting.

3. The same comparison as above, but with the lowest technologically feasible channel losses. This results in the largest distance between nodes necessary for repeater nodes to be beneficial and would establish the usefulness of the protocol for long-distance quantum communication.

4. The system needs to outperform the best system without a repeater node that has been demonstrated so far.

5. The entangled pair rate is higher than the rate a hypothetical ideal system could achieve without repeater nodes using the best currently available photon channel.

The fifth criterion would be a final, unequivocal test of the quantum repeater concept, but a quantum repeater would already be of practical interest if it met the other criteria. All operations of a repeater implementation have to be efficient to beat the third criterion and such a system might therefore also be the most efficient one without repeater nodes, such that the third and fourth criterion coincide. In any case, the current distance record for heralded entanglement is 1.3 km [8] and the fourth criterion is hence not available for longer distances, yet. Therefore, the third criterion is the one that can be evaluated to show practical relevance of a quantum repeater system. Comparing the system with itself also has the advantage that the situations with and without repeater nodes can be evaluated in exactly the same way, which allows to directly assess the impact of the repeater nodes. For these reasons, the third criterion will be used in this chapter to evaluate repeater performance.

So far, possible reductions in fidelity by the repeater nodes have been neglected. There are multiple ways to modify these criteria to account for potential errors. The first one is to set a threshold fidelity with a target state and count all entangled pairs that exceed

that fidelity. If the systems clear the threshold with and without repeater nodes, the entangled pair rates can be directly compared. The other extreme is to demand that every purified state of the system with repeater nodes has a fidelity with the target state that is at least as high as the fidelity of the state produced by the system without repeater nodes. The entangled pair rate can then be multiplied with the purification efficiency for comparison. If the modified rate of the system with repeater nodes is higher, it is certainly better in all applications. However, for some applications, the system with repeater nodes might already outperform the system without if just the rate is higher, but the fidelity is slightly lower. To address these situations, the tradeoff between rate and fidelity needs to be quantified. This can be achieved by choosing an entanglement measure [166] and compare the entanglement contained in an ensemble of states produced in a given time interval. However, the entanglement quantified by these measures is not necessarily extractable, so it is not immediately clear how useful the measure is in a particular setting. If the application is quantum key distribution, the secret fraction, i.e., the fraction of unconditionally secure key bits that can be extracted from one entangled state by classical postprocessing [167], is a convenient measure for the tradeoff between fidelity and rate. Multiplied with the entangled pair rate, the secret fraction gives the length of the secret key per unit time, which can be easily compared across different systems. It is, however, specific to quantum key distribution and useless to assess the suitability in other quantum communication protocols. The choice of the method to account for potential errors introduced in the repeater nodes is thus not universal, but depends on the intended application.

5.1.2 Other approaches

Since the original proposal for quantum repeaters [20], very active research has been conducted theoretically and experimentally to develop a system that could fulfill the criteria mentioned in the previous section. The first proposal for an implementation was the Duan-Lukin-Cirac-Zoller protocol [168] that showed how to implement a quantum repeater with atomic ensembles and linear optics. However, this simplicity comes at the price of intrinsically low efficiency. Although the exponential speedup provided by a quantum repeater would in theory enable a quantum repeater at any efficiency, this requires quantum memories with exceptionally long storage time. These storage times could be reduced by multiplexing multiple quantum memories, such that a generated pair only needs to be stored until one of the multiple entanglement distribution attempts running in parallel has succeeded [169]. Since the publication of the original proposal, much progress has been made in improving protocols, storage time, efficiency, and multi-mode capability of atomic ensembles, but so far no system good enough in all aspects has emerged that could be used to demonstrate a quantum repeater [170]. The same protocols can also be applied to ion-doped solids, which have the potential advantage that their large inhomogeneously broadened absorption could be used to store many temporal modes in the same crystal [171].

A different approach is taken by research on single emitters. These are not as easily multiplexed as ensembles, but have the advantage that deterministic entanglement swapping is possible [172], which increases the potential rate of entangled pairs. Therefore, there have been proposals how to implement a quantum repeater with single neutral atoms and ions, quantum dots, and nitrogen-vacancy centers [173, 174]. The necessary

properties, which are highly efficient gates between stored qubits [175, 176], long coherence times for stored qubits [177], and an efficient interface to photons [34, 35], have been shown individually for single emitters, but remain to be combined in a single system.

Besides these potential implementations of a quantum repeater that are close to the original proposal, there are also alternative concepts being investigated. Instead of mediating entanglement distribution with single photons, bright laser pulses could be used to carry quantum information encoded in continuous variables [178, 179]. These schemes perform entanglement distribution with unity efficiency and thus promise an increased rate, but transmission losses degrade the fidelity. Therefore, repeater stations would need to be fairly close together and frequent entanglement purification would be necessary. The loss in fidelity can be traded against efficiency, by adjusting the brightness of the pulse and in the single photon limit, the qubit-based scheme is recovered [180].

All of the previously mentioned schemes are based on the idea of large-distance entanglement swapping, which requires classical communication of the measurement results between nodes. The necessary time for these communications to happen and thus the repetition rate is limited by the speed of light. The repeater could therefore be operated much faster if the information to correct errors due to photon loss or protocol operations was sent with the qubit, such that the remote node can immediately perform the corrections. By encoding the quantum information in fault-tolerant blocks, ultra-fast long-distance quantum communication would be possible [181]. However, the demands required of the quantum-logical operations are quite challenging, equal to a small-scale fault-tolerant quantum computer.

In summary, there are many promising approaches how to build a quantum repeater, but none of them is at the stage, where it is feasible to implement them, yet.

5.2 Entanglement generation at telecom wavelength

In principle, a quantum repeater could be operated at any wavelength, because the better scaling ensures that a system with repeater nodes will always outperform a system without, if the distance is far enough. However, if the attenuation at the chosen wavelength is high, this would require a large amount of nodes and memories with extremely long coherence times. To be competitive in long-distance quantum communication over optical fibers, a quantum repeater is therefore virtually required to distribute entanglement using photons at a telecom wavelength to minimize attenuation in the fibers. Implementing this with single atoms in optical cavities by a direct coupling of an atomic ground state with a telecom wavelength photon would require an atomic transition from such a state at that wavelength. Unfortunately, there are no suitable transitions for atoms that are easily laser-cooled and an indirect method has to be found to utilize the advantages of atomic systems for quantum communication. Very active research has recently been going into the development of external devices that can convert the frequency of photons carrying quantum information [40, 41]. Another approach that is being pursued is the generation of two-color entanglement by spontaneous parametric down-conversion with one photon at telecom wavelength and one compatible with a quantum memory for photons [182, 183]. After storage of the latter photon, the quantum memory is entangled with the telecom photon, which can be used to distribute the entanglement.

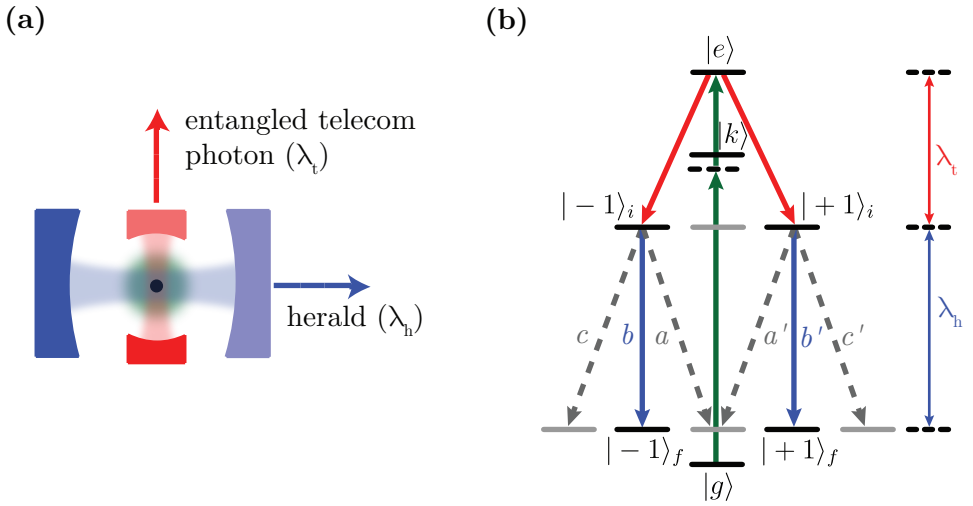

Figure 5.1: (a) Experimental setup for the generation of entanglement between a single atom and a telecom photon using a cascaded scheme. The atom (black dot) is trapped at the crossing point of two cavity modes. The red cavity is the entangling cavity at wavelength λ_t and the blue cavity is the heralding cavity at wavelength λ_h. Both cavities are single-sided, with one mirror having a higher transmission (indicated by lighter colors) than the other. (b) Required scheme of atomic energy levels. The black lines and solid arrows indicate the ideal process, starting from initial state $|g\rangle$. Gray lines stand for additional energy levels not part of the ideal scheme and gray dashed arrows show potential unwanted decay paths. The letters $a^{(\prime)}$ – $c^{(\prime)}$ indicate the relative transition amplitudes. Adapted from Ref. [184].

These efforts have the disadvantage that they require an external device with different technology that needs to be matched to the quantum memory. This additional complexity and the additional inefficiencies that are likely to arise in these approaches could be avoided by finding a scheme to directly generate entanglement at telecom wavelength with a single atom. This can be achieved by using transitions at telecom wavelengths between excited states and then transfer the atomic part of the resulting state to a long-lived ground state. These transitions have been used for wavelength conversion [40] and entanglement generation using cascaded transitions [42] in atomic ensembles. In the following, it will be explained how a related cascaded scheme can be used to generate entanglement between a single atom and a telecom photon with high efficiency due to cavity enhancement.

5.2.1 Cascaded scheme

The experimental setup required for the scheme is depicted in Fig. 5.1a. A single atom is trapped at the crossing point of two perpendicular cavity modes. The cavities are both single-sided and one of them is at a wavelength λ_h in the near-infrared or visible spectrum, corresponding to an atomic transition from its ground state. This cavity will be called the *heralding cavity*. The other cavity, called the *entangling cavity*, is at

wavelength λ_t, addressing a transition between excited states, which should be at a telecom wavelength. The atom is excited by control lasers perpendicular to the plane spanned by the cavities.

The level scheme of the atom is required to be similar to those of bosonic alkali atoms in the manner depicted in Fig. 5.1b. To store the atomic part of the generated entanglement, two long-lived states $|\pm1\rangle_\mathrm{f}$ are necessary, which are assumed to be Zeeman sub-levels with $m_\mathrm{F} = \pm1$. The same is assumed for two intermediate states $|\pm1\rangle_\mathrm{i}$, which are short-lived and coupled to $|\pm1\rangle_\mathrm{f}$ via a π-transition at λ_h. The intermediate states are coupled by a transition at λ_t to the excited state $|e\rangle$, which has $m_\mathrm{F} = 0$. An initialization procedure, e.g., optical pumping, leaves the atom in the initial state $|g\rangle$, which also features $m_\mathrm{F} = 0$. The control laser has two frequencies and mediates a two-photon transition from $|g\rangle$ to $|e\rangle$, far detuned from an intermediate state $|k\rangle$. The heralding cavity is resonant with the transition from $|f\rangle$ to $|i\rangle$ and one of the polarization eigenmodes is π-polarized. The entangling cavity is resonant with the transition from $|i\rangle$ to $|e\rangle$ and supports σ^-- and σ^+-polarization. This description is consistent with the quantization axis pointing along the axis of the entangling cavity.

After initialization in $|g\rangle$, a two-photon control pulse can be used to produce a telecom photon on the transition from $|e\rangle$ to $|\pm1\rangle_\mathrm{i}$, similar to direct entanglement schemes at near infrared wavelengths [34]. The envelope of this photon can be controlled with the shape of the control pulse. If the cooperativity of the atom with the entangling cavity is large, the photon is emitted into the entangling cavity with probability close to unity in a superposition of the polarization states $|\sigma^+\rangle_\mathrm{t}$ and $|\sigma^-\rangle_\mathrm{t}$. Correspondingly, the atom is transferred into a superposition of the states $|-1\rangle_\mathrm{i}$ and $|+1\rangle_\mathrm{i}$. Because of the symmetry of the atomic states, the magnitudes of the transition matrix elements have to be equal and the system is in the maximally entangled state

$$|\Psi_1\rangle = \frac{1}{\sqrt{2}}\left(|-1\rangle_\mathrm{i}\,|\sigma^+\rangle_\mathrm{t} + \mathrm{e}^{\mathrm{i}\phi}\,|+1\rangle_\mathrm{i}\,|\sigma^-\rangle_\mathrm{t}\right). \tag{5.5}$$

The relative sign of the transition matrix elements for the chosen transitions determines the relative phase ϕ, which can take the values 0 and π.

As $|\pm1\rangle_\mathrm{i}$ quickly decay, this entangled state between the atom and a photon at λ_t is short-lived and not suitable to store the entanglement. Instead, the target state is the state

$$|\Psi_2\rangle = \frac{1}{\sqrt{2}}\left(|-1\rangle_\mathrm{f}\,|\sigma^+\rangle_\mathrm{t} + \mathrm{e}^{\mathrm{i}\tilde{\phi}}\,|+1\rangle_\mathrm{f}\,|\sigma^-\rangle_\mathrm{t}\right), \tag{5.6}$$

where the relative phase $\tilde{\phi}$ can again take the values 0 and π. This state can be reached by the emission of a π-polarized photon at λ_h. A high-cooperativity heralding cavity that is resonant with this transition and only supports π-polarization enhances emission via this decay path compared to all other undesired decay paths and enables efficient collection of the π-polarized photon. This photon heralds the successful completion of the scheme and the creation of the desired entangled state. If no such photon is detected, spontaneous emission might have occurred and the scheme can be restarted. A quantum repeater system requires high success probabilities for entanglement generation. These can be achieved with this scheme, if both cavities are single-sided and have high-cooperativity coupling to the chosen transition, i.e., if they are optimized for single-photon production as outlined in Sec. 2.1.

Element	$\|f\rangle$	$\|i\rangle$	$\|e\rangle$	λ_h	λ_t
Rubidium	$5^2S_{1/2}$	$5^2P_{1/2}$	$4^2D_{3/2}$	795 nm	1476 nm
	$5^2S_{1/2}$	$5^2P_{3/2}$	$4^2D_{3/2}$	780 nm	1529 nm
	$5^2S_{1/2}$	$5^2P_{1/2}$	$6^2S_{1/2}$	795 nm	1324 nm
	$5^2S_{1/2}$	$5^2P_{3/2}$	$6^2S_{1/2}$	780 nm	1367 nm
Cesium	$6^2S_{1/2}$	$6^2P_{1/2}$	$7^2S_{1/2}$	895 nm	1359 nm
	$6^2S_{1/2}$	$6^2P_{3/2}$	$7^2S_{1/2}$	852 nm	1470 nm
Francium	$7^2S_{1/2}$	$7^2P_{1/2}$	$8^2S_{1/2}$	817 nm	1333 nm

Table 5.1: The elements and atomic states with which the cascaded entanglement scheme could be implemented to generate entanglement between an atom and a photon at telecom wavelength. Atomic level data from Ref. [185].

All bosonic alkali atoms have transitions that are suitable for the described scheme. Of particular interest are those elements which have a fitting transition at telecom wavelength and are listed in Tab. 5.1. Out of these, rubidium offers the widest choice of wavelengths for the telecom photon. The isotope ^{87}Rb has a nuclear spin of 3/2, which is the lowest available in naturally occurring isotopes of bosonic alkali atoms and limits the number of additional hyperfine states that could complicate atomic state preparation. Therefore, ^{87}Rb is the prime candidate to implement the scheme.

5.2.2 Implementation with ^{87}Rb

To judge the potential of the cascaded entanglement generation scheme, it is necessary to choose a particular implementation to analyze in detail. The choice of the excited state determines the telecom band the entangled photons are in. Rayleigh scattering is reduced in the S-band (1460 nm–1530 nm) compared to the O-band (1260 nm–1360 nm) [159], such that the typical fiber attenuation is lower in the former band. Choosing the $4^2D_{3/2}$ state of rubidium[1] therefore extends the range of the generated entangled photons compared to the $6^2S_{1/2}$ state. As the intermediate state, the $5^2P_{1/2}$ state offers the advantage of a larger hyperfine splitting and thus a cleaner scheme compared to the $5^2P_{3/2}$ state. With these states, one way to implement the scheme is the following (see Fig. 5.2): The hyperfine state $|F{=}1; m_\mathrm{F}{=}0\rangle$ of the state $5^2S_{1/2}$ is chosen as the initial state $|g\rangle$ and $|F{=}2; m_\mathrm{F}{=}\pm1\rangle$ as the final states $|\pm1\rangle_\mathrm{f}$. The $5^2P_{1/2}\,|F'{=}1; m_\mathrm{F}{=}\pm1\rangle$ states are taken as the intermediate states $|\pm1\rangle_\mathrm{i}$ and the $4^2D_{3/2}\,|F''{=}1; m_\mathrm{F}{=}0\rangle$ state as the excited state $|e\rangle$. The intermediate state $|k\rangle$ for the two-photon control can be implemented with the $5^2P_{3/2}$ state. With this choice, two π-polarized control lasers at wavelengths of 780 nm and 1529 nm are necessary to excite the atom from $|g\rangle$ to $|e\rangle$. The entangling cavity needs to be resonant at $\lambda_\mathrm{t} = 1476$ nm, which puts the resulting

[1] The $4^2D_{5/2}$ state is 13 GHz detuned from the $4^2D_{3/2}$ state and would be another option at almost the same wavelength. However it offers no advantage and limits the available schemes, because it does not couple to the $5^2P_{1/2}$ state.

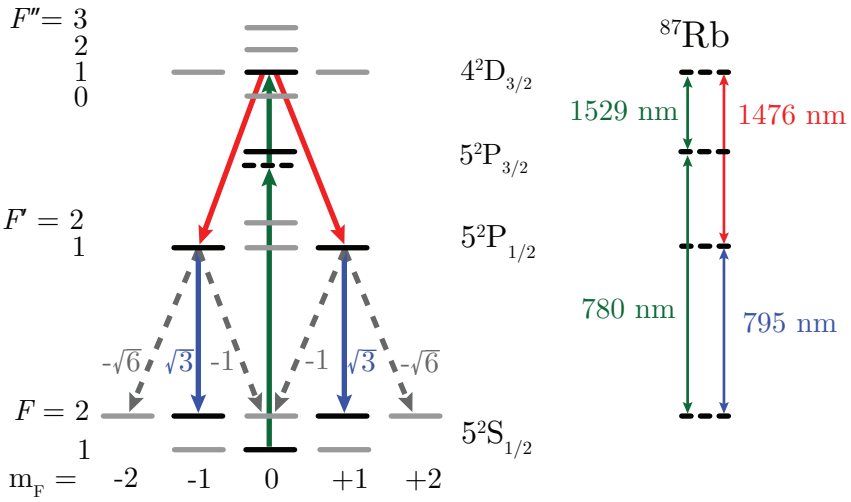

Figure 5.2: Atomic energy levels for a specific implementation of the cascaded entanglement generation scheme with ^{87}Rb (compare Fig. 5.1). For clarity, the level spacings are not to scale and Zeeman substates of the hyperfine levels irrelevant for the scheme are not drawn. Adapted freom Ref. [184].

entangled telecom photons in the S-band of optical fiber communication. The herald photons will be emitted in the near-infrared from the heralding cavity resonant at $\lambda_\mathrm{h} = 795\,\mathrm{nm}$.

Cavity parameters

CO_2 laser-machined mirrors as described in Ch. 3 are ideally suited for the cavities required by this scheme, because they provide high cooperativity, enable single-sided cavities, and can be fabricated in a size small enough for the desired geometry of perpendicular cavities with single atoms coupled to both modes. Therefore, the cavity parameters chosen to analyze the implementation are derived from the results described in Ch. 3. This fulfills two purposes. The first is to provide a realistic setting that estimates how the scheme performs with current technology and the second is to assess the suitability of the described cavities for quantum communication protocols.

The entangling cavity is assumed to be consisting of two fiber mirrors with the standard fiber diameter of 125 µm. According to the considerations in Sec. 2.4 concerning the possibility of trapping an atom with a far off-resonant dipole trap, the length of this cavity is taken to be 75 µm. Asymmetric radii of curvature of 200 µm for the output coupler and 100 µm for the high reflector result in a maximum coupling efficiency of 96 % at the output coupler between the cavity mode at λ_t and the mode of a standard telecom single-mode fiber with a mode-field diameter of 10 µm (see Sec. 2.4.1). The waist of this cavity mode is 4.8 µm. Due to the asymmetry of the mirror curvatures, the waist position is not at the center of the cavity, where the atom is assumed to be trapped, but the mode radius there is increased to 5.3 µm. The decay rates of the $4^2D_{3/2}$ state have been calculated by Safronova *et al.* [186] and are $\Gamma_\mathrm{ei} = 2\pi \times 1.62\,\mathrm{MHz}$ for decay to the $5^2P_{1/2}$ state and $\Gamma_\mathrm{ek} = 2\pi \times 0.30\,\mathrm{MHz}$ for decay to the $5^2P_{3/2}$ state. $|F''{=}1; m_\mathrm{F}{=}0\rangle$

decays at λ_t to $|F'{=}1; m_F{=}{\pm}1\rangle$ with a probability of 5/12 each and the matrix elements of these decay paths have opposite signs, such that $\theta = \pi$ in the intermediate state (Eq. (5.5)). Inserting these parameters into Eq. (2.7) results in a coupling strength $|g_t| = 2\pi \times 70\,\mathrm{MHz}$.

From Fig. 3.28, parasitic losses of 20 ppm per mirror can be inferred for a cavity length of 75 µm at a wavelength of 780 nm. At the larger wavelength λ_t, scattering losses due to microroughness decrease (cf. Eq. (3.10)), but losses due to mirror size increase because of the larger mode. In total, the losses are expected to be similar and the parasitic losses at λ_t are assumed to be the same as at $\lambda = 780\,\mathrm{nm}$. The transmission of the mirrors can be freely chosen before the coating process and 10 ppm are chosen for the high reflector and 600 ppm for the output coupler. With these parameters, the decay rate for the cavity field is $\kappa_t^{oc} = 2\pi \times 95\,\mathrm{MHz}$ for decay by transmission through the high reflector and an additional $\kappa_t^{l} = 2\pi \times 8\,\mathrm{MHz}$ for decay caused by all other loss channels. The entangling cavity should support degenerate polarization eigenmodes which can be achieved with the methods described in Ch. 4.

For later extension to a quantum repeater node, the heralding cavity needs to be long enough to fit two entangling cavities inside, perpendicular to it (cf. Sec. 5.4 and Fig. 5.7). A cavity length of 400 µm could accommodate two fiber cavities with a fiber diameter of 125 µm and a lateral separation of 200 µm. Therefore, the heralding cavity is assumed to have this length and identical radii of curvature of 500 µm. The mode waist of such a cavity is 7.9 µm at λ_h=795 nm. The decay rate on the rubidium D_1-line from $5^2P_{1/2}$ to $5^2S_{1/2}$ is $\Gamma_{if} = 2\pi \times 5.75\,\mathrm{MHz}$ and the relative transition strength from $|F'{=}1; m_F{=}{\pm}1\rangle$ to $|F{=}2; m_F{=}{\pm}1\rangle$ is 1/4 each. The matrix elements for both transitions have the same sign, such that the phase of the intermediate state is unchanged in the final state, i.e., $\tilde{\theta} = \theta = \pi$. Using these values, the calculated coupling strength for the heralding cavity is $g_h = 2\pi \times 16.3\,\mathrm{MHz}$.

A fiber cavity with a length of 400 µm is difficult to achieve with the mirrors presented in Ch. 3, and fiber integration is not necessary for the heralding cavity, because the herald photon does not need to be transmitted to another location, but can be immediately detected. Therefore, CO_2 laser-machined glass plates are assumed as mirror substrates. According to Fig. 3.29[2], 20 ppm losses per mirror are possible at λ_h. Together with 10 ppm transmission of the high reflector, this leads to total losses of 50 ppm and a corresponding field decay rate of $\kappa_h^{l} = 2\pi \times 1.5\,\mathrm{MHz}$. A transmission of 400 ppm for the output coupler results in $\kappa_h^{oc} = 2\pi \times 11.9\,\mathrm{MHz}$. This cavity is assumed to have a large frequency splitting of polarization eigenmodes, with one of the eigenmodes being aligned to π-polarization with respect to the quantization axis of the system. The other eigenmode is assumed to be far detuned, such that its influence can be neglected in the simulation. As discussed in Sec. 4.5 this is not the case if the eccentricity of the mirrors is the sole cause of frequency splitting, such that additional birefringence would need to be induced to fulfill this assumption.

[2] Note that the data in that figure shows a measurement of a half-symmetric cavity. To get the value for a symmetric cavity of a certain length, the losses of the CO_2 laser-machined mirror at half the length needs to be extracted from that measurement.

Efficiency

Using these parameters, the system was numerically simulated to calculate the expected efficiency of the proposed entanglement generation scheme. The interaction Hamiltonian for the ideal system in rotating wave approximation is:

$$\begin{aligned} H_{\text{ideal}}/\hbar = {} & g_{\text{t}} \left(\sigma_{\text{e},-1_{\text{i}}} a_{\text{t},\sigma^+} + \sigma_{\text{e},+1_{\text{i}}} a_{\text{t},\sigma^-} + \text{h.c.}\right) \\ & + g_{\text{h}} \left(\left(\sigma_{-1_{\text{i}},-1_{\text{f}}} + \sigma_{+1_{\text{i}},+1_{\text{f}}}\right) a_{\text{h},\pi} + \text{h.c.}\right) \\ & + \frac{\Omega}{2} \left(\sigma_{\text{g,e}} + \sigma_{\text{e,g}}\right), \end{aligned} \tag{5.7}$$

where $\sigma_{\text{x,y}}$ denotes the atomic transition operator from state $|y\rangle$ to state $|x\rangle$, $a_{\text{t(h)},\text{p}}$ the photon annihilation operator for the mode with polarization p in the entangling (herald) cavity, and Ω the two-photon Rabi frequency.

Atomic and cavity decay can be modeled incoherently with the Lindblad superoperator

$$L\left[A, \rho\right] = \frac{1}{2}\left(2A\rho A^\dagger - \rho A^\dagger A - A^\dagger A \rho\right) \tag{5.8}$$

acting on the density matrix ρ, the atomic operators

$$\begin{aligned} A_{\text{a}} = \Bigg\{ & \sqrt{\Gamma_{\text{ei}} + \Gamma_{\text{ek}}}\, \sigma_{\text{w,d}};\ \sqrt{\frac{1}{6}\Gamma_{\text{ei}} + \Gamma_{\text{ek}}}\, \sigma_{\text{w,e}};\ \sqrt{\frac{5}{12}\Gamma_{\text{ei}}}\, \sigma_{-1_{\text{i}},\text{e}};\ \sqrt{\frac{5}{12}\Gamma_{\text{ei}}}\, \sigma_{+1_{\text{i}},\text{e}}; \\ & \sqrt{\frac{1}{4}\Gamma_{\text{if}}}\, \sigma_{-1_{\text{f}},-1_{\text{i}}};\ \sqrt{\frac{1}{4}\Gamma_{\text{if}}}\, \sigma_{+1_{\text{f}},+1_{\text{i}}};\ \sqrt{\frac{3}{4}\Gamma_{\text{if}}}\, \sigma_{\text{w},-1_{\text{i}}};\ \sqrt{\frac{3}{4}\Gamma_{\text{if}}}\, \sigma_{\text{w},+1_{\text{i}}} \Bigg\}. \end{aligned} \tag{5.9}$$

and the cavity operators

$$A_{\text{c}} = \left\{\sqrt{2\kappa_{\text{t}}}\, a_{\text{t},\sigma^+};\ \sqrt{2\kappa_{\text{t}}}\, a_{\text{t},\sigma^-};\ \sqrt{2\kappa_{\text{t}}}\, a_{\text{h},\pi}\right\}. \tag{5.10}$$

These operators take into account that the level structure of ^{87}Rb contains extra levels not present in the ideal system. To keep the dimensionality of the Hilbert space manageable, far-detuned levels were neglected and a dump level $|w\rangle$ was introduced as the final destination of all atomic decay outside the ideal system. The only levels that could not be addressed this way were the hyperfine states of the $4^2D_{3/2}$ state, which have small hyperfine constants [187] and thus cannot be treated as far-detuned. Due to the polarization of the control laser and the selection rules of a two-photon process that is off-resonant from the intermediate state, the hyperfine states with quantum number $F'' = 0$ and $F'' = 2$ cannot be excited and only the $|F''{=}3; m_{\text{F}}{=}0\rangle \equiv |d\rangle$ state can become relevant. This state has a detuning of $\Delta_{\text{d}} = 124\,\text{MHz}$ [187] from state $|F''{=}1; m_{\text{F}}{=}0\rangle$ and can be excited by the two-photon control if it is short and thus has a high bandwidth. This would reduce the efficiency of the entangled-photon generation, because this state does not couple resonantly to the entangling cavity. The Hamiltonian of the system thus has to be modified to account for this state:

$$H_{\text{sys}}/\hbar = H_{\text{ideal}}/\hbar + \Delta_{\text{d}}\sigma_{\text{d,d}} + \frac{\Omega}{2}\left(\sigma_{\text{g,d}} + \sigma_{\text{d,g}}\right) \tag{5.11}$$

The corresponding Lindblad master equation

$$\frac{\text{d}}{\text{d}t}\rho = -\frac{\text{i}}{\hbar}\left[H_{\text{sys}}, \rho\right] + \sum_{\text{A}\in(\text{A}_{\text{a}}\cup\text{A}_{\text{c}})} L\left[A, \rho\right] \tag{5.12}$$

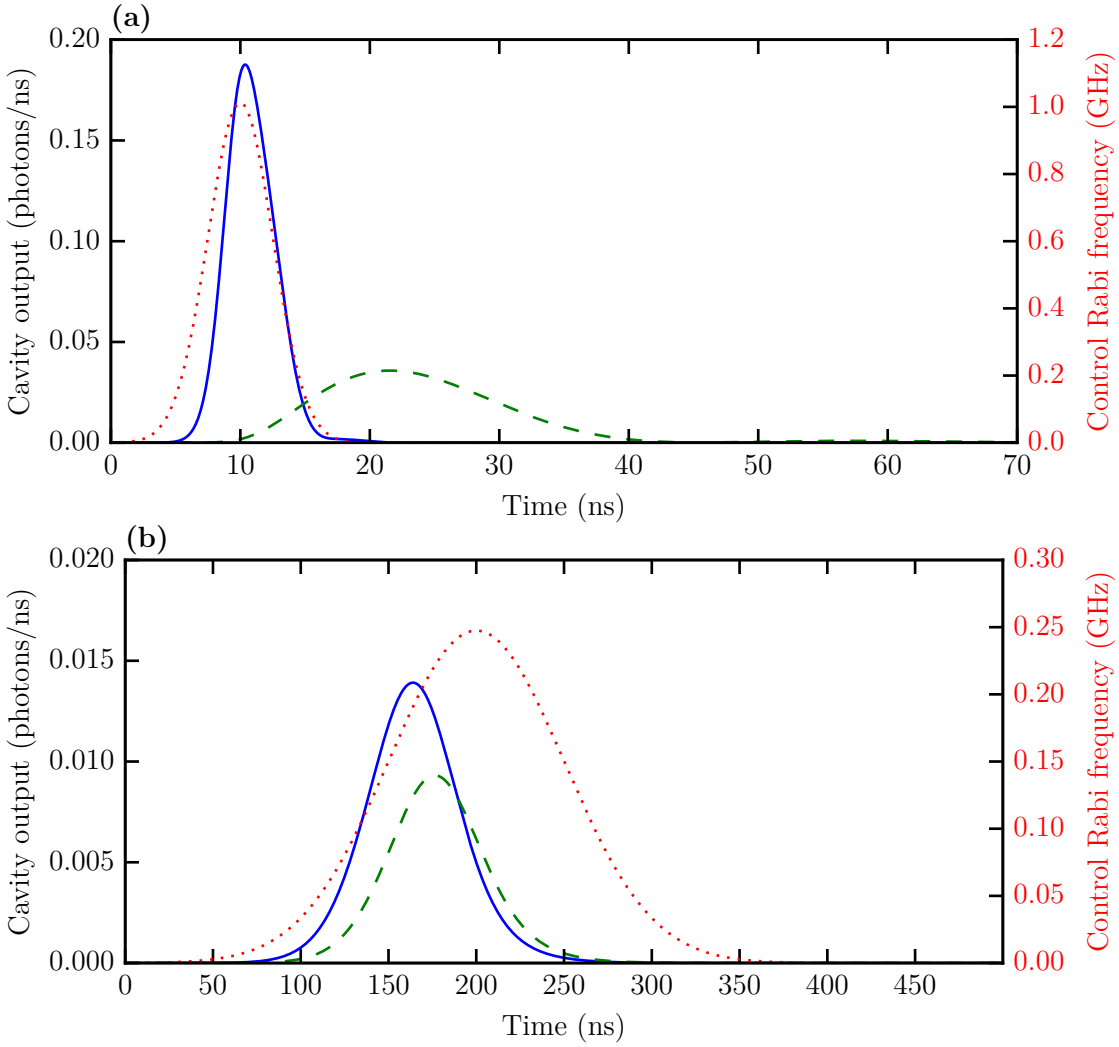

Figure 5.3: Expectation value of the output of the entangling cavity (solid blue line) and the heralding cavity (dashed green line) for two different control pulses. The control pulse (dotted red line, right vertical axis) is a Gaussian function with a full width at half maximum of (a) 5.9 ns and (b) 118 ns. For the short control pulse depicted in (a) the bandwidth of the entangled and herald photon is limited by the coupling strengths and the bandwidths of the respective cavities. Spectral and temporal correlations are therefore suppressed. For the long control pulse depicted in (b) the envelope and bandwidth of the photon is determined by the control pulse, creating spectral and temporal correlations between entangled and herald photon (cf. Fig. 5.5). In both cases, the probability to emit an entangled photon is 1.4 times higher than the probability to emit a herald photon, mainly because the cooperativity for the latter process is lower, which results a higher probability for spontaneous emission. Adapted from Ref. [184].

was integrated to calculate the independent expectation value of the entangling- and heralding-cavity output (Fig. 5.3). For short control pulses, the spectral and temporal properties of the herald and entangled photon are independently determined by the coupling strength and the bandwidth of the respective cavities. The bandwidth of the herald photon is therefore different from the bandwidth of the entangled photon and only weak correlations exist between these properties. For long control pulses, the bandwidth of the two-photon state is determined by the bandwidth of the control pulse and the arrival times of the herald and entangled photon are more strongly correlated, because most of the time the herald photon will be emitted slightly after the entangled photon (see also Fig. 5.5). In this case, the frequencies of the two photons is also correlated, because their sum is constrained by the narrow bandwidth of the two-photon state.

The overall success probability p_{ht} is the probability that both processes succeed, i.e., an entangled telecom photon is emitted into the optical fiber and a herald photon is emitted through the output coupler of the heralding cavity. This probability could only be extracted from the independent expectation values if the probabilities for both processes were uncorrelated. However, there are correlations between these processes; e.g., spontaneous decay of state $|e\rangle$ to a state that does not couple to the heralding cavity will prevent emission into the entangling cavity as well as into the heralding cavity. Therefore, a Monte-Carlo wave-function method [188–190] was employed to investigate correlations between the cavity outputs. From this information, $p_{\mathrm{ht}} = 0.57$ was extracted for long control pulses. This value was independent of the length of the control pulse, except for very short control pulses, which resulted in significant excitation of the detuned hyperfine state $|d\rangle$ and thus in a reduced efficiency (see Fig. 5.4). For long control pulses, the success probability is mainly limited by spontaneous decay of the $5^2P_{1/2}$ state, which prevents the generation of a herald photon (24 % probability), and parasitic losses in the entangling and heralding cavity (8 % and 7 % probability, respectively). Further improvements in the fabrication and coating processes of the CO_2 laser-machined mirrors could reduce the intrinsic losses of the cavities, which would also allow higher cooperativities while maintaining the single-sidedness (see Sec. 2.1). This could increase the efficiency of the scheme to the point where it is almost deterministic.

5.2.3 Fidelity

The protocol requires the atom to be initialized in $|g\rangle$, which can be achieved by optical pumping. There is no fundamental limit how well the state can be prepared and a detailed comparison of the various strategies that could be employed for optimal preparation is beyond the scope of this work. Therefore, it is assumed that initialization is perfect, i.e., in every trial the state $|g\rangle$ is prepared with unit efficiency. As further assumptions, the two-photon control is far detuned from $|k\rangle$, such that no state besides those considered can be excited, and the hyperfine splitting of the intermediate state $|i\rangle$ is much larger than the bandwidths and coupling strengths of the cavities, which is the case for $5^2P_{1/2}$ and the parameters listed above. If these conditions hold, the fidelity of the intermediate state with the ideal state $|\Psi_1\rangle$ only depends on the geometry of the system, and a fidelity very close to unity should be possible. The correct mapping from the intermediate state to the final state is heralded by the emission of a π-polarized herald photon at wavelength λ_{h}. The probability for such an event to be a dark count of the detector is negligible when state-of-the-art detectors are used, because a very short interval of interest can be

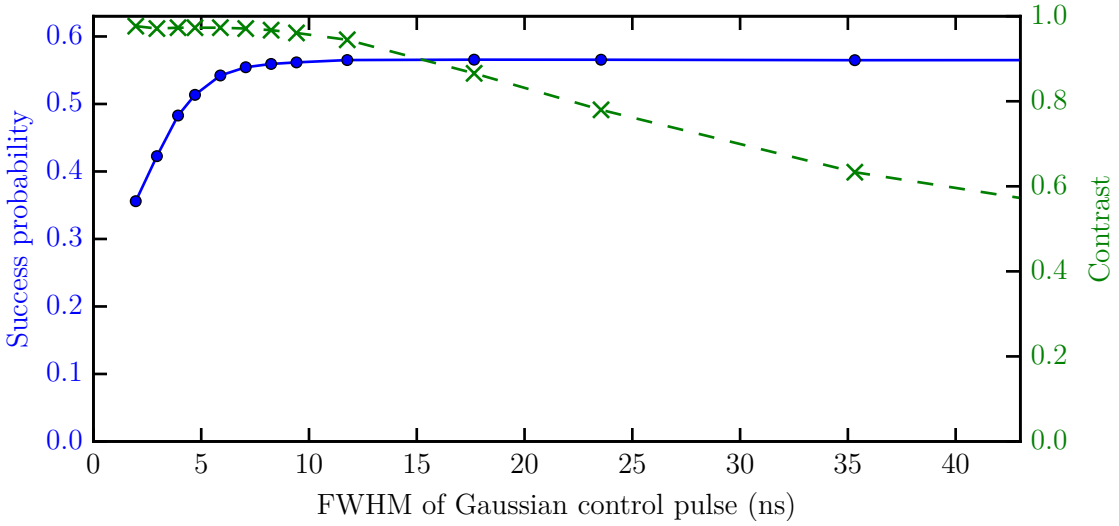

Figure 5.4: Overall success probability p_{ht} (blue dots and solid line, left axis) and expected contrast in a two-photon interference experiment (green crosses and dashed line, right axis, see Sec. 5.2.4) as a function of the full width at half maximum (FWHM) of a Gaussian control pulse. For each point, the amplitude of the control pulse was set to the minimum value that depletes the initial state, using a threshold of $< 1\,\%$ remaining population. The results of numerical simulations (dots and crosses) haven been connected by lines to guide the eye. The efficiency is close to constant for long pulses, but drops for very short pulses. The reverse is true for the contrast and the best working point to optimize both values is between 5 ns and 10 ns FWHM of the control pulse. In the following the value 5.9 ns will be used for the FWHM of the control pulse. Adapted from Ref. [184].

selected and the efficiency to get a photon out of the cavity in this interval is high. A selection on those events with a detection of a herald photon of the correct polarization should therefore result in a very high fidelity for the final entangled state between the photon at λ_{t} and the atomic state. Nevertheless there are effects that could potentially deteriorate the fidelity, although they are of marginal importance for the particular implementation and parameters chosen here.

Free-space decay

Any excited atom-cavity system with finite cooperativity has a chance for decay of the atomic state via free-space emission. This disrupts the ideal protocol and might result in the creation of a state different from the desired one. However, in most of the cases, no telecom photon or no herald photon is emitted from the cavity and the lack of a detection of either signals an error that can be used to discard the atomic states. This results in a reduced efficiency but not a reduced fidelity, such that only erroneous processes that result in the creation of at least one telecom photon and one herald photon can affect the fidelity. Such processes can occur if the intermediate states $|\pm 1\rangle_{\mathrm{i}}$ can decay back to the initial state $|g\rangle$ or any other state that can be excited by the two photon control. In

that case there is a chance to create a second or even multiple telecom photons, resulting in an undesired multi-photon entangled state. Because the atomic part of this state can contain a contribution of the intermediate states $|\pm 1\rangle_{\mathrm{i}}$, this state can be accompanied by a correctly polarized herald photon and can therefore not be discarded by selection. In principle, the presence of multiple telecom photons could be detected, but especially after transmission through a lossy channel, a fraction of these events cannot be detected.

There are two possibilities to minimize multi-photon events. First, an implementation should be chosen in such a way to minimize decay from the intermediate states to the initial state, such that with high probability, spontaneous emission puts the atom in a state that cannot be excited by the control lasers. Second, the protocol can be executed quickly compared to the duration of atomic decay, such that in most of the cases the control lasers are already turned off when spontaneous decay occurs and the atom cannot be reexcited. In the limit of fast excitation, for example with a picosecond pulsed laser [191], multi-photon events would be eliminated. However, if the pulse is too short, any possibility of influencing the temporal envelope of the generated photons with the control lasers disappears, and the pulse might get too spectrally broad. This would result in the excitation of detuned states, like $|d\rangle$, which do not couple to the entangling cavity, and thus in reduced efficiency.

The Monte Carlo wave-function method was used to estimate the amount of multi-photon contributions for the particular implementation and parameters described in Sec. 5.2.2 and a short control pulse with a full width at half maximum (FWHM) of 5.9 ns. An upper bound was obtained by assuming the worst case, which is the dump level being equal to the initial state, i.e., all decay to the outside of the simulated system ends up in a state that can be efficiently excited by the control laser. A comparison of the number of desired quantum trajectories to the number of those resulting in the generation of multiple telecom photons and at least one herald photon, yielded a bound of less that 0.4 % for events that can not be discarded by selection on correct herald photons. In the realistic case, not all decay will end up in a state that can be efficiently excited, so the real fraction of multi-photon events is expected to be even lower.

Second polarization mode

So far, the second polarization mode of the heralding cavity has been assumed to be far detuned. If this is not the case and the second polarization mode is near-resonant or even degenerate, it can enhance decay of the intermediate state $|\Psi\rangle_1$ to a state that contains the $m_{\mathrm{F}} = 0$ Zeeman sublevel and, in case of $F \geq 2$, the $m_{\mathrm{F}} = \pm 2$ Zeeman sublevel of $|f\rangle$. This process emits a photon with a linear polarization perpendicular to π into the cavity, which can be detected and selected against. A degenerate second polarization mode therefore obviously reduces the efficiency. In addition, it also introduces a state-dependent probability for the generation of π-polarized herald photons and thus reduces the fidelity of the final state.

To show the mechanism and calculate the size of this effect, the intermediate state $|\Psi_1\rangle$ (Eq. (5.5)) is rewritten in a linear polarization basis for the entangled telecom photon:

$$|\Psi_1\rangle = \frac{1}{\sqrt{2}} \left(|\Psi_{1,\mathrm{H}}\rangle + |\Psi_{1,\mathrm{V}}\rangle \right) \tag{5.13}$$

with

$$\begin{aligned} |\Psi_{1,\mathrm{H}}\rangle &= \frac{1}{\sqrt{2}} |H\rangle_{\mathrm{t}} \left(|-1\rangle_{\mathrm{i}} - |+1\rangle_{\mathrm{i}}\right) \\ |\Psi_{1,\mathrm{V}}\rangle &= \frac{1}{\sqrt{2}} |V\rangle_{\mathrm{t}} \left(|-1\rangle_{\mathrm{i}} + |+1\rangle_{\mathrm{i}}\right). \end{aligned} \tag{5.14}$$

Here, it is assumed that the phase $\theta = \tilde{\theta} = \pi$, results for the other possible phase combinations are analogous.

The polarization eigenmodes of the heralding cavity are assumed to be polarized along π and V. H-polarization is then parallel to the heralding cavity axis, i.e., the longitudinal polarization, and is not supported by the cavity. The worst case is degeneracy between these polarization eigenmodes, which results in the same enhancement factor of the heralding cavity for each decay path, such that the final state is determined just by the relative transition amplitudes $a^{(\prime)}$, $b^{(\prime)}$, and $c^{(\prime)}$ (see Fig. 5.1). Because free-space decay is isotropic, it can never result in a state-dependent decay probability. Therefore, it is assumed to be insignificant in the following calculation of the worst case. Under these assumptions, $|\Psi_1\rangle$ decays to $|\Psi_3\rangle = 1/\sqrt{2}\,(|\Psi_{3,\mathrm{H}}\rangle + |\Psi_{3,\mathrm{V}}\rangle)$ with

$$\begin{aligned} |\Psi_{3,\mathrm{H}}\rangle = &\frac{1}{\sqrt{\frac{|a+a'|^2}{2} + |b|^2 + |b'|^2 + \frac{|c|^2+|c'|^2}{2}}} |H\rangle_{\mathrm{t}} \\ &\times \Bigg[|\pi\rangle_{\mathrm{h}} \left(b\,|-1\rangle_{\mathrm{f}} - b'\,|+1\rangle_{\mathrm{f}}\right) \\ &+ \frac{1}{\sqrt{2}} |V\rangle_{\mathrm{h}} \left(c\,|-2\rangle_{\mathrm{f}} + c'\,|+2\rangle_{\mathrm{f}} + (a+a')\,|0\rangle_{\mathrm{f}}\right) \Bigg] \end{aligned} \tag{5.15}$$

and

$$\begin{aligned} |\Psi_{3,\mathrm{V}}\rangle = &\frac{1}{\sqrt{\frac{|a-a'|^2}{2} + |b|^2 + |b'|^2 + \frac{|c|^2+|c'|^2}{2}}} |V\rangle_{\mathrm{t}} \\ &\times \Bigg[|\pi\rangle_{\mathrm{h}} \left(b\,|-1\rangle_{\mathrm{f}} - b'\,|+1\rangle_{\mathrm{f}}\right) \\ &+ \frac{1}{\sqrt{2}} |V\rangle_{\mathrm{h}} \left(c\,|-2\rangle_{\mathrm{f}} + c'\,|+2\rangle_{\mathrm{f}} + (a-a')\,|0\rangle_{\mathrm{f}}\right) \Bigg]. \end{aligned} \tag{5.16}$$

Due to the symmetry of Clebsch-Gordan coefficients, $a' = \pm a$, $b' = \pm b$, and $c' = \pm c$ and the choice of basis states is such that all transition amplitudes are real. If $a' = +a$, the term $a - a' = 0$ vanishes and $|\Psi_{1,\mathrm{V}}\rangle$ does not decay to $|0\rangle_{\mathrm{f}}$ via the heralding cavity, because of destructive interference, while the heralding cavity enhances the decay from $|\Psi_{1,\mathrm{H}}\rangle$ to $|0\rangle_{\mathrm{f}}$. In that case, $|\Psi_{1,\mathrm{V}}\rangle$ has a higher probability to emit a π-polarized herald photon, because it has less decay paths than $|\Psi_{1,\mathrm{H}}\rangle$. If $a' = -a$, the situation is reversed, and $|\Psi_{1,\mathrm{H}}\rangle$ is more likely to emit a correctly polarized herald photon. In either case, a state dependency of the emission is introduced, which results in unequal amplitudes of the final entangled state upon selection on events with a π-polarized herald photon. Therefore the final state cannot be maximally entangled, but its entanglement depends on the value of the transition amplitude $|a|$ compared to $|b|$ and $|c|$.

To quantify the reduction in fidelity, the case $a' = a$, $b' = b$, and $c' = c$ is explicitly calculated. All other cases can be calculated the same way with the same result for

the fidelity reduction. The normalized final state $|\Psi_3\rangle$ selected on the emission of a π-polarized herald photon is

$$\begin{aligned}|\Psi_3\rangle &= \frac{1}{\sqrt{\tilde{\mathcal{N}}}} \langle\pi|_\mathrm{h} \left(|\Psi_{3,\mathrm{H}}\rangle + |\Psi_{3,\mathrm{V}}\rangle\right) \\ &= \frac{1}{\sqrt{\mathcal{N}}} \left[\sqrt{2b^2+c^2}\,|H\rangle_\mathrm{t} \left(|-1\rangle_\mathrm{f} - |+1\rangle_\mathrm{f}\right) + \sqrt{2a^2+2b^2+c^2}\,|V\rangle_\mathrm{t} \left(|-1\rangle_\mathrm{f} + |+1\rangle_\mathrm{f}\right)\right],\end{aligned} \tag{5.17}$$

where $\tilde{\mathcal{N}}$ and $\mathcal{N} = 4(a^2+2b^2+c^2)$ are normalization constants. This state is not maximally entangled, but has a reduced fidelity with the ideal final state $|\Psi_2\rangle$ of

$$F = |\langle\Psi_2|\Psi_3\rangle|^2 = \frac{1}{2} + \frac{1}{2}\frac{\sqrt{(2a^2+2b^2+c^2)\,(2b^2+c^2)}}{a^2+2b^2+c^2}. \tag{5.18}$$

A fidelity close to unity is reached if $|a|$ is small compared to $|b|$ and $|c|$. This is the case for the transition from $5^2P_{1/2}\,|F'{=}1\rangle$ to $5^2S_{1/2}\,|F{=}2\rangle$ in ^{87}Rb that is used in the implementation proposed in the previous section. There, $a = a' = -1$, $b = b' = \sqrt{3}$, and $c = c' = -\sqrt{6}$ and the resulting reduction in fidelity is $1 - F = 0.15\,\%$ in the worst case of the heralding cavity having degenerate polarization eigenmodes. For implementations with different transitions, the effect can be worse. For example the transition from $5^2P_{1/2}\,|F{=}1\rangle$ to $5^2S_{1/2}\,|F{=}1\rangle$ for the same isotope has $a = -a' = -1$, $b = -b' = 1$, and $c = c' = 0$, and a corresponding fidelity reduction of $1 - F = 2.9\,\%$.

The size of the effect decreases with increasing detuning of the second polarization mode of the heralding cavity and vanishes if it is far detuned. This is also the condition for maximum efficiency, such that for optimum performance, the frequency splitting of polarization eigenmodes should be as large as possible.

5.2.4 Indistinguishability

Once entanglement has been created between a single atom and a telecom photon, the entanglement must be distributed to provide heralded entanglement between remote nodes. This could be either achieved by heralded storage of the entangled photon at the remote node [37] or by an optical Bell state measurement on the polarization of two telecom photons entangled with an atom at their node of origin [192, 193]. So far, no scheme has been found to implement the former efficiently with telecom photons and alkali atoms, so entanglement distribution has to be implemented with the latter method. An optical BSM is based on two-photon interference at a beam splitter and only provides the correct result if the photons are indistinguishable in their temporal, spectral, and spatial properties. It has been shown that photons from spatially separated sources with single atoms in optical cavities interfere under exactly controlled experimental conditions, with the contrast limited by the movement of the atoms [194]. This limitation would be reduced with photons that have a duration of a few nanoseconds, which is much shorter than the inverse of typical trap frequencies of less than 1 MHz, and could be eliminated with atoms cooled to the ground state [86]. I should therefore be possible to generate indistinguishable photons with a scheme similar to the one presented in Ref. [194].

However, the cascaded scheme for entanglement generation poses the additional challenge that the herald photon at each node can potentially reveal information about

the temporal or spectral properties of the corresponding entangled telecom photon, which allows to determine the source of a telecom photon and renders telecom photons from different sources distinguishable. Cascaded decay via two photons in free space will result in strongly correlated arrival time distributions for the two photons, because the photon created by the second part of the cascade can never be emitted before the photon emitted by the first part, but will, in most of the cases, be emitted with a short delay. The first photon therefore has an exponentially rising envelope up to the detection time of the second photon, when conditioned on the arrival time of the latter [195]. If the heralded entanglement generation scheme would be implemented without cavities, it would, for example, be possible to exclude that a telecom photon emitted after a herald photon came from the same source, thus revealing that it was generated by and is entangled with the other node. In that case the photons would be perfectly distinguishable and would not interfere, such that no entanglement is created between the remote nodes. The problem could be circumvented by imposing the additional condition of similar detection time to the herald photons and discarding all events where this was not the case. This would, however, severely limit the efficiency.

The correlation between the emission times of herald and entangled telecom photon can be at least partially erased by the cavities, because the cavity does not immediately decay after a photon has been emitted into it but stores the photon on average for one lifetime of the cavity. If the lifetime of the heralding cavity is much longer than the duration of the wave packet of the entangled telecom photon, the arrival-time distribution will solely depend on the properties of the heralding cavity and not be correlated with the arrival time of the telecom photon. In that case, the detection time of the herald photons contain no information about the temporal properties of the telecom photons and distinguishability by that criterion is prevented. This would be ideally implemented by a short entangling cavity with large coupling strength to the atom that quickly decays in combination with a short control pulse to generate a telecom photon with a narrow envelope in time. The heralding cavity should have a longer lifetime, which can be achieved by increasing the cavity length.

Numerical calculation of the photon indistinguishability

As a measure for the indistinguishability of the telecom photons generated by the cascaded entanglement scheme for the parameters given in Sec. 5.2.2, the expected interference contrast C in a Hong-Ou-Mandel experiment [194, 196, 197] was calculated. This required knowledge of the arrival time distribution of the telecom photons, conditioned on the detection time of the herald photons. The Monte-Carlo wave-function method was used to simulate a large number of arrival-time pairs. To estimate a smooth distribution of the events as a function of the arrival time of herald and telecom photon, the simulated data was processed with a kernel density estimator [198, 199]. A two-dimensional Gaussian function was chosen as the kernel with the bandwidth set to $6\kappa_\mathrm{t}$ and $6\kappa_\mathrm{h}$ for the axis corresponding to the arrival time of the telecom and herald photon, respectively. As the output of a kernel density estimator depends on the bandwidth of the kernel if the dataset is finite, the bandwidth was chosen to be larger than the bandwidth of any process occurring in the system, such that the resulting distribution is likely undersmoothed, in order to derive a lower bound for the indistinguishability. The resulting density function was evaluated at different arrival times of the herald photon to generate the

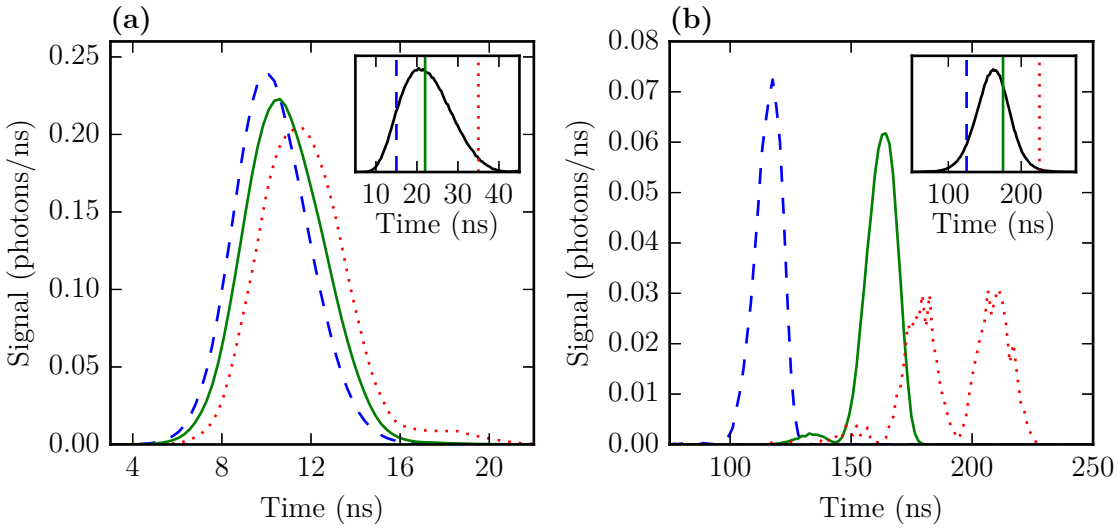

Figure 5.5: Envelope of a telecom photon entangled with the atom conditioned on the detection of an early (dashed blue line), average (solid gree line), and late (dotted red line) herald photon. The insets show the unconditional probability for detection of a herald photon with these detection times marked in the respective line style. (a) Control pulse with a FWHM of 5.9 ns (cf. Fig. 5.3a) with herald detection at 15 ns, 22 ns, and 35 ns (all times are relative to the times axes of Fig. 5.3). Correlations between arrival time of the herald photon and the telecom photon are weak, therefore the resulting telecom photons are near-indistinguishable. (b) Control pulse with a FWHM of 118 ns (cf. Fig. 5.3b) with herald detection at 125 ns, 175 ns, and 225 ns. There are strong temporal correlations between herald and telecom photons, such that the latter can be distinguished if the arrival time of the former is different. The dotted red line shows signs of undersmoothing due to finite sample size. The oscillations of the photon envelope are caused by Rabi oscillations with frequency $2g_{\mathrm{h}}$.

conditional arrival time distributions of the telecom photons. Examples for a short and a long control pulse are shown in Fig. 5.5. The short control pulse resulted in a telecom photon with a duration shorter than the lifetime of the heralding cavity, resulting in nearly indistinguishable photons. In contrast, when the situation of a long control pulse was simulated, the envelope of the generated two-photon state had a much longer duration than the lifetime of the cavity (see Fig. 5.3). Projecting this two photon state by detecting one of them, also projects the arrival time of the other photon, resulting in very narrow conditional distributions such that telecom photons can be distinguished if the respective herald photons are detected at different times.

From the conditional probability distributions, the contrasts conditioned on a detection of the herald photons at specific times can be calculated. An average over these contrasts weighted by the arrival time distribution for the herald photons yields the average contrast C. The fidelity of a remote entangled state created by an optical BSM is $F = \frac{1}{2}(1 + C)$ [200], under the assumption that no errors are introduced by other processes.

The expected average contrast was calculated for Gaussian control pulses of different

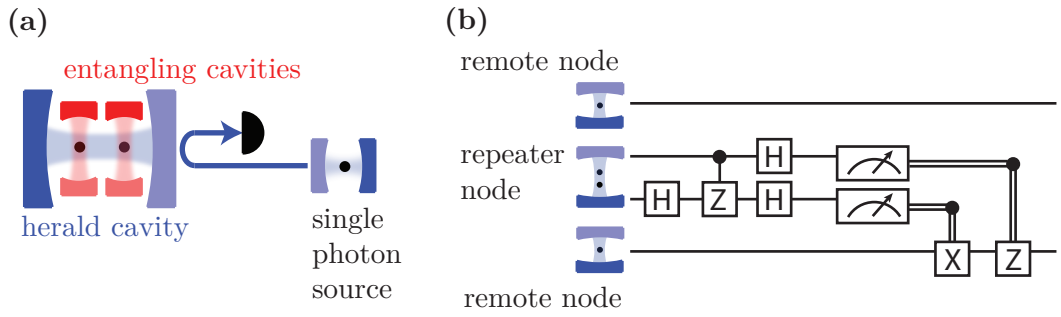

Figure 5.6: (a) Proposed experimental setup at one node to perform entanglement swapping. Two atoms are simultaneously coupled to the mode of the heralding cavity. A single photon source, which could be another single atom coupled to a cavity, produces a single photon that is reflected off the resonant heralding cavity and detected afterwards. Detection of this auxiliary photon heralds the success of the gate. (b) Circuit diagram of the entanglement swapping protocol. The aforementioned setup equals a controlled-Z gate between the two atoms at the repeater node. This gate combined with single-qubit Hadamard gates (H) and state-detection of the atoms at the repeater nodes forms an entanglement swapping protocol. The resulting two-atom state between atoms at the two outer nodes is one of the four Bell states, which can be mapped to a specific Bell state with single-qubit rotations (X and Z) that depend on the outcome of the state detection.

width and is compared against the expected efficiency in Fig. 5.4. For long control pulses, the efficiency is high, but the indistinguishability is reduced, because of correlations between arrival times. For very short control pulses, there is little correlation between arrival times, resulting in near-indistinguishability of the generated telecom photons and high contrast regardless of the arrival time of the herald photons, but the efficiency is low. For the considered parameters, control pulses between 5 ns and 10 ns are optimal, because both efficiency and contrast are near their respective maxima. At a control pulse FWHM of 5.9 ns, a contrast of $C = 0.97$ can be reached with efficiency $p_{\mathrm{ht}} = 0.54$, which suggests that fidelities close to 0.99 should be efficiently possible with the realistic parameters described in Sec. 5.2.2.

The fidelity could be further improved at the cost of efficiency by selecting on events with close arrival times for herald and telecom photons, because the duration of the telecom and herald photon exceeds the timing resolution of most commercially available single-photon counters. In the limit of stringent selection on identical arrival times for either the herald or entangled photons and if there is not other effect that renders the telecom photons distinguishable, a contrast of unity could be reached.

5.3 Entanglement swapping

The key idea of a quantum repeater is to perform entanglement distribution over independent links, store the entanglement in quantum memories until success on every

link, and then use entanglement swapping to create entanglement between the end points of a link chain. This requires at least two entanglement distribution links to remote nodes for each repeater node. Entangling cavities based on fiber mirrors have a small enough size that a parallel pair fits into a heralding cavity with the parameters described in Sec. 5.2.2, with their axes perpendicular to the heralding cavity axis and a single atom trapped in each entangling cavity in such a way that they both couple to the heralding cavity (see Fig. 5.6a). This allows to use the heralding cavity for heralding the entanglement creation in both entangling cavities, if a control pulse is applied to each atom in an alternating pattern while the other atom is detuned, for example by applying a local light shift. With this setup it is possible to perform the entanglement generation and distribution schemes outlined in the previous sections individually to each atom until they have succeeded for both.

Entanglement storage

Once entanglement has been created, it needs to be stored. The energy difference between the Zeeman substates $|-1\rangle_\mathrm{f}$ and $|+1\rangle_\mathrm{f}$, which form the atomic part of the final state of the entanglement generation scheme (Eq. (5.6)), is susceptible to fluctuations of the effective magnetic field [201], which limits the coherence time of this state. To extend the possible storage time, the atomic part of the entangled state can be transferred to states that have similar energy shifts when exposed to magnetic fields and are thus much less sensitive to magnetic field fluctuations [202]. A state-selective, high-fidelity microwave or Raman pulse could be used to transfer one of the Zeeman states (e.g., $|-1\rangle_\mathrm{f}$) to the other hyperfine ground state with the same m_F, such that the atomic qubit is encoded in the states $|0\rangle \equiv |F{=}2; m_\mathrm{f}{=}{+}1\rangle$ and $|1\rangle \equiv |F{=}1; m_\mathrm{f}{=}{-}1\rangle$. The Zeeman shift of these two states is equal to first order, when a moderate magnetic field of about 3.23 G is applied, which extends the possible coherence time to several seconds [38, 39].

Atomic Bell-state measurement

To complete entanglement swapping, a mechanism to detect the collective Bell state of the two quantum memories is required. For a quantum repeater, the efficiency of the entanglement swapping scheme is crucial, because an entanglement swapping attempt might be at the end of a time-consuming entanglement build-up, all of which would have to be repeated if the entanglement swapping attempt fails. In principle, it would be an option to map the atomic state to a photonic state and then perform an optical Bell state measurement (BSM). However, this requires two potentially inefficient mapping processes and photon detections and is intrinsically limited to an efficiency of 50 %, because an optical BSM using linear optics cannot discriminate between the Bell states $|\Phi^-\rangle$ and $|\Phi^+\rangle$ [203]. It is therefore more efficient to perform the BSM directly on the atoms. The heralding cavity, which can couple to both atoms, is an obvious choice to provide an interaction mechanism to perform that collective measurement and multiple schemes to perform a cavity-mediated two-atom quantum gate have been proposed [204–206]. Of these, the gate based on the reflection of a single photon from the cavity [36, 205] is the most suitable, because it requires a single-sided cavity and can operate with high efficiency even in the intermediate coupling regime [36]. The gate is based on the mechanism that the reflected photon introduces a phase shift of π if the cavity

does not couple to an atom, but no phase shift if the cavity is resonantly coupled to an atom with sufficiently high cooperativity. Of the states $|0\rangle$ and $|1\rangle$ described above, only $|0\rangle$ couples to the π-polarized cavity mode resonant with the transition from $|f\rangle$ to $|i\rangle$ (compare the level scheme in Fig. 5.2). The reflected photon only introduces a phase shift of $|\pi\rangle$, if both atoms are in $|1\rangle$, because in any other case at least one atom is resonant with the cavity and no phase shift occurs [43]. The reflection of a photon is therefore equivalent to a controlled-Z quantum gate between the two atoms.

With this controlled-Z gate, single-qubit rotations by microwave or Raman pulses, and cavity-assisted, hyperfine-state detection [48, 56], the quantum circuit for entanglement swapping depicted in Fig. 5.6b can be implemented. The Hadamard single-qubit rotations and the controlled-Z gate map the four Bells states onto four separable atomic states, which can be unambiguously detected with hyperfine-state detection performed individually on each atom. After this operation on two atoms at a repeater node that were entangled with two atoms at remote nodes, the latter are entangled and in one of the four Bell states, depending on the result of the state detection. This results also indicates which single-qubit rotations to apply at one of the remote nodes in order to obtain the same Bell state in every attempt.

Efficiency

The controlled-Z gate fails if the photon is not reflected by the cavity, either because it never arrived there, or because of parasitic losses in the cavity. These cases can be ruled out if the photon is detected after reflection, which can thus be used as a herald for the successful operation of the gate. If all events without detection of the reflected photon are discarded, which will be necessary to reach high fidelity with realistic parameters, a photon-detector efficiency η_h below unity will further decrease the efficiency. The efficiency of the entanglement swapping protocol is therefore

$$p_\mathrm{es} = p_\mathrm{p}\eta_\mathrm{h}R_\mathrm{avg}. \tag{5.19}$$

Here, p_p is the probability of a photon arriving at the cavity, which is given by the efficiency of the single-photon source including possible transmission losses. R_avg is the reflectivity of the heralding cavity, averaged over the possible number of atoms that are resonantly coupled to the cavity. During the BSM, both atoms are equally likely to be in $|0\rangle$ or $|1\rangle$, such that

$$R_\mathrm{avg} = \frac{1}{4}\left(R_0 + 2R_1 + R_2\right), \tag{5.20}$$

where R_0, R_1, and R_2 are the reflectivities if the cavity is empty, or is coupled to one or two atoms, respectively. These values account for the probability of the photon being lost, either by spontaneous emission or because of cavity decay via any other path than the output coupler. These losses are minimized if the coupled atom-cavity system has high cooperativity and the transmission of the output coupler is dominant compared to all other losses. In the limit of a perfectly single-sided cavity and infinite cooperativity, the efficiency reaches unity. To calculate the expected efficiency for the proposed system, the parameters listed in Sec. 5.2.2 are used. The coupling strength for the heralding cavity g_h has to be modified, because in a system with two entangling cavities and two atoms, the atoms cannot be both trapped at the center of the heralding cavity. Instead, it is assumed that the atoms are trapped on the heralding cavity axis, $\pm 100\,\mu\mathrm{m}$ from

its center. At these points, the cavity field is weaker than at the center, reducing the coupling to $g_\mathrm{h} = 15.1\,\mathrm{MHz}$. These parameters result in $R_0 = 60\,\%$, $R_1 = 55\,\%$, and $R_2 = 73\,\%$. The average of these values over all possibilities is $R_\mathrm{avg} = 61\,\%$.

For the detection efficiency, a value of $\eta_\mathrm{h} = 80\,\%$, is assumed, which can be achieved with current technology [207]. Single atoms trapped in optical cavities are also highly efficient single photon sources [208] and with optimized parameters, efficiencies exceeding $p_\mathrm{p} = 80\,\%$ can be easily reached (compare Fig. 2.3). Single-qubit rotations and state detection of atomic states can be implemented in such a way to give a result in every trial and therefore have an efficiency of unity. The total success probability of the entanglement swapping process is therefore $p_\mathrm{es} = 39\,\%$

Fidelity

A state-dependent reflectivity of the cavity and selection on the detection of a reflected photon can distort the amplitudes of a quantum state and lead to a reduced fidelity. The worst case is an equal superposition of those atomic states that have the highest reflectivity differential. With the parameters listed above, $|\Psi\rangle = (|00\rangle + |01\rangle)/\sqrt{2}$ is an example for such a state. The gate would map this state to the state

$$|\tilde{\Psi}\rangle = \frac{1}{\sqrt{R_2 + R_1}} \left(\sqrt{R_2}\,|00\rangle + \sqrt{R_1}\,|01\rangle\right). \tag{5.21}$$

The fidelity of this state with the ideal state is

$$\begin{aligned} F = \left|\langle\Psi|\tilde{\Psi}\rangle\right|^2 &= \left|\frac{1}{\sqrt{2(R_2 + R_1)}} \left(\langle 00| + \langle 01|\right) \left(\sqrt{R_2}\,|00\rangle + \sqrt{R_1}\,|01\rangle\right)\right|^2 \\ &= \frac{\left(\sqrt{R_2} + \sqrt{R_1}\right)^2}{2R_2 + 2R_1}. \end{aligned} \tag{5.22}$$

The reflectivity is determined by the single-sidedness of the cavity and the cooperativity of the system. With these two parameters the reflectivities R_0 and R_1 can be tuned to the same value. However, for a finite cooperativity, R_1 and R_2 differ, such that this reduction of fidelity is intrinsic to the scheme. Only in the limit of infinite cooperativities, R_1 and R_2 both approach unity and the difference vanishes. Nevertheless, the effect can be minimized if the cooperativity is high and even a significant difference has only a small effect. For the parameters listed above with a 18 % difference in reflectivity, the reduction in fidelity by this effect is at most 0.5 %. The detection of the individual hyperfine state of the atoms could potentially introduce additional errors, but these should be small because the atoms are assumed to be separated by 200 µm, are therefore easily addressable with laser beams, and cavity-assisted state-detection of hyperfine states has been shown to reach fidelities very close to unity [48]. Errors will therefore be mainly technical, with the most important error source being the mode matching between the mode of the incident auxiliary photon and the cavity mode [36]. The heralding cavity is assumed to be based on laser-machined glass plates, for which the mode can be matched in free space with an unrestricted number of optical elements. Therefore, mode-matching close to unity and a high-fidelity implementation of this entanglement swapping protocol should be possible.

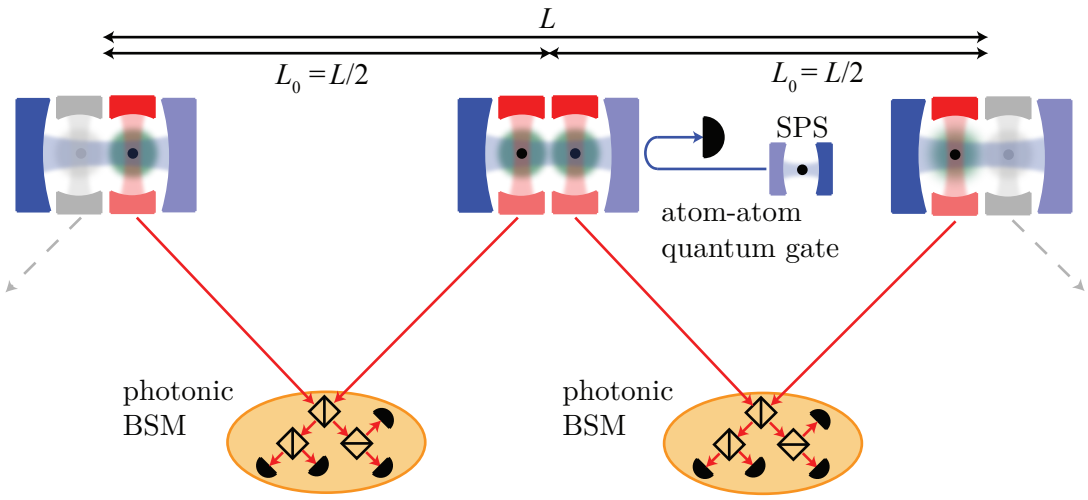

Figure 5.7: Scheme for a quantum repeater with two elementary links ($N = 2$), i.e., two end nodes and one central repeater node. Entanglement generation between a single atom and a telecom photon according to the scheme discussed in Sec. 5.2 is performed concurrently in every entangling cavity (red). Herald photons in the near infrared are collected by the herald cavities (blue). The telecom photons are interfered at a beam splitter to perform entanglement distribution via photonic Bell-state measurements. The herald cavities are used to perform an atom-atom gate mediated by the reflection of a photon generated by a single-photon source (SPS). Together with single-qubit rotations and state-detections, this gate implements entanglement swapping between the atoms (Sec. 5.3). The grayed-out cavities and arrows indicate the possibility to extend the system with further repeater nodes. From Ref. [184].

5.4 Quantum repeater performance

The protocols for entanglement generation, entanglement distribution, and entanglement swapping described in the previous section can be combined to a quantum repeater protocol (see Fig. 5.7). The elementary unit of this scheme is a quantum repeater node that consists of two atoms, each coupled to a telecom-wavelength entangling cavity, and a perpendicular heralding cavity that couples to both atoms. An elementary link between neighboring nodes is formed by an optical BSM, i.e., the interference of two telecom photons from these nodes at a beam splitter and detection with a polarization-sensitive setup. Two links connecting two end nodes with one repeater node form the most simple implementation of the proposed repeater protocol. The scheme can be easily extended by inserting identical additional repeater nodes and thereby increasing the number of links. In the following, the performance of such schemes with realistic parameters (see Tab. 5.2) will be analyzed and compared to the situation without repeater nodes.

Parameter	Symbol	Assumed Value	
		Entangling cavity	Herald cavity
Radius of curvature (output coupler)	R_{oc}	200 µm	500 µm
Radius of curvature (high reflector)	R_{hr}	100 µm	500 µm
Cavity length	L	75 µm	400 µm
Transmission (output coupler)	T_{oc}	600 ppm	400 ppm
Parasitic losses	$T_{\mathrm{hr}} + \mathcal{L}$	50 ppm	50 ppm
Coupling efficiency to fiber mode	ϵ	96 %	–
Photon-detector efficiency	η	80 %	80 %
Distance atom–center of cavity	d_{c}	0 µm	100 µm
Single-photon-source efficiency	p_{p}	80 %	
Cycle time between attempts	t_{cyc}	100 µs	
Speed of light in fiber	c_{f}	$2 \times 10^5\,\mathrm{km\,s^{-1}}$	
Attenuation length of fiber	L_{att}	22 km	

Table 5.2: All parameters that have been assumed for the calculation of the repeater performance. All other parameters are derived from these and the properties of ^{87}Rb.

5.4.1 Success rate

For successful entanglement distribution between adjacent nodes, first a telecom photon and a herald photon needs to be generated at each node, which happens with probability p_{ht}. As a compromise between efficiency and indistinguishability (Fig. 5.4), a control pulse of 5.9 ns FWHM duration is assumed, which results in $p_{\mathrm{ht}} = 0.53$ when the reduced coupling of the heralding cavity to atoms not trapped at its center is accounted for. Second, detection of the herald photons with probability η_{h} needs to be successful. As in Sec. 5.3, a photon detection efficiency of $\eta_{\mathrm{h}} = 0.8$ is assumed. Third, the optical BSM needs to be successful. Conditioned on two incident photons, this probability is $\eta_{\mathrm{t}}^2/2$, where η_{t} is the detection efficiency for the telecom photons, which is assumed to be $\eta_{\mathrm{t}} = \eta_{\mathrm{h}} = 0.8$ The factor 1/2 accounts for the inability to distinguish the $\Phi^{+/-}$ Bell states in an optical BSM, such that only those trials can be considered successful where one of the $\Psi^{+/-}$ states has been detected. The total probability for successful entanglement distribution ignoring attenuation in the fiber links is therefore

$$p_0 = \frac{1}{2}\left(p_{\mathrm{ht}}\eta_{\mathrm{h}}\eta_{\mathrm{t}}\right)^2, \tag{5.23}$$

which is $p_0 = 5.8\,\%$ for the parameters given here.

With this number and Eq. (5.3), the expected number of trials $\langle Z_{\mathrm{N}}\rangle$ to generate N entangled pairs can be calculated. If the entanglement swapping scheme was successful

in every trial, this number would be equal to the expected number of attempts $\langle n_\mathrm{N} \rangle$ until the entire protocol has succeeded and one entangled pair has been created between quantum memories at the end nodes. However, the proposed entanglement swapping mechanism has a failure probability $1 - p_\mathrm{es}$. Because the mechanism is heralded, this failure can be detected, but the involved entangled pairs have to be discarded and entanglement has to be reestablished, which increases the expected number of trials. The exact size of that increase depends on the strategy when entanglement swapping is attempted and two different strategies will be considered in the following.

The first strategy is to build up entanglement until all N pairs are entangled and then perform $N - 1$ entanglement swapping attempts. If all attempts succeed, one entangled pair is created. If one or more attempts fail, all entangled pairs are discarded and the protocol is restarted from the beginning. With this approach, the expected number of trials to create one entangled pair is

$$\langle n_\mathrm{N} \rangle = \frac{\langle Z_\mathrm{N} \rangle}{p_\mathrm{es}^{N-1}} \tag{5.24}$$

The other considered strategy takes the opposite approach. Instead of delaying all entanglement swapping attempts until the end, each entanglement swapping step is attempted as soon as the necessary entangled pairs have been generated. If that attempt fails, only the involved pairs are discarded and all other entangled pairs are kept. For $N = 2$, these strategies are obviously equivalent, because there is only one entanglement swapping attempt involved. However, for $N > 2$, the second strategy results in a larger average number of entanglement distribution attempts for each instance of the protocol. However, each instance of that protocol will succeed eventually, thereby reducing the total number of trials to generate an entangled pair. It is difficult to find a closed-form expression for $\langle n_\mathrm{N} \rangle$ in this case, because the entanglement swapping process can fail repeatedly, which leads to an infinite amount of possibilities of how the protocol can succeed. Therefore, a Monte Carlo simulation of the protocol was performed for $N = 4$ and different values of the total distance L with 10^6 runs per calculated point, and $\langle n_4 \rangle$ was determined by extracting the mean number of trials from the generated data (see Fig. 5.8).

To convert $\langle n_\mathrm{N} \rangle$ into the expected duration of the protocol $\langle T_\mathrm{N} \rangle$, it was assumed that the protocol is perform synchronously at every node with a fixed duration for every attempt and the atom is cooled and repumped with a sequence of duration τ after each trial. In that case the expected time until the protocol succeeds over distance $L = NL_0$ is

$$\langle T_\mathrm{N} \rangle = \langle n_\mathrm{N} \rangle \left(\frac{L_0}{c_\mathrm{f}} + \tau \right) \tag{5.25}$$

For a typical propagation speed of light in optical fibers $c_\mathrm{f} = 2 \times 10^5\,\mathrm{km\,s^{-1}}$ and a conservative estimate of $\tau = 100\,\mu\mathrm{s}$ for the time necessary to cool and repump the atom, the possible repetition rate over long distances is limited by the communication time L_0/c_f. For example, with these parameters, the repetition rate at $L_0 = 80\,\mathrm{km}$ is limited to 2 kHz, although the time allocated for cooling and pumping the atom would allow a repetition rate of 10 kHz.

In principle, the protocol does not need to be synchronized at each node and the timings could be dynamically adjusted to minimize the time between attempts. For

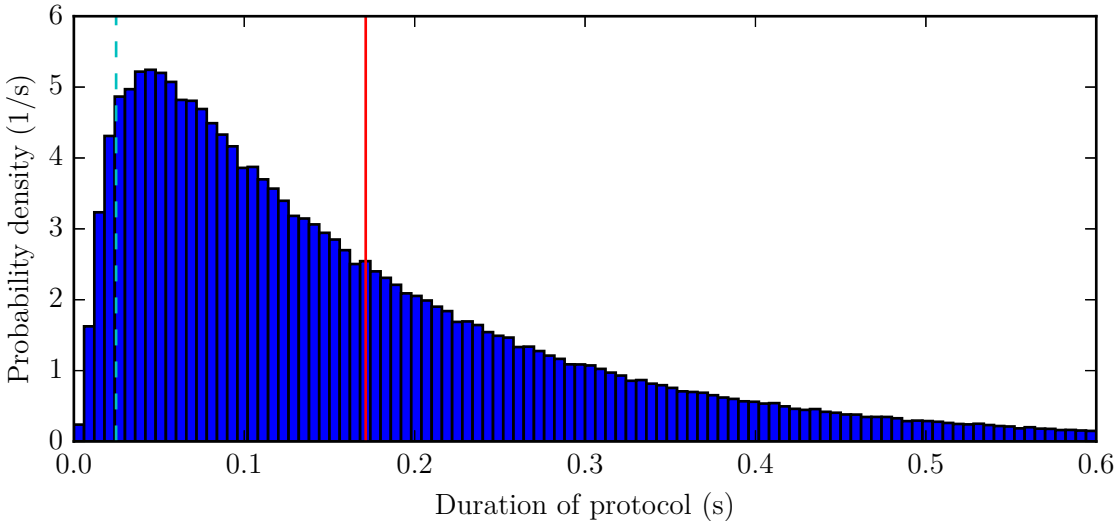

Figure 5.8: Probability density distribution for successfully generating an entangled pair as a function of the protocol duration, for the case of attempting entanglement swapping as soon as possible and keeping uninvolved pairs in case of failure. The distribution was calculated by a Monte Carlo simulations for $N = 4$ and $L = 99\,\mathrm{km}$ using 10^6 simulated runs of the protocol. The red vertical line marks the expectation value. Due to the long tail of the distribution, the expectation value is larger than the median value, with 63 % of the runs having a shorter duration than the expected value. For comparison, the cyan dashed line marks the expected protocol duration for the other entanglement swapping strategy under the same conditions, which results in an entangled pair only in 5.9 % of the cases.

example, the atom could be immediately cooled and repumped if the entanglement generation process did not result in a successful detection of the herald photon, and it would not be necessary to wait for the result of the photonic BSM. However, such dynamical adjustments would need to be communicated to the other node, such that the telecom photons arrive at the same time and interfere at the place of the photonic BSM. Such adjustments would therefore also be limited by the communication time with little potential gain.

The inverse $1/\langle T_\mathrm{N}\rangle$ of the expected duration to generate one entangled pair between the memories at the end nodes was calculated for different total distances L, using the parameters listed in this section. The resulting expected entangled pair rate is shown in Fig. 5.9 for $N = 1$, $N = 2$, and $N = 4$. For the latter, the different strategies of keeping or discarding entangled pairs when entanglement swapping fails are also compared. The calculation for $N = 1$ corresponds to entanglement distribution with only one elementary link and no repeater node between the end nodes. It serves as a reference for the third performance criterion listed in Sec. 5.1.1, which was the comparison of a repeater system with and without repeater nodes. This direct entanglement procedure has reduced overhead compared to repeater protocols and is thus the best-performing protocol if the distance is short. The addition of one repeater node increases that overhead, but improves the scaling as outlined in Sec. 5.1 and breaks even at 41 km total distance. At

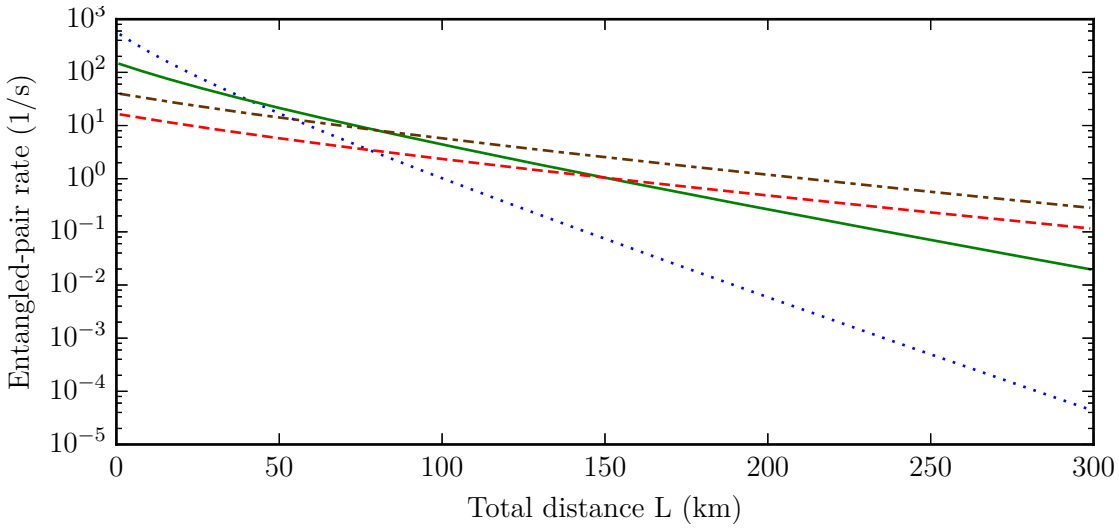

Figure 5.9: Expected rate of entangled pairs at end nodes separated by total distance L. The blue dashed line indicates the situation without repeater, which corresponds to $N = 1$. The green solid line denotes the situation with one repeater node ($N = 2$). The remaining two lines both indicate $N = 4$, with the red dashed line corresponding to restart from the beginning on failure of entanglement swapping and the brown dash-dotted line denoting entanglement swapping as soon as possible and keeping entangled pairs if possible. The protocol with no repeater node has a lower overhead and is therefore the best strategy for short distances. Protocols with more repeater nodes have a higher overhead, but better scaling, such that they are clearly superior over a larger distance. From Ref. [184].

a separation of 100 km, the repeater protocol with one repeater node is clearly superior and generates entangled pairs approximately four times faster than direct entanglement.

Extending the repeater protocol to the next swap level requires three repeater nodes and four elementary links. Such a system would outperform the single-repeater-node system after 150 km and would lead to a performance improvement over the $N = 1$ case of 14 at this distance. If entangled pairs are not all discarded after a failed entanglement swapping attempt, but uninvolved entangled pairs are kept, the entangled-pair rate increases by another factor of approximately 2.4. As a result, the addition of two additional repeater nodes already leads to an improvement after a distance of 82 km if this strategy is chosen.

5.4.2 Required memory time

The analysis of the entangled-pair rate suggests that any repeater implementation could beat direct transmission if the total distance is long enough. However, increasing the distance also increases the time the quantum memories have to store the entangled pairs. Realistic implementations will suffer from decoherence of the stored quantum states, which will limit the maximum duration of the repeater protocol. It is therefore important to consider the expected required storage time, i.e., the interval between the

generation of the first entangled pair that contributes to the final state and the successful completion of the protocol. This time must be compared to the coherence time of the quantum memories to estimate whether the latter is sufficient to enable completion of the protocol without excessive degradation of the stored state. It is assumed that all memories decohere equally and it does not matter whether an entangled pair is stored at its original location or has been transferred to another memory by entanglement swapping.

If the protocol is restarted from the beginning whenever an entanglement swapping attempt fails, the expected required storage can be calculated by employing Eq. (5.3) and the repetition rate. Once the first entangled pair has been generated and is stored in quantum memories suffering from decoherence, $N-1$ entangled pairs still have to be generated in a repeater protocol consisting of N elementary links. This does not account for the case that two entangled pairs are generated in the same attempt, which would be 3×10^{-3} for the parameters considered here and $L = 0$ and exponentially decreases further with increasing distance. This case is therefore neglected. The expected number of cycles $\langle m_{\mathrm{N}} \rangle$ the first entangled pair has to be stored is therefore

$$\langle m_{\mathrm{N}} \rangle = \langle Z_{\mathrm{N}-1} \rangle + 1, \tag{5.26}$$

where the additional cycle accounts for the trial that it takes to generate the first entangled pair itself. Analogous to Eq. (5.25), this number of cycles can be converted into time by multiplying it with the time allocated for one attempt.

The analysis is more complicated if only the pairs involved in a failed entanglement swapping attempt are discarded, because any generated entangled pair might be discarded later on and thus might not have to be stored until the end of the protocol. Therefore, $\langle m_4 \rangle$ was extracted from the Monte Carlo simulations of the repeater protocol that were used to calculate $\langle n_4 \rangle$. For each run, the required storage time was the interval between the simulated generation of the first entangled pair that was never discarded and the end of the protocol. The expectation value was calculated as the average over 10^6 runs. A bootstrap [209] was performed on the calculated values to estimate the 95 % confidence interval to be smaller than ± 0.2 %.

The results for $N = 2$ and $N = 4$ with both entanglement-swapping strategies are shown in Fig. 5.10. The single repeater node requires a storage time of 59 ms (980 ms) for a total distance of 100 km (200 km). Increasing the number of repeater nodes increases the overhead, such that a larger storage time is required for short distances, but improves the scaling for longer distances. Three repeater nodes decrease the required storage time at the two distances mentioned above to 53 ms and 260 ms if uninvolved entangled pairs are kept in case of a failed entanglement swapping attempt. A further decrease is possible by discarding all pairs in case of a failed entanglement swapping attempt, which limits the duration of the protocol and cuts the required storage time by a factor of 2.4 for the considered parameters, resulting in 22 ms and 110 ms for 100 km and 200 km, respectively.

The two strategies when to perform entanglement swapping are not the only possibilities how entangled-pair rate can be traded against required storage time. For example, a limit to the number of attempted entanglement swapping attempts could be imposed to cut the long tail of the distribution (compare Fig. 5.8). As an alternative, a time limit could be set at which the protocol terminates if it has not been successful yet.

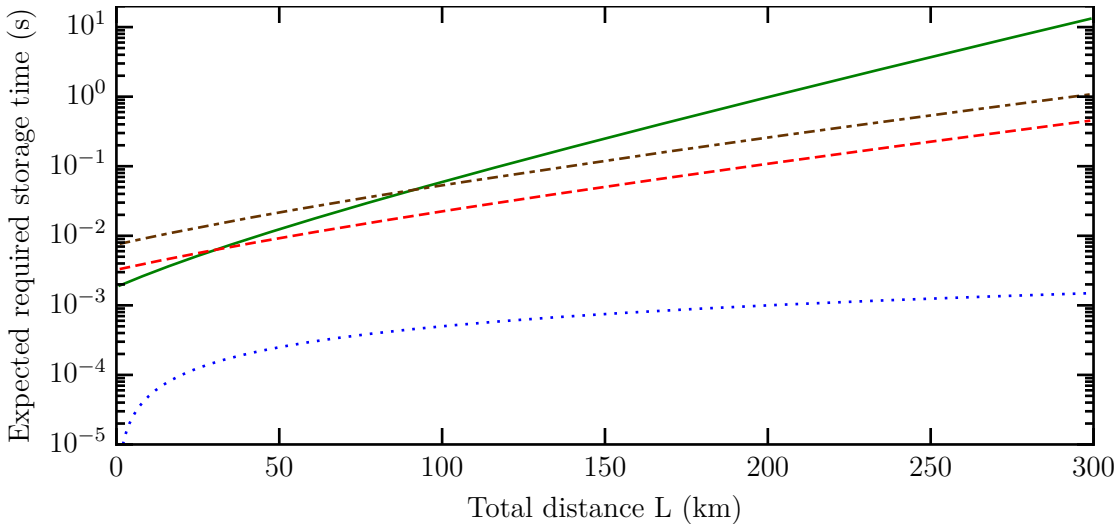

Figure 5.10: Expected required time an entangled pair needs to be stored in quantum memories for the repeater protocols to succeed. The coherence time of the atoms used as memories should be much larger than this value for a given distance L to prevent severe degradation of the final state. The line styles corresponding to different repeater protocols are the same as in Fig. 5.9. Similar to the entangled pair rate, increasing the number of repeater nodes improves the scaling, but comes at the cost of larger overhead. Without repeater nodes, the entanglement only has to be stored for the time it takes to communicate between the end nodes. Adapted from Ref. [184].

With these strategies, the repeater could be optimized to extract the highest possible entangled pair rate out of a system with limited coherence.

The values for the storage time given here are the expected times the quantum states need to be stored and provide a timescale on which decoherence should be minimal. Therefore, the coherence time of the atom has to be much longer than that to minimize the effect of decoherence on the fidelity of the final state. If this is not the case, a specific error model for the decoherence of the system would be needed to quantify the influence of the storage time on the fidelity. For the suggested states in ^{87}Rb, coherence times of several seconds have been demonstrated in magnetic traps [38, 39]. It should therefore be possible to reach the required storage time for the quantum repeater protocols and the parameters discussed here with a setup optimized for high coherence.

5.4.3 Secret-key rate

In order to asses the suitability of an imperfect repeater protocol for device-independent quantum key distribution, it is necessary to convert the entangled-pair rate into a secret-key rate by calculating the secret fraction. This also allow for a combined analysis of efficiency and fidelity of the protocol for this particular application. In absence of experimental data, this requires the creation of an error model that details which errors the implementation of the protocol could introduce. As detailed in Sec. 5.2.4, the heralded entanglement generation process between an atom and a telecom photon does

not result in perfectly indistinguishable photons. It is therefore necessary to consider the implications of a contrast C below unity in the photonic BSM for the repeater protocol. If the photons are distinguishable, they do not interfere and the resulting state is a mixed state. However, classical correlations remain, such that the created state is not fully random. For example, if the input states are perfect and the result of the photonic BSM would indicate the state $|\Psi^+\rangle = (|10\rangle + |01\rangle)/\sqrt{2}$, the density matrix for the resulting mixed state for $C < 1$ after entanglement distribution is

$$\rho_{\mathrm{ed}} = C\,|\Psi^+\rangle\langle\Psi^+| + \frac{1}{2}(1-C)\,(|10\rangle\langle 10| + |01\rangle\langle 01|)\,. \tag{5.27}$$

A second important error source might be the two-atom gate used for entanglement swapping. To analyze the influence that potential errors introduced by the gate can have on the protocol, a generic error model is assumed. In this model, the gate with operator $\mathcal{G}_{\mathrm{k,l}}$ between qubits k and l has a probability P to perfectly execute[3] and result in the density matrix $\mathcal{G}_{\mathrm{k,l}}\rho_{\mathrm{i}}\mathcal{G}_{\mathrm{k,l}}^{\dagger}$ for an initial density matrix ρ_{i}. If the gate fails, the state of the involved qubits is completely random with density matrix $\rho_{\mathrm{k,l}}^{\mathrm{m}} = \mathbb{1}/4$. In either case, all other qubits are not affected by the gate at all. Under these assumptions, the density matrix for the mixed state after application of the gate is

$$\rho_{\mathrm{g}} = P\mathcal{G}_{\mathrm{k,l}}\rho_{\mathrm{i}}\mathcal{G}_{\mathrm{k,l}}^{\dagger} + (1-P)\rho_{\mathrm{k,l}}^{\mathrm{m}} \otimes \mathrm{Tr}_{\mathrm{k,l}}\rho_{\mathrm{i}}, \tag{5.28}$$

where $\mathrm{Tr}_{\mathrm{k,l}}$ denotes the partial trace over qubits k and l. The fidelity of this state with the ideal state is $F = (1+3P)/4$. This error model could be refined to account for specific errors encountered in the experiment, and other errors, like decoherence of the quantum memories, errors occurring during single-qubit gates, or degradation of the photonic qubit during transmission, could be modeled in the same manner. To limit the parameter space, only the two error sources listed above with parameters C and P will be considered in the following, representative for errors that occur during entanglement distribution and entanglement swapping.

The tensor product of two instances of ρ_{ed} yields the two-pair state after entanglement distribution. The gate error model of Eq. (5.28) is applied to this state and the other operations required to complete entanglement swapping are assumed to be implemented perfectly. The resulting density matrix after entanglement swapping is

$$\begin{aligned}\rho_{\mathrm{es}} = PC^2\,|\Psi^+\rangle\langle\Psi^+| + \frac{1}{4}(1-P)\mathbb{1} \\ + \left(PC(1-C) + \frac{1}{2}(1-C)^2P\right)(|10\rangle\langle 10| + |01\rangle\langle 01|)\end{aligned} \tag{5.29}$$

This state can be rewritten in the Bell basis by applying the identity $|10\rangle\langle 10| + |01\rangle\langle 01| = |\Psi^+\rangle\langle\Psi^+| + |\Psi^-\rangle\langle\Psi^-|$, which results in

$$\rho_{\mathrm{es}} = \lambda_1\,|\Psi^+\rangle\langle\Psi^+| + \lambda_2\,|\Psi^-\rangle\langle\Psi^-| + \lambda_3\,|\Phi^+\rangle\langle\Phi^+| + \lambda_4\,|\Phi^-\rangle\langle\Phi^-| \tag{5.30}$$

[3] The calculation here is only concerned with undetectable errors, which will impact the final state. All errors that can be detected affect only the efficiency and it is assumed that the state has been renormalized after all events with a detected error have been discarded.

with

$$\begin{aligned} \lambda_1 &= \frac{1}{4}\left(1+P+2PC^2\right) & \lambda_3 &= \frac{1}{4}(1-P) \\ \lambda_2 &= \frac{1}{4}\left(1+P-2PC^2\right) & \lambda_4 &= \frac{1}{4}(1-P). \end{aligned} \tag{5.31}$$

With these equations, the secret fraction for entanglement-based quantum key distribution can be calculated by following Ref. [167]. The resulting error rate ϵ_{x},ϵ_{y},ϵ_{z} for the three bases are

$$\epsilon_{\mathrm{x}} = \lambda_2 + \lambda_4 = \frac{1}{2}\left(1-PC^2\right), \tag{5.32a}$$

$$\epsilon_{\mathrm{y}} = \lambda_2 + \lambda_3 = \frac{1}{2}\left(1-PC^2\right), \tag{5.32b}$$

$$\epsilon_{\mathrm{z}} = \lambda_3 + \lambda_4 = \frac{1}{2}\left(1-P\right). \tag{5.32c}$$

Because the error rate is lower in the z-basis, it is an advantage to generate the key in this basis, such that the quantum bit error rate $Q = \epsilon_{\mathrm{z}}$, and results in other bases are only used to estimate the error rates. In this case, the unconditional fraction in the limit of infinitely long keys is

$$r = 1 - h(Q) - \epsilon_{\mathrm{z}} h\left(\frac{1+\left(\epsilon_{\mathrm{x}}-\epsilon_{\mathrm{y}}\right)/\epsilon_{\mathrm{z}}}{2}\right) - \left(1-\epsilon_{\mathrm{z}}\right) h\left(\frac{1-\left(\epsilon_{\mathrm{x}}+\epsilon_{\mathrm{y}}+\epsilon_{\mathrm{z}}\right)/2}{1-\epsilon_{\mathrm{z}}}\right), \tag{5.33}$$

with the binary entropy $h(p) = -p\log_2(p) - (1-p)\log_2(1-p)$.

The calculation can be extended to $N = 4$ by building the tensor product of two instances of ρ_{es} (Eq. (5.29)) and applying another imperfect entanglement swapping procedure to it. The resulting error rates are

$$\epsilon_{\mathrm{x}}^{(N=4)} = \frac{1}{2}\left(1-P^3C^4\right), \tag{5.34a}$$

$$\epsilon_{\mathrm{y}}^{(N=4)} = \frac{1}{2}\left(1-P^3C^4\right), \tag{5.34b}$$

$$\epsilon_{\mathrm{z}}^{(N=4)} = \frac{1}{2}\left(1-P^3\right) = Q^{(N=4)}. \tag{5.34c}$$

The secret fraction as a function of the interference contrast and the fidelity a perfect input state would have after being subject to the atom-atom gate used for entanglement swapping is shown in Fig. 5.11. If the interference contrast and the gate fidelity are both perfect, the secret fraction is unity, i.e., from one entangled pair, one secret bit can be extracted. If these values decrease, the secret fraction very quickly drops. For an interference contrast of $C = 0.97$ and $N = 2$, the fidelity of a perfect input state needs to be $F = 95\,\%$ ($F = 89\,\%$) to retain a secret fraction of $r = 0.5$ ($r = 0.25$) and if $F < 83\,\%$ no unconditionally secure key can be extracted at all. An extension to $N = 4$ raises the requirements for the interference contrast and the gate fidelity. For the same interference contrast, $F = 99\,\%$ ($F = 97\,\%$) is necessary for a secret fraction of $r = 0.5$ ($r = 0.25$) and the minimum fidelity for a nonzero secret fraction is $F = 95\,\%$.

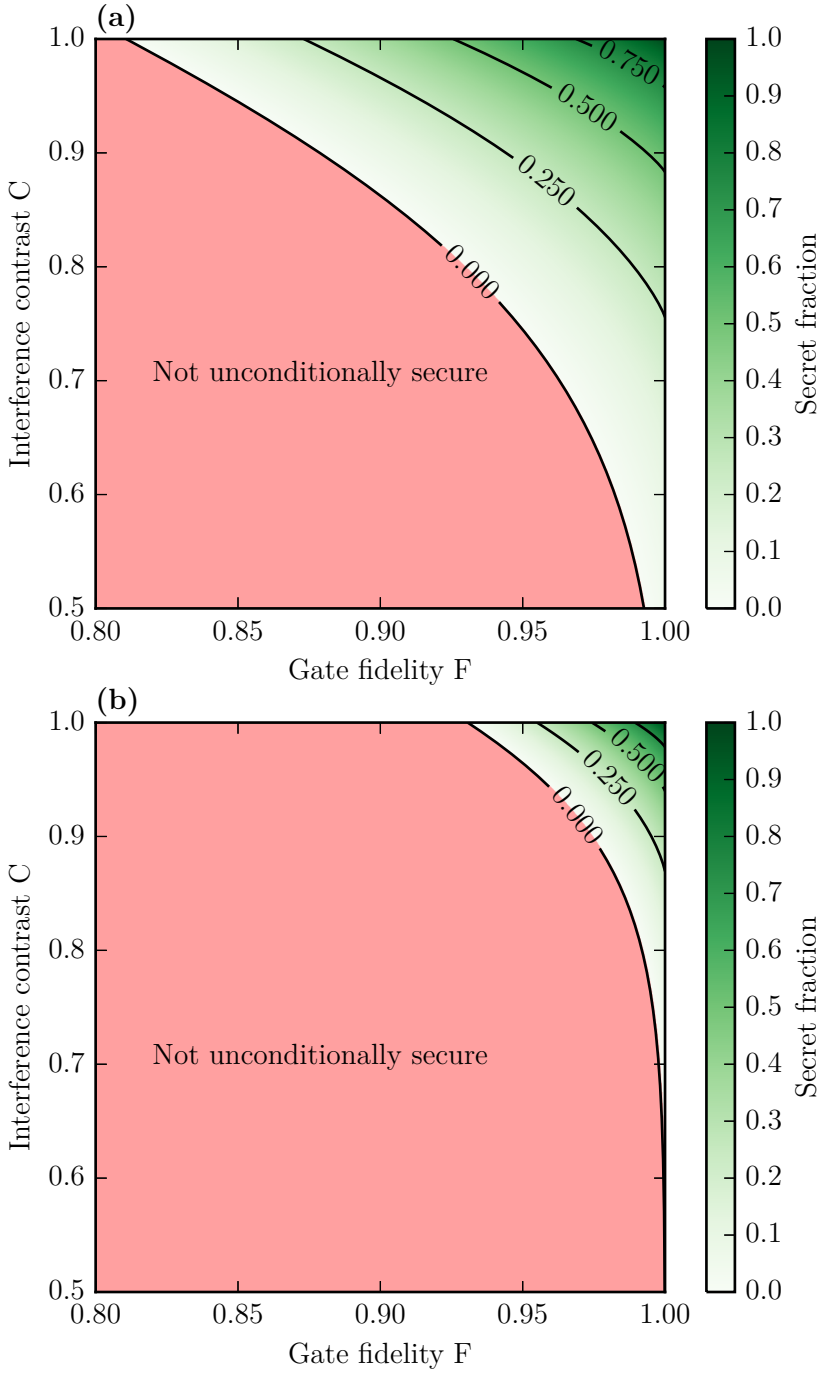

Figure 5.11: Secret fraction as a function of the interference contrast and the fidelity of a perfect input state after the application of the entanglement-swapping gate for a repeater protocol with (a) $N = 2$ and (b) $N = 4$. In both cases, a considerable secret fraction can only be achieved if the gate fidelity and the interference contrast are both high, with the requirements increasing for more repeater nodes. If one of the errors is too big, no unconditionally secure key can be extracted at all (area shaded red).

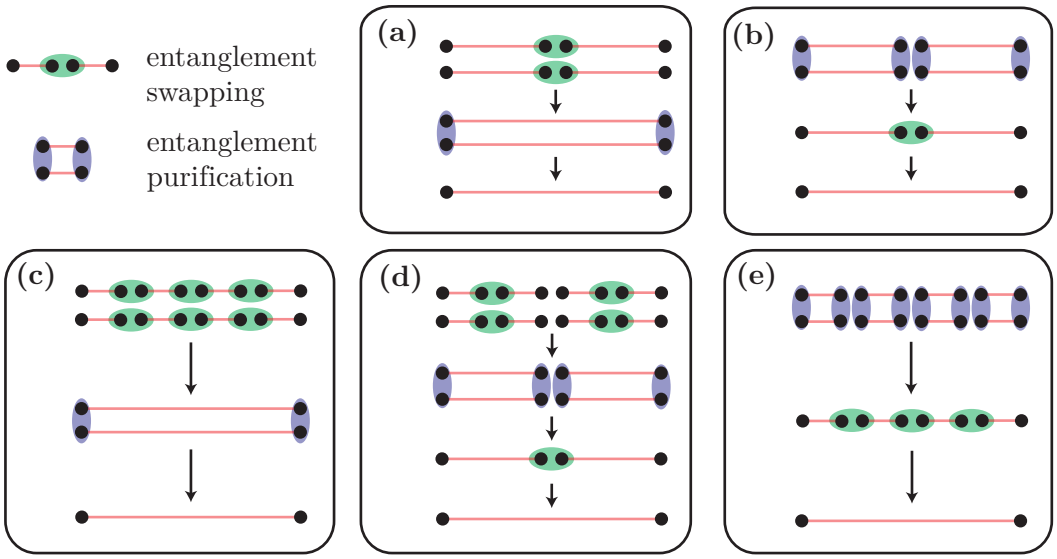

Figure 5.12: Different protocols of entanglement swapping and one round of entanglement purification for $N = 2$ (a,b) and $N = 4$ (c–e) . One can either perform entanglement swapping first and then purify the final state (left, (a) and (c)) or purify first at each node and then swap (right, (b) and (e)). For $N > 2$ other combinations between these two extreme choices can be found. The colored ellipses indicate the atom-atom gates that need to be performed. Starting with entanglement purification generally increases the number of required gates.

5.4.4 Entanglement purification

Errors occurring during operations of a quantum repeater protocol accumulate and reduce the overlap of the target state with the state that is actually produced. Increasing the number of repeater nodes also increases the number of operations that have to be performed, such that the probability to get the desired final state decreases exponentially with the number of nodes. To cover very long distances, it is therefore essential for a quantum repeater to correct the accumulated errors by entanglement purification [20]. Entanglement purifcation protocols take multiple input states that are not maximally entangled to generate one state with increased entanglement.

An implementation of the protocol proposed by Deutsch et al. [160] requires atom-atom gates, single-qubit rotations, and state detection, all of which is possible with the quantum repeater node proposed in this chapter. Although the gate proposed in Sec. 5.3 can only mediate interactions between atoms in the same cavity, there is a variant that can perform gates between atoms in remote cavities by reflecting a single photon subsequently from both cavities [43]. With this remote gate, any number of entanglement purification rounds could be performed by providing multiple copies of each repeater node and performing remote gates between those.

However, the entanglement purification protocol itself might introduce errors, possibly so severe that there is no gain in entanglement purification. To quantify the effect of entanglement purification, the error models described in Sec. 5.4.3 are assumed. As the

atom-atom gates for entanglement swapping and entanglement purification share the same physical mechanism, they are likely suffering from the same error sources in an experimental implementation. It is therefore assumed that all atom-atom gates have the same error probability P. There are different possibilities how to order entanglement swapping and entanglement purification in a repeater protocol (see Fig. 5.12). In one extreme case, multiple entangled pairs are generated at the end nodes without entanglement purification, which is then only performed at the end of the protocol. The opposite case is to perform entanglement purification directly after entanglement swapping and then swap the purified entangled pairs to generate one entangled pair at the end nodes.

The protocol variants for one round of entanglement purification and $N = 2$ and $N = 4$ were analyzed by assuming imperfect entanglement distribution with interference contrast C and calculating the final density matrix ρ_f and the fidelity $F = \langle\Psi^+|\rho_\mathrm{f}|\Psi^+\rangle$ with the desired $|\Psi^+\rangle$ state after the protocol has been performed with imperfect gates that fail with probability $1 - P$. For $N = 2$ these fidelities are

$$F_0^{(N=2)} = \frac{1 + P(1 + 2C^2)}{4} \tag{5.35a}$$

$$F_\mathrm{a} = \frac{1 + P^4 + 2C^4P^4 + 2C^2P^3(1 + P)}{4 + 4C^4P^4} \tag{5.35b}$$

$$F_\mathrm{b} = \frac{1 + P^5 + C^4P^4(1 + P) + 2C^2(P^2 + 5P^5)}{4(1 + C^2P^2)^2}, \tag{5.35c}$$

for the protocol without purification and those depicted in Fig. 5.12a,b. The fidelities for $N = 4$ and the variants shown in Fig. 5.12c–e are

$$F_0^{(N=4)} = \frac{1 + P^3(1 + 2C^4)}{4} \tag{5.36a}$$

$$F_\mathrm{c} = \frac{1 + P^8 + 2C^8P^8 + 2C^4P^5(1 + P^3)}{4 + 4C^8P^8} \tag{5.36b}$$

$$F_\mathrm{d} = \frac{1 + P^9 + C^8P^8(1 + P) + 2C^4P^4(1 + 2P^3 + 3P^5)}{4(1 + C^4P^4)^2} \tag{5.36c}$$

$$\begin{aligned} F_\mathrm{e} = {} & \frac{1}{4(1 + C^2P^2)^4}\left[1 + P^{11} + C^8P^8(1 + P^3) + 4C^2(P^2 + P^{11})\right. \\ & \left. + 4C^6(P^6 + P^{11}) + C^4(6P^4 + 38P^{11})\right] \end{aligned} \tag{5.36d}$$

The fidelity difference between F_0 and F_a, F_b, F_c, and F_e as a function of the gate fidelity $F = (1 + 3P)/4$ and interference contrast C is shown in Fig. 5.12. For high interference contrast, it is best to purify at the end of the protocol. That strategy minimizes the number of necessary atom-atom gates and is thus least sensitive to gate errors. As discussed in Sec. 5.2.4, an interference contrast of $C = 0.97$ could be reached. In this case, the gate fidelity would need to be more than $F > 97\,\%$ for $N = 2$ and $F > 95\,\%$ for $N = 4$ in order to obtain any gain from entanglement purification. If the interference contrast is considerably below unity, entanglement purification as early in the protocol as possible is the strategy that is most beneficial [210]. In combination with low gate errors, this is also the situation where entanglement purification would lead to the largest improvements in fidelity. In any case, the fidelity of the gates needs to be

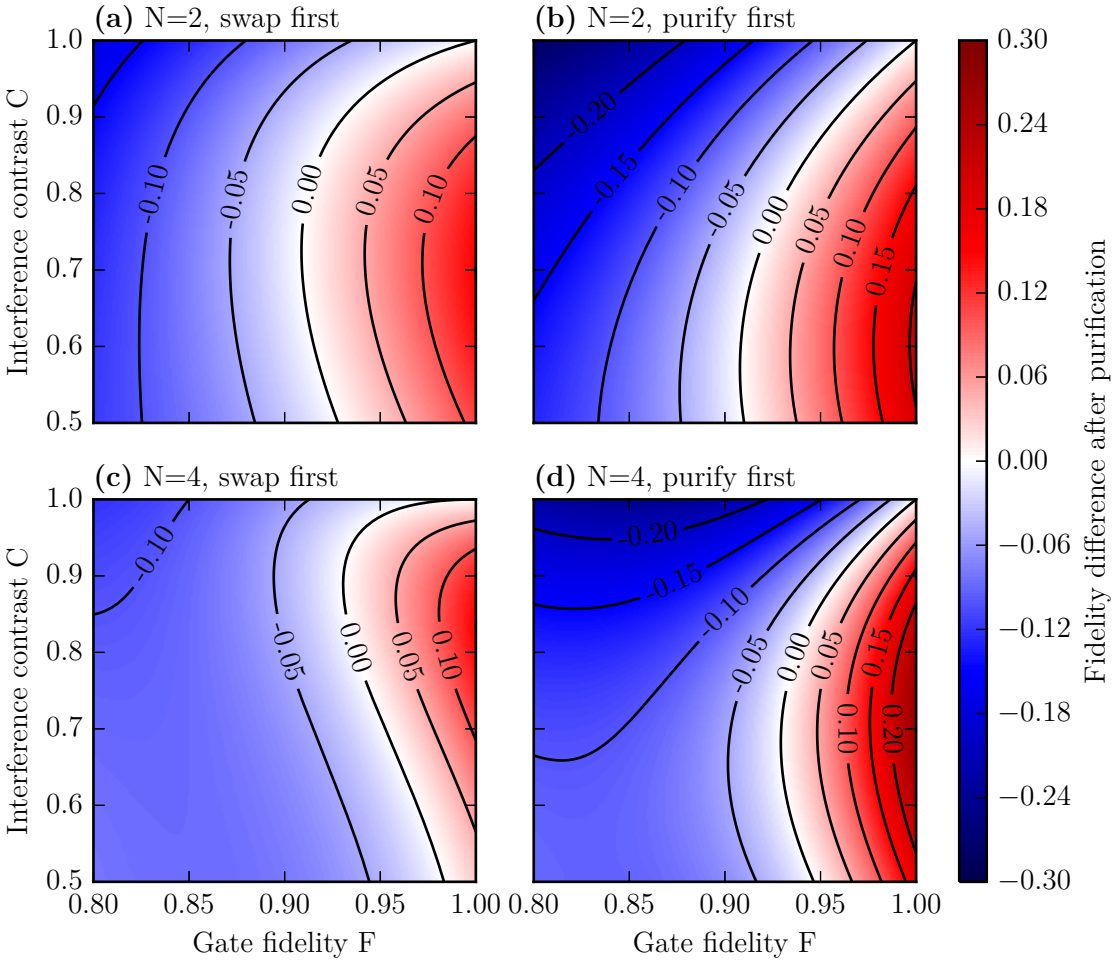

Figure 5.13: Difference in fidelity of the final entangled state with and without purification. Red shading indicates an increase in fidelity after purification, and blue shadings denotes a net loss in fidelity due to errors introduced during purification. (a) and (b) show the different protocols for $N = 2$ (cf. Fig. 5.12a and Fig. 5.12b, respectively), and (c) and (d) show the extreme cases for $N = 4$ (cf. Fig. 5.12c and cf. Fig. 5.12e, respectively). If the interference contrast is near unity, it is better to perform entanglement swapping first, because less atom-atom gates need to be performed (see Fig. 5.12). But if the contrast is bad, it is better to purify first and then swap. Entanglement purification has the most benefit for intermediate contrast and near-perfect gates.

quite high for any gain to be possible at all. For $N = 2$ that threshold is at $F > 91\,\%$ and for $N = 4$ it is at $F < 93\,\%$.

If the atom-atom gates were executed perfectly, any target fidelity could in principle be reached with multiple rounds of entanglement purification. However, this comes at a cost of efficiency, for several reasons. First, entanglement purification requires at least two entangled pairs to generate one pair, such that the final number of entangled pairs is cut at least in half. Second, entanglement purification requires its input pairs to exist concurrently, such that once one entangled pair is generated, it needs to be stored until the other pairs are also ready. This reduces the rate compared to concurrent independent generation of several pairs. Finally, the purification process does not succeed with unity efficiency, but fails with a probability that depends on the fidelity of the input states.

In the context of quantum key distribution this tradeoff between fidelity and efficiency can be quantified with the secret-key rates (see Sec. 5.4.3). These are compared for the different protocols in Fig. 5.14. It is evident that if the interference contrast and thus the fidelity of the input states is high enough, the potential improvements in fidelity are not sufficient to offset the loss in efficiency. This is the case if $C \geq 0.55$ for $N = 2$ and $C \geq 0.83$ for $N = 4$. The greatest factor in the secret-key rate can be gained if the interference contrast is quite bad, such that the resulting entangled state without purification does not meet the threshold required to extract an unconditionally secure key, resulting in a secret-key rate of zero. A purified state exceeding that threshold would result in a nonzero secret-key rate and could therefore be required to generate a secret key at all. However, the secret-key rate would be quite low in this case, which could only be improved with higher-fidelity input states, which would then not benefit as greatly from entanglement purification. This suggests that the best strategy is to prioritize enhancements of the fidelities of all substeps of the repeater protocol and only turn to entanglement purification if there is no other way to meet a required threshold fidelity [170]. Considering that the entanglement distribution process proposed here should be able to reach an interference contrast of $C = 0.97$ and the atom-atom gates will not work without errors, the repeater implementation with few nodes proposed here is unlikely to benefit from entanglement purification.

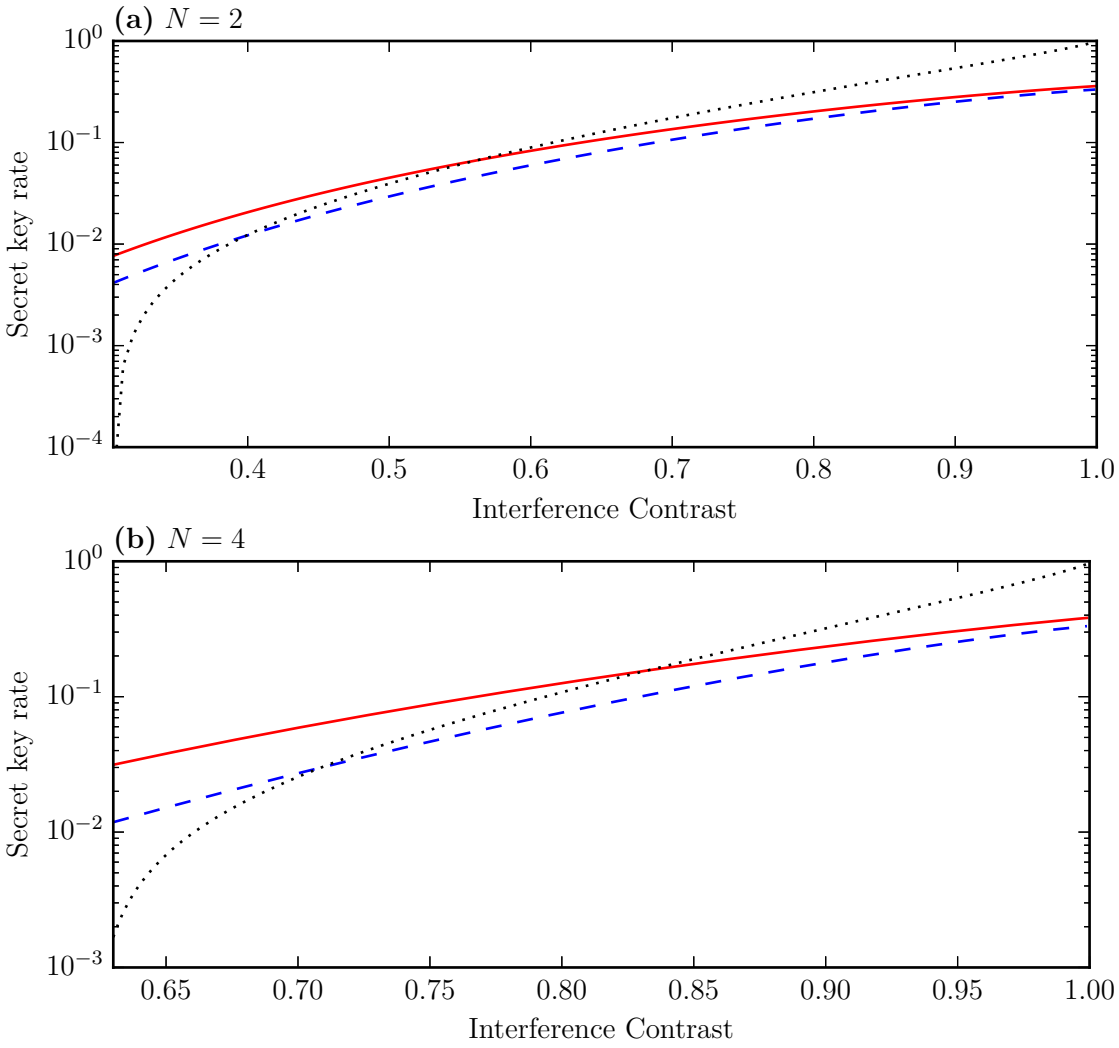

Figure 5.14: Secret-key rate of various purification protocols for perfect atom-atom gates and (a) $N = 2$ and (b) $N = 4$. The rates have been normalized to the secret-key rate of a repeater protocol with fidelity unity and without purification. The black dotted lines show the rates without purification as a function of the interference contrast. In comparison, the blue dashed lines show the protocols with entanglement purification last (see Fig. 5.12a,c) and the red solid lines show the protocols with entanglement purification first (see Fig. 5.12b,e). Although all rates increase with better interference contrast, the benefit of entanglement purification is reduced and turns into a loss if the interference contrast is high enough.

6 Summary and outlook

During the project that is the subject of this thesis, fiber cavities suitable for quantum communication experiments with single atoms have been developed. End facets of optical fibers were shaped with a CO_2 laser, resulting in near-spherical surfaces with microroughness below 0.2 nm RMS. After the application of a highly reflective coating, these surfaces had ultra-low parasitic losses, such that cavities consisting of two fiber mirrors showed a finesse of up to 1.9×10^5, which is the highest finesse for a fiber cavity reported so far. The parameters chosen for the CO_2 laser machining allowed the fabrication of structures approaching the diameter of the fiber, which allowed the construction of high-finesse fiber cavities with a length of up to 180 µm, limited by the radius of curvature of the mirrors. This allows for more than enough optical access to an atom trapped at the center of such a cavity in future experiments and opens up the possibility of a crossed-cavity geometry. The dominant source of the frequency splitting of polarization eigenmodes has been understood to originate from the geometry of the cavity mirrors and the derived analytical model has been experimentally confirmed. The gained knowledge can be used in the construction of future cavities, such that the polarization eigenmodes are either degenerate or have a large frequency splitting.

Although the developed fiber cavities are already at a stage, where they could be successfully used in quantum communication experiments with single atoms, there is still potential for further improvements. An issue during the fabrication of the fiber mirrors was the shot-to-shot reproducibility. Increasing it would allow for better targeting and fine-tuning of the mirror geometry. The most promising approaches would be better stabilization of the CO_2 laser power in pulsed operation and improved preparation of the fiber end facets, for example by polishing them to a flat surface with a defined angle before the fabrication process. A more reproducible process would also aid the derivation of a quantitative model that could be used to guide future fabrication efforts. The observed difference in the behavior of single-mode and multi-mode fibers when subjected to a CO_2 laser pulse points to an influence of the fiber core on the shape of the surface. Exploring different dopants and dopant concentrations might be a path to get single-mode fibers with a shape even closer to spherical, such that losses in long cavities due to imperfect surfaces are minimized. The losses could also be reduced by a coating of better quality. The measurements of the quality of mirrors applied on reference substrate suggested that 6 ppm losses are caused by the coating itself, compared to 1 ppm that have been achieved previously [92]. As there is no apparent reason why reaching these lower losses might not be possible with fiber cavities, work together with commercial coating companies might be able to reduce the intrinsic losses. For experiments at telecom wavelengths, the coatings would also need to be tested at these wavelength. Although there is no indication that the coatings should perform worse at these wavelengths, a confirmation is necessary. Directly coupling the cavity mode to a single-mode fiber is a simple way to integrate these devices into a fiber-optic network, but the efficiency is intrinsically limited by the wave-front curvature of the cavity mode. This limitation could be overcome

by combining single-mode fibers with micro-optic components to provide perfect mode matching, e.g., with a piece of graded-index fiber of defined length functioning as lens [211]. Finally, the full potential of the control over the frequency splitting of polarization eigenmodes can only be realized if both spherical and cylindric structures can be realized while maintaining the quality of the resulting surfaces. Reproducibly achieving extreme values of the mirror eccentricity could be a subject of further investigation.

A potential application of the developed cavity technology is the construction of a quantum repeater node that can enhance entanglement generation between distant nodes. The scheme presented in this thesis enables entanglement generation with alkali atoms directly at telecom wavelength, eliminating the need for wavelength conversion. The produced telecom photons are expected to be highly indistinguishable, which should allow for high-fidelity entanglement distribution with a photonic Bell-state measurement. Two entangling cavities at telecom wavelength could be placed into one herald cavity due to the small outer dimensions of fiber cavities. This geometry would allow to perform atom-atom gates mediated by photons reflected off the herald cavity. These gates could be used to implement efficient entanglement swapping and even entanglement purification, all functionally integrated into one repeater node. Numerical simulations based on the parameters that were achieved in the fiber-mirror fabrication show the possibility for the repeater node to outperform direct entanglement generation without further developments in cavity technology.

Toward this goal of a quantum repeater, there are a few intermediate steps that are yet to be taken. On the technical side, an experimental platform needs to be developed that can load, cool, and control single atoms at the crossing points of multiple cavity nodes. This platform must be reliable enough, such that multiple instance can run concurrently in the multi-node network that is required to demonstrate the full repeater scheme. The first step toward this goal is an experiment with a single atom coupled to two crossed cavity modes. This would not only serve as a technology demonstration, but the ability to independently tune two cavity modes strongly coupled to an atom would open up a new range of experiments. These experiments include, for example, the generation of two-mode squeezed states [212] or cross phase modulation of two photons due to giant Kerr nonlinearities in four-level electromagnetically induced transparency [213, 214].

There are also steps toward a quantum repeater that could be addressed in existing single-atom–cavity experiments. The quantum repeater concept relies on the ability to store quantum states long enough for the protocol to complete. The necessary coherence for the suggested states has been shown in small atomic ensembles in magnetic traps [38, 39]. However, it has not yet been demonstrated for a single atom trapped in a cavity and needs to be investigated to determine and reduce the limiting decoherence mechanisms, which could then be used to derive an error model for the decoherence during the storage of entangled pairs. Another aspect of the proposed repeater scheme that needs to be explored is the atom-atom gate mediated by the reflection of a single photon. The phase-shift mechanism required for this gate has already been demonstrated to be suitable for atom-photon gates [36]. Combined with the emerging ability to perform experiments with two atoms coupled to one cavity mode in a controlled manner [215–217], a reflection-based atom-atom gate could soon be demonstrated. An investigation of the main sources of error in such an experiment could be used to refine the generic error model that was used in the derivation of fidelity and secret-key rate for the proposed protocol.

The demonstration of an elementary quantum network with single atoms in optical cavities [50] has shown the great potential of these system for quantum communication. This potential could be amplified by the new capabilities offered by the small size and large coupling strength that fiber cavities can provide. The possibility to directly couple single atoms to telecom-wavelength photons could be used to extend the distance between end nodes for distributing heralded entanglement by more than an order of magnitude. This range for quantum communication could be increased further with quantum repeaters. Further development of these systems could one day realize the dream of a global infrastructure for quantum communication [218].

Bibliography

[1] A. Einstein, B. Podolsky, and N. Rosen. Can Quantum-Mechanical Description of Physical Reality Be Considered Complete? *Phys. Rev.* **47**, 777 (1935).

[2] N. Bohr. Can Quantum-Mechanical Description of Physical Reality be Considered Complete? *Phys. Rev.* **48**, 696 (1935).

[3] E. Schrödinger and M. Born. Discussion of Probability Relations between Separated Systems. *Math. Proc. Cambridge Philos. Soc.* **31**, 555 (1935).

[4] J. S. Bell. On the Einstein-Podolsky-Rosen Paradox. *Physics (College Park)* **1**, 195 (1964).

[5] S. J. Freedman and J. F. Clauser. Experimental Test of Local Hidden-Variable Theories. *Phys. Rev. Lett.* **28**, 938 (1972).

[6] A. Aspect, J. Dalibard, and G. Roger. Experimental Test of Bell's Inequalities Using Time- Varying Analyzers. *Phys. Rev. Lett.* **49**, 1804 (1982).

[7] M. A. Rowe, D. Kielpinski, V. Meyer, C. A. Sackett, W. M. Itano, C. Monroe, and D. J. Wineland. Experimental violation of a Bell's inequality with efficient detection. *Nature* **409**, 791 (2001).

[8] B. Hensen et al. Loophole-free Bell inequality violation using electron spins separated by 1.3 kilometres. *Nature* **526**, 682 (2015).

[9] L. K. Shalm et al. Strong Loophole-Free Test of Local Realism. *Phys. Rev. Lett.* **115**, 250402 (2015).

[10] M. Giustina et al. Significant-Loophole-Free Test of Bell's Theorem with Entangled Photons. *Phys. Rev. Lett.* **115**, 250401 (2015).

[11] C. H. Bennett and G. Brassard. Quantum cryptography: Public key distribution and coin tossing. *Proc. IEEE Int. Conf. Comput. Syst. Signal Process.* 175 (1984).

[12] A. Ekert. Quantum cryptography based on Bell's theorem. *Phys. Rev. Lett.* **67**, 661 (1991).

[13] A. Acín, N. Gisin, and L. Masanes. From Bell's Theorem to Secure Quantum Key Distribution. *Phys. Rev. Lett.* **97**, 120405 (2006).

[14] U. Vazirani and T. Vidick. Fully Device-Independent Quantum Key Distribution. *Phys. Rev. Lett.* **113**, 140501 (2014).

[15] C. H. Bennett, G. Brassard, C. Crépeau, R. Jozsa, A. Peres, and W. K. Wootters. Teleporting an unknown quantum state via dual classical and Einstein-Podolsky-Rosen channels. *Phys. Rev. Lett.* **70**, 1895 (1993).

[16] J. I. Cirac, A. K. Ekert, S. F. Huelga, and C. Macchiavello. Distributed quantum computation over noisy channels. *Phys. Rev. A* **59**, 4249 (1999).

[17] C. Monroe, R. Raussendorf, A. Ruthven, K. R. Brown, P. Maunz, L.-M. Duan, and J. Kim. Large-scale modular quantum-computer architecture with atomic memory and photonic interconnects. *Phys. Rev. A* **89**, 022317 (2014).

[18] T. Inagaki, N. Matsuda, O. Tadanaga, M. Asobe, and H. Takesue. Entanglement distribution over 300 km of fiber. *Opt. Express* **21**, 23241 (2013).

[19] J. G. Rarity, P. R. Tapster, P. M. Gorman, and P. Knight. Ground to satellite secure key exchange using quantum cryptography. *New J. Phys.* **4**, 82 (2002).

[20] H.-J. Briegel, W. Dür, J. Cirac, and P. Zoller. Quantum Repeaters: The Role of Imperfect Local Operations in Quantum Communication. *Phys. Rev. Lett.* **81**, 5932 (1998).

[21] A. Kuzmich, W. P. Bowen, A. D. Boozer, A. Boca, C. W. Chou, L.-M. Duan, and H. J. Kimble. Generation of nonclassical photon pairs for scalable quantum communication with atomic ensembles. *Nature* **423**, 731 (2003).

[22] B. Julsgaard, J. Sherson, J. I. Cirac, J. Fiurášek, and E. S. Polzik. Experimental demonstration of quantum memory for light. *Nature* **432**, 482 (2004).

[23] J. Simon, H. Tanji, J. K. Thompson, and V. Vuletić. Interfacing collective atomic excitations and single photons. *Phys. Rev. Lett.* **98**, 183601 (2007).

[24] G. Hétet, J. J. Longdell, A. L. Alexander, P. K. Lam, and M. J. Sellars. Electro-optic quantum memory for light using two-level atoms. *Phys. Rev. Lett.* **100**, 023601 (2008).

[25] H. de Riedmatten, M. Afzelius, M. U. Staudt, C. Simon, and N. Gisin. A solid-state light-matter interface at the single-photon level. *Nature* **456**, 773 (2008).

[26] K. Hennessy, A. Badolato, M. Winger, D. Gerace, M. Atatüre, S. Gulde, S. Fält, E. L. Hu, and A. Imamoğlu. Quantum nature of a strongly coupled single quantum dot-cavity system. *Nature* **445**, 896 (2007).

[27] A. Faraon, P. E. Barclay, C. Santori, K.-M. C. Fu, and R. G. Beausoleil. Resonant enhancement of the zero-phonon emission from a colour centre in a diamond cavity. *Nat. Photonics* **5**, 301 (2011).

[28] M. Munsch, N. S. Malik, E. Dupuy, A. Delga, J. Bleuse, J.-M. Gérard, J. Claudon, N. Gregersen, and J. Mørk. Dielectric GaAs antenna ensuring an efficient broadband coupling between an InAs quantum dot and a Gaussian optical beam. *Phys. Rev. Lett.* **110**, 177402 (2013).

[29] A. Kuhn, M. Hennrich, and G. Rempe. Deterministic single-photon source for distributed quantum networking. *Phys. Rev. Lett.* **89**, 067901 (2002).

[30] M. Keller, B. Lange, K. Hayasaka, W. Lange, and H. Walther. Continuous generation of single photons with controlled waveform in an ion-trap cavity system. *Nature* **431**, 1075 (2004).

[31] J. D. Thompson, T. G. Tiecke, N. P. de Leon, J. Feist, A. V. Akimov, M. Gullans, A. S. Zibrov, V. Vuletić, and M. D. Lukin. Coupling a single trapped atom to a nanoscale optical cavity. *Science* **340**, 1202 (2013).

[32] S. Kato and T. Aoki. Strong Coupling between a Trapped Single Atom and an All-Fiber Cavity. *Phys. Rev. Lett.* **115**, 093603 (2015).

[33] R. Thompson, G. Rempe, and H. Kimble. Observation of normal-mode splitting for an atom in an optical cavity. *Phys. Rev. Lett.* **68**, 1132 (1992).

[34] T. Wilk, S. C. Webster, A. Kuhn, and G. Rempe. Single-atom single-photon quantum interface. *Science* **317**, 488 (2007).

[35] H. P. Specht, C. Nölleke, A. Reiserer, M. Uphoff, E. Figueroa, S. Ritter, and G. Rempe. A single-atom quantum memory. *Nature* **473**, 190 (2011).

[36] A. Reiserer, N. Kalb, G. Rempe, and S. Ritter. A quantum gate between a flying optical photon and a single trapped atom. *Nature* **508**, 237 (2014).

[37] N. Kalb, A. Reiserer, S. Ritter, and G. Rempe. Heralded Storage of a Photonic Quantum Bit in a Single Atom. *Phys. Rev. Lett.* **114**, 220501 (2015).

[38] P. Treutlein, P. Hommelhoff, T. Steinmetz, T. W. Hänsch, and J. Reichel. Coherence in Microchip Traps. *Phys. Rev. Lett.* **92**, 203005 (2004).

[39] C. Deutsch, F. Ramirez-Martinez, C. Lacroûte, F. Reinhard, T. Schneider, J. N. Fuchs, F. Piéchon, F. Laloë, J. Reichel, and P. Rosenbusch. Spin Self-Rephasing and Very Long Coherence Times in a Trapped Atomic Ensemble. *Phys. Rev. Lett.* **105**, 020401 (2010).

[40] A. G. Radnaev, Y. O. Dudin, R. Zhao, H. H. Jen, S. D. Jenkins, A. Kuzmich, and T. A. B. Kennedy. A quantum memory with telecom-wavelength conversion. *Nat. Phys.* **6**, 894 (2010).

[41] B. Albrecht, P. Farrera, X. Fernandez-Gonzalvo, M. Cristiani, and H. de Riedmatten. A waveguide frequency converter connecting rubidium-based quantum memories to the telecom C-band. *Nat. Commun.* **5**, 3376 (2014).

[42] T. Chanelière, D. N. Matsukevich, S. D. Jenkins, T. A. B. Kennedy, M. S. Chapman, and A. Kuzmich. Quantum Telecommunication Based on Atomic Cascade Transitions. *Phys. Rev. Lett.* **96**, 093604 (2006).

[43] L.-M. Duan, B. Wang, and H. J. Kimble. Robust quantum gates on neutral atoms with cavity-assisted photon scattering. *Phys. Rev. A* **72**, 032333 (2005).

[44] D. Hunger, T. Steinmetz, Y. Colombe, C. Deutsch, T. W. Hänsch, and J. Reichel. A fiber Fabry–Perot cavity with high finesse. *New J. Phys.* **12**, 065038 (2010).

[45] A. Muller, E. B. Flagg, J. R. Lawall, and G. S. Solomon. Ultrahigh-finesse, low-mode-volume Fabry-Perot microcavity. *Opt. Lett.* **35**, 2293 (2010).

[46] D. Hunger, C. Deutsch, R. J. Barbour, R. J. Warburton, and J. Reichel. Laser micro-fabrication of concave, low-roughness features in silica. *AIP Adv.* **2**, 012119 (2012).

[47] H. Kaupp, C. Deutsch, H.-C. Chang, J. Reichel, T. W. Hänsch, and D. Hunger. Scaling laws of the cavity enhancement for nitrogen-vacancy centers in diamond. *Phys. Rev. A* **88**, 053812 (2013).

[48] R. Gehr, J. Volz, G. Dubois, T. Steinmetz, Y. Colombe, B. L. Lev, R. Long, J. Estève, and J. Reichel. Cavity-Based Single Atom Preparation and High-Fidelity Hyperfine State Readout. *Phys. Rev. Lett.* **104**, 203602 (2010).

[49] P. Münstermann, T. Fischer, P. W. H. Pinkse, and G. Rempe. Single slow atoms from an atomic fountain observed in a high-finesse optical cavity. *Opt. Commun.* **159**, 63 (1999).

[50] S. Ritter, C. Nölleke, C. Hahn, A. Reiserer, A. Neuzner, M. Uphoff, M. Mücke, E. Figueroa, J. Bochmann, and G. Rempe. An elementary quantum network of single atoms in optical cavities. *Nature* **484**, 195 (2012).

[51] J. Volz, R. Gehr, G. Dubois, J. Estève, and J. Reichel. Measurement of the internal state of a single atom without energy exchange. *Nature* **475**, 210 (2011).

[52] E. Jaynes and F. Cummings. Comparison of quantum and semiclassical radiation theories with application to the beam maser. *Proc. IEEE* **51**, 89 (1963).

[53] E. Purcell. Spontaneous Emission Probabilities at Radio Frequencies. *Phys. Rev.* **69**, 681 (1946).

[54] J. Bochmann, M. Mücke, G. Langfahl-Klabes, C. Erbel, B. Weber, H. P. Specht, D. L. Moehring, and G. Rempe. Fast Excitation and Photon Emission of a Single-Atom-Cavity System. *Phys. Rev. Lett.* **101**, 223601 (2008).

[55] C. K. Law and H. J. Kimble. Deterministic generation of a bit-stream of single-photon pulses. *J. Mod. Opt.* **44**, 2067 (1997).

[56] J. Bochmann. *Coherent Dynamics and State Detection of Single Atoms in a Cavity*. PhD thesis. Technische Universität München, 2010.

[57] T. Aoki, B. Dayan, E. Wilcut, W. P. Bowen, A. S. Parkins, T. J. Kippenberg, K. J. Vahala, and H. J. Kimble. Observation of strong coupling between one atom and a monolithic microresonator. *Nature* **443**, 671 (2006).

[58] C. Junge, D. O'Shea, J. Volz, and A. Rauschenbeutel. Strong Coupling between Single Atoms and Nontransversal Photons. *Phys. Rev. Lett.* **110**, 213604 (2013).

[59] I. Shomroni, S. Rosenblum, Y. Lovsky, O. Bechler, G. Guendelman, and B. Dayan. All-optical routing of single photons by a one-atom switch controlled by a single photon. *Science* **345**, 903 (2014).

[60] J. Petersen, J. Volz, and A. Rauschenbeutel. Chiral nanophotonic waveguide interface based on spin-orbit interaction of light. *Science* **346**, 67 (2014).

[61] Y. Akahane, T. Asano, B.-S. Song, and S. Noda. High-Q photonic nanocavity in a two-dimensional photonic crystal. *Nature* **425**, 944 (2003).

[62] T. Yoshie, A. Scherer, J. Hendrickson, G. Khitrova, H. M. Gibbs, G. Rupper, C. Ell, O. B. Shchekin, and D. G. Deppe. Vacuum Rabi splitting with a single quantum dot in a photonic crystal nanocavity. *Nature* **432**, 200 (2004).

[63] L. Tong, R. R. Gattass, J. B. Ashcom, S. He, J. Lou, M. Shen, I. Maxwell, and E. Mazur. Subwavelength-diameter silica wires for low-loss optical wave guiding. *Nature* **426**, 816 (2003).

[64] E. Vetsch, D. Reitz, G. Sagué, R. Schmidt, S. T. Dawkins, and A. Rauschenbeutel. Optical Interface Created by Laser-Cooled Atoms Trapped in the Evanescent Field Surrounding an Optical Nanofiber. *Phys. Rev. Lett.* **104**, 203603 (2010).

[65] S. Slama, S. Bux, G. Krenz, C. Zimmermann, and P. W. Courteille. Superradiant Rayleigh Scattering and Collective Atomic Recoil Lasing in a Ring Cavity. *Phys. Rev. Lett.* **98**, 053603 (2007).

[66] F. Brennecke, T. Donner, S. Ritter, T. Bourdel, M. Köhl, and T. Esslinger. Cavity QED with a Bose-Einstein condensate. *Nature* **450**, 268 (2007).

[67] Y. Colombe, T. Steinmetz, G. Dubois, F. Linke, D. Hunger, and J. Reichel. Strong atom-field coupling for Bose-Einstein condensates in an optical cavity on a chip. *Nature* **450**, 272 (2007).

[68] M. Wolke, J. Klinner, H. Kessler, and A. Hemmerich. Cavity cooling below the recoil limit. *Science* **337**, 75 (2012).

[69] P. F. Herskind, A. Dantan, J. P. Marler, M. Albert, and M. Drewsen. Realization of collective strong coupling with ion Coulomb crystals in an optical cavity. *Nat. Phys.* **5**, 494 (2009).

[70] J. D. Thompson, B. M. Zwickl, A. M. Jayich, F. Marquardt, S. M. Girvin, and J. G. E. Harris. Strong dispersive coupling of a high-finesse cavity to a micromechanical membrane. *Nature* **452**, 72 (2008).

[71] I. Favero, S. Stapfner, D. Hunger, P. Paulitschke, J. Reichel, H. Lorenz, E. M. Weig, and K. Karrai. Fluctuating nanomechanical system in a high finesse optical microcavity. *Opt. Express* **17**, 12813 (2009).

[72] J. McKeever, J. R. Buck, A. D. Boozer, A. Kuzmich, H.-C. Nägerl, D. M. Stamper-Kurn, and H. J. Kimble. State-Insensitive Cooling and Trapping of Single Atoms in an Optical Cavity. *Phys. Rev. Lett.* **90**, 133602 (2003).

[73] S. Nussmann, M. Hijlkema, B. Weber, F. Rohde, G. Rempe, and A. Kuhn. Submicron Positioning of Single Atoms in a Microcavity. *Phys. Rev. Lett.* **95**, 173602 (2005).

[74] G. R. Guthöhrlein, M. Keller, K. Hayasaka, W. Lange, and H. Walther. A single ion as a nanoscopic probe of an optical field. *Nature* **414**, 49 (2001).

[75] B. Weber, H. P. Specht, T. Müller, J. Bochmann, M. Mücke, D. L. Moehring, and G. Rempe. Photon-Photon Entanglement with a Single Trapped Atom. *Phys. Rev. Lett.* **102**, 030501 (2009).

[76] M. Hennrich, T. Legero, A. Kuhn, and G. Rempe. Vacuum-Stimulated Raman Scattering Based on Adiabatic Passage in a High-Finesse Optical Cavity. *Phys. Rev. Lett.* **85**, 4872 (2000).

[77] A. Kuhn, M. Hennrich, T. Bondo, and G. Rempe. Controlled generation of single photons from a strongly coupled atom-cavity system. *Appl. Phys. B* **69**, 373 (1999).

[78] M. Lax, W. H. Louisell, and W. B. McKnight. From Maxwell to paraxial wave optics. *Phys. Rev. A* **11**, 1365 (1975).

[79] A. E. Siegman. *Lasers*. Sausalito: University Science Books, 1986.

[80] K. Durak, C. H. Nguyen, V. Leong, S. Straupe, and C. Kurtsiefer. Diffraction-limited Fabry–Perot cavity in the near concentric regime. *New J. Phys.* **16**, 103002 (2014).

[81] H. Mabuchi, Q. A. Turchette, M. S. Chapman, and H. J. Kimble. Real-time detection of individual atoms falling through a high-finesse optical cavity. *Opt. Lett.* **21**, 1393 (1996).

[82] C. J. Hood, M. S. Chapman, T. W. Lynn, and H. J. Kimble. Real-Time Cavity QED with Single Atoms. *Phys. Rev. Lett.* **80**, 4157 (1998).

[83] M. Khudaverdyan, W. Alt, I. Dotsenko, T. Kampschulte, K. Lenhard, A. Rauschenbeutel, S. Reick, K. Schörner, A. Widera, and D. Meschede. Controlled insertion and retrieval of atoms coupled to a high-finesse optical resonator. *New J. Phys.* **10**, 073023 (2008).

[84] M. Koch, C. Sames, A. Kubanek, M. Apel, M. Balbach, A. Ourjoumtsev, P. W. H. Pinkse, and G. Rempe. Feedback cooling of a single neutral atom. *Phys. Rev. Lett.* **105**, 173003 (2010).

[85] P. B. R. Nisbet-Jones, J. Dilley, D. Ljunggren, and A. Kuhn. Highly efficient source for indistinguishable single photons of controlled shape. *New J. Phys.* **13**, 103036 (2011).

[86] A. Reiserer, C. Nölleke, S. Ritter, and G. Rempe. Ground-state cooling of a single atom at the center of an optical cavity. *Phys. Rev. Lett.* **110**, 223003 (2013).

[87] A. Reiserer, S. Ritter, and G. Rempe. Nondestructive detection of an optical photon. *Science* **342**, 1349 (2013).

[88] J. Gallego, S. Ghosh, S. K. Alavi, W. Alt, M. Martinez-Dorantes, D. Meschede, and L. Ratschbacher. High-finesse fiber Fabry–Perot cavities: stabilization and mode matching analysis. *Appl. Phys. B* **122**, 47 (2016).

[89] A. Bick, C. Staarmann, P. Christoph, O. Hellmig, J. Heinze, K. Sengstock, and C. Becker. The role of mode match in fiber cavities. *Rev. Sci. Instrum.* **87**, 013102 (2016).

[90] E.-G. Neumann. *Single-Mode Fibers*. Vol. 57. Springer Series in Optical Sciences. Berlin: Springer, 1988.

[91] W. B. Joyce and B. C. DeLoach. Alignment of Gaussian beams. *Appl. Opt.* **23**, 4187 (1984).

[92] G. Rempe, R. J. Thompson, H. J. Kimble, and R. Lalezari. Measurement of ultralow losses in an optical interferometer. *Opt. Lett.* **17**, 363 (1992).

[93] M. Trupke, E. A. Hinds, S. Eriksson, E. A. Curtis, Z. Moktadir, E. Kukharenka, and M. Kraft. Microfabricated high-finesse optical cavity with open access and small volume. *Appl. Phys. Lett.* **87**, 211106 (2005).

[94] C. Derntl, M. Schneider, J. Schalko, A. Bittner, J. Schmiedmayer, U. Schmid, and M. Trupke. Arrays of open, independently tunable microcavities. *Opt. Express* **22**, 22111 (2014).

[95] G. W. Biedermann, F. M. Benito, K. M. Fortier, D. L. Stick, T. K. Loyd, P. D. D. Schwindt, C. Y. Nakakura, R. L. Jarecki, and M. G. Blain. Ultrasmooth microfabricated mirrors for quantum information. *Appl. Phys. Lett.* **97**, 181110 (2010).

[96] P. R. Dolan, G. M. Hughes, F. Grazioso, B. R. Patton, and J. M. Smith. Femtoliter tunable optical cavity arrays. *Opt. Lett.* **35**, 3556 (2010).

[97] A. D. Pfister, M. Salz, M. Hettrich, U. G. Poschinger, and F. Schmidt-Kaler. A Quantum Repeater Node with Trapped Ions: A Realistic Case Example. *Appl. Phys. B* **122**, 89 (2016).

[98] Z. Di, H. V. Jones, P. R. Dolan, S. M. Fairclough, M. B. Wincott, J. Fill, G. M. Hughes, and J. M. Smith. Controlling the emission from semiconductor quantum dots using ultra-small tunable optical microcavities. *New J. Phys.* **14**, 103048 (2012).

[99] M. Steiner, H. M. Meyer, C. Deutsch, J. Reichel, and M. Köhl. Single Ion Coupled to an Optical Fiber Cavity. *Phys. Rev. Lett.* **110**, 043003 (2013).

[100] J. Miguel-Sánchez, A. Reinhard, E. Togan, T. Volz, A. Imamoglu, B. Besga, J. Reichel, and J. Estève. Cavity quantum electrodynamics with charge-controlled quantum dots coupled to a fiber Fabry-Perot cavity. *New J. Phys.* **15**, 045002 (2013).

[101] R. Albrecht, A. Bommer, C. Deutsch, J. Reichel, and C. Becher. Coupling of a Single Nitrogen-Vacancy Center in Diamond to a Fiber-Based Microcavity. *Phys. Rev. Lett.* **110**, 243602 (2013).

[102] B. Petrak, N. Djeu, and A. Muller. Purcell-enhanced Raman scattering from atmospheric gases in a high-finesse microcavity. *Phys. Rev. A* **89**, 023811 (2014).

[103] M. Mader, J. Reichel, T. W. Hänsch, and D. Hunger. A scanning cavity microscope. *Nat. Commun.* **6**, 7249 (2015).

[104] P. A. Temple, W. H. Lowdermilk, and D. Milam. Carbon dioxide laser polishing of fused silica surfaces for increased laser-damage resistance at 1064 nm. *Appl. Opt.* **21**, 3249 (1982).

[105] D. K. Armani, T. J. Kippenberg, S. M. Spillane, and K. J. Vahala. Ultra-high-Q toroid microcavity on a chip. *Nature* **421**, 925 (2003).

[106] M. von Allmen and A. Blatter. *Laser-Beam Interactions with Materials*. Vol. 2. Springer Series in Materials Science. Berlin: Springer, 1995.

[107] R. Kitamura, L. Pilon, and M. Jonasz. Optical constants of silica glass from extreme ultraviolet to far infrared at near room temperature. *Appl. Opt.* **46**, 8118 (2007).

[108] W. J. Witteman. *The CO_2 Laser*. Vol. 53. Springer Series in Optical Sciences. Berlin: Springer, 1987.

[109] S. T. Yang, M. J. Matthews, S. Elhadj, V. G. Draggoo, and S. E. Bisson. Thermal transport in CO_2 laser irradiated fused silica: In situ measurements and analysis. *J. Appl. Phys.* **106**, 103106 (2009).

[110] E. Mendez, K. M. Nowak, H. J. Baker, F. J. Villarreal, and D. R. Hall. Localized CO_2 laser damage repair of fused silica optics. *Appl. Opt.* **45**, 5358 (2006).

[111] H. S. Carslaw and J. C. Jaeger. *Conduction of Heat in Solids*. 2nd ed. Oxford: Oxford University Press, 1959.

[112] B. Petrak, K. Konthasinghe, S. Perez, and A. Muller. Feedback-controlled laser fabrication of micromirror substrates. *Rev. Sci. Instrum.* **82**, 123112 (2011).

[113] M. Uphoff, M. Brekenfeld, G. Rempe, and S. Ritter. Frequency splitting of polarization eigenmodes in microscopic Fabry–Perot cavities. *New J. Phys.* **17**, 013053 (2015).

[114] H. E. Bennett and J. O. Porteus. Relation Between Surface Roughness and Specular Reflectance at Normal Incidence. *J. Opt. Soc. Am.* **51**, 123 (1961).

[115] H. Davies. The reflection of electromagnetic waves from a rough surface. *Proc. IEE - Part IV Inst. Monogr.* **101**, 209 (1954).

[116] T. A. Birks, J. C. Knight, and P. S. Russell. Endlessly single-mode photonic crystal fiber. *Opt. Lett.* **22**, 961 (1997).

[117] J. Knight, T. Birks, R. Cregan, P. Russell, and J.-P. de Sandro. Large mode area photonic crystal fibre. *Electron. Lett.* **34**, 1347 (1998).

[118] J. Lee, G. Vrijsen, I. Teper, O. Hosten, and M. A. Kasevich. Many-atom-cavity QED system with homogeneous atom-cavity coupling. *Opt. Lett.* **39**, 4005 (2014).

[119] J. R. Sites, P. Gilstrap, and R. Rujkorakarn. Ion Beam Sputter Deposition Of Optical Coatings. *Opt. Eng.* **22**, 447 (1983).

[120] E. Atanassova, T. Dimitrova, and J. Koprinarova. AES and XPS study of thin RF-sputtered Ta_2O_5 layers. *Appl. Surf. Sci.* **84**, 193 (1995).

[121] B. Brandstätter et al. Integrated fiber-mirror ion trap for strong ion-cavity coupling. *Rev. Sci. Instrum.* **84**, 123104 (2013).

[122] D. Z. Anderson, J. C. Frisch, and C. S. Masser. Mirror reflectometer based on optical cavity decay time. *Appl. Opt.* **23**, 1238 (1984).

[123] J. Poirson, F. Bretenaker, M. Vallet, and A. Le Floch. Analytical and experimental study of ringing effects in a Fabry–Perot cavity. Application to the measurement of high finesses. *J. Opt. Soc. Am. B* **14**, 2811 (1997).

[124] D. Kleckner, W. T. M. Irvine, S. S. R. Oemrawsingh, and D. Bouwmeester. Diffraction-limited high-finesse optical cavities. *Phys. Rev. A* **81**, 043814 (2010).

[125] J. Benedikter, T. Hümmer, M. Mader, B. Schlederer, J. Reichel, T. W. Hänsch, and D. Hunger. Transverse-mode coupling and diffraction loss in tunable Fabry–Pérot microcavities. *New J. Phys.* **17**, 053051 (2015).

[126] S. L. Hohmann. *Using optical fibre cavities to create multi-atom entanglement by quantum Zeno dynamics*. PhD thesis. Université Pierre-et-Marie-Curie, 2015.

[127] H. Takahashi, J. Morphew, F. Oručević, A. Noguchi, E. Kassa, and M. Keller. Novel laser machining of optical fibers for long cavities with low birefringence. *Opt. Express* **22**, 31317 (2014).

[128] K. Ott, S. Garcia, R. Kohlhaas, K. Schüppert, P. Rosenbusch, R. Long, and J. Reichel. Millimeter-long Fiber Fabry-Perot cavities. *Opt. Express* **24**, 9839 (2016).

[129] F. Della Valle, U. Gastaldi, G. Messineo, E. Milotti, R. Pengo, L. Piemontese, G. Ruoso, and G. Zavattini. Measurements of vacuum magnetic birefringence using permanent dipole magnets: the PVLAS experiment. *New J. Phys.* **15**, 053026 (2013).

[130] A. Cadène, P. Berceau, M. Fouché, R. Battesti, and C. Rizzo. Vacuum magnetic linear birefringence using pulsed fields: status of the BMV experiment. *Eur. Phys. J. D* **68**, 16 (2014).

[131] M. Durand, J. Morville, and D. Romanini. Shot-noise-limited measurement of sub–parts-per-trillion birefringence phase shift in a high-finesse cavity. *Phys. Rev. A* **82**, 031803 (2010).

[132] T. Müller, K. B. Wiberg, P. H. Vaccaro, J. R. Cheeseman, and M. J. Frisch. Cavity ring-down polarimetry (CRDP): theoretical and experimental characterization. *J. Opt. Soc. Am. B* **19**, 125 (2002).

[133] H. Huang and K. K. Lehmann. Effects of linear birefringence and polarization-dependent loss of supermirrors in cavity ring-down spectroscopy. *Appl. Opt.* **47**, 3817 (2008).

[134] J. L. Hall, J. Ye, and L.-S. Ma. Measurement of mirror birefringence at the sub-ppm level: Proposed application to a test of QED. *Phys. Rev. A* **62**, 013815 (2000).

[135] S. Kuhr et al. Ultrahigh finesse Fabry-Pérot superconducting resonator. *Appl. Phys. Lett.* **90**, 164101 (2007).

[136] J. J. Klein and B. P. Nigam. Birefringence of the Vacuum. *Phys. Rev.* **135**, B1279 (1964).

[137] F. Brandi, F. Della Valle, A. M. De Riva, P. Micossi, F. Perrone, C. Rizzo, G. Ruoso, and G. Zavattini. Measurement of the phase anisotropy of very high reflectivity interferential mirrors. *Appl. Phys. B Lasers Opt.* **65**, 351 (1997).

[138] S. Moriwaki, H. Sakaida, T. Yuzawa, and N. Mio. Measurement of the residual birefringence of interferential mirrors using Fabry-Perot cavity. *Appl. Phys. B Lasers Opt.* **65**, 347 (1997).

[139] M. Brekenfeld. *Faserbasierte Fabry-Perot Resonatoren ultrahoher Finesse.* Diploma thesis [unpublished]. Technische Universität München, 2013.

[140] C. J. Hood, H. J. Kimble, and J. Ye. Characterization of high-finesse mirrors: Loss, phase shifts, and mode structure in an optical cavity. *Phys. Rev. A* **64**, 033804 (2001).

[141] M. Farries and A. Rogers. Temperature dependence of the Kerr effect in a silica optical fibre. *Electron. Lett.* **19**, 890 (1983).

[142] A. M. Smith. Polarization and magnetooptic properties of single-mode optical fiber. *Appl. Opt.* **17**, 52 (1978).

[143] C.-L. Tien, C.-C. Lee, and C.-C. Jaing. The measurement of thin film stress using phase shifting interferometry. *J. Mod. Opt.* **47**, 839 (2000).

[144] H. Kogelnik and T. Li. Laser beams and resonators. *Proc. IEEE* **54**, 1312 (1966).

[145] A. L. Cullen. On the accuracy of the beam-wave theory of the open resonator. *IEEE Trans. Microw. Theory Tech.* **24**, 534 (1976).

[146] C. W. Erickson. High Order Modes in a Spherical Fabry-Perot Resonator. *IEEE Trans. Microw. Theory Tech.* **23**, 218 (1975).

[147] P. K. Yu and K. M. Luk. High-order azimuthal modes in the open resonator. *Electron. Lett.* **19**, 539 (1983).

[148] K.-M. Luk. Improvement in the resonant formula of a spherical Fabry-Perot resonator with unequal mirrors. *J. Opt. Soc. Am. A* **3**, 3 (1986).

[149] M. Zeppenfeld and P. W. H. Pinkse. Calculating the fine structure of a Fabry-Perot resonator using spheroidal wave functions. *Opt. Express* **18**, 9580 (2010).

[150] M. A. Bandres and J. C. Gutiérrez-Vega. Ince-Gaussian modes of the paraxial wave equation and stable resonators. *J. Opt. Soc. Am. A* **21**, 873 (2004).

[151] L. C. Flatten, A. A. P. Trichet, and J. M. Smith. Spectral engineering of coupled open-access microcavities. *Laser Photon. Rev.* **10**, 257 (2016).

[152] N. Brunner, D. Cavalcanti, S. Pironio, V. Scarani, and S. Wehner. Bell nonlocality. *Rev. Mod. Phys.* **86**, 419 (2014).

[153] M. Riebe et al. Deterministic quantum teleportation with atoms. *Nature* **429**, 734 (2004).

[154] M. D. Barrett et al. Deterministic quantum teleportation of atomic qubits. *Nature* **429**, 737 (2004).

[155] W. Pfaff et al. Unconditional quantum teleportation between distant solid-state quantum bits. *Science* **345**, 532 (2014).

[156] D. L. Moehring, P. Maunz, S. Olmschenk, K. C. Younge, D. N. Matsukevich, L.-M. Duan, and C. Monroe. Entanglement of single-atom quantum bits at a distance. *Nature* **449**, 68 (2007).

[157] J. Hofmann, M. Krug, N. Ortegel, L. Gérard, M. Weber, W. Rosenfeld, and H. Weinfurter. Heralded entanglement between widely separated atoms. *Science* **337**, 72 (2012).

[158] H. Bernien et al. Heralded entanglement between solid-state qubits separated by three metres. *Nature* **497**, 86 (2013).

[159] T. Miya, Y. Terunuma, T. Hosaka, and T. Miyashita. Ultimate low-loss single-mode fibre at 1.55 μm. *Electron. Lett.* **15**, 106 (1979).

[160] D. Deutsch, A. Ekert, R. Jozsa, C. Macchiavello, S. Popescu, and A. Sanpera. Quantum Privacy Amplification and the Security of Quantum Cryptography over Noisy Channels. *Phys. Rev. Lett.* **77**, 2818 (1996).

[161] C. Bennett, G. Brassard, S. Popescu, B. Schumacher, J. Smolin, and W. Wootters. Purification of noisy entanglement and faithful teleportation via noisy channels. *Phys. Rev. Lett.* **76**, 722 (1996).

[162] E. Knill and R. Laflamme. *Concatenated Quantum Codes.* arXiv: quant-ph/9608012 [eprint], 1996.

[163] L. Hartmann, B. Kraus, H.-J. Briegel, and W. Dür. Role of memory errors in quantum repeaters. *Phys. Rev. A* **75**, 032310 (2007).

[164] L. Jiang, J. M. Taylor, K. Nemoto, W. J. Munro, R. Van Meter, and M. D. Lukin. Quantum repeater with encoding. *Phys. Rev. A* **79**, 032325 (2009).

[165] N. K. Bernardes, L. Praxmeyer, and P. van Loock. Rate analysis for a hybrid quantum repeater. *Phys. Rev. A* **83**, 012323 (2011).

[166] M. B. Plenio and S. Virmani. An introduction to entanglement measures. *Quantum Inf. Comput.* **7**, 1 (2007).

[167] V. Scarani, H. Bechmann-Pasquinucci, N. Cerf, M. Dušek, N. Lütkenhaus, and M. Peev. The security of practical quantum key distribution. *Rev. Mod. Phys.* **81**, 1301 (2009).

[168] L.-M. Duan, M. D. Lukin, J. I. Cirac, and P. Zoller. Long-distance quantum communication with atomic ensembles and linear optics. *Nature* **414**, 413 (2001).

[169] O. A. Collins, S. D. Jenkins, A. Kuzmich, and T. A. B. Kennedy. Multiplexed memory-insensitive quantum repeaters. *Phys. Rev. Lett.* **98**, 060502 (2007).

[170] N. Sangouard, C. Simon, H. de Riedmatten, and N. Gisin. Quantum repeaters based on atomic ensembles and linear optics. *Rev. Mod. Phys.* **83**, 33 (2011).

[171] C. Simon, H. de Riedmatten, M. Afzelius, N. Sangouard, H. Zbinden, and N. Gisin. Quantum Repeaters with Photon Pair Sources and Multimode Memories. *Phys. Rev. Lett.* **98**, 190503 (2007).

[172] M. Riebe, T. Monz, K. Kim, A. S. Villar, P. Schindler, M. Chwalla, M. Hennrich, and R. Blatt. Deterministic entanglement swapping with an ion-trap quantum computer. *Nat. Phys.* **4**, 839 (2008).

[173] L. Childress, J. M. Taylor, A. S. Sørensen, and M. D. Lukin. Fault-tolerant quantum repeaters with minimal physical resources and implementations based on single-photon emitters. *Phys. Rev. A* **72**, 052330 (2005).

[174] L. Childress, J. M. Taylor, A. S. Sørensen, and M. D. Lukin. Fault-Tolerant Quantum Communication Based on Solid-State Photon Emitters. *Phys. Rev. Lett.* **96**, 070504 (2006).

[175] F. Schmidt-Kaler, H. Häffner, M. Riebe, S. Gulde, G. P. T. Lancaster, T. Deuschle, C. Becher, C. F. Roos, J. Eschner, and R. Blatt. Realization of the Cirac-Zoller controlled-NOT quantum gate. *Nature* **422**, 408 (2003).

[176] F. Jelezko, T. Gaebel, I. Popa, M. Domhan, A. Gruber, and J. Wrachtrup. Observation of coherent oscillation of a single nuclear spin and realization of a two-qubit conditional quantum gate. *Phys. Rev. Lett.* **93**, 130501 (2004).

[177] C. Langer et al. Long-lived qubit memory using atomic ions. *Phys. Rev. Lett.* **95**, 060502 (2005).

[178] P. van Loock, T. D. Ladd, K. Sanaka, F. Yamaguchi, K. Nemoto, W. J. Munro, and Y. Yamamoto. Hybrid quantum repeater using bright coherent light. *Phys. Rev. Lett.* **96**, 240501 (2006).

[179] T. D. Ladd, P. van Loock, K. Nemoto, W. J. Munro, and Y. Yamamoto. Hybrid quantum repeater based on dispersive CQED interactions between matter qubits and bright coherent light. *New J. Phys.* **8**, 184 (2006).

[180] P. van Loock, N. Lütkenhaus, W. J. Munro, and K. Nemoto. Quantum repeaters using coherent-state communication. *Phys. Rev. A* **78**, 062319 (2008).

[181] S. Muralidharan, J. Kim, N. Lütkenhaus, M. D. Lukin, and L. Jiang. Ultrafast and fault-tolerant quantum communication across long distances. *Phys. Rev. Lett.* **112**, 250501 (2014).

[182] E. Saglamyurek, N. Sinclair, J. Jin, J. A. Slater, D. Oblak, F. Bussières, M. George, R. Ricken, W. Sohler, and W. Tittel. Broadband waveguide quantum memory for entangled photons. *Nature* **469**, 512 (2011).

[183] C. Clausen, I. Usmani, F. Bussières, N. Sangouard, M. Afzelius, H. de Riedmatten, and N. Gisin. Quantum storage of photonic entanglement in a crystal. *Nature* **469**, 508 (2011).

[184] M. Uphoff, M. Brekenfeld, G. Rempe, and S. Ritter. An integrated quantum repeater at telecom wavelength with single atoms in optical fiber cavities. *Appl. Phys. B* **122**, 46 (2016).

[185] A. Kramida, Y. Ralchenko, J. Reader, and NIST ASD Team. *NIST Atomic Spectra Database (ver 5.3)*. [Online]. National Institute of Standards and Technology, Gaithersburg, 2015.

[186] M. S. Safronova and U. I. Safronova. Critically evaluated theoretical energies, lifetimes, hyperfine constants, and multipole polarizabilities in ^{87}Rb. *Phys. Rev. A* **83**, 052508 (2011).

[187] H. S. Moon, W.-K. Lee, and H. S. Suh. Hyperfine-structure-constant determination and absolute-frequency measurement of the Rb $4D_{3/2}$ state. *Phys. Rev. A* **79**, 062503 (2009).

[188] J. Dalibard, Y. Castin, and K. Mølmer. Wave-function approach to dissipative processes in quantum optics. *Phys. Rev. Lett.* **68**, 580 (1992).

[189] R. Dum, P. Zoller, and H. Ritsch. Monte Carlo simulation of the atomic master equation for spontaneous emission. *Phys. Rev. A* **45**, 4879 (1992).

[190] L. Tian and H. J. Carmichael. Quantum trajectory simulations of two-state behavior in an optical cavity containing one atom. *Phys. Rev. A* **46**, R6801 (1992).

[191] P. Maunz, D. L. Moehring, S. Olmschenk, K. C. Younge, D. N. Matsukevich, and C. Monroe. Quantum interference of photon pairs from two remote trapped atomic ions. *Nat. Phys.* **3**, 538 (2007).

[192] M. Żukowski, A. Zeilinger, M. A. Horne, and A. K. Ekert. "Event-ready-detectors" Bell experiment via entanglement swapping. *Phys. Rev. Lett.* **71**, 4287 (1993).

[193] H. Weinfurter. Experimental Bell-State Analysis. *Europhys. Lett.* **25**, 559 (1994).

[194] C. Nölleke, A. Neuzner, A. Reiserer, C. Hahn, G. Rempe, and S. Ritter. Efficient Teleportation Between Remote Single-Atom Quantum Memories. *Phys. Rev. Lett.* **110**, 140403 (2013).

[195] G. K. Gulati, B. Srivathsan, B. Chng, A. Cerè, D. Matsukevich, and C. Kurtsiefer. Generation of an exponentially rising single-photon field from parametric conversion in atoms. *Phys. Rev. A* **90**, 033819 (2014).

[196] C. K. Hong, Z. Y. Ou, and L. Mandel. Measurement of subpicosecond time intervals between two photons by interference. *Phys. Rev. Lett.* **59**, 2044 (1987).

[197] C. Nölleke. *Quantum state transfer between remote single atoms*. PhD thesis. Technische Universität München, 2013.

[198] M. Rosenblatt. Remarks on Some Nonparametric Estimates of a Density Function. *Ann. Math. Stat.* **27**, 832 (1956).

[199] E. Parzen. On Estimation of a Probability Density Function and Mode. *Ann. Math. Stat.* **33**, 1065 (1962).

[200] W. Rosenfeld, J. Hofmann, N. Ortegel, M. Krug, F. Henkel, C. Kurtsiefer, M. Weber, and H. Weinfurter. Towards high-fidelity interference of photons emitted by two remotely trapped Rb-87 atoms. *Opt. Spectrosc.* **111**, 535 (2011).

[201] W. Rosenfeld, J. Volz, M. Weber, and H. Weinfurter. Coherence of a qubit stored in Zeeman levels of a single optically trapped atom. *Phys. Rev. A* **84**, 022343 (2011).

[202] D. M. Harber, H. J. Lewandowski, J. M. McGuirk, and E. A. Cornell. Effect of cold collisions on spin coherence and resonance shifts in a magnetically trapped ultracold gas. *Phys. Rev. A* **66**, 053616 (2002).

[203] K. Mattle, H. Weinfurter, P. G. Kwiat, and A. Zeilinger. Dense Coding in Experimental Quantum Communication. *Phys. Rev. Lett.* **76**, 4656 (1996).

[204] A. S. Sørensen and K. Mølmer. Measurement Induced Entanglement and Quantum Computation with Atoms in Optical Cavities. *Phys. Rev. Lett.* **91**, 097905 (2003).

[205] L.-M. Duan and H. Kimble. Scalable Photonic Quantum Computation through Cavity-Assisted Interactions. *Phys. Rev. Lett.* **92**, (2004).

[206] J. Borregaard, P. Kómár, E. M. Kessler, A. S. Sørensen, and M. D. Lukin. Heralded Quantum Gates with Integrated Error Detection in Optical Cavities. *Phys. Rev. Lett.* **114**, 110502 (2015).

[207] F. Marsili et al. Detecting single infrared photons with 93% system efficiency. *Nat. Photonics* **7**, 210 (2013).

[208] M. Mücke, J. Bochmann, C. Hahn, A. Neuzner, C. Nölleke, A. Reiserer, G. Rempe, and S. Ritter. Generation of single photons from an atom-cavity system. *Phys. Rev. A* **87**, 063805 (2013).

[209] B. Efron. Bootstrap Methods: Another Look at the Jackknife. *Ann. Stat.* **7**, 1 (1979).

[210] S. Bratzik, S. Abruzzo, H. Kampermann, and D. Bruss. Quantum repeaters and quantum key distribution: The impact of entanglement distillation on the secret key rate. *Phys. Rev. A* **87**, 062335 (2013).

[211] W. Emkey and C. Jack. Analysis and evaluation of graded-index fiber lenses. *J. Light. Technol.* **5**, 1156 (1987).

[212] R. M. Serra, C. J. Villas-Bôas, N. G. de Almeida, and M. H. Y. Moussa. Frequency up- and down-conversions in two-mode cavity quantum electrodynamics. *Phys. Rev. A* **71**, 045802 (2005).

[213] A. Imamoglu, H. Schmidt, G. Woods, and M. Deutsch. Strongly interacting photons in a nonlinear cavity. *Phys. Rev. Lett.* **79**, 1467 (1997).

[214] S. Rebić, S. M. Tan, A. S. Parkins, and D. F. Walls. Large Kerr nonlinearity with a single atom. *J. Opt. B Quantum Semiclassical Opt.* **1**, 490 (1999).

[215] B. Casabone, K. Friebe, B. Brandstätter, K. Schüppert, R. Blatt, and T. E. Northup. Enhanced quantum interface with collective ion-cavity coupling. *Phys. Rev. Lett.* **114**, 023602 (2015).

[216] R. Reimann, W. Alt, T. Kampschulte, T. Macha, L. Ratschbacher, N. Thau, S. Yoon, and D. Meschede. Cavity-modified collective Rayleigh scattering of two atoms. *Phys. Rev. Lett.* **114**, 023601 (2015).

[217] A. Neuzner, M. Körber, O. Morin, S. Ritter, and G. Rempe. Interference and dynamics of light from a distance-controlled atom pair in an optical cavity. *Nat. Photonics* **10**, 303 (2016).

[218] H. J. Kimble. The quantum internet. *Nature* **453**, 1023 (2008).

Publications

An integrated quantum repeater at telecom wavelength with single atoms in optical cavities.
M. Uphoff, M. Brekenfeld, G. Rempe, and S. Ritter.
Appl. Phys. B **122**, 46 (2016).

Frequency splitting of polarization eigenmodes in microscopic Fabry–Perot cavities.
M. Uphoff, M. Brekenfeld, G. Rempe, and S. Ritter.
New J. Phys. **17**, 013053 (2015).

An elementary quantum network of single atoms in optical cavities.
S. Ritter, C. Nölleke, C. Hahn, A. Reiserer, A. Neuzner, M. Uphoff, M. Mücke, E. Figueroa, J. Bochmann, and G. Rempe.
Nature **484**, 195 (2012).

A single-atom quantum memory
H. P. Specht, C. Nölleke, A. Reiserer, M. Uphoff, E. Figueroa, S. Ritter, and G. Rempe.
Nature **473**, 190 (2011).

Acknowledgments

These days, experimental physics is always a team effort. At the end of this work, I would like to thank the numerous people who made its existence possible.

Starting a new experiment with new methods and technology was an adventure into the unknown. Prof. Gerhard Rempe gave me the opportunity and the resources to pursue these ideas.

From the time, when the experiment was just an idea and the lab was not even empty, to the final draft of the resulting papers, Dr. Stephan Ritter was invaluable for the project. His door was always open to take on any arising issue, no matter whether it was a difficult physics problem or just a mundane detail.

Manuel Brekenfeld joined the lab not long after it had been set up and had a large part in the success of the project over all the years we have worked together. His thorough investigation of possible sources of the frequency splitting of polarization eigenmodes resulted in the non-paraxial theory presented in this thesis. He also had an amazingly steady hand when it came to align the miniature mechanics necessary for handling optical fibers. I wish him and Dominik Niemietz the best success in continuing the experiments with fiber cavities.

The experiments would not have been possible without the support of the technicians Josef Bayerl, Tobias Urban, Franz Denk, Helmut Stehbeck, and Thomas Wiesmeier. Special thanks go to Josef Bayerl and Tobias Urban and the MPQ workshop for the design and the construction of the assembly that held the fibers for the ion-beam sputtering coating process.

The students Johannes Lang, Markus Krottenmüller, and Robert Schittko all left their mark in the lab with their ideas and the devices they built.

After introducing me to lab work during my diploma thesis, Holger Specht went to industry, but did not lose contact. He provided the atomic-force-microscopy measurements of the fiber end facets that are presented in this thesis.

Finally, I would like to thank all the members of the Quantum Dynamics division over the last years, who have contributed to such a nice working atmosphere, who have taken part in discussions about physics and have given new ideas to work on, who have provided access to the treasure trove of lab equipment that their lab has become, and who took part in the recreational activities in- and outside the institute that cleared the mind for new ideas.